Passive and Active Mechanical Responses of Axons

by

Sukh Veer

A thesis submitted for the degree of

Doctor of Philosophy

to the

Jawaharlal Nehru University



Soft Condensed Matter Group
Raman Research Institute
Bangalore, INDIA

May 2026

Copyright © Sukh Veer, May 2026

For my family,

and for my late sister,

whose memory guides me always

Declaration

I, **Sukh Veer** (Enrolment No. RRI/2017/09), declare that the work reported in this thesis titled **'Passive and active mechanical responses of axons'** is entirely original. This thesis has been composed by me at **Raman Research Institute (RRI)** under the supervision of Professor **Pramod A Pullarkat** and is the result of my own work unless otherwise stated. I further declare that the subject matter presented in this thesis has not previously formed the basis for awarding any degree, diploma, membership, associateship, fellowship, or any other similar title of any university or institution. I also declare that this thesis has been checked using the plagiarism software DRILLBIT.

Prof. Pramod A Pullarkat
(Thesis Supervisor)
Raman Research Institute
Bengaluru-560080, India

Sukh Veer
(Student)
Raman Research Institute
Bengaluru-560080, India

Certificate

This is to certify that the thesis entitled **'Passive and active mechanical responses of axons'**, submitted by **Sukh Veer** for the award of the degree of **Doctor of Philosophy** of Jawaharlal Nehru University is his original work. This has not been published or submitted to any other University for any other degree or diploma.

Prof. Tarun Souradeep
(Director)
Raman Research Institute
Bengaluru-560080, India

Prof. Pramod A Pullarkat
(Thesis Supervisor)
Raman Research Institute
Bengaluru-560080, India

Acknowledgements

My PhD journey has been marked by both challenges and achievements, and it has also been a period of significant personal growth. I am deeply grateful to the many individuals whose support and encouragement made the completion of this thesis possible. I would like to take this opportunity to sincerely acknowledge and thank them for their invaluable contributions.

I would like to begin by expressing my deepest gratitude to my family for their unconditional love, encouragement, and patience throughout this journey. Their constant support has given me the strength and determination to pursue my goals, even during the most challenging times. I am especially thankful for the many sacrifices they made and for always believing in my abilities, even when I doubted myself. My late sister instilled in me the value of cherishing the time we have with family, my mother and sisters taught me the meaning of unconditional love, and my father showed me the importance of making sacrifices for loved ones without seeking recognition. At times, our differing beliefs presented challenges, but they ultimately contributed to my personal growth and resilience. Without their love and faith, this work would not have been possible.

I am profoundly grateful to my supervisor, Prof. Pramod Pullarkat, for his invaluable guidance, mentorship, and encouragement throughout my doctoral research. His patience, insightful feedback, and unwavering support at every stage have not only shaped this thesis but also helped me grow as an independent researcher. I am especially thankful for the academic freedom he granted me, which allowed me to explore ideas and develop my own approach to research. I also greatly value the times when our perspectives differed, as his thoughtful criticism and alternative viewpoints encouraged me to think more deeply, consider different possibilities, and learn how to present and defend my ideas convincingly. Beyond being an excellent mentor, I deeply appreciate him as a person for his

kindness, integrity, and generosity. It has been a privilege to learn under his supervision.

I am grateful to my advisory committee members, Prof. Sayantan Majumdar and Prof. Shashi Thutupalli, for regularly reviewing my progress and providing valuable feedback and guidance throughout my doctoral journey. I would also like to thank my coursework professors — Prof. V. A. Raghunathan, Prof. Gautam Vivek Soni, Prof. Ranjini Bandyopadhyay, Prof. Sanjib Sabhapandit, and Prof. Pramod A. Pullarkat - for their inspiring lectures and the strong academic foundation they provided. In addition, I had the privilege of auditing courses at IISc, where I greatly benefited from the teachings of Prof. Sriram Ramaswamy, Prof. Shashi Thutupalli, and Prof. Vijay Krishnamurthy.

I would also like to sincerely thank my collaborators — Prof. Andrew Callan-Jones, Sushil Dubey, Prof. Sayantan Majumdar, Prof. Hema Somanathan, Chinmay Hemant Joshi, Prof. Aurnab Ghose, and Shivani Bodas — for their stimulating discussions, constructive suggestions, and willingness to share their expertise. Their contributions have significantly enriched the scope and depth of this work.

My heartfelt thanks extend to my labmates for providing a friendly, supportive, and motivating atmosphere in the lab. I am especially grateful for the numerous discussions, brainstorming sessions, and the camaraderie that made the long research hours both productive and enjoyable. A special thanks to Sushil Dubey for teaching me many essential things at the beginning of my PhD, and to Arsalan for the tracking code as well as for helping with photographs of the setup and Ashish for many insightful discussions. I am also thankful to my present lab members—Deepak, Pooja, Makrand, Antaran, and Gayathri—and to my previous lab members—Preteesh, Madhu, Gopika, Laxmi, Shrinivas, Niharika, Amal, Shivani, Suriya, Prashanti, Abhigyaan, Sayooj, Praveen, Rahul, Divyang, Binsha, Ritu and Hari—for their constant help and support in various ways during my PhD journey.

I gratefully acknowledge the Soft Condensed Matter (SCM) department at RRI for providing an excellent academic environment, scientific resources, and a culture of open exchange of ideas, all of which have been crucial for this work. I would also like to sincerely thank the SCM group secretaries — Radhakrishna, Amudha, Chaitanya, and Gayathri — along with the staff members Raja, Murali, Naveen, and Ishaq for their kind support. I am thankful as well to Vasudha, Srinivasa, and Vinay. A special thanks goes to Serene and Yatheendran for their immense help and for always being so gentle and warm with me. I am also indebted to the RRI administration for efficiently managing official and formal matters during my time here. In addition, I am grateful to C. S. R. Murthy, Naresh, Vidya, Radha, Shailaja, Harini, and Marisa for their valuable assistance.

My heartfelt thanks go to the RRI workshop staff — including Ibrahim, Anand, Sivasakthi, Kannan, and others — for their skillful technical assistance, which was essential for carrying out several parts of the experiments.

I am sincerely grateful to the library staff, in particular Meera, Manjunath, and Nagaraj, for their support. I also wish to thank the members of the computer department, especially Jacob, Sridhar, and others, for their technical assistance. My thanks further extend to the Purchase and Accounts sections, as well as to G. B. Suresh, Sachin, Muneeswaran, and the staff of the civil and electrical departments for their valuable help.

I am also grateful to the RRI medical facility and its doctors—Dr. Archana, Dr. Prasaad, Dr. Sanjay Rao and Mr. B.G. Shridhar—for their care and support. My appreciation also goes to nurses R. Shanthamma and Preethi H. P. for their assistance.

I would like to acknowledge my teachers — Vimal, Sudheer, Sanjay, Alok, Sachin, Raj Bihari, and Vimilesh — for their encouragement and inspiration.

I sincerely thank my close friends Anish, Vinay, and Avika for their unwavering

support and companionship. I am especially grateful to my friends at RRI — Anand, Chandeshwer, Saurabh, Ashish, Nancy, Vishnu, Arslan, Hari Krishna, Sukanya, Puneet and many others — for their constant support, encouragement, and the fun moments we shared together. I also extend my thanks to my friends Mayank, Priya, Vipin, Vaishali, Smita, Anuj and Bharti for their encouragement and kindness.

Last but not least, I am thankful to those whose critical questions and perspectives challenged my ideas, as they helped me refine my thinking and strengthened this work. Just as importantly, I am grateful to the people in my personal life whose differing views and constructive criticism have shaped my character, encouraged self-reflection, and contributed greatly to my personal growth. Their influence has been invaluable, and I carry these lessons with me beyond this thesis.

Sukh Veer
Bangalore
May 2026

Synopsis

The nervous system is a remarkably complex network that enables the body to sense, respond, and adapt to the world around it [1]. At the heart of this system are neurons and glial cells [2], with neurons responsible for receiving, processing and transmitting electrical signals and glial cells providing critical support. Among the most essential parts of a neuron are its axons, long slender projections that carry signals across long distances within the body. These axons, along with dendrites, are constantly subjected to mechanical forces, not only during traumatic events like brain injuries [3, 4] but also during everyday normal physical activities involving limb movements [5, 6], such as walking, running, jumping, and playing contact sports [7], as well as during processes like tissue growth [8,9]. Brain injuries, particularly traumatic brain injuries (TBI), can cause serious mechanical deformation of axons and their cytoskeleton [4], leading to structural damage, disrupted communication between neurons, and long-term cognitive and behavioral impairments. Thus, understanding how axons and their cytoskeleton respond to these forces, both in injury and in normal function is crucial.

As part of this thesis, we build upon micro-extensional rheometer (MER) originally developed by Giri et al. [10], which we subsequently modified and employed in our previous studies [11–13], along with additional refinements presented in this thesis. In addition to these experimental advancements, this thesis focuses

on studying axon mechanics and exploring the underlying cytoskeletal responses. Furthermore, we develop mathematical models of axonal mechanics, solving them numerically and some analytically, to complement our experimental findings. Finally, we investigate the axonal cytoskeleton's structural response to mechanical perturbations, using a home-built stretcher device designed for this purpose and STED nanoscopy.

Advancements in the Micro-Extensional Rheometer

The MER was further refined to meet the evolving needs of axonal experiments. Several LabVIEW programs were refined and developed to implement different rheological protocols in feedback mode, including step strain, successive step strains, and cyclic ramp loading. Additionally, the elastic modulus of the optical fiber was re-calibrated by fixing one end in a horizontal position and hanging a weight at the other end. These values were then used to estimate the force constant of the cantilever. We also enhanced our setup to be capable of simultaneous force measurements and fluorescence imaging while stretching axons.

Exploring axonal strain relaxation, tension responses and cytoskeletal dynamics

To study axonal strain relaxation, we stretched axons cultured on glass coverslips using the MER and monitored their relaxation back to the initial state after release. We observed that axons exhibit viscoelastic strain relaxation behavior. To investigate the effect of time-dependent processes such as stress relaxation and potential cytoskeletal rearrangements on strain relaxation, we carried out experiments where axons were first stretched and released immediately, allowing them to relax. After the relaxation was complete, the axons were stretched again and held in the stretched position for 10 minutes, during which both stresses and the cytoskeleton adjusted toward a new steady state before being released. We found that axon strain relaxation is slower when axons are held in the stretched

position for 10 minutes before release, compared to immediate release, an effect of waiting time that can be linked to underlying cytoskeletal rearrangements. Additionally, we performed cytoskeleton perturbation experiments by altering the stability of microtubules, actin filaments, to examine how these cytoskeletal elements influence the strain relaxation behavior. Our results indicate that microtubule stabilization slows down while microtubule destabilization increases the strain relaxation rate. Moreover, actin destabilization also slows down strain relaxation rate. Our experiments also suggest that strain relaxation in thicker axons is slower than in thinner axons, showing a possible dependence of relaxation dynamics on axonal diameter. This difference could be due to variations in the number of or an altered ratio of cytoskeletal filaments, which can influence the relaxation behavior. This thesis also discusses tension measurements under cyclic ramp and step strain conditions, which are anticipated to further enhance our understanding of axonal mechanical responses.

Investigation of axonal buckling behavior

In this part of the thesis, we investigate the buckling behavior of axons following stretch and release. A striking feature observed in the stretch-and-release experiments is that axons commonly develop waviness upon release from the cantilever after imposing a 20% strain. This buckling is significantly more pronounced when axons are released after a 10-minute waiting period, compared to immediate release. Over time, buckling gradually subsides, suggesting dynamic structural rearrangements within the axon. This behavior indicates that the waiting period before release may allow internal stresses to relax and redistribute, and the cytoskeleton to rearrange thereby amplifying the buckling response. Notably, the characteristic wavelengths of the axonal buckling decreases monotonically as the relaxation progresses. We also observed that microtubule stability affects the characteristic wavelengths of axonal buckling. For instance, when we stabilized microtubules using Taxol, a microtubule-stabilizing drug, axons exhibited buckling with relatively longer wavelengths. This suggests that microtubule stability,

as well as the number of microtubules within the bundle, can influence the axonal buckling behavior and its characteristic wavelengths.

Modeling axonal response to mechanical stimuli

We have developed simplified trial models to capture the mechanical responses of axons, specifically initially focusing on strain and tension relaxation behavior. Our results suggest that the passive mechanical behavior of axons can be understood by considering a parallel combination of two types of viscoelastic elements: one behaving like a viscoelastic solid and the other like a viscoelastic liquid. Motivated by this observation, we first explored a parallel combination of the Kelvin-Voigt and Maxwell models, where the Kelvin-Voigt model represents a viscoelastic solid, and the Maxwell model represents a viscoelastic liquid. One limitation of this combination is that it does not allow for step strain application, whereas step strain experiments were performed on axons. To address this limitation, we also considered a parallel combination of the Zener and Maxwell models. In these models, all mechanical parameters (elastic and viscous moduli) were assumed to be linear (strain-independent), which is a further simplification compared to the potential nonlinear mechanical behavior of axons. To better align with axonal cytoskeleton dynamics and overcome the limitations mentioned, we are also developing extended models by incorporating protein-based mechanisms, such as folding-unfolding dynamics (e.g., spectrin [12]) and binding-unbinding behaviors (e.g., tau proteins interacting with microtubules). We also developed a simplified model for the buckling behavior of the axons, treating the microtubule core as a viscoelastic rod that behaves like a fluid at long timescales, embedded in an elastic medium. This model captures key features of the buckling behavior, including the emergence of short-wavelength buckling due to compression from cortical relaxation.

Exploring cytoskeletal structural changes in axons following mechanical stimuli

In this part of the thesis, we explore the structural rearrangements and changes in the axonal cytoskeleton following mechanical perturbation. For example, we explore how the actin-spectrin membrane periodic skeleton (MPS) reorganizes following mechanical perturbations. To investigate this, cells are cultured on PDMS sheets, stretched using a home-built stretcher, fixed and stained, and then imaged using STED nanoscopy.

Summary

In this thesis, I will first describe the improvements made to the MER setup. Building upon this, I present experiments on axonal strain relaxation and buckling under mechanical loading, providing insights into the viscoelastic nature of axons. I also will discuss tension measurements performed under ramp and step strain conditions to probe the axonal mechanical responses further. Subsequently, I will introduce modeling aimed at capturing axonal behavior, starting with simplified viscoelastic models and moving toward extended models incorporating protein-based mechanisms such as spectrin folding-unfolding and tau binding-unbinding dynamics. A simplified model to describe axonal buckling behavior observed in the experiments will also be presented. Finally, I will present structural responses of cytoskeletal filaments in axons under mechanical perturbations.

List of publications

1. Sushil Dubey, Chinmay Hemant Joshi, Sukh Veer, Divya Uma, Hema Somanathan, Sayantan Majumdar, and Pramod A Pullarkat. Strain softening and stiffening responses of spider silk fibers probed using a micro-extension rheometer. Soft Matter, 16(2):487–493, 2020. DOI. https://doi.org/10.1039/C9SM01572H.

2. Sushil Dubey, Sukh Veer, RV Seshagiri Rao, Chirag Kalelkar, and Pramod A Pullarkat. Investigation of soft and living matter using a micro-extensional rheometer. Journal of Physics: Condensed Matter, 33(8):084003, 2020. DOI. https://doi.org/10.1088/1361-648X/abc943.

3. Sushil Dubey, Nishita Bhembre, Shivani Bodas, Sukh Veer, Aurnab Ghose, Andrew Callan-Jones, and Pramod Pullarkat. The axonal actin-spectrin lattice acts as a tension buffering shock absorber. Elife, 9:e51772, 2020. DOI. https://doi.org/10.7554/eLife.51772.

4. Himanshu Marwah, Hetarth Bhatt, Neeraj Fartyal, Rohit Nautiyal, Sukh Veer, Pramod A Pullarkat, and Sreenath Balakrishnan. Biaxial stretcher with vision-based force sensing for estimating anisotropy of single cells. DOI: 10.1007/s12213-026-00206-w.

Prof. Pramod A Pullarkat
(Thesis Supervisor)
Raman Research Institute
Bengaluru-560080, India

Sukh Veer
(Student)
Raman Research Institute
Bengaluru-560080, India

Contents

1 Introduction **1**

1.1 Neuronal cells . . . 2

1.2 Morphology of neurons . . . 2

1.2.1 Dendrites . . . 2

1.2.2 Cell body (soma) . . . 3

1.2.3 Axon . . . 3

1.2.4 Growth cone and axon terminal . . . 3

1.3 Neuron types and and functions . . . 4

1.3.1 Based on function . . . 4

1.3.2 Based on structure or morphology . . . 4

1.4 Neuronal cytoskeleton . . . 5

1.4.1 Microtubules and microtubule associated proteins (MAPs) 6

1.4.2 Actin filaments and spectrin . . . 8

1.4.3 Neurofilaments . . . 9

1.5 Motivation for studying axonal mechanics . . . 11

1.6 Mechanical behavior of axons . . . 13

1.7 Cytoskeletal dynamics and contribution under mechanical perturbations . . . 16

1.7.1 Microtubule and MAPs response to mechanical perturbations 16

1.7.2 Contribution of actin-spectrin periodic skeleton to axonal responses . . . 17

1.7.3 Neurofilament reorganization and mechanical adaptation . 19

1.8 Active contraction of the axon 20
1.9 Contributions of this study to understanding axonal mechanics . . 20

2 Instrumentation 23
2.1 Introduction 23
2.2 Operating principle and technical details of the Micro-Extensional Rheometer (MER) 24
2.2.1 Fluorescence imaging mode 28
2.3 Calibration of the optical fiber 29
2.4 Calibration of one-dimensional piezo actuator 32
2.5 Spatial resolution of the PSD 34
2.6 Feedback control and experimental software 36
2.7 Development and validation of rheological protocols 38
2.8 Preparation of the Cantilever 41
2.9 Comparison of cantilever and axonal force responses in a viscous medium. 44

3 Experimental analysis of axonal strain relaxation and cytoskeletal contributions 47
3.1 Introduction 47
3.2 Method 48
3.2.1 Axonal strain relaxation protocol 48
3.2.2 Axonal tracking and strain relaxation calculation 50
3.2.3 Modifications to the cytoskeleton 51
3.3 Results 51
3.3.1 Axonal strain relaxation after stretch and release 51
3.3.2 Effect of waiting time on axonal strain relaxation 52
3.4 The role of different cytoskeletal filaments in axonal strain relaxation 54
3.5 Role of the Axonal Diameter in Axonal Strain Relaxation 60
3.6 Discussion and possible explanation 62
3.7 Conclusion and summary 65

4 Theoretical modeling of axonal strain relaxation dynamics 67

4.1 Introduction and motivation 67

4.2 Analytical models previously used to describe axonal viscoelasticity 68

4.3 Computational models for viscoelastic behavior of axons 72

4.4 Modeling the mechanical responses of the actin–spectrin scaffold . 74

4.5 Axon as Kelvin–Voigt and Maxwell models in parallel 82

4.5.1 Creep and recovery response of the Kelvin-Voigt and Maxwell models in parallel 84

4.5.2 Analytical solution for the parallel combination of Kelvin-Voigt and Maxwell models: 86

4.5.3 Influence of model parameters on strain relaxation and characteristic time scales 89

4.6 Motivation for the Zener–Maxwell model 93

4.7 Zener and maxwell models in parallel combination 95

4.7.1 Stretching and releasing (strain relaxation) 96

4.7.2 Analytical solution for the parallel combination of Zener and Maxwell models: 96

4.7.3 Strain relaxation vs model parameters (varying elastic and viscus modulus) 99

4.8 Conclusion and summary 101

5 Buckling response of axons to mechanical stimuli 103

5.1 Introduction 103

5.2 Earlier studies on axonal buckling 104

5.3 Method 106

5.4 Axonal buckling under mechanical stretch and release 107

5.5 Effect of microtubule stabilization on buckling wavelength 109

5.6 Previous modeling approaches to axonal buckling 111

5.7 Model of axonal buckling 114

5.8 Model details 115

5.8.1 Model geometry . . . 115
5.8.2 Force balance along the rod . . . 116
5.8.3 Torque balance and moment-curvature Relation . . . 118
5.8.4 Moment-Curvature relation . . . 118
5.8.5 Linear stability analysis . . . 119
5.8.6 Marginal stability and cutoff wavelength . . . 119
5.8.7 Effect of bending rigidity and viscosity in the Maxwell model with elastic foundation . . . 122
5.9 Effect of the axonal cortex as a viscoelastic solid . . . 124
5.9.1 Influence of bending rigidity and viscosity in the Maxwell model with Kelvin–Voigt foundation . . . 126
5.10 Conclusion . . . 127

6 Investigating cytoskeletal structural changes in the axons after mechanical stimuli 133
6.1 Introduction . . . 133
6.2 Device design and stretching protocol . . . 134
6.3 Strain measurement in PDMS sheet . . . 135
6.4 Immunostaining and super-resolution imaging protocol . . . 137
6.5 Assessment of MPS spacing reproducibility . . . 138
6.6 Quantitative analysis of MPS periodicity in control and stretched axons . . . 140
6.7 Discrepancy between applied strain and MPS periodicity change . . . 142
6.8 Confirming axonal stretch following PDMS stretching . . . 143
6.9 Possible influence of axonal curvature on the observed periodicity shift . . . 144
6.10 Conclusion . . . 146

7 Summary and future directions 147
7.1 Overview of the Chapter . . . 147
7.2 Key findings and contributions . . . 147

7.3 Future direction 149
7.3.1 Rate-dependent axonal mechanics using linear loading-unloading protocols 149
7.3.2 Axonal mechanics at physiological temperature 149
7.3.3 Extensions of viscoelastic models 150
7.3.4 Structural dynamics of the axonal cytoskeleton during stretching 150

Chapter 1

Introduction

The nervous system is a highly intricate and an essential network responsible for processing, transmitting, storing information, and regulating the activities of many organs throughout the body [1]. In this system, neurons and glial cells play central roles, serving as the primary contributors to brain functionality [2], while vascular and extracellular matrix also provide critical structural and regulatory support [14,15]. Neurons are essential for receiving, integrating, and transmitting electrical impulses, as well as forming the networks that store and process memories, while glial cells provide nourishment, insulation, waste removal, immune defense, and overall maintenance that support neuronal function. Neurons receive signals through their dendrites, integrate them in the cell body, and transmit the processed information via their axons to terminals, where they communicate with other neurons or target tissues. Axons and dendrites vary significantly in size. For instance, in humans, dendrites typically extend from a few micrometers to a few millimeters [16] in length, while axons can range from several micrometers to over a meter [17]. The elongated geometry of axons makes them highly specialized for long-range signal transmission but also uniquely vulnerable to mechanical perturbations, underscoring the need to understand their mechanical properties. Disruptions to axonal signal conduction, whether due to injury or neurodegenerative disease—can severely compromise nervous system function. Although

significant progress has been made in neuroscience, the mechanical behavior of axons and the role of individual cytoskeletal components in shaping this response remain incompletely understood, motivating further investigations.

1.1 Neuronal cells

Neurons, also known as neuronal cells, are fundamental building blocks of the nervous system. They are highly specialized cells responsible for receiving, transmitting and processing information throughout the entire nervous system. These cells play a crucial role in enabling communication between different parts of the body, allowing us to perceive and respond to the external environment and regulate various physiological processes.

1.2 Morphology of neurons

Neurons have a unique morphology (Figure 1.1) that distinguishes them from other cells in the body. They are composed of distinct structures, such as dendrites, the cell body (soma), an axon, and either a growth cone during development or axon terminals in mature neurons.

1.2.1 Dendrites

Dendrites are branched extensions that extend from the cell body [18, 19]. These structures primarily receive signals from other neurons or sensory receptors through specialized junctions called synapses. At chemical synapses, neurotransmitters bind to ligand-gated ion channels on the dendritic membrane, triggering signal transmission toward the cell body [20]. In addition, electrical synapses allow direct ionic current flow between neurons via gap junctions, providing faster and often bidirectional communication [21].

1.2.2 Cell body (soma)

The cell body is the central part of the neuron, containing the nucleus and other essential organelles [18, 19]. It maintains metabolic functions, produces many proteins and sends processed information via the axon [22].

1.2.3 Axon

Axons are thin, cylindrical projections that extend from cell bodies and can reach lengths of up to 1 m in humans [9] and up to 30 m in whales [23] and diameters varying between 0.1 and 20 μm [24, 25]. They conduct electrical impulses, known as action potentials, away from the cell body to their terminals, where they transmit them to other neurons or target cells.

1.2.4 Growth cone and axon terminal

The growth cone is a dynamic palm like structure at the tip of a developing axon that guides it toward its target. Once the axon reaches its destination, the growth cone disassembles, and the axon terminal forms, allowing release of neurotransmitters to facilitate communication with other neurons, muscles, or glands [26].

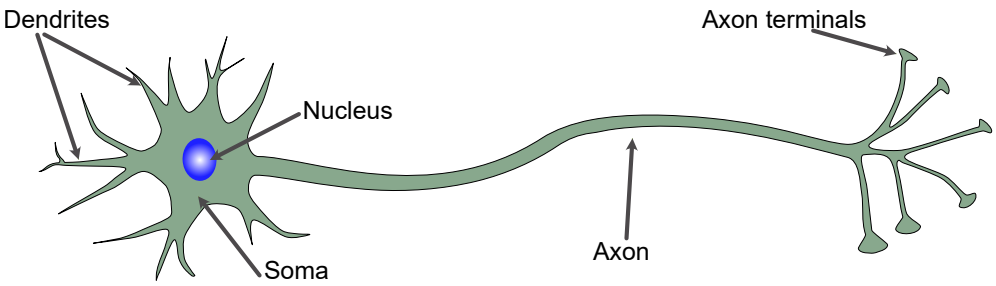


Figure 1.1: A simplified schematic showing the main morphological components of a neuron. The schematic shows dendrites that receive incoming signals, the cell body (soma) containing the nucleus, and an axon — a thin, tubular process that can extend from a few hundred microns to up to a meter in humans — which transmits electrical impulses to the axon terminals, relaying signals to other neurons or target cells.

1.3 Neuron types and and functions

In both the Central Nervous System (CNS) and Peripheral Nervous System (PNS), various types of neurons exist, each serving specific functions within the neural network. Neurons can be divided based on their structure and function, providing a framework for understanding their diverse roles in the nervous system.

1.3.1 Based on function

Based on function neurons can be classified into sensory neurons, motor neurons, and interneurons [27]. Sensory neurons transmit sensory information from specialized receptor cells, such as photoreceptors in the retina, hair cells in the ear, and mechanoreceptors in the skin, to the CNS for processing. Motor neurons carry signals from the CNS to muscles and glands, controlling voluntary and involuntary actions. Interneurons are connectors between sensory and motor neurons.

1.3.2 Based on structure or morphology

Based on structure, neurons can be classified into unipolar, bipolar, multipolar, and pseudounipolar [28] (Figure 1.2). Unipolar neurons have a single neurite extending from the cell body. They are commonly found in sensory pathways of invertebrates. Bipolar neurons have two distinct processes, one dendrite and one axon, extending from opposite sides of the cell body. These neurons are specialized for sensory functions and are found in the retina, olfactory epithelium, and inner ear. Multipolar neurons, the most common type in the central nervous system, have one axon and multiple dendrites, allowing them to integrate large amounts of information. They play key roles in motor control and associative functions. Pseudounipolar neurons initially develop as bipolar neurons. However, their two processes fuse into a single projection that later splits into two branches.

They are primarily found in sensory neurons of the peripheral nervous system.

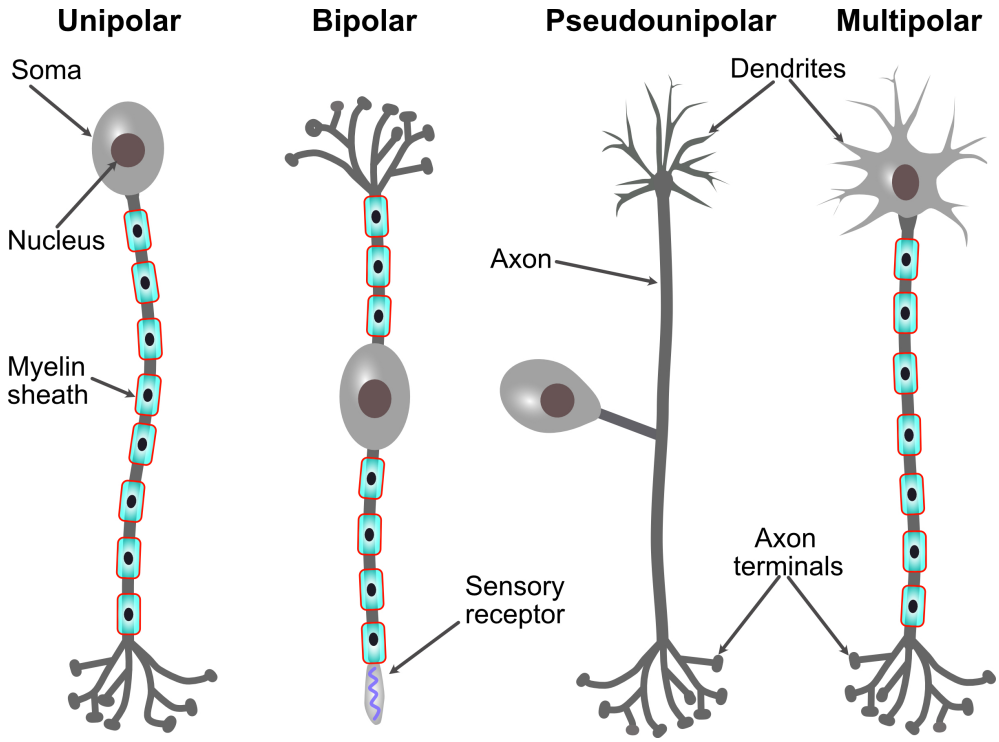


Figure 1.2: Morphological classification of neurons based on the number of neuronal processes. Neurons are classified as unipolar, bipolar, pseudounipolar, or multipolar based on their processes. Unipolar neurons have a single process and are common in invertebrates. Bipolar neurons have one axon and one dendrite, typically found in sensory organs. Pseudounipolar neurons have a single process that splits into two branches and are found in the dorsal root ganglia. Multipolar neurons, the most common type in the CNS, have one axon and multiple dendrites.

1.4 Neuronal cytoskeleton

The neuronal cytoskeleton is a complex and dynamic network of protein filaments that provides structural support, maintains cell shape, and facilitates intracellular transport. It plays a crucial role in various neuronal processes, including axonal and dendritic growth, synaptic plasticity, and the overall maintenance of neuronal function. The three main components of the neuronal cytoskeleton are microtubules, microfilaments (actin filaments), and neurofilaments. The organization of the neuronal cytoskeleton within the axon is illustrated in Figure 1.3.

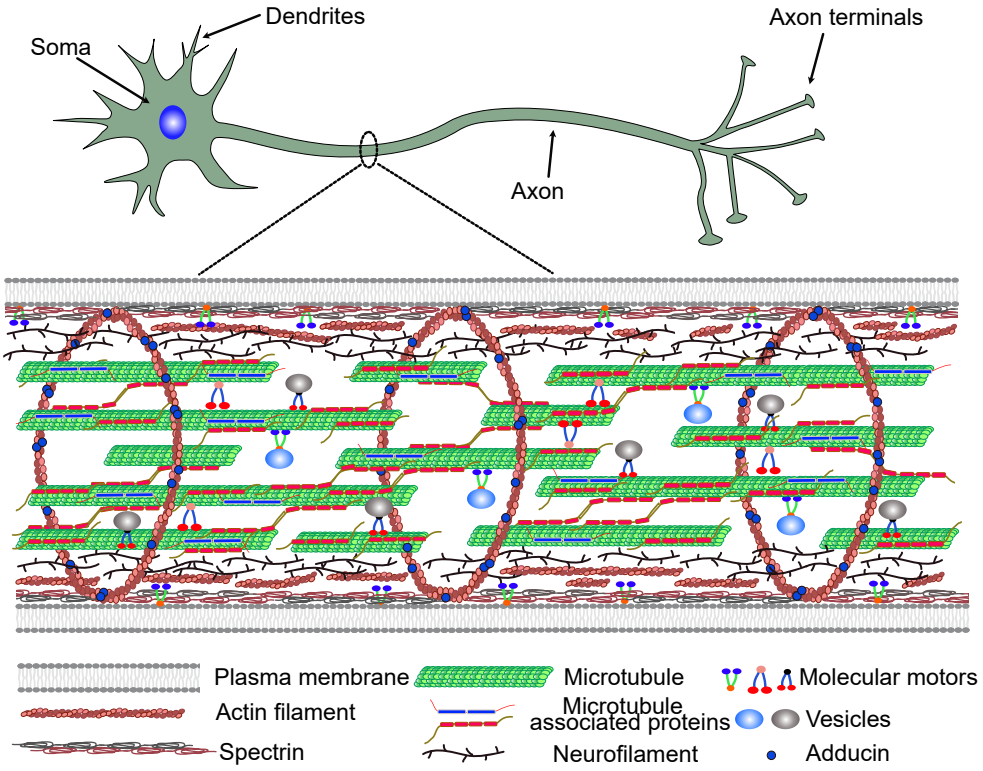


Figure 1.3: Schematic of axon and axonal cytoskeleton. The axonal cytoskeleton contains a polarized array of microtubules, stabilized and cross-linked by microtubule-associated proteins such as Tau. These microtubules, with their plus ends directed toward the growth cone, serve as tracks for molecular motor–driven transport and are surrounded by neurofilaments that provide structural stability. Neurofilaments are also interspersed within the microtubule bundle. Surrounding this core is a cortical scaffold composed of periodic filamentous actin (F-actin) rings, interconnected by $\alpha\beta$-spectrin tetramers aligned along the axonal shaft. The spacing of these actin–spectrin units, approximately 190 nm, reflects the length of a spectrin tetramer. Additional actin structures, such as waves and trails, and numerous crosslinking proteins further integrate the cytoskeleton with the plasma membrane.

1.4.1 Microtubules and microtubule associated proteins (MAPs)

Microtubules, the largest cytoskeletal elements in neurons, are hollow cylindrical structures with an inner diameter of about ~15 nm, an outer diameter of about ~25 nm [29], and lengths ranging from a few micrometers (µm) to hundreds of micrometers [30–33]. They are composed of α- and β-tubulin protein subunits that first form $\alpha\beta$-dimers. During microtubule assembly, tubulin dimers polymerize into protofilaments that interact laterally with one another, and about

13 protofilaments together form the characteristic hollow microtubule cylinder. Microtubules are the most rigid filaments in the cytoskeleton, with a persistence length of approximately ~2 mm [29], which is defined via the decay of the tangent–tangent correlation along the filament contour, $\langle \mathbf{t}(s)\cdot\mathbf{t}(0)\rangle = \exp\left(-s/\ell_p\right)$, where $\mathbf{t}(s)$ denotes the unit tangent vector at contour length s and ℓ_p is the persistence length. Microtubules being inherently polar structures, are organized into distinct polarity patterns that support their structural and functional roles. In mature axons, microtubules are organized with uniform polarity, with plus ends directed toward the distal end. In contrast, dendrites generally have a mixed microtubule organization, with both plus- and minus-end-out orientations [34]. Here, polarity refers to the structural and dynamic asymmetry of microtubules, with the plus end being more dynamic and the minus end relatively stable [35]. Microtubules provide essential structural support and serve as railway tracks for motor proteins, such as kinesins and dyneins, which transport cellular organelles and cargo along them, facilitating efficient anterograde and retrograde transport [34, 36]. In axons, microtubules assemble into bundle-like structures that fill the axonal core, while MAPs, along with molecular motors such as kinesins and dyneins, help cross-link, regulate, and interact with microtubules in various ways. This organization is shown in *in-vitro* preparations, where microtubules polymerized in the presence of tau form tightly packed bundles cross-linked by tau proteins [37] (Figure 1.4). Similarly, microtubules in dendrites also form bundles, although the organization, the associated MAPs and the interacting motor proteins may differ between axons and dendrites. For example, tau is primarily associated with axonal microtubules, while MAP2, which is more abundant in dendrites, contributes to microtubule spacing and structural organization in axons and dendrites, respectively [38]. The differential association of MAPs in axons and dendrites reflects their distinct structural and functional requirements. Notably, microtubule organization is not same across all neurons; variations in microtubule arrangement and spacing are observed among different axonal types and across species [39].

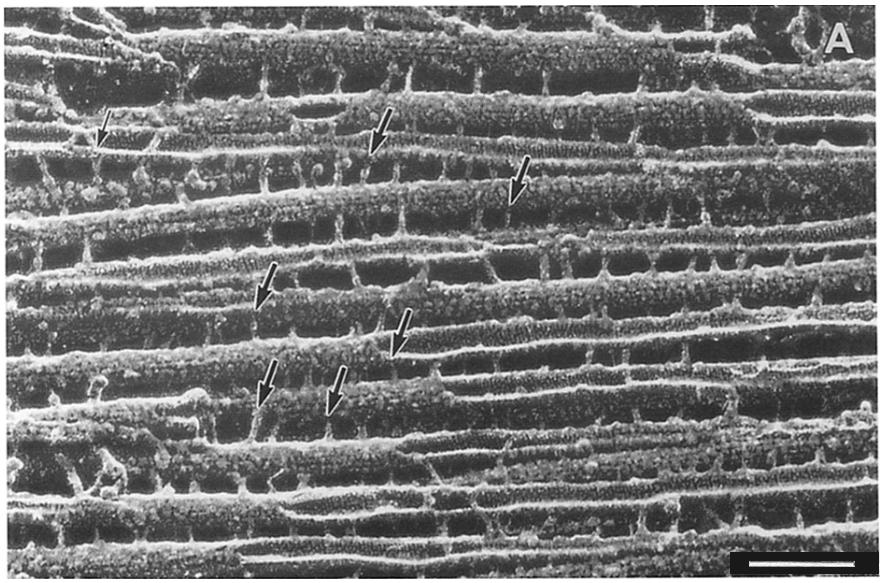


Figure 1.4: Higher-magnification electron micrographs of quick-frozen, deep-etched microtubule pellets polymerized in the presence of tau. The microtubules are organized into tightly packed bundles, with cross-bridges formed by tau proteins clearly visible (indicated by arrows). Scale bar = 100 nm. Adapted from Hirokawa et al., 1988 [37].

1.4.2 Actin filaments and spectrin

Actin filaments are thin, semi-flexible filaments with a persistence length of about 10-17 μm and a diameter of approximately ~7 nm [40]. These polar biopolymers, known as filamentous actin (F-actin), are composed of globular actin (G-actin) monomers arranged into a double-stranded helical structure. F-actin is predominantly found in the axonal cortical mesh beneath the plasma membrane, providing structural support, and forms dense bundles in neuronal filopodia. In the cell body, F-actin is organized into a dynamic network that facilitates intracellular trafficking and maintains cellular architecture. Additionally, actin filaments form dynamic structures inside axons: actin trails, which originate from actin hotspots and are short, filamentous extensions that grow locally, and actin waves, which are propagating accumulations of F-actin moving along the axon [41, 42]. Together with neuronal spectrin, also known as brain spectrin, a specialized cytoskeletal protein found in neurons, actin forms a one-dimensional membrane periodic structure (MPS) in axons [43, 44]. This MPS is characterized by a repeating pattern

of actin rings bridged by spectrin tetramers, with an average periodicity of ~180 nm (Figure 1.5). In dendrites, periodic structures similar to the MPS are also formed but are less prevalent and less well-defined than those in axons [45].

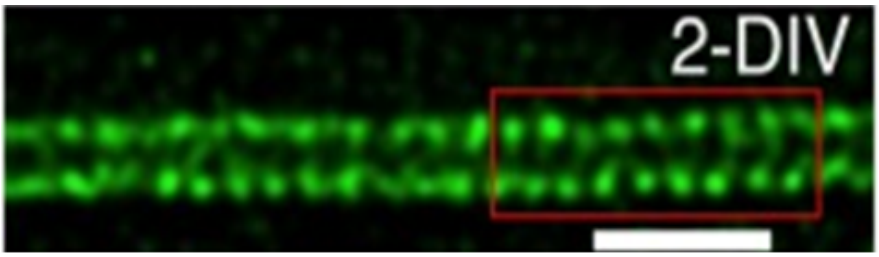


Figure 1.5: Representative super-resolution (STED) image of an axon from the DMSO vehicle control group, immunolabeled with a primary anti-βII-spectrin antibody and an Alexa Fluor 488-conjugated anti-mouse secondary antibody. The periodic spectrin ring pattern along the axon is clearly visible. Scale bar = 2 μm. The boxed region highlights a segment where the spectrin lattice is more clearly visible. Figure adapted from Dubey et al. [12].

Actin filaments play a crucial role in maintaining the neuron's shape, providing mechanical strength, and facilitating cell movement and motility. They are involved in growth cone motility during neurite outgrowth and the formation and stabilization of dendritic spines, which are small protrusions on dendrites where synapses form. These structures are essential for synaptic plasticity, the process by which synaptic connections between neurons are strengthened or weakened in response to activity and experience.

1.4.3 Neurofilaments

Neurofilaments (NFs) are intermediate filaments specific to neurons. They have a diameter of about ~10 nm and persistence length about ~100 nm [46]. They are composed of different subunits, including neurofilament light (NF-L), neurofilament medium (NF-M), and neurofilament heavy (NF-H) [47]. The assembly ratio of neurofilament subunits is primarily influenced by neuron type [48], developmental stage [49], age [50], and neurodegenerative diseases [51]. Neurofilaments are typically organized in parallel along the axon (Figure 1.6), with higher densities observed in thicker, more myelinated axons [52]. In smaller or unmyelinated

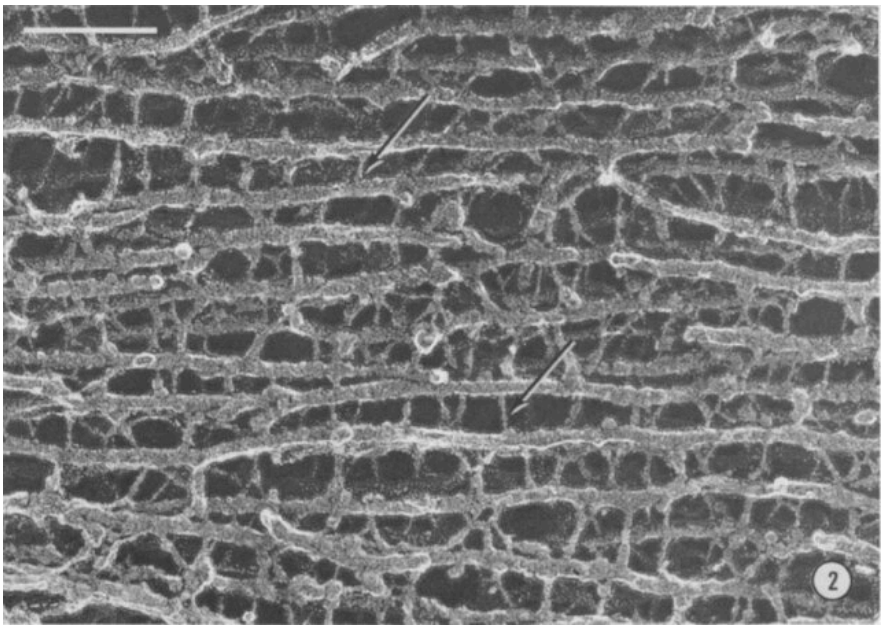


Figure 1.6: Electron micrographs showing axonal neurofilaments isolated from Triton-extracted spinal cord tissue. Samples were incubated with nonimmune IgG followed by a secondary IgG, and subsequently processed for visualization using the quick-freeze, deep-etch electron microscopy technique. Arrows indicate cross-bridges linking adjacent neurofilaments, formed by their extended sidearms. Scale bar 0.1 μm. Adapted from Hirokawa et al., 1984 [56].

axons, the neurofilament organization may be less structured. In vertebrate neurons, they form a dense meshwork that supports and maintains the shape of the axon, helping preserve its diameter and structural integrity during mechanical stresses [53], and also contributing to overall axonal stability during electrical signal (action potentials) propagation [54]. Neurofilaments, in coordination with microtubules, form a dynamic and integrated cytoskeletal network. The three cytoskeletal filaments-actin, neurofilaments, and microtubules are interconnected by specialized linker proteins known as plakins, which help maintain structural integrity and enable interaction between these components [46, 55].

Beyond these primary cytoskeletal filaments, neurons rely on several other key components to maintain their structural integrity and functionality. Molecular motor proteins, such as kinesins and dyneins, drive intracellular transport along microtubules, ensuring the efficient movement of organelles, vesicles, and other cargo within the neuron [57]. Myosin motors interact with actin filaments, play-

ing essential roles in axonal transport, growth cone motility, and synaptic function [58]. Additionally, cross-linking proteins, including spectraplakins, plectin, and filamin, facilitate the interaction between different cytoskeletal elements, enhancing mechanical stability and cytoskeletal organization [59]. Linker proteins such as ankyrins and plastin further contribute to cytoskeletal coordination in neurons: ankyrins tether membrane components to the actin–spectrin network, while plastin cross-links actin filaments into bundles, together promoting mechanical resilience [60, 61]. Together, these components create a highly composite and dynamic and interconnected cytoskeletal network essential for neuronal structure, transport, and function.

1.5 Motivation for studying axonal mechanics

The brain, as the central nervous system organ, plays a pivotal role regulating bodily functions, and empowering us to think, learn, and make decisions. During brain injuries, which are conditions that can result from sudden impact or acceleration-deceleration forces applied to the head, the brain is mechanically deformed [3, 4]. Additionally, brain also endure deformation during activities like contact sports [7] (e.g., boxing), where strain can vary depending on the impact. Axons in the brain can experience stretching, shear, compressive, and bending deformations due to mechanical forces during these conditions [62], potentially resulting in damage to their structure and function. Such injuries are common in traumatic brain injury (TBI), where axonal damage is a major pathological hallmark [62]. This damage can lead to immediate effects like axonal breakage and swelling, which results from both cytoskeletal disruption and cargo accumulation due to interrupted axonal transport [62]. Over time, it may lead to neuronal death [63] and the release of neurotoxins [64], which can also harm neighbouring healthy neurons. These kinds of changes following traumatic injury can temporarily or permanently disrupt neural communication, causing symptoms like loss of consciousness [65], confusion [66] and motor deficits [67] with more severe

cases leading to coma [68]. Over time, progressive damage impairs intracellular signaling and synaptic function, leading to cognitive decline [69], sensory and motor dysfunction [70], and behavioral changes [71]. In severe cases, this damage may contribute to neurodegenerative conditions such as chronic traumatic encephalopathy (CTE) and Alzheimer's disease [69].

Axonal injury is not limited to the brain; axons in the peripheral nervous system are also vulnerable to mechanical stress. Stretch or traction on peripheral nerves—for example during dislocations, limb over-extension, or violent limb movements—can exceed their elastic limits, leading to structural damage and rupture of axons [72]. This stretch-induced deformation of peripheral nerve axons leads to structural damage and functional impairment, resulting in motor and sensory deficits [73]. Although peripheral axons possess the capacity for regeneration, recovery following stretch-induced damage is often slow and incomplete [74, 75].

Interestingly, axons are subjected to mechanical forces not only during injuries but also during normal physiological activities involving limb movements, such as walking, running and jumping [5, 6]. For example, the mammalian sciatic and median nerves can experience localized strains of up to 30% during these activities [6], while strains in the brain during similar physical activities are generally in the range of 2-5%. In extreme cases, axons in nerves running along the mouth floor of certain species, such as baleen whales, can elongate up to 160% during feeding [76].

Since axons are largely irreplaceable [77–79] and difficult to regenerate, particularly in the CNS [78–80], studying axonal mechanics is important for understanding how axons respond to mechanical forces and for guiding strategies to prevent or reduce axonal damage in both normal and pathological conditions. Axons are known to exhibit viscoelastic properties when subjected to mechanical perturbations [12, 81, 82]. This dual response allows axons to resist deformation (elastic response) and dissipate excess energy over time (viscous response), which

plays a crucial role in their ability to regulate axonal tension, ensuring proper electrical signal transmission. If tension is not adequately maintained, it can lead to neuronal misfire or complete failure to fire [83], disrupting regular neural activity and impairing overall nervous system function. Moreover, this viscoelastic behavior supports the axon's ability to return to its original length once mechanical forces are removed [12], thereby preserving the structural integrity and dimensions of the axon. In the context of neuronal injuries, these viscoelastic properties influence how axons deform under stress and how they recover, affecting their susceptibility to injury and their potential for repair. Despite significant advances, our understanding of axon mechanics and the dynamics of the axonal cytoskeleton remains incomplete. While we know that axons exhibit complex mechanical behaviors and are influenced by various forces, the full scope of how they respond to these forces under different conditions is still not fully understood. This knowledge is pivotal for designing strategies that prevent or reduce axonal damage, both in traumatic conditions like TBI and during everyday physiological loading. Furthermore, insights into axon mechanics can inspire the development of biomimetic materials and neural interface technologies [84], highlighting axons as intrinsically interesting biomaterials to study.

1.6 Mechanical behavior of axons

There have been several experimental attempts to study and quantify the mechanical behavior of axons. For instance, early work by Steven Heidmann and Dennis Bray, using calibrated glass microneedles to stretch axons in cultured PC12 cells and chick dorsal root ganglion (DRG) neurons, demonstrated that axons behave like viscoelastic materials, responding with both immediate elastic recoil and slower, adaptive deformation while maintaining internal tension [85–87]. When the base of a flexible microneedle, placed in contact with an axon, was suddenly displaced (Figure 1.7A) , the axon exhibited an immediate increase in strain, followed by a slower, gradual deformation that leveled off over about few

minutes (Figure 1.7B curve a). During this period, the internal tension relaxed from a peak value to a stable resting level of approximately 30 micro dynes (0.3 nN) (Figure 1.7C). Upon release of the applied force, the axon recovered its original length within roughly a minute. Interestingly, when higher stretching forces were applied, axons not only resisted the tension but also grew in response to it (Figure 1.7B curve b), suggesting a link between mechanical tension and axonal growth [87,88]. This axonal growth in response to applied force is known as *towed growth*. Moreover, a linear relationship between the applied tension and the axon elongation resulting from towed growth was observed. Taher Saif's team applied controlled stretching to *Drosophila* axons using micromechanical force sensors. The axons were loaded to a predetermined level of stretch (typically less than 50% of their length) within 1–2 minutes [89]. After reaching the target stretch, the force sensors were held fixed, and the evolution of force and axonal strain was recorded. The experiment concluded by unloading the axon through the removal of the applied force (Figure 1.7D). In the initial phase of loading, corresponding to the high loading rate, axons behaved like elastic springs, exhibiting a linear force–deformation relationship (Figure 1.7E). During the hold phase, the force in the axon relaxed over time, while the axon simultaneously elongated, reflecting the viscoelastic response as axon length and probe deflection are coupled (Figure 1.7F). After release, axons actively regulated their tension, indicating intrinsic mechanical feedback mechanisms that help preserve structural stability. The viscoelastic behavior of PC12 neurites has also been demonstrated by examining their response to externally applied drag forces [90].

In addition to stretch-based studies, local mechanical properties of axons, such as stiffness, viscoelasticity, and relaxation behavior, have been quantitatively characterized using techniques like Atomic-Force-Microscope (AFM) [91,92] and magnetic tweezers [93]. For instance, using AFM to apply local compression, Ouyang et al. [91] demonstrated that axonal stiffness is highly dependent on cytoskeletal integrity, particularly microtubules and neurofilaments and that mechanical stiffness was reduced when these filaments are depolymerized. Similarly, Gong

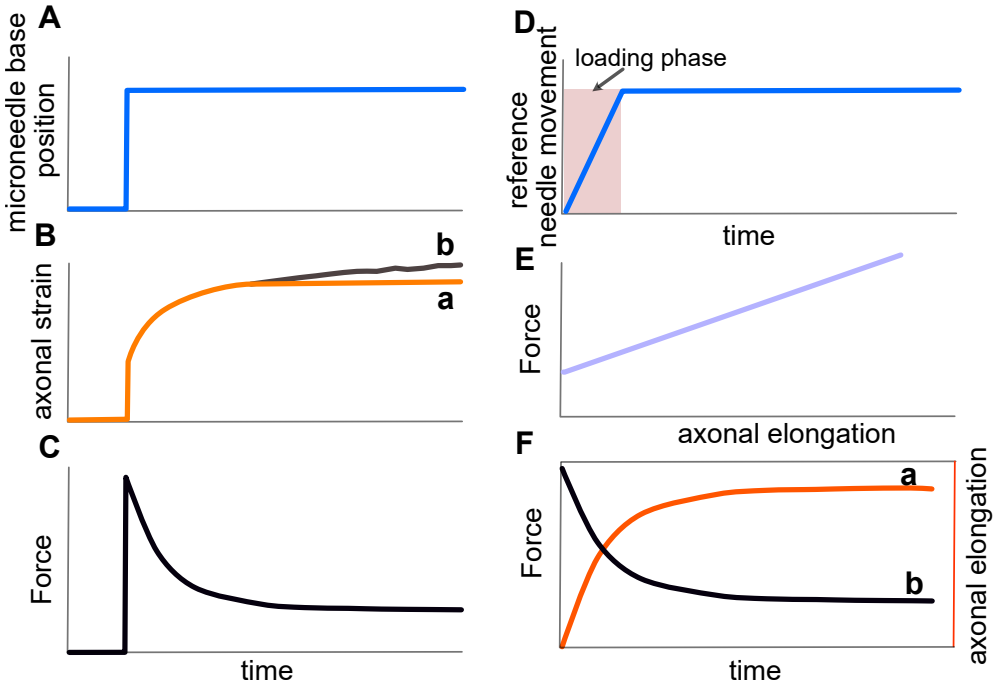


Figure 1.7: Viscoelastic response of axons. **(A)** Movement of the base of the microneedle to apply extension to the axon. **(B)** Axonal length evolution following stretching. The curve shows an initial rapid elastic extension, followed by slower viscoelastic stretching where strain levels off over time (curve a). Curve b illustrates axonal towed growth in response to applied tension exceeding 100 microdynes. **(C)** Force relaxation in the axon. The force decreases over time as the axon undergoes viscoelastic deformation, corresponding to the elongation behavior shown B (curve a). **(D)** Loading protocol for Drosophila axons: axons were stretched to less than 50% of their original length over 1–2 minutes, after which the micromechanical force sensors was held fixed before unloading. **(E)** Axon displays a linear relationship between force and extension during the fast-loading phase. **(F)** Axon exhibits viscoelastic elongation (curve a) and force relaxation (curve b) during the hold phase of the experiment.

et al. [92] revealed distinct relaxation timescales in neurites, indicating complex viscoelastic behavior that varies with loading rate. Magnetic tweezer studies reported that neuronal microcompartments exhibit distinct mechanical behaviors, with the soma being soft and solid-like due to the nucleus, and neurites stiffer and viscous-like due to neurofilaments [93].

1.7 Cytoskeletal dynamics and contribution under mechanical perturbations

Following axonal deformation, a cascade of events occurs within the axon, involving cytoskeletal remodeling and rearrangement as part of the cellular response to mechanical strain. Such changes contribute to restoring axonal integrity, allowing the axon to adapt to the mechanical perturbation and potentially facilitate recovery mechanisms. However, when deformation is rapid or exceeds physiological tolerance, the cytoskeleton can instead undergo structural failure, leading to cellular dysfunction and impaired axonal transport.

1.7.1 Microtubule and MAPs response to mechanical perturbations

Microtubules (MTs) and their associated proteins undergo distinct structural and functional changes upon axonal stretch. Rapid mechanical stretching can lead to direct breakage of microtubules [94] at specific points, disrupting cytoskeletal integrity and potentially initiating axonal degeneration. During sudden stretch, cross-linking proteins such as tau are thought to exert forces on microtubules, potentially contributing to their breakage [95] (Figure 1.8A). Other microtubule-associated or motor proteins may play similar roles, though their contributions remain less well understood. This mechanical damage often results in a partial interruption of axonal transport, where cargo movement along broken microtubules is impaired but may continue via intact microtubules [94]. However, when microtubules move slowly in response to stretch, MAPs such as tau dynamically unbinds and rebinds, allowing microtubules to slide against each other without breaking and facilitating cytoskeletal reorganization and adaptation to mechanical stress [96] (Figure 1.8B).

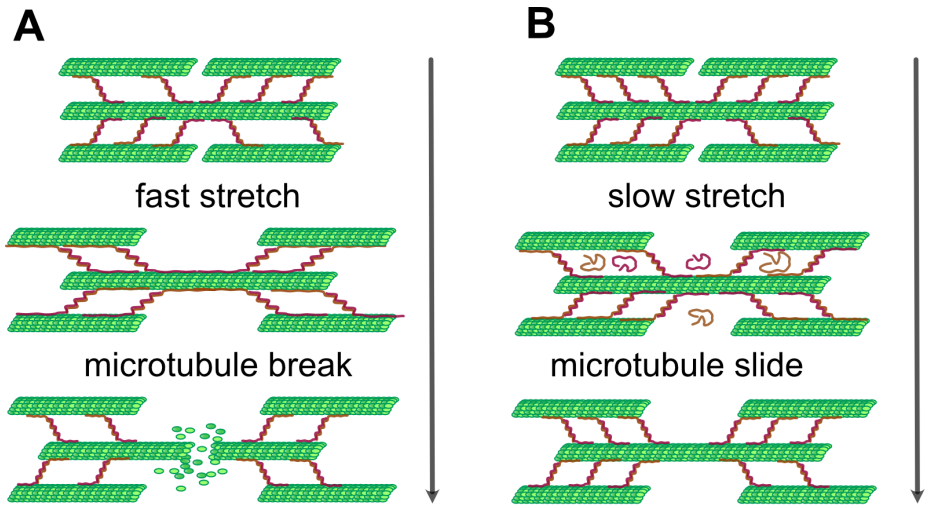


Figure 1.8: Mechanical responses of axonal microtubules to stretch. (A) Rapid axonal stretch can lead to direct breakage of microtubules at specific points. Cross-linking proteins, such as Tau, may exert forces on microtubules, contributing to their breakage. **(B)** During slower axonal stretch, microtubules can slide past each other as MAPs like tau dynamically unbind and rebind. This allows cytoskeletal reorganization and adaptation to mechanical stress without microtubule breakage.

1.7.2 Contribution of actin-spectrin periodic skeleton to axonal responses

The structural role of spectrin was highlighted by findings that the absence of β-spectrin leads to axonal breakage during locomotion in C. elegans [97]. Further work showed that β-spectrin contributes not only to axonal stability but also to touch sensation [98]. For example, anterior ventral microtubule (AVM) touch receptor neurons can detect gentle mechanical stimuli and accommodate length changes during body bending without damage, whereas mutations in the tetramerization domain of β-spectrin result in sensory neuron defects under compressive stress. More recently, optical fibre-based force measurements demonstrated that actin and spectrin are major determinants of the axonal elastic modulus under stretch. The resulting tension–extension curves revealed a buffering

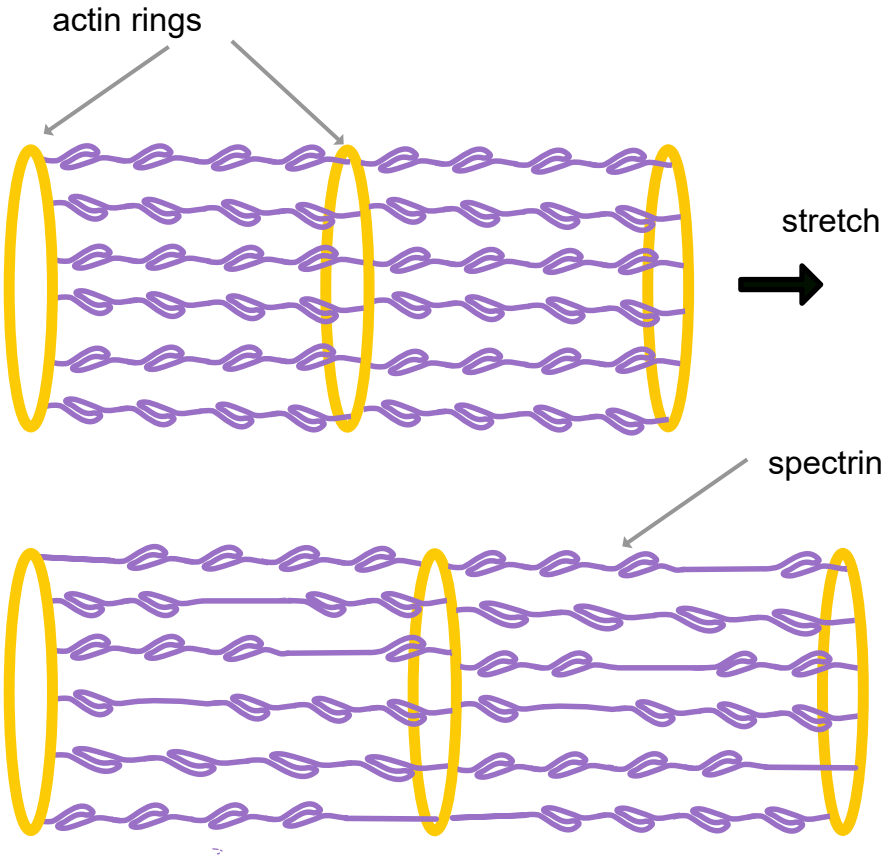


Figure 1.9: Mechanical response of the MPS. The top panel shows the MPS under resting conditions, with an arrow indicating the direction of applied stretch. The bottom panel illustrates the MPS during stretch, highlighting partial unfolding of spectrin domains. This unfolding allows the MPS to dissipate mechanical tension and adapt to axonal deformation, contributing to cytoskeletal resilience.

effect, where tension plateaued after an initial increase [12]. This behavior arises from the unfolding of spectrin proteins, enabling the membrane-associated periodic skeleton (MPS) to dissipate mechanical tension and adapt to deformation (Figure 1.9). In addition, the MPS has been shown to regulate axonal diameter [99, 100], a property essential for efficient action potential propagation and axonal transport [100].

1.7.3 Neurofilament reorganization and mechanical adaptation

Under mechanical deformation, such as stretching or compression, NFs exhibit remarkable adaptability. Individual neurofilaments can elongate up to 3.4 times their original length under axial tension before breaking [101] and simultaneously exhibit significant thinning, likely due to partial unraveling of their filamentous structure [102]. Magnetic tweezer creep tests and related studies reveal that while neurofilaments contribute to cell body stiffness and enhance axonal viscoelasticity, microtubules play a more dominant role in supporting the axon's elastic and structural properties [91, 93]. NFs also interact synergistically with other cytoskeletal components, including microtubules [103] and actin filaments [54, 104]. This interplay facilitates a coordinated response to mechanical forces [105], allowing the neuron to adapt its cytoskeletal architecture as needed. Such interactions are essential for distributing mechanical loads and preserving the functional performance of neurons. In pathological conditions, disruptions in NF organization or function can lead to compromised axonal mechanics. For instance, neurodegenerative diseases often feature NF aggregation, which impairs their normal spacing and interactions, leading to axonal rigidity and dysfunction [46, 51].

Beyond these primary cytoskeletal elements, other proteins also contribute to the mechanical properties of neurons. Cross-linking proteins, including spectraplakins, plectin, and filamin, help distribute mechanical stress across cytoskeletal networks, enhancing structural stability [59, 106, 107]. Adaptor proteins, such as ankyrins, link the cytoskeleton to membrane components, supporting axonal integrity under mechanical perturbations [108]. Cell adhesion molecules, including L1 cell adhesion molecule (L1CAM) and neural cell adhesion molecule (NCAM), contribute to force distribution by mediating interactions with the extracellular matrix and neighboring cells, playing roles in axon-glia interactions and nerve regeneration [109]. Together, these proteins play essential roles in reinforcing axonal mechanics and ensuring the neuron's ability to withstand me-

chanical challenges.

1.8 Active contraction of the axon

Active contraction of an axon involves a dynamic process in which the axonal length diminishes over time [81, 110, 111] driven by a series of internal cellular mechanisms. This phenomenon occurs in response to various chemical [112, 113], threshold-dependent mechanical [114], or pathological stimuli [115, 116], triggering a cascade of molecular events within the axon. Contractile forces generated primarily by actin–myosin interactions [110, 111, 117], coupled with the disassembly [118] or reconfiguration [112] of microtubules, drive axonal shortening, while molecular motors such as dynein and kinesin modulate this process by cross-linking filaments, coordinating cytoskeletal organization [119, 120], and, in the case of certain kinesin isoforms, generating extensional forces along microtubules [121] (Figure 1.10). These axonal contraction processes are integral to cellular dynamics during developmental remodeling, synaptic pruning, and in response to injury, neurodegenerative conditions, or physiological signaling pathways that regulate axonal morphology and functionality. Understanding these mechanisms provides insights into neuronal plasticity and adaptation in both physiological and pathological contexts.

1.9 Contributions of this study to understanding axonal mechanics

This study advances our understanding of axonal mechanics by integrating experimental innovations, systematic experiments, and theoretical modeling, and provides insights into how the axonal cytoskeleton responds to mechanical stress. Refinement of the micro-extensional rheometer, enabled precise measurements of strain relaxation, tension dynamics, and buckling behavior in axons. These experiments uncovered the viscoelastic nature of axons, the critical influence of cy-

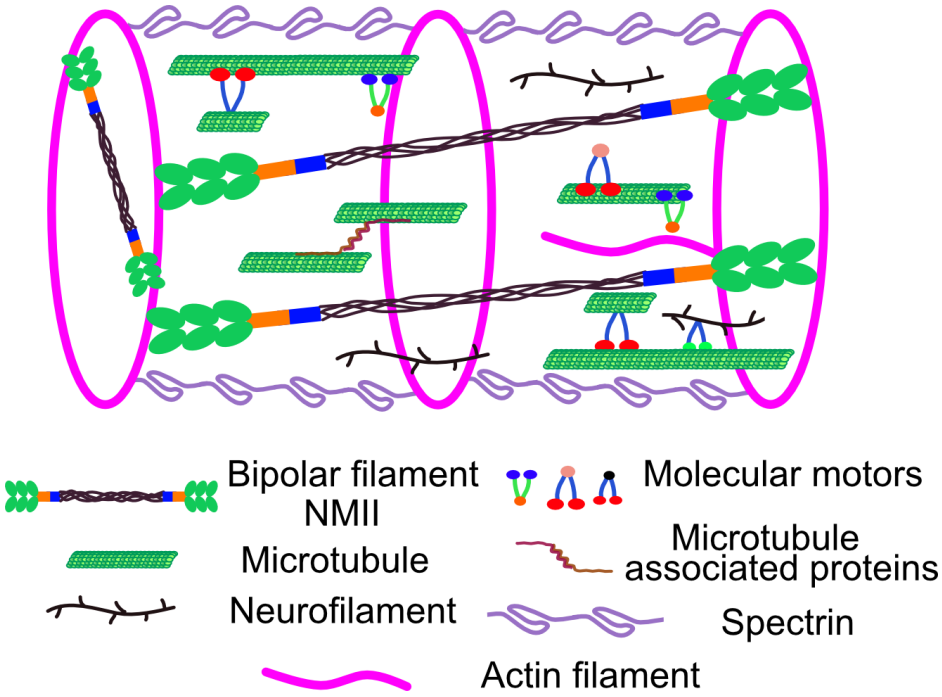


Figure 1.10: Schematic representation of active axonal contraction mechanisms. This schematic illustrates the cytoskeletal components and molecular machinery involved in active contraction in axons. Bipolar non-muscle myosin II (NMII) filaments interact with the cortical actin cytoskeleton to generate contractile forces, while microtubules, cross-linked by MAPs and molecular motors, provide structural resistance to contraction. Short microtubules can be transported by molecular motors and may generate either extensional or contractile forces depending on their relative position with respect to long stationary microtubules and the type of motor involved.

toskeletal elements such as microtubules, actin, and spectrin, and the dependence of relaxation dynamics on axonal geometry. Theoretical models further provided mechanistic insight by linking observed behaviors to protein-based processes like spectrin unfolding and tau–microtubule interactions. Finally, super-resolution imaging established direct evidence of cytoskeletal rearrangements under mechanical perturbation. Together, these findings not only provide a comprehensive framework for axonal mechanics but also highlight mechanisms by which neurons withstand and adapt to mechanical stress, with broader implications for understanding neuronal resilience and vulnerability in health and disease.

Chapter 2

Instrumentation

2.1 Introduction

This chapter describes the modifications made to a home-built force apparatus known as the Micro-Extension Rheometer (MER) [10]. The MER is primarily designed to study the mechanical behavior of biological or synthetic materials under controlled extension at microscopic scale [11, 12, 122]. It can also be used the investigation of active fluctuations, such as those observed in bacterial suspensions serving as an active bath [13]. Additionally, the MER can assist in the calibration of a biaxial stretching device [123]. In order to implement new extensional rheological protocols like cyclic ramp strain, several key components of the system—such as the optical fiber cantilever, piezo actuator, and position-sensitive detector (PSD)—were systematically calibrated to ensure accurate force and displacement measurements. Once the hardware calibration was established, LabVIEW programs were optimized and subsequently tested with mock samples to validate them in executing rheological protocols, with a feedback control mechanism ensuring correct protocol application.

Furthermore, the experimental setup was upgraded to allow force measurement and fluorescence imaging to be performed simultaneously. This integration pro-

vides the possibility of combining controlled stretching and force quantification with the visualization of cytoskeletal dynamics during mechanical loading. This chapter presents the design principles, calibration procedures, and validation tests of the MER.

2.2 Operating principle and technical details of the Micro-Extensional Rheometer (MER)

The MER is designed by integrating optical fiber–based force sensing with piezoelectric actuation, position-sensitive detection, and optical imaging. A schematic of the MER is shown in Figure 2.1A, and a photograph of the setup is presented in Figure 2.2. The force-sensing cantilevers were prepared from single-mode optical fibers (P1-630A-FC, Thorlabs Inc.) with a uniform cylindrical geometry, having an initial outer cladding diameter of 125 μm and a core diameter of approximately 4.3 μm, designed for 632.2 nm wavelength operation. Cantilever preparation, including diameter tuning and measurement methods, is described in detail in section 2.8. The force constant k of the cantilever is obtained by modeling it as an ideal cylindrical cantilever beam:

$$k = \frac{3EI}{L^3}, \qquad I = \frac{\pi d^4}{64}, \tag{2.1}$$

where E is the Young's modulus of the fiber and I is the area moment of inertia. The base of the cantilever is mounted on a piezoelectric actuator (P-841.60, Physik Instrumente GmbH, Germany) with a travel range of 94 μm, providing displacement with a precision of ≈10 nm. The piezo actuator is operated in closed-loop mode via its built-in strain-gauge sensor and controlled using a piezo servo controller (E-625.SR, Physik Instrumente, USA). The piezo-actuated cantilever is positioned on a Zeiss AxioObserver D1 microscope (Carl Zeiss GmbH, Germany) using a joystick-controlled XYZ motorised micromanipulator (XenoWorks, Sutter Instruments), allowing precise positioning. One end of the optical fiber is coupled

to a 17-mW TEM_{00} He-Ne laser (25-LHR-925, CVI Melles-Griot, USA) using an fiber connector (F240FC-B, Thorlab Inc., USA).

The sample is illuminated using green light, and both the illumination light and the red laser light emerging from the free end of the fiber cantilever are collected by the microscope objective. The collected light passes through a beam splitter located below the objective, which divides the light into two optical paths: one directed to a PSD mounted at the microscope's side port for force detection, and the other routed to a charge-coupled device (CCD) camera (Andor Luca R604, Andor Technology, Ireland) for real-time imaging. A band-pass filter (FL632.8-10, Thorlabs Inc., USA) placed in front of the PSD blocks the green illumination light, allowing only the red He-Ne laser light from the cantilever tip to reach the detector, whereas a 550 nm short-pass filter (FES0550, Thorlabs Inc., USA) placed in front of the camera transmits only the green illumination light.

The PSD used in this setup is a two-dimensional area detector that provides the centroid position of an incident laser spot in real time. During measurements, the spot was maintained within the linear response region of the device to ensure accurate readout. The PSD is operated under a reverse bias, which establishes an electric field across the depletion region. Absorption of photons generates electron–hole pairs that drift through the resistive silicon layer toward the collection electrodes. Due to the high spatial uniformity of the doped layers, the photocurrent measured at each electrode depends on the distance between that electrode and the centroid of the incident light spot. Ratios of these photocurrents, computed using a dedicated PSD signal-processing circuit (C-9069, Hamamatsu Photonics, Japan), enable tracking of the cantilever tip displacement.

The cantilever deflection during measurement is calculated as:

$$\delta = D - d, \tag{2.2}$$

where D is the displacement of the cantilever base applied by the piezo actuator

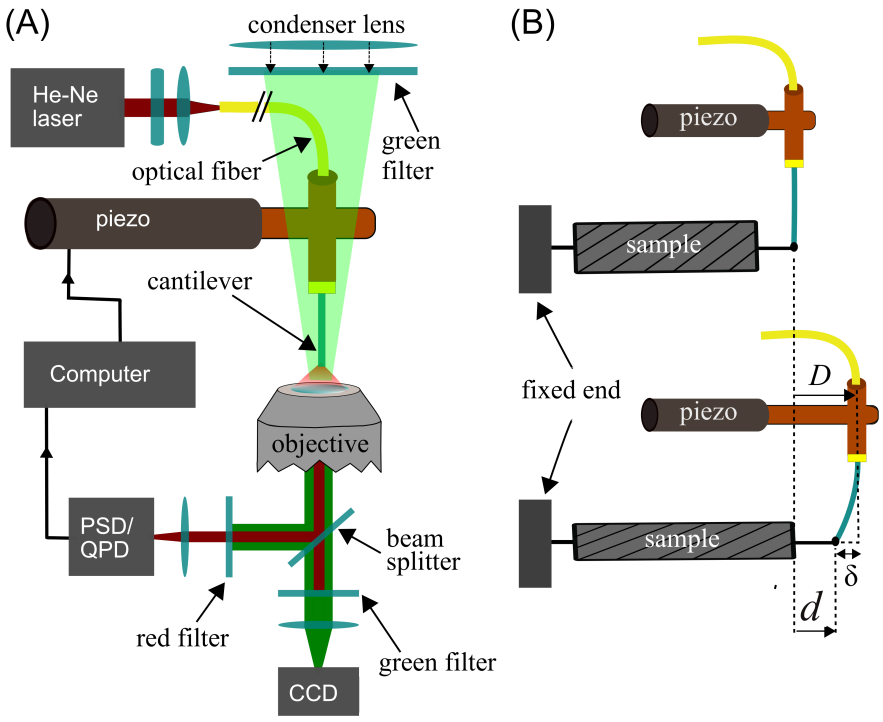


Figure 2.1: Schematic of the setup. (A) A schematic of the MER setup. This device uses an optical fiber as a force sensing cantilever. One end of the optical fiber is connected to a 17mW He-Ne laser (632.8 nm) and the other end is used as a cantilever. The base of the cantilever is attached to a closed loop piezoelectric drive. The tip of the cantilever that stretches the sample is tracked by imaging the laser light exiting from the tip on to a PSD. The sample is illuminated using green light. A beam splitter is used to split the light collected by the objective between a CCD camera and the PSD. Appropriate filters are used in front of camera and PSD to separate the illumination and the laser lights. **(B)** Sample is stretched by moving the piezoelectric actuator by a distance D, producing a sample extension d. The force applied to the sample is calculated from the cantilever deflection δ, using the relation $F = -k(D - d) = -k\delta$, where k is the cantilever spring constant. Schematic adapted from our published work (Dubey et al., 2020) [13].

and d is the measured tip displacement or sample extension obtained from the PSD (Figure 2.1B). The force F experienced by the cantilever is then:

$$F = -k\,\delta. \tag{2.3}$$

For extension experiments, the cantilever tip is brought into contact with the sample placed at the objective's focal plane, and the piezo actuator, regulated by a LabVIEW-based closed-loop feedback system-controls the deformation while the

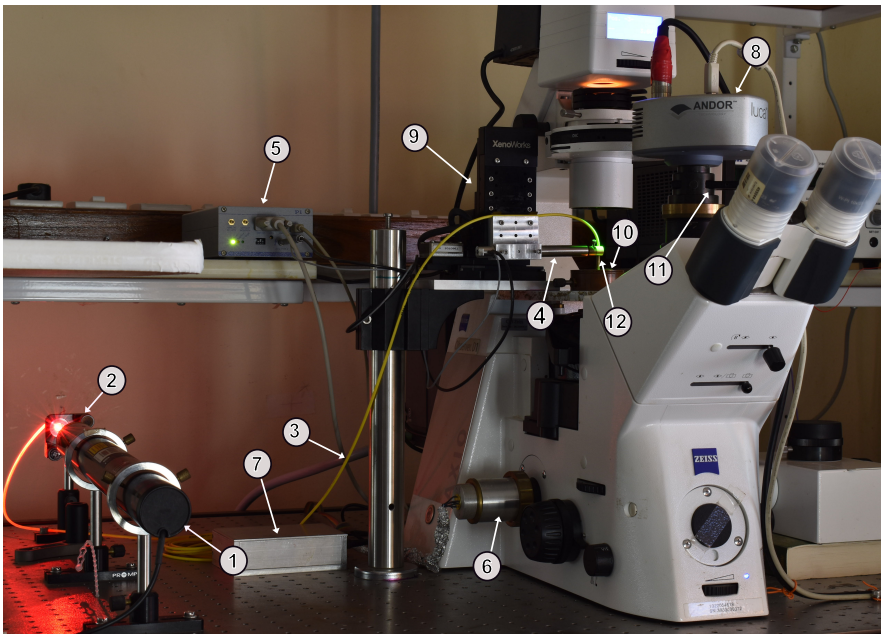


Figure 2.2: Photograph of the force device. Labels indicating: 1-He-Ne laser, 2-fiber coupler, 3-optical fiber, 4, 5-piezo and piezo controller, 6,7-PSD and electronics, 8-CCD camera, 9- XYZ positioning system, 10-sample incubator, 11-green/excitation filter, 12-cantilever holder.

resulting force is measured. In cases where the sample is fixed at both ends—such as axonal stretching (Figure 2.3A), the cantilever applies displacement perpendicular to the sample at its midpoint to produce extension. The sample strain is determined geometrically from its initial length L_0 and midpoint displacement d:

$$\gamma = \frac{\sqrt{L_0^2 + 4d^2} - L_0}{L_0}. \tag{2.4}$$

The tension in the sample is calculated from the measured force and geometry as (Figure 2.3B):

$$T(t) = \frac{F(t)}{2\sin\theta}, \qquad \sin\theta = \frac{d}{\sqrt{d^2 + (L_0/2)^2}}. \tag{2.5}$$

To enable simultaneous imaging, image sequences from the CCD camera are recorded. This integrated optical configuration provides both quantitative force measurements and real-time imaging, making the MER a versatile platform for probing the rheological behavior of soft materials and biological systems.

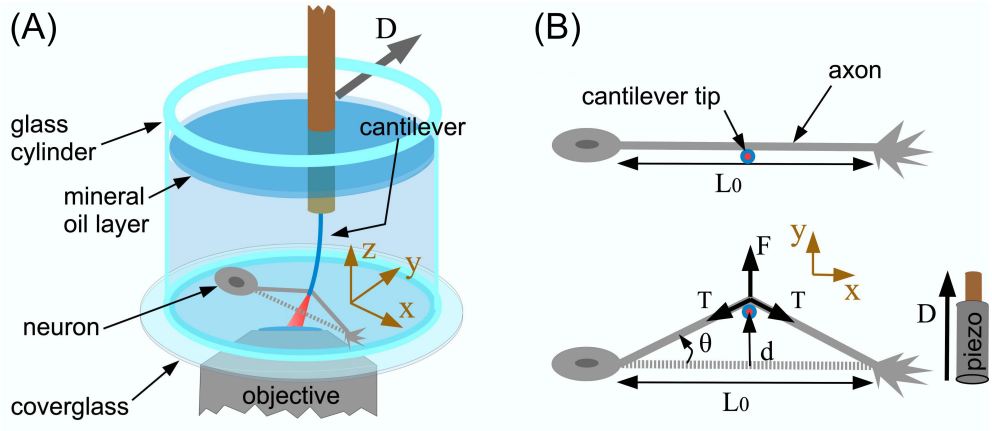


Figure 2.3: Schematic of the axonal stretching setup and tension calculation geometry. **(A)** An axon anchored at both ends—at the cell body and the growth cone—is stretched by applying a perpendicular displacement at its midpoint using the fiber cantilever. **(B)** Illustration of the stretching protocol and the geometric parameters used to determine axonal strain and tension T from the initial length L_0, cantilever tip displacement d, and force on the cantilever F. Adapted from Dubey et al., 2020 [13]

2.2.1 Fluorescence imaging mode

We made the MER capable of observing structural changes using fluorescence imaging in a sample while simultaneously measuring the forces it experiences during stretching. To implement this, the epifluorescence filter cube of the microscope, which is normally positioned below the objective, is used. The emission filter from this cube is removed and placed in front of the CCD camera to ensure that it does not interfere with detection of the laser light from the cantilever tip by the PSD. This configuration allows accurate tracking of cantilever deflection while enabling fluorescence imaging of the sample (Figure 2.4A). To demonstrate this capability, we used neuronal cells genetically modified to express soluble green fluorescent protein (GFP) in their cytoplasm. The axon, which is the tubular extension of the neuron, was stretched using an etched optical fiber as the cantilever, shown schematically in (Figure 2.4B). A fluorescence image of the stretched axon along with the laser spot from the cantilever tip is presented in (Figure 2.4C), illustrating the simultaneous measurement of mechanical response and structural visualization.

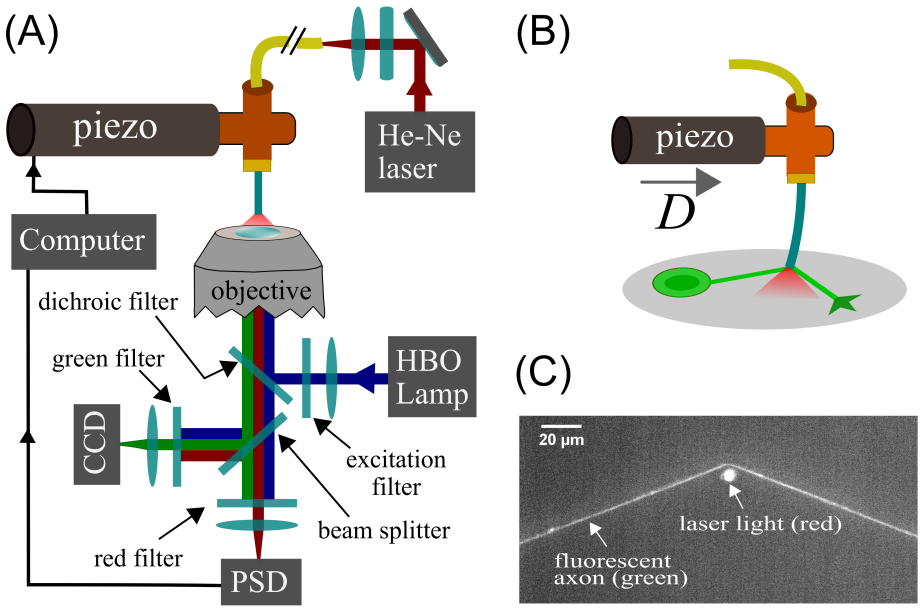


Figure 2.4: Fluorescence imaging during axonal stretching. (A) Fluorescence imaging is performed using a short-arc mercury lamp (HBO) and the epifluorescence filter module of the Zeiss AxioObserver D1 microscope (filter set 13: Ex. BP 470/20, dichroic FT 495, Em. 505–530). The emission filter is removed from the filter cube and placed in front of the CCD camera so that the laser light from the cantilever tip can reach PSD. **(B)** Schematic illustrating the stretching of a genetically labeled axon. **(C)** Fluorescence image of a stretched axon expressing soluble GFP. The green fluorescence signal from the axon and the red laser spot at the cantilever tip are captured simultaneously using a monochrome CCD camera. Figure adapted from our previously published work, Dubey et al., 2020 [13].

2.3 Calibration of the optical fiber

The average elastic modulus of the optical fibre material (inner and outer glass cores) is obtained by using the one end fixed in horizontal position and hanging weight at another end. A small piece of optical fibre (few mm in length) is inserted in a syringe needle, and the base of the fibre is glued and mounted on a micro-manipulator stage in a horizontal position, as shown in Figure (2.5). Care was taken to avoid the spread of glue along the fiber, which could otherwise alter its mechanical response. A hook of a thin metal wire (about 100 μm dia.) is glued to the tip of the cantilever as shown in the inset of figure (2.5). The force constant of this optical fibre acting as a cantilever is obtained by loading it with small

pieces of thin metal wires of known weights. The deflection of the cantilever is measured using a microscope consisting of a 20× objective, 125 mm focal length tube lens placed horizontally and a complementary metal-oxide semiconductor camera (DCC1545MGL, Thorlabs Inc., United States). The force constant (k) of the cantilever is obtained by the formula

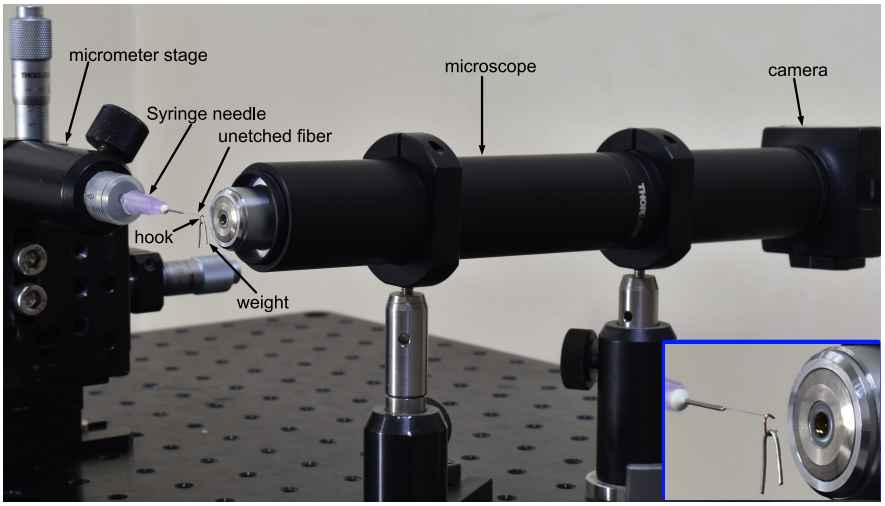


Figure 2.5: Cantilever calibration setup. A piece of unetched optical fiber is inserted into a syringe needle and is glued at the base using superglue. Then the syringe needle is mounted on a micrometer stage. The free end of the cantilever is imaged using a 20 x objective, a tube lens and a camera. A tiny hook made of metal wire is glued at the free end of the optical fiber and is loaded with pieces of metal wires of known weight (see inset) and the corresponding deflections are recorded

$$k = \frac{F}{\delta} \tag{2.6}$$

where $F = mg$ is the force exerted by the load m, which is the mass of the hanging wire and δ is the deflection of the tip of the cantilever. For a cylindrical cantilever with a load suspended at the tip, the Young's modulus of the material is given by [124]

$$E = \frac{FL^3}{3I\delta} \tag{2.7}$$

where L is the length and I is the area moment of inertia of the cantilever and is givne by

$$I = \frac{\pi R^2}{4} \tag{2.8}$$

where R is the radius of cantilever. The expression for the force constant can be obtained using equation 2.6, 2.7 and 2.8, and is given by

$$k = \frac{3\pi E R^4}{4L^3} \tag{2.9}$$

For a fixed length (unetched) cantilever, we have used different weights and calculated the value of k from each loading, to obtain an average value of k. We repeated this procedure for different lengths of cantilevers to obtain the plot shown in Figure (2.6). The slope of the plot gives the Young's modulus of the cantilever which is found to be 58.9 GPa with a confidence level of 95%.

In addition to the statistical uncertainty from the fit, the accuracy of the calibration was estimated from the measurement precision of the individual quantities: the applied force (mass) was measured with a balance having 0.1 mg resolution, the cantilever length was measured using a micrometer screw gauge (precision ~ 0.01 mm), the tip deflection was measured with a 20× objective for which the optical resolution is $\sim 1\ \mu$m, and the fiber radius was measured with a 40× objective (diffraction-limited resolution $\sim 0.86\ \mu$m). Propagating these independent uncertainties through the expression for Young's modulus yields a combined relative uncertainty of approximately 3.1%, representing the overall accuracy of the cantilever calibration for typical cantilever lengths and applied loads used in the experiment.

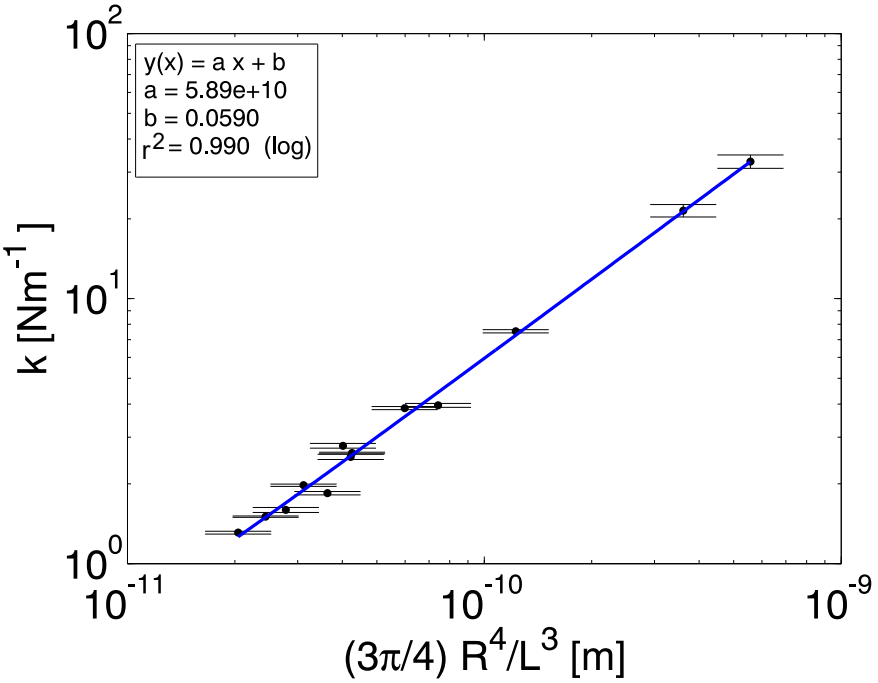


Figure 2.6: Cantilever calibration plot. Dependence of the cantilever force constant on its radius R and length L. Unetched fibers of different lengths were loaded with different known weights. The data were fitted to a straight line, and the resulting fit is shown on log–log axes for clarity. The slope gives the Young's modulus of the cantilever material. Each data point is averaged over minimum ten measurements using different weights for the same cantilever. The error bars are the standard errors from the mean (SEM).

2.4 Calibration of one-dimensional piezo actuator

To calibrate the one-dimensional piezo actuator, a pre-calibrated CCD camera was used as a reference. The spatial resolution of the camera, in microns per pixel, was determined using a microscope calibration slide (AX0001, OB-M, Olympus Corp., Japan) with a least count of 10 µm. For piezo calibration, a short length (< 1 mm) of an unetched fiber is used as a rigid cantilever so that the piezo displacement D can be tracked using the PSD or camera.

The fiber was mounted on the piezo actuator, with one end coupled to the laser via a fiber coupler. The laser light exiting the fiber was focused onto the camera. The

actuator, equipped with an integrated strain gauge for feedback, was controlled in closed-loop mode using a single-axis piezo servo controller via USB.

For calibration, the piezo was moved in discrete steps. At each position, images were recorded, and the motion of the laser spot was tracked using a MATLAB script that computed the intensity weighted centroid of the laser spot on recorded images by the camera. The measured positions were then plotted against the commanded displacements to generate the calibration curve. The measured positions from the CCD camera plotted against the corresponding displacements recorded by the piezo's integrated strain gauge are shown in Figure 2.7. The results demonstrate that 10 nm steps are clearly resolved at 40× magnification.

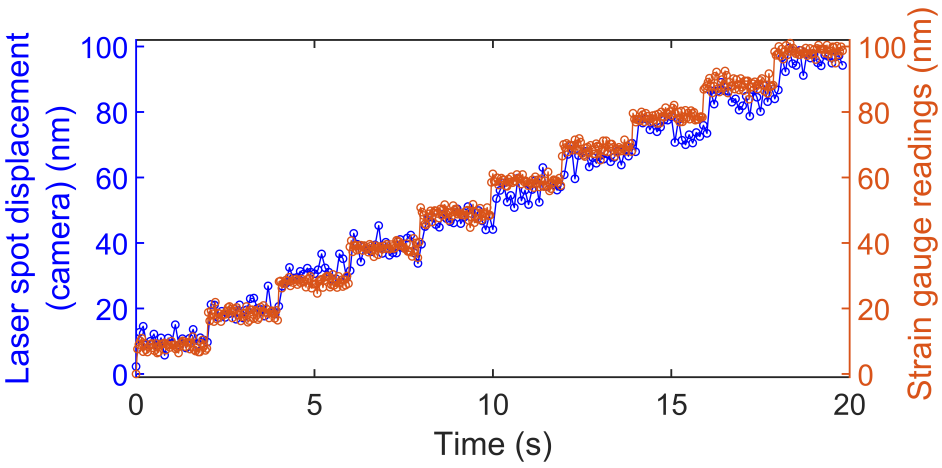


Figure 2.7: Piezo actuator displacement (orange circle) recorded using strain gauge sensor and corresponding laser spot position on the camera (blue circles) plotted as a function of time, during stepwise motion with 10 nm increments.

Next, to evaluate the linearity of the piezo actuator across its full range, the average positions measured from the camera at each step were plotted against the corresponding readings from the piezo's strain gauge. Larger steps of 5 μm were applied to cover the full travel range of the piezo actuator quickly, thereby minimizing the effects of drift. Raw data from the camera and the piezo strain gauge were each averaged over a 2 s interval to reduce detector noise. For the camera signal, this averaging also helps suppress possible vibration-induced fluctuations. A linear fit to the data yielded a slope close to unity, indicating correspondence

between the two measurement methods (Figure 2.8). This analysis confirms the accuracy and linearity of the combined piezo–camera system over the operational range.

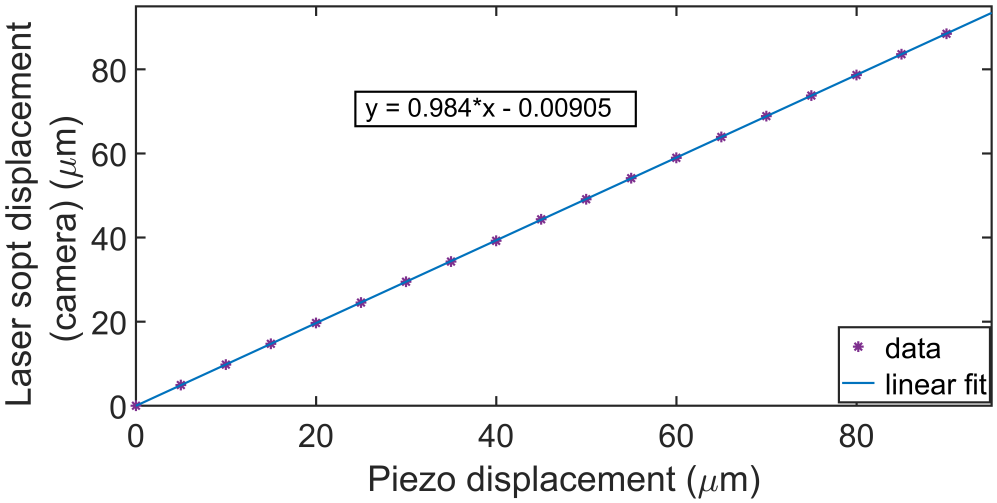


Figure 2.8: Linearity of the piezo actuator. The plot shows the relationship between the commanded piezo displacement (μm) and the corresponding laser spot displacement measured from the camera (μm). The linear dependence with a slope close to 1 indicates that the piezo actuator performs accurately, with the measured motion matching the expected displacement.

2.5 Spatial resolution of the PSD

Data from the PSD was acquired through the signal-processing circuit, which uses a 12-bit acquisition card. Given the 5.7 mm resistive length of the PSD, the theoretical digitization-limited spatial resolution at the detector plane is obtained by dividing this length by the 2^{12} output levels, yielding approximately 1.39 μm per count. Without magnification, this represents the smallest resolvable displacement. When imaged through an objective of magnification M_0, the effective resolution at the sample plane becomes 1.39 μm/M_0, giving about 34.8 nm at 40× magnification.

To determine the actual noise level of the PSD system, we recorded the position of a rigid fiber tip using the same procedure as in the camera calibration. Since the fiber does not move, any fluctuation in the measured position reflects system

noise or digitization limits. The PSD time trace at 40× magnification shows that the observed fluctuations are consistent with the expected digitization-limited resolution (approximately 35 nm) (Figure 2.9A), confirming that electronic noise is negligible compared to quantization noise. Furthermore, when the piezo actuator was aligned with the PSD x-axis and driven in discrete 35 nm steps, the steps were clearly resolved after temporal averaging of the PSD position data (Figure 2.9B), providing an independent verification of the effective spatial resolution.

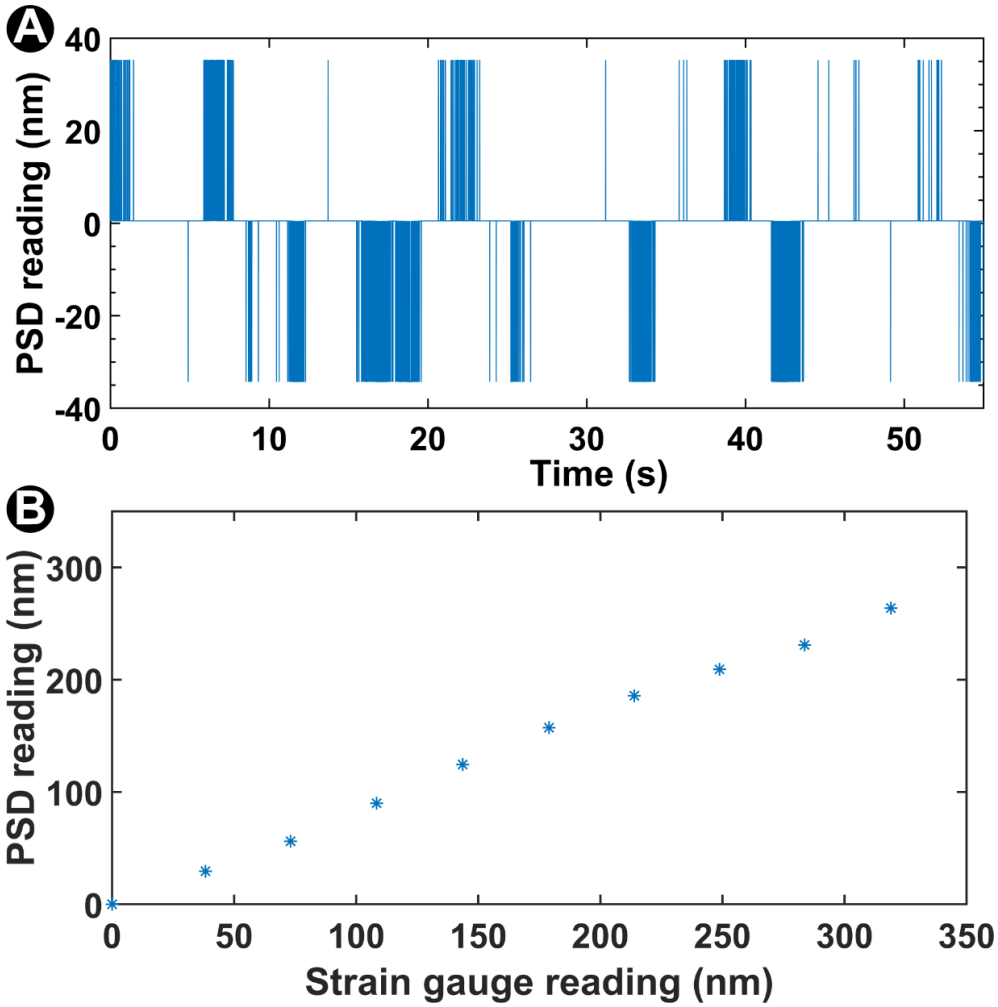


Figure 2.9: Spatial noise estimation and effective resolution of the PSD. (**A**) Time trace of the PSD signal at 40× magnification showing fluctuations consistent with the digitization-limited spatial resolution (approximately 35 nm). (**B**) PSD response when the piezo actuator is aligned with the PSD x-axis and moved in discrete 35 nm steps. After temporal averaging of the PSD signal, the individual steps are clearly resolved.

2.6 Feedback control and experimental software

Strain-controlled experiments in the MER are implemented through custom LabVIEW programming based softwares that operates through a closed-loop feedback algorithm. A representative front panel corresponding to one strain-controlled protocol is shown in Figure 2.10. The interfaces for other implemented protocols differ in their specific control logic but are similar in overall structure and operation.

At the beginning of an experiment, the user provides the geometric parameters of the cantilever, including its length and diameter. These parameters are used to calculate the cantilever spring constant, which is required to convert measured cantilever deflection into force. For samples that are stretched from the midpoint and fixed at both ends, such as axons and silk filaments, the initial end-to-end length of the sample is also specified and is used to determine the cantilever tip displacement corresponding to the prescribed strain protocol. The PSD and piezo actuator are then initialized, and their current positions are recorded as reference values.

Following initialization, the piezo actuator is incrementally displaced toward the target strain setpoint. After each adjustment, the instantaneous strain is calculated from the measured PSD signal and piezo position and compared with the desired value. If a discrepancy is detected, the feedback loop updates the piezo position to reduce the error. Once the target strain is reached, the algorithm continues to monitor the system and compensates for deviations arising from sample relaxation, thereby maintaining the selected strain over time.

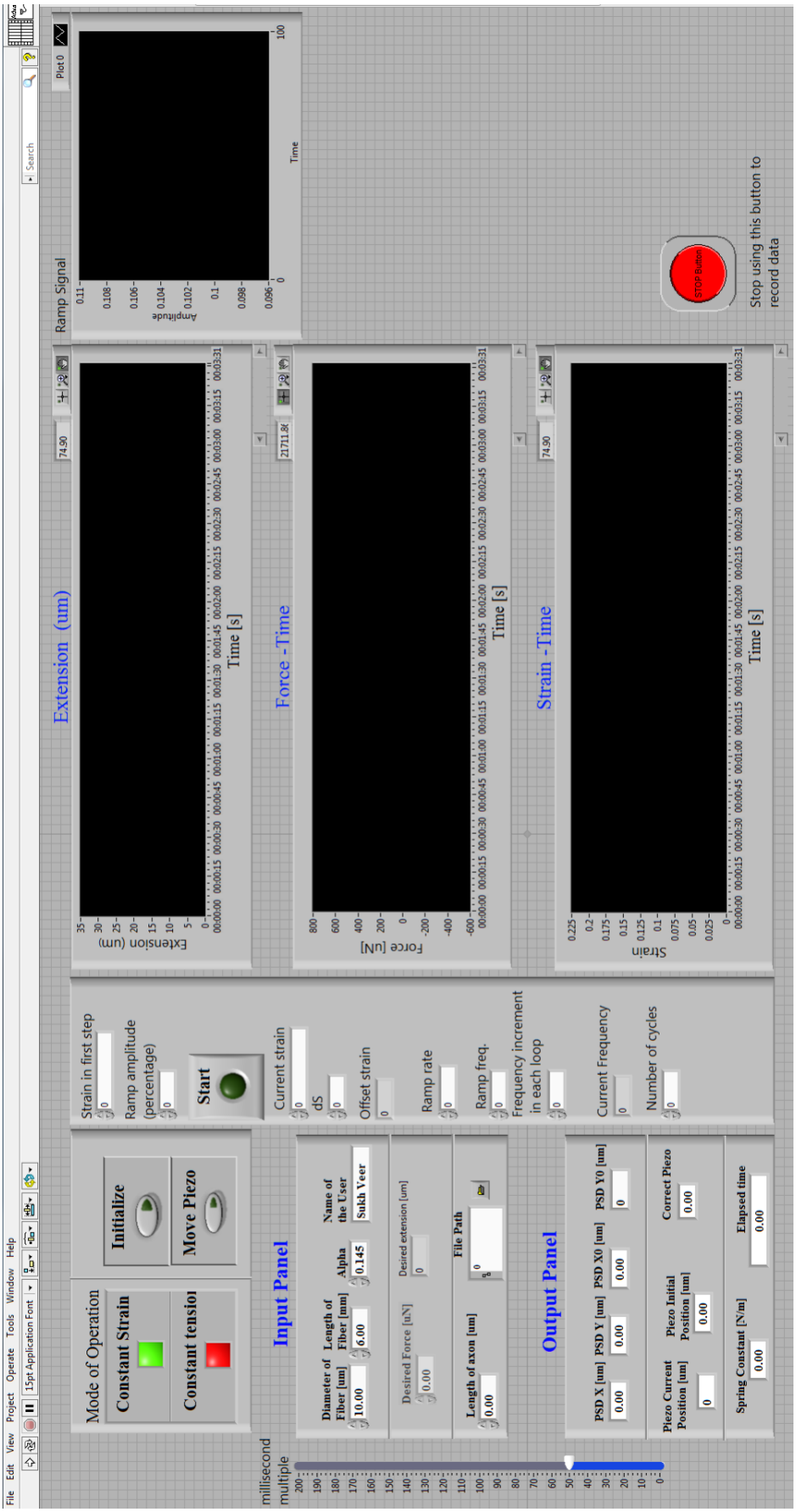


Figure 2.10: Screenshot of the MER controller software for a linear loading–unloading protocol. The software uses a feedback-loop algorithm to control strain

A schematic flowchart summarizing the sequence of operations and decision steps implemented in the feedback algorithm is shown in Figure 2.11.

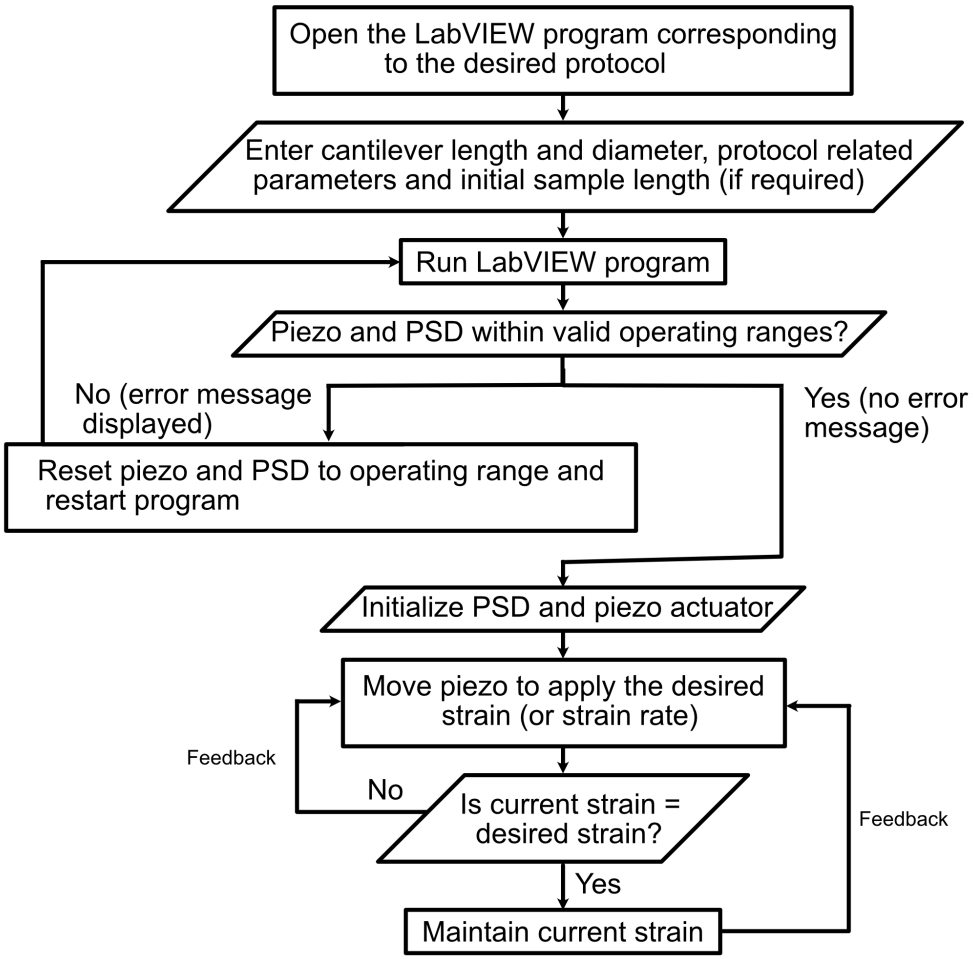


Figure 2.11: Flowchart of the closed-loop feedback algorithm used for strain-controlled MER experiments, showing user input, system initialization, automated range checking, and feedback-based adjustment of piezo displacement to reach and maintain the prescribed strain.

2.7 Development and validation of rheological protocols

This section describes the general procedure used to test and validate strain-controlled protocols. Before applying these methods to actual samples, validation measurements were performed on a short piece of the optical fiber as mock sample

with similar stiffnes to assess the performance and reliability of the protocols under controlled conditions (Figure 2.12). Optical fiber piece was positioned on a glass coverslip, with one end immobilized using adhesive while the opposite end remained free. The coverslip was mounted at the base of a plastic cylinder containing a central aperture, such that the free end of the fiber extended into the dish chamber. The cantilever was brought into contact with this free end of the mock sample and used to impose controlled displacements. The dish was filled with cell culture medium to replicate the refractive index and viscous environment present during axonal measurements.

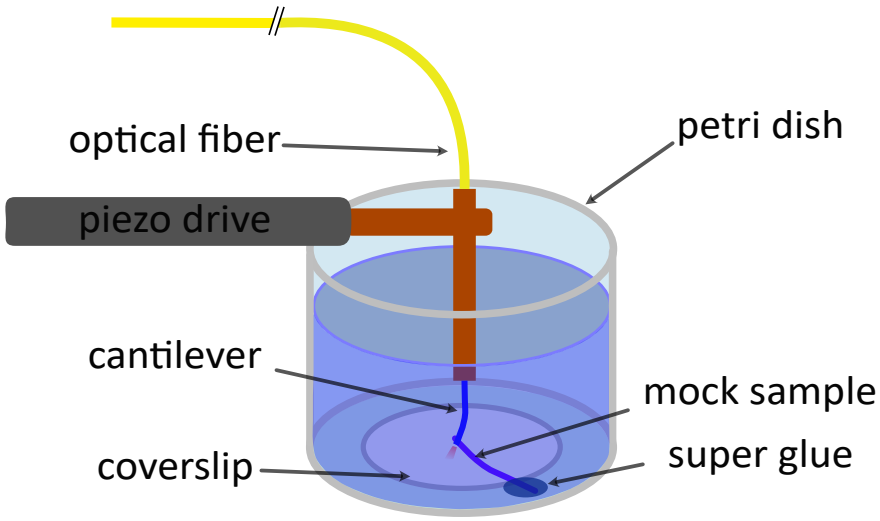


Figure 2.12: Deflecting of the mock sample (a separate optical fiber segment) using a cantilever. A cantilever was used to apply mechanical deformation to a mock sample, which consisted of another segment of optical fiber affixed to a coverslip. All mechanical testing was performed on this setup. The piezo actuator was programmed to execute a range of strain protocols, including multi-step stretching, combined step-and-oscillation inputs, and linear loading-unloading.

Both tip-displacement–controlled and strain-controlled rheological protocols were implemented in our setup, including step loading, step loading with superimposed oscillations, square-wave loading, and ramp protocols. In tip-displacement–controlled protocols, the cantilever tip follows the prescribed waveform directly, whereas in strain-controlled protocols the sample strain is defined and the corresponding cantilever displacement is computed accordingly. As an example, for

samples fixed at both ends, the cantilever displacement required to achieve a given strain is obtained from the geometric relation in equation 2.4. Since the validation procedure is common to all of these methods, only a protocol consisting of initial step displacement followed by a ramp protocol, implemented at fixed amplitude with varying frequency, is presented here as a representative example (Figure 2.13). Ramp protocol can be used to perform loading–unloading cycles, from which the hysteresis and energy dissipation can be calculated.

Next, to further confirm that the applied displacement signal corresponds to a true ramp, the signal at 0.01 Hz was analyzed in the frequency domain using a fast Fourier transform (FFT). Prior to the FFT, the DC component was removed to eliminate any offset. The FFT of the 0.01 Hz ramp shows a primary peak at 0.01 Hz, followed by smaller peaks at 0.03, 0.05, 0.07, … Hz with decreasing amplitude (Figure 2.14). This pattern of odd harmonics (1f, 3f, 5f, …) with decreasing amplitude is characteristic of a ramp waveform, confirming that the applied signal closely follows the intended ramp profile.

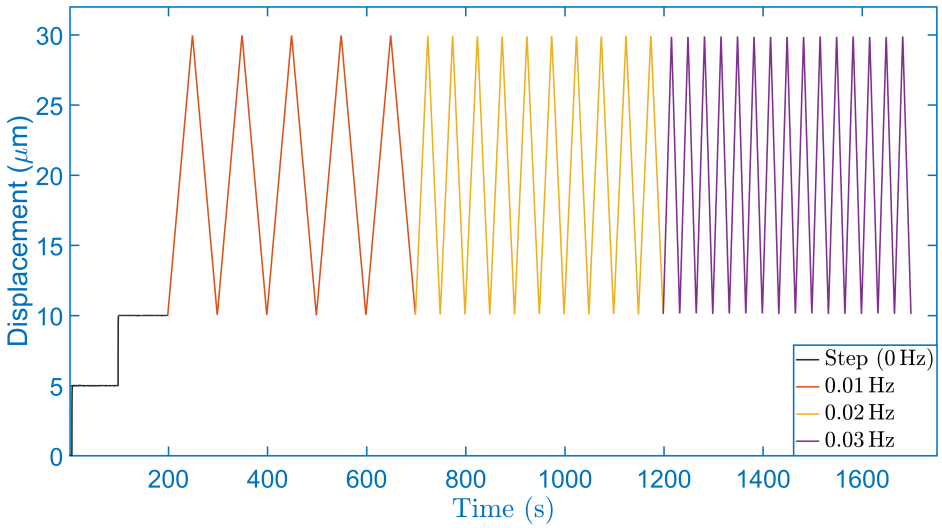


Figure 2.13: Step-strain followed by ramp protocol. The figure shows a series of initial step strains (black) followed by a ramp applied at fixed amplitude with varying frequency (0.01, 0.02 and 0.03 Hz).

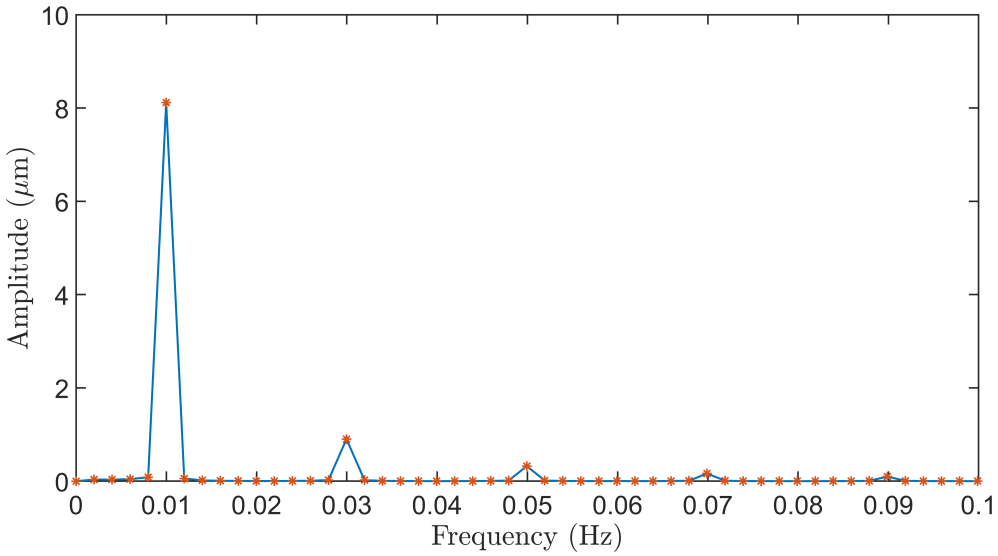


Figure 2.14: Frequency response of the 0.01 Hz ramp protocol. The frequency spectrum of the ramp signal shows a primary peak at 0.01 Hz, followed by smaller peaks at 0.03, 0.05, 0.07, … Hz with decreasing amplitude. This pattern of odd harmonics (1f, 3f, 5f, …) is characteristic of a ramp waveform, confirming that the applied displacement signal closely follows the intended ramp profile.

2.8 Preparation of the Cantilever

Optical fibers with their original diameter (~ 125 μm) are not sufficiently sensitive to measure the forces exerted by axons, which are on the order of nanonewtons. To enhance the force sensitivity of the cantilever, the optical fiber was etched down to a diameter of approximately 10 μm. Cantilevers with diameters of ~ 10 μm and lengths of 6–7 mm are sufficiently compliant to measure these forces.

To prepare an etched cantilever suitable for pulling axons, 48% and 24% hydrofluoric acid (HF) solutions were used in small plastic cylindrical containers with stable bases. The 24% solution was prepared by diluting the commercially available 48% HF. One end of a single-mode optical fiber was used to create the cantilever: the outer jacket was stripped with a blade and the inner plastic coating was burned off to expose the glass fiber (Figure 2.15A). The base of the bare fiber was coated with nail polish (Figure 2.15B) to prevent etching, since HF reacts strongly with silica but only weakly with the organic polymer

matrix of nail polish. This left approximately 1 cm of exposed glass for etching. The fiber was secured to a long plastic rod and immersed in 48% HF up to the nail-polish barrier, with gentle stirring to promote uniform etching. It was then transferred to 24% HF for further etching; the lower concentration helps prevent rapid dissolution of the fiber.

Each etching step typically lasts about 30 minutes, but the required duration can vary depending on the amount of fiber material already dissolved in the acid—since we reuse the solutions, the effective HF concentration decreases over time. After the expected etching period, the cantilever was positioned horizontally above a 40× microscope objective and imaged using a camera and ImageJ. ImageJ was further used to measure the diameter of the cantilever from the acquired images. Figure 2.15C shows the fiber before and after etching.

The fiber diameter was then measured at multiple positions to assess whether the cantilever had been etched uniformly and had reached the desired diameter. If not, the fiber was returned to the acid for additional etching. After etching was complete, the unetched end which, has a factory installed fiber coupler (FC) was connected to the laser, and the symmetry of the laser spot emitted from the etched tip was inspected. If the spot was asymmetric, the cantilever end was trimmed with a sharp scalpel until a nearly symmetric spot was obtained (Figure 2.15D). Finally, the cantilever length was measured with a vernier scale, and the optical fiber was mounted vertically on the piezoelectric drive, which was in turn fixed to an XYZ micromanipulation stage.

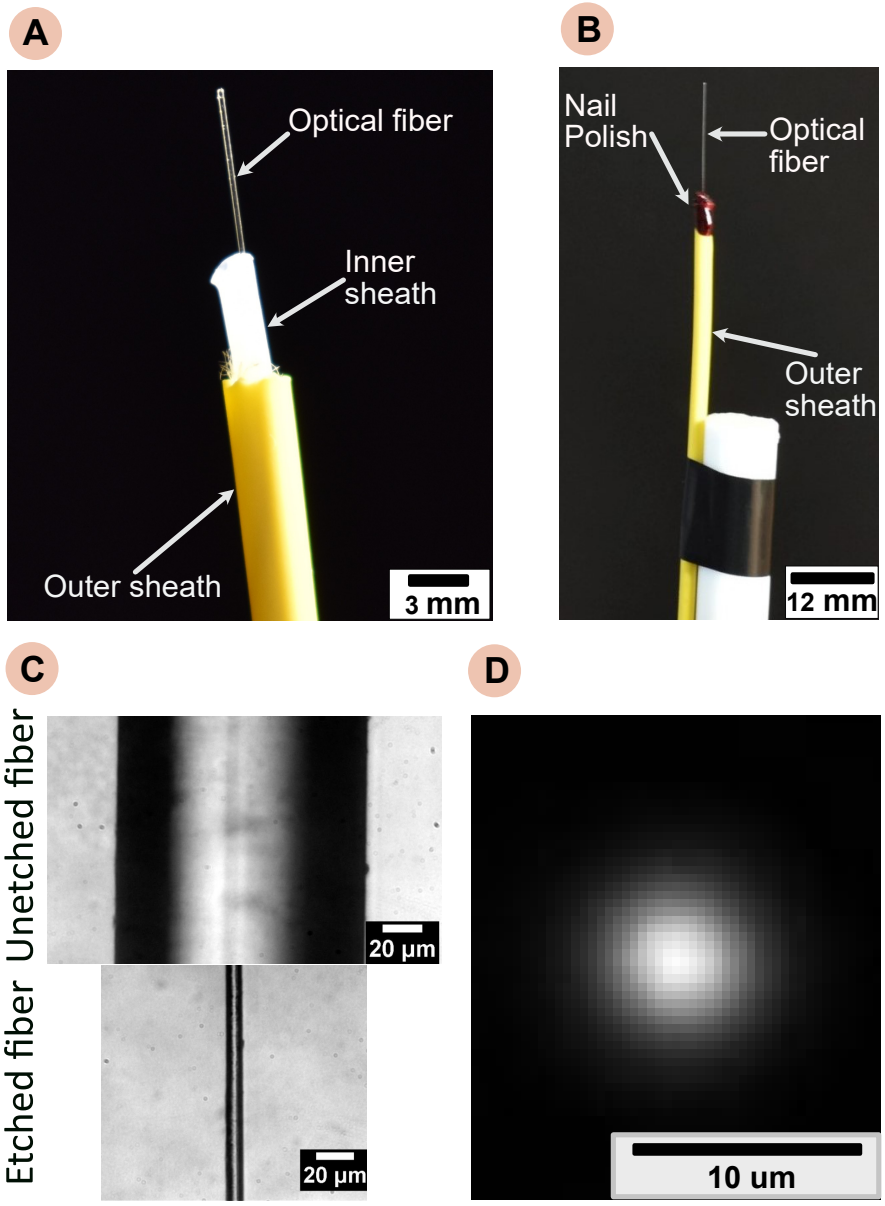


Figure 2.15: Preparation of the optical fiber cantilever (A) An optical fiber with portions of the inner plastic sheath and the bare glass fiber exposed. **(B)** The white plastic sheath is burnt off till where the outer sheath ends and then nail polish is applied at the base of the fiber before etching. Nail polish protects the fiber during HF etching, as its organic components do not react with HF. **(C)** A comparison of the unetched and etched optical fiber. **(D)** Laser spot at the fiber tip imaged on a camera, showing a Gaussian intensity profile used as a criterion for selecting fibers for experiments.

2.9 Comparison of cantilever and axonal force responses in a viscous medium.

For accurate calculation of forces exerted by axons (or other biological samples), the mechanical response of the etched optical-fiber cantilever should be characterized in a fluid environment. Hydrodynamic drag acting on the cantilever can introduce additional forces that contribute to the measured deflection and therefore must be quantified. For this purpose, the cantilever was displaced by a few micrometers—comparable to the displacements used to apply approximately 1% strain to axons—using the piezo actuator in an aqueous medium, and the resulting force was recorded over time. These measurements provided two key quantities: the hydrodynamic drag force acting on the cantilever and the cantilever relaxation dynamics following step displacements. The drag force obtained in this controlled setting was very small in magnitude, substantially lower than the forces measured during axonal stretching in step strain protocol (Figure 2.16).

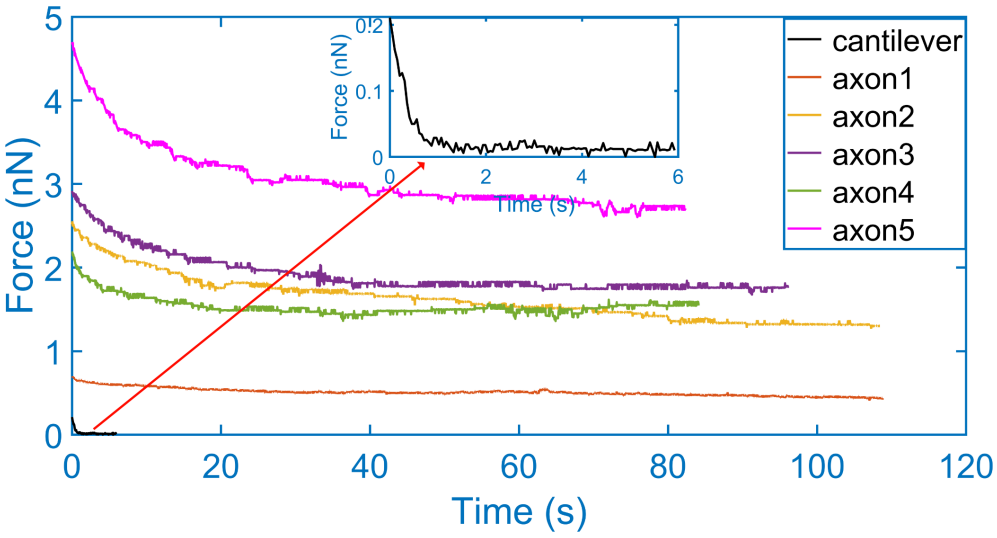


Figure 2.16: Force response of the cantilever in a viscous medium compared with axonal forces. The black curve represent the cantilever drag force in the absence of an axon, while each colored trace corresponds to an individual axon subjected to a 1% step strain. The cantilever drag force is small relative to the forces measured during axonal stretching, indicating that the measured responses are dominated by axonal mechanics. The inset shows a zoomed view of the cantilever force over time, highlighting its rapid relaxation following displacement.

Conclusion

This chapter presented the operating principles and technical implementation of the MER, followed by the calibration of its key components, including the optical fiber cantilever, piezo actuator, and PSD, to enable accurate force and displacement measurements. LabVIEW programs incorporating feedback control were then developed to implement strain- and displacement-controlled rheological protocols, and these routines were tested and validated using mock optical-fiber samples. Finally, the force response of the cantilever in a viscous medium was compared with that measured during axonal stretching, showing that cantilever–fluid interactions are negligible compared to axonal forces. Together, these results establish the MER as a reliable and well-characterized platform for mechanical measurements on biological samples axon in particular.

Chapter 3

Experimental analysis of axonal strain relaxation and cytoskeletal contributions

3.1 Introduction

Strain relaxation in axons serves as a key indicator of their viscoelastic behavior and mechanical integrity, providing insight into their ability to recover from deformation once external forces are removed. Following mechanical stretching, axons do not instantaneously return to their original length once the applied force is removed, but instead undergo gradual strain relaxation over time [85,89,125,126]. This time-dependent response reflects the complex viscoelastic nature of the axonal cytoskeleton, shaped primarily by microtubules, neurofilaments, the actin–spectrin lattice, and molecular motors. Together, these components enable axons to redistribute and regulate mechanical stresses over time, leading to the gradual relaxation observed in experiments. Such viscoelastic recovery is crucial in everyday physiological contexts, where axons routinely experience transient and sustained deformations during normal head and body movements, locomotion [5,6], and even during minor impacts or sports-related mechanical loads [7].

Understanding these dynamics is also important for injury biomechanics, where abnormal or excessive strain can exceed the normal relaxation capacity and lead to cytoskeletal damage.

In this chapter, we examine axonal strain relaxation under both immediate and delayed stretch–release protocols, enabling us to probe rapid responses and adaptive behavior under sustained stretch, similar to the prolonged deformation experienced during activities such as bending or sitting. To further understand the cytoskeletal contributions to this mechanical response, we also investigate the effect of cytoskeletal perturbing agents. By selectively perturbing components such as microtubules or actin filaments, we assess how these cytoskeletal element influences axonal relaxation dynamics.

3.2 Method

3.2.1 Axonal strain relaxation protocol

To examine the temporal and structural dependencies of axonal strain relaxation, we subjected axons of chick Dorsal Root Ganglia (DRG) neurons grown on plain glass surfaces for four days in-vitro (4DIV) to stretch deformations and then allowed them to relax back to their initial state as shown in Figure 3.1 (see Appendix A for cell culture details). Four DIV axons are chosen because it has been shown that MPS takes at least four days to form along the entire axon in chick DRG neurons [12]. The stretching was performed in a controlled manner using the custom-designed MER [10, 13] which is discussed in detail in Chapter 2 (Instrumentation). In order to minimize active contractile responses and probe passive viscoelastic responses, we perform experiments at room temperature (25±1 °C). The activity of molecular motors is known to decrease exponentially with temperature, following an Arrhenius-type dependence [127]. To stretch an axon, the tip of a rigid cylindrical glass cantilever, a few millimeters in length and ≈10 μm in diameter, is placed in contact with the mid-point of a floating axonal segment

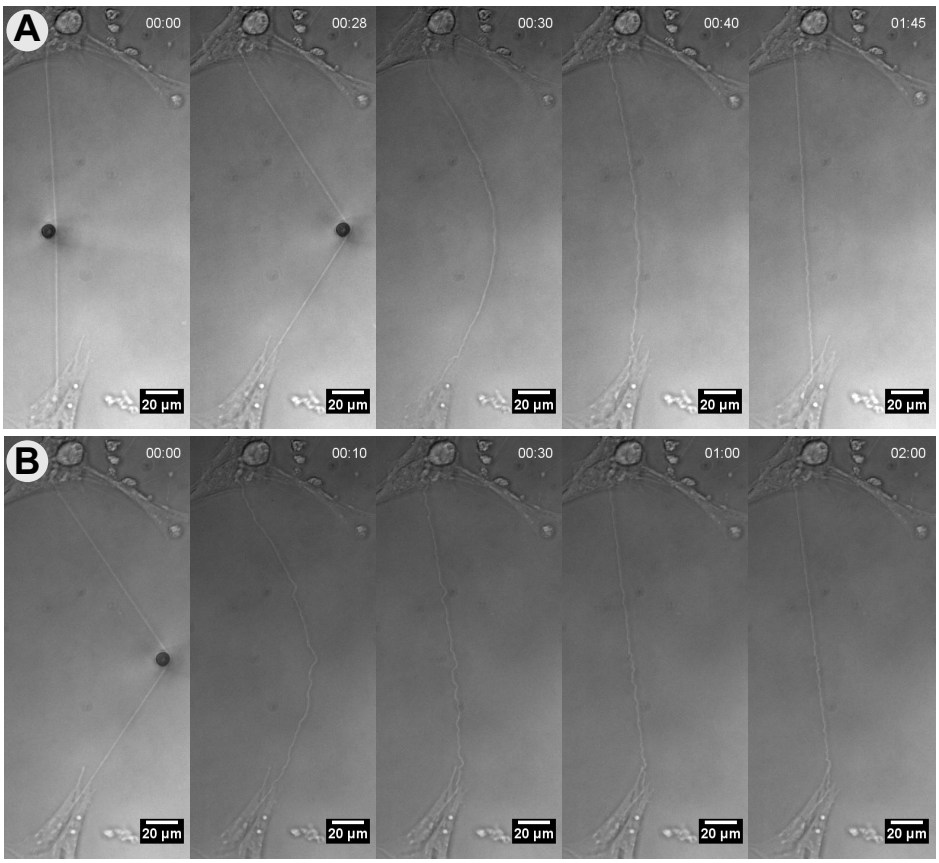


Figure 3.1: Axonal response to stretch-and-release vs. stretch-wait-release experiments. (A) Image sequence showing the strain relaxation of an initially straight axons which is stretched to a strain of ≈20% using a cantilever (dark circle) and then immediately released from the cantilever. Time is indicated in min:sec. **(B)** Image sequence showing the same axon as above when it is stretched by the same amount and released after maintaining the stretch for 10 min.

which is firmly anchored to the surface at two ends (Figure 3.1A). To check whether the axon is floating between fixed boundaries, the side of the microscope is tapped to observe if the axon vibrates. The initial length of the axon is measured to determine the maximum tip displacement. The tip is then displaced laterally at a strain rate of ≈1%/s to stretch the axon to a final imposed strain of ≈20%. The cantilever is then moved vertically (perpendicular to the plane of the axon) to release the axon and let it relax back to its initial conformation. The strain relaxation process that occurs after release is quantified by tracking the contour length of the axon by performing image analysis on the recorded video

microscopy images as shown in Figure 3.2. A brief description of the tracking and strain calculation is provided in the next subsection. Two types of experiments are performed. First, axon are pulled and released immediately. This immediate release phase offers insights into the immediate effects of stretch, observing how axons respond to rapid deformation and subsequent relaxation. After completion of the initial strain relaxation, the same axon is stretched once more and maintained in this extended state for a duration of about ten minutes and then released. The axon was held in the stretched state for ten minutes to allow sufficient relaxation before release. This duration was chosen because even a small strain step (1%) relaxes on the order of minutes [12]. The relaxation time varies with the applied strain—it initially increases with strain and then decreases-and thus a ten-minute hold ensures complete relaxation across all strain levels. Unlike immediate release, this prolonged stretch phase allows us to understand the adaptive mechanisms of axons over time.

3.2.2 Axonal tracking and strain relaxation calculation

Axonal contour lengths during relaxation experiments were quantified using a custom-written MATLAB program. Phase-contrast images acquired during stretching and release were processed to identify axonal contours (Figure 3.2). From the contour length l of the axon, strain is calculated using the formula $\varepsilon(t) = (l(t) - l_0)/l_0$, where $\varepsilon(t)$ is the amount of strain at any given time and l_0 is the is the contour length of the axon in the relaxed configuration. In practice, this value is close to the corresponding end-to-end (straight-line) distance, with small deviations arising from tracking noise. The full tracking workflow, including image-processing steps and algorithm implementation, is provided in Appendix B.

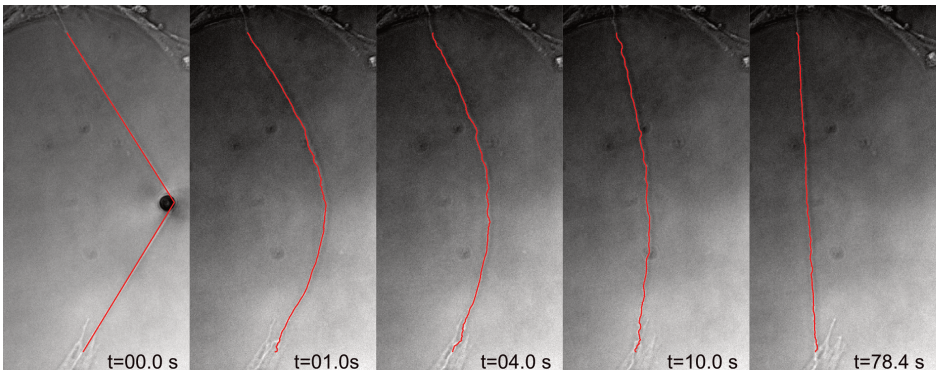


Figure 3.2: Representative images of a single axon with overlaid tracking results. Frame-by-frame tracking was obtained using custom MATLAB program. Tracked positions along the axon are shown in red color which is used for further analysis. Details of the tracking method are provided in the Appendix B.

3.2.3 Modifications to the cytoskeleton

Various cytoskeleton-disrupting drugs, including Nocodazole (M1404, Sigma-Aldrich), Latrunculin-A (L5163, Sigma-Aldrich), and Paclitaxel (Taxol) (T7402, Sigma-Aldrich), were solubilized in dimethyl sulfoxide (DMSO). Throughout the experiments, the final concentration of DMSO was maintained below 1%, and DMSO alone was used as the vehicle control. The specific concentrations of these agents used in each experiment are detailed in the corresponding sections.

3.3 Results

3.3.1 Axonal strain relaxation after stretch and release

Axonal strain relaxation for multiple individual axons following release after stretch is shown in Figure 3.3. In both experimental conditions—immediate release (Figure 3.3A) and release after a 10-minutes (Figure 3.3B) hold—axons exhibited a characteristic response where strain decreased sharply at first and then relaxed more gradually over time, reflecting the viscoelastic behavior of the axons and their cytoskeleton. These observations confirm that axons exhibit viscoelastic strain relaxation regardless of whether the release occurs immediately (0

min) or after a prolonged holding period (10 min). Quantitative analysis of the relaxation dynamics for both conditions is presented in the following subsection.

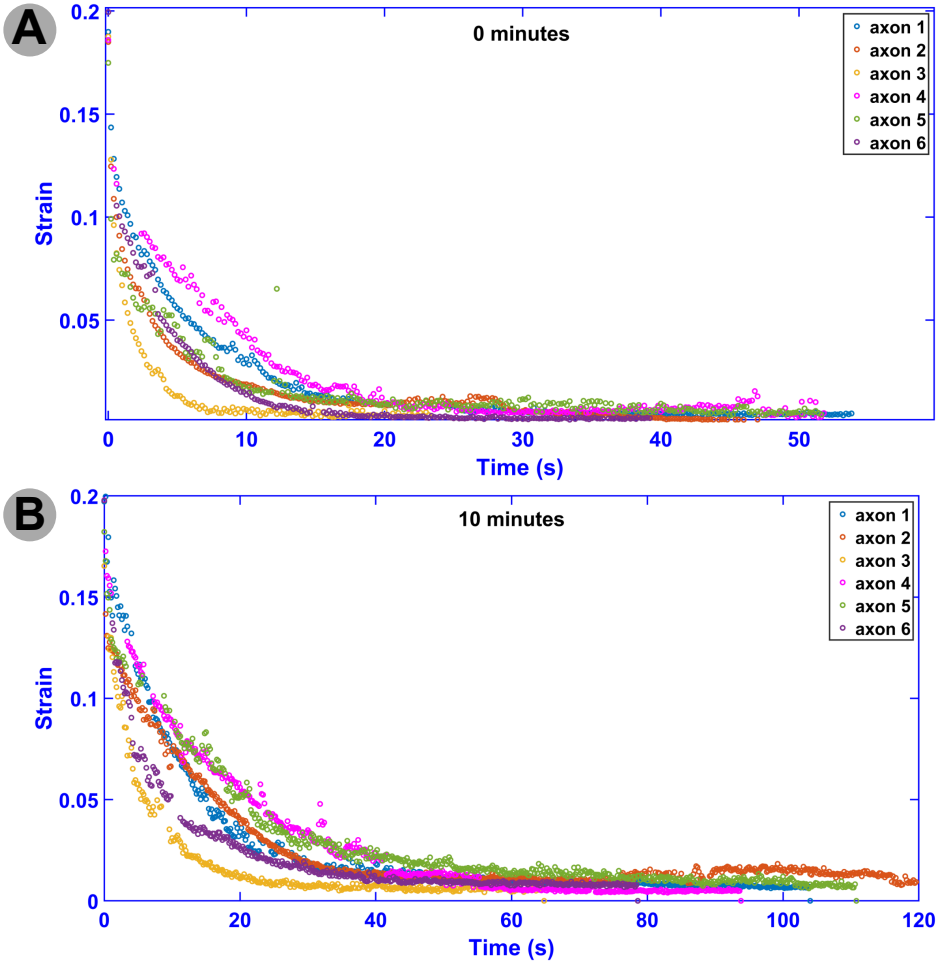


Figure 3.3: Axon exhibit viscoelastic strain relaxation. Strain relaxation profiles of same axons are shown under two experimental conditions: **(A)** immediate release after stretching and **(B)** release after maintaining the axons in a stretched state for 10 minutes. Each colored curve represents an individual axon, with matching colors in **A** and **B** corresponding to the same axon across both conditions. Both plots demonstrate that axons exhibit viscoelastic relaxation behavior.

3.3.2 Effect of waiting time on axonal strain relaxation

To investigate the influence of the adaptive response on axonal mechanical behavior, strain relaxation was compared between axons released immediately after stretch and those released following a 10-minute hold, as shown in Figure 3.4. Axons released after the prolonged stretch exhibited slower relaxation relative

to immediate-release, indicating a temporal modulation of viscoelastic behavior. Analysis of the strain–time curves revealed that the data were adequately fitted by the sum of two exponential functions of the form $ae^{-t/\tau_f} + be^{-t/\tau_s} + c$ as shown in the inset of Figure 3.4. This suggests that axonal relaxation occurs in at least two distinct phases—an initial faster decay followed by a slower, more gradual relaxation—captured respectively by the fast and slow time constants τ_f and τ_s.

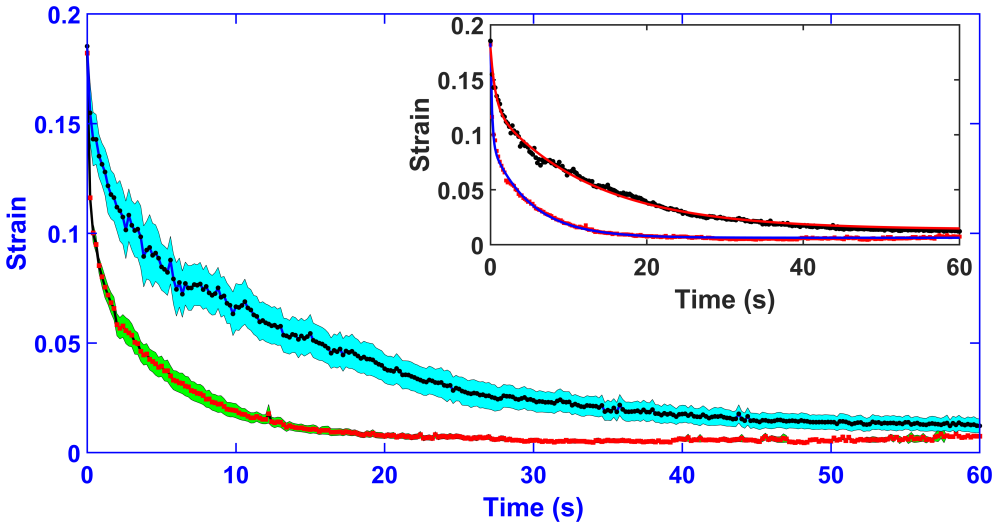


Figure 3.4: Axons exhibit slower strain relaxation after prolonged stretch. Plots showing the strain relaxation response of axons after they are stretched and released immediately (red symbols) or after a wait time of 10 min (black symbols). The solid lines are averages (for n=14 axons) and the shaded regions indicate the standard error of mean (SEM). Note that the strain relaxation for the stretch-wait-release case is significantly slower compared to immediate release. The inset shows the plots of the averaged data fitted to double exponential functions of the form $ae^{-t/\tau_f} + be^{-t/\tau_s} + c$.

Although the fit displayed in the Figure 3.4 represents the average strain–relaxation curve, the relaxation time constants τ_f and τ_s were extracted from fits to individual axons. The average values obtained were $\tau_f = 0.19 \pm 0.03$ s and $\tau_s = 5.02 \pm 0.57$ s before the 10-minute hold, and $\tau_f = 0.88 \pm 0.25$ s and $\tau_s = 14.41 \pm 1.92$ s afterward (error bars are the standard error of mean (SEM)). Notably, both τ_f and τ_s increased following the prolonged stretch (Figure 3.5), indicating a slowing of both relaxation phases. These results demonstrate that while axons retain their inherent viscoelastic properties, the rate of strain relaxation is influenced by the duration of applied stretch, highlighting the dynamic and time-dependent nature

of axonal mechanics and suggesting that the underlying viscoelastic parameters may be modulated during the waiting period, potentially due to cytoskeletal dynamics or structural reorganization.

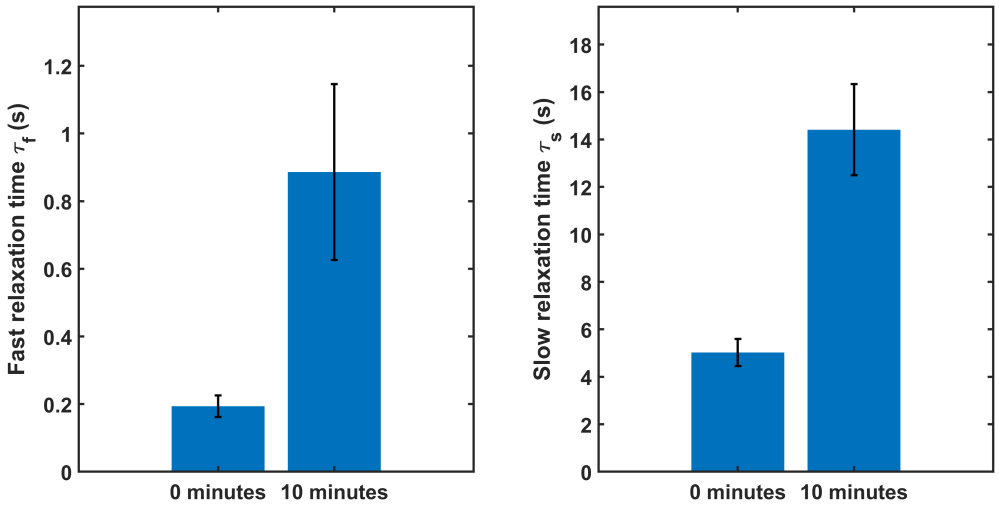


Figure 3.5: Relaxation time constants before and after prolonged stretch. Bar plots showing the fast (τ_f) and slow (τ_s) relaxation time constants extracted from biexponential fits of individual axonal (n = 14) strain–relaxation curves. Both relaxation time constants increased after the 10-minute hold, indicating a slowing of fast and slow viscoelastic phases (error bars represent SEM).

3.4 The role of different cytoskeletal filaments in axonal strain relaxation

After characterizing the strain relaxation response of normal neurons in culture, we examined the relaxation behavior of axons treated with cytoskeleton-perturbing drugs to determine how different cytoskeletal components contribute to the observed mechanical response. The axonal cytoskeleton is primarily composed of three major filament systems: microtubules, filamentous actin (F-actin), and neurofilaments. In this study, we focus specifically on microtubules and F-actin, as these networks are closely associated with axonal mechanical behavior and are expected to play central roles. To probe their role in axonal strain relaxation, we selectively stabilized or disrupted microtubules and actin filaments using pharmacological agents and compared the resulting relaxation dynamics.

By quantifying the changes in strain relaxation across these perturbations, we assessed how modifying each component influences the axonal response to stretch. In each case, axons were incubated at 37 °C for 30 min, and experiments were then performed at 25±1 °C.

We first investigated the role of microtubules by disrupting them using Nocodazole (16 μM), which depolymerizes microtubules and reduces the overall microtubule mass. Faster axonal retraction compared to control after nocodazole treatment has been reported in Drosophila axons [110]. Therefore, weakening the microtubule network is expected to alter axonal strain relaxation. As shown in Figure 3.6, axons treated with Nocodazole also exhibited clear viscoelastic strain relaxation following stretch release, with a characteristic biphasic profile (shown in the inset of Figure 3.6) similar to that observed in control axons.

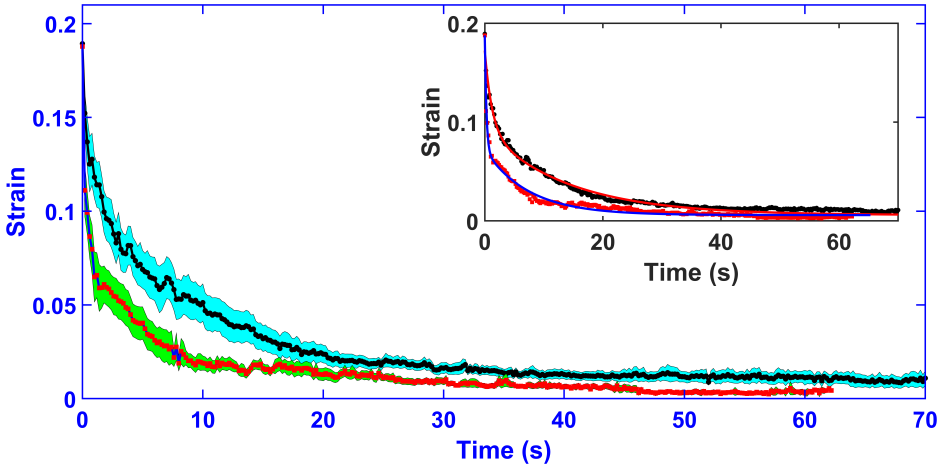


Figure 3.6: Strain relaxation of axons treated with Nocodazole under immediate and delayed release conditions. Strain relaxation profiles of axons shown as mean responses (n = 10 axons) pretreated with 16 μM Nocodazole (microtubule-disrupting agent) for 30 min. Symbols corresponding to immediate release are highlighted in red, and those for delayed release after 10 min hold time are highlighted in black. Error bars (SEM) are shown. The inset shows representative average data fitted to a double-exponential function.

Next, we examined the effect of microtubule stabilization by treating axons with Paclitaxel (Taxol, 10 μM), a drug known to enhance microtubule stability and increase microtubule mass in axons [128, 129]. As shown in Figure 3.7, Taxol-

treated axons similarly exhibited biphasic viscoelastic strain relaxation following release.

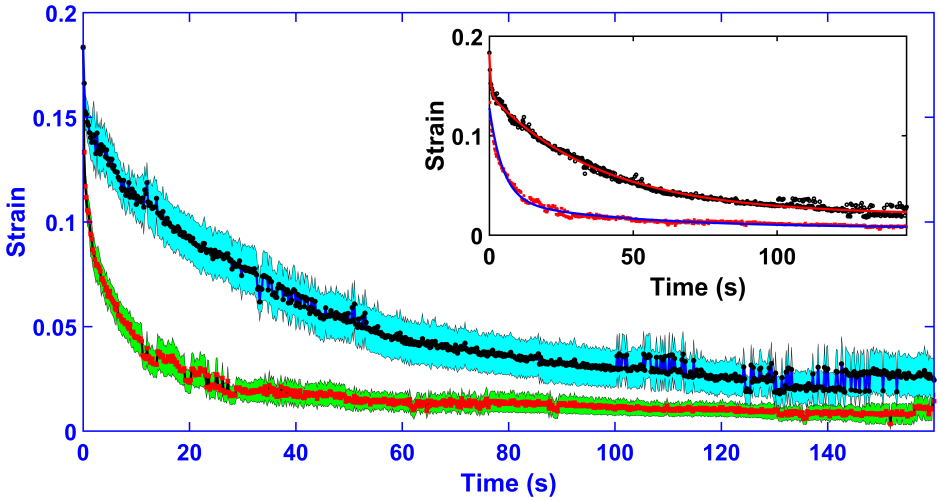


Figure 3.7: Effect of microtubule stabilization by Taxol on axonal strain relaxation. Mean strain relaxation profiles for axons (n = 10) treated with 10 μM Paclitaxel (Taxol) for 30 min under immediate (red) and delayed (black symbol) release protocols. Inset shows double-exponential fits to the average data.

To investigate the role of actin filament-based structures such as MPS, cells were first pre-treated with Taxol (10 μM for 30 min) followed by treatment with the actin-disrupting drug Latrunculin-A (Lat-A, 1 μM for 30 min). This sequential treatment was used because previous studies have shown that disrupting actin structures can also destabilize microtubules due to cytoskeletal crosstalk [130,131]. Figure 3.8 shows the relaxation response after actin disruption following prior microtubule stabilization. Across all pharmacological conditions, axons continued to display viscoelastic, biphasic relaxation, and the 10-minute hold consistently slowed the relaxation phase, indicating that this slowing is not abolished by disrupting either microtubules or actin.

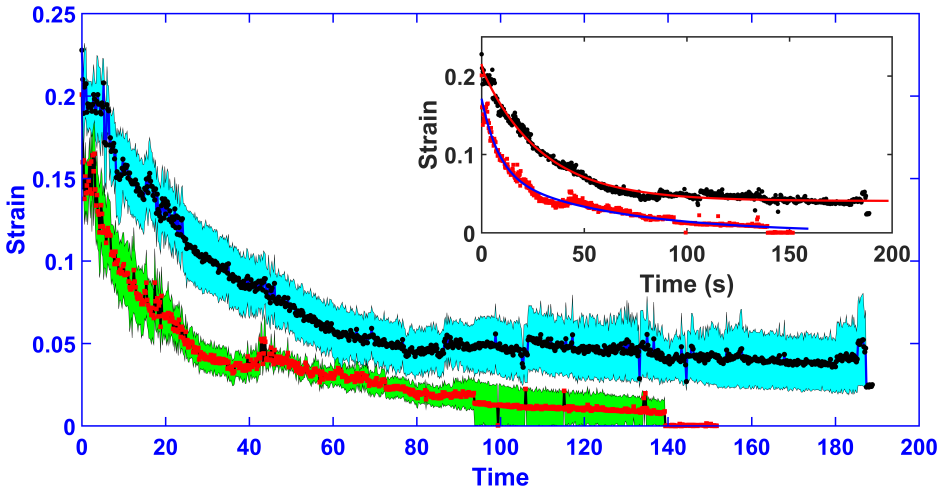


Figure 3.8: Influence of actin disruption on strain relaxation following microtubule stabilization. Axons (n = 7) were first treated with 10 μM Taxol for 30 min to stabilize microtubules, followed by 1 μM Latrunculin-A for 30 min to destabilize actin filaments. Strain relaxation curves for immediate (red) and delayed (black) release reveal additional slowing associated with actin disruption. Inset shows double-exponential fits to the average data.

To evaluate how cytoskeletal perturbations influence the dynamics of axonal strain recovery, and to determine whether these treatments alter any aspect of the strain relaxation behavior beyond the robust viscoelastic and biphasic response observed in all conditions, we compared the raw averaged strain–time curves for immediate (0 min.) and delayed (10 min.) release across all treatments (Figure 3.9). This comparison enables us to assess how modifying microtubule or actin organization affects the rate and extent of relaxation under both rapid and sustained stretch conditions.

For the immediate release condition (0 min.), Nocodazole-treated axons do not exhibit any major deviation in their relaxation profile relative to untreated controls (Figure 3.9A). In contrast, microtubule stabilization with Taxol leads to a noticeably slower relaxation response, and the combined Taxol + Lat-A treatment produces the slowest relaxation among all conditions. This progressive slowing with actin disruption following microtubule stabilization points to an important contribution of cortical actin structures in facilitating efficient strain recovery, particularly under rapid release.

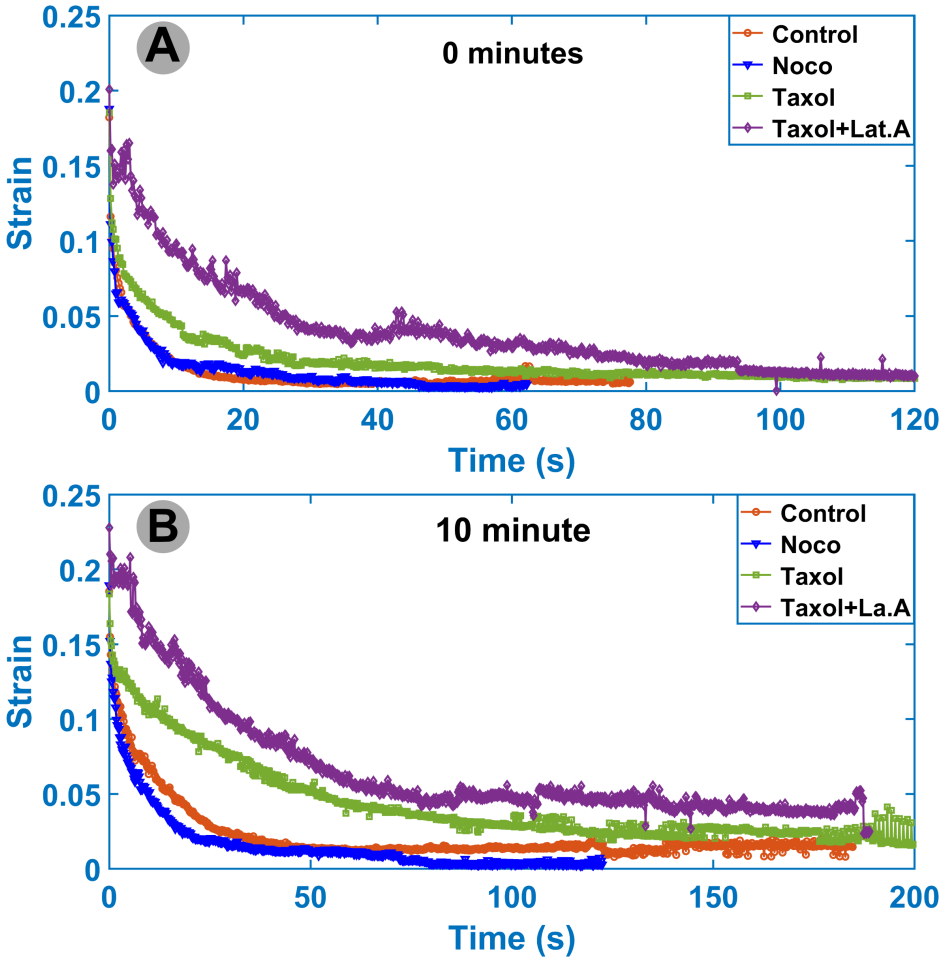


Figure 3.9: Comparison of strain relaxation dynamics across cytoskeletal perturbations. Raw averaged strain–time curves for axons subjected to immediate release (A, 0 min) and delayed release (B, 10 min) following stretch, plotted for all experimental conditions (Control, Nocodazole, Taxol, and Taxol + Lat-A). The curves highlight differences in relaxation rate under each perturbation, with minimal deviation from control for Nocodazole at 0 min, and progressively slower relaxation for Taxol and Taxol + Lat-A, particularly under the 10-min delayed release condition. Sample sizes: Control (n=14), Nocodazole (n=10), Taxol (n=10), and Taxol + Lat-A (n=7) axons.

Under the 10-min delayed release condition, a clearer distinction between treatments emerges. Nocodazole-treated axons relax faster than control, whereas Taxol-treated axons exhibit considerably slower relaxation (Figure 3.9B). The combined Taxol + Lat-A treatment remains the slowest case, suggesting that both microtubules and cortical actin contribute to maintaining axonal mechanical resistance and regulating the adaptive response that develops during sustained stretch.

The corresponding relaxation time constants, τ_f and τ_s, extracted from the double-exponential fits, are presented in Figure 3.10 and Table 3.1.

Table 3.1: Fast and slow relaxation times obtained from biexponential fits under immediate (0 min) and delayed (10 min) release conditions for different drug treatments. Values are reported as mean ± SEM.

Condition	0 min release		10 min release	
	τ_f (s)	τ_s (s)	τ_f (s)	τ_s (s)
Control	0.19 ± 0.03	5.02 ± 0.57	0.88 ± 0.26	14.41 ± 1.92
Nocodazole	0.20 ± 0.02	5.73 ± 1.34	0.38 ± 0.11	10.02 ± 1.47
Taxol	0.64 ± 0.17	21.23 ± 7.85	1.64 ± 0.62	47.88 ± 6.80
Taxol + Lat-A	3.96 ± 1.70	23.71 ± 2.44	4.30 ± 1.41	59.28 ± 20.70

Consistent with the raw strain trends, when microtubules are disrupted using Nocodazole, both τ_f and τ_s remain largely unchanged under the immediate release condition. However, for the delayed release condition, both time constants tend to decrease, suggesting that Nocodazole-treated axons may relax more rapidly. In contrast, microtubule stabilization with Taxol leads to increases in both τ_f and τ_s for immediate as well as delayed release. The combined treatment of Taxol followed by Lat-A produces the largest increase in relaxation times across both conditions.

Together, these results highlight that axonal relaxation dynamics arise from coordinated interactions between microtubules and cortical actin, motivating future investigations into the mechanisms underlying this adaptive viscoelastic response.

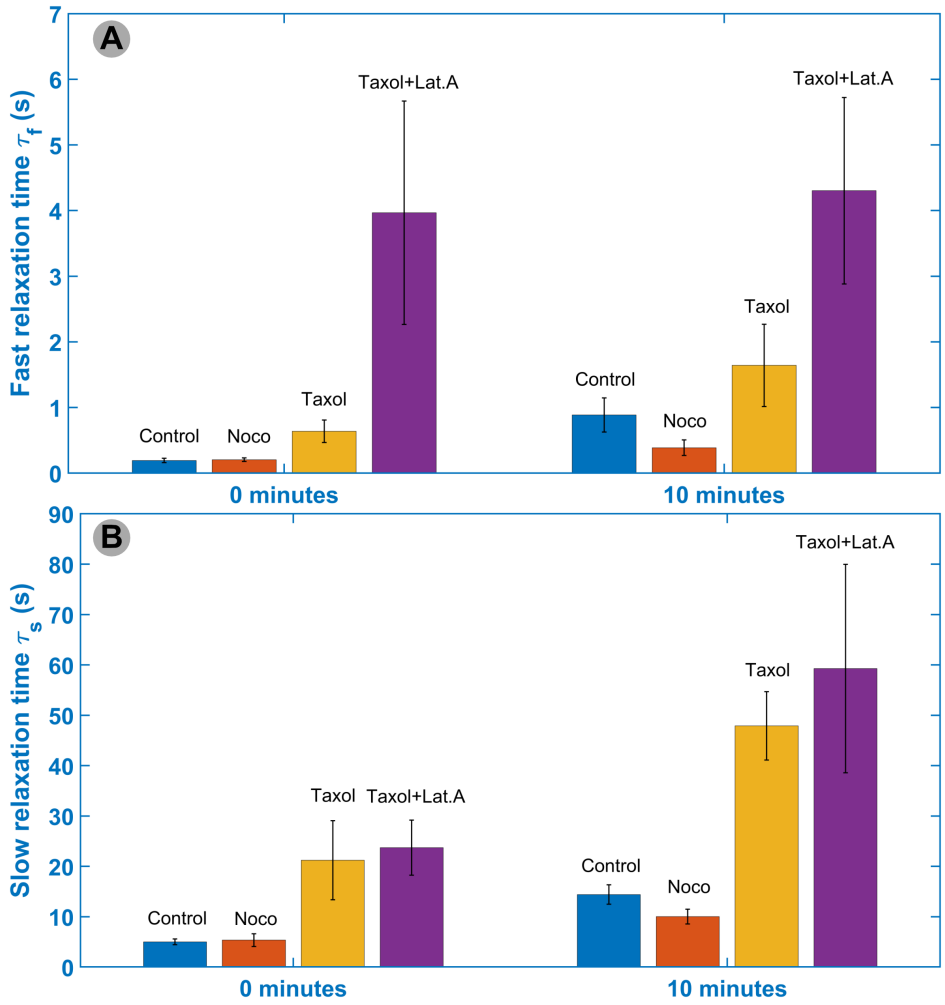


Figure 3.10: Comparison of strain relaxation times for control and drug treated axons. The strain relaxation curves are fitted to a double exponential fit to obtain a fast relaxation time τ_f and a slow relaxation time τ_s. **(A)** Plot showing the differences in the fast relaxation timescale (τ_f) for control and drug treated axons, with and without a 10 min wait time before release. **(B)** Slow relaxation timescale (τ_s) for control and drug treated axons, with and without a 10 min wait time before release. Control (n=14), Nocodazole (n=10), Taxol (n=10), and Taxol+Lat-A (n=6) axons.

3.5 Role of the Axonal Diameter in Axonal Strain Relaxation

The diameter of axons is regulated by the amount and organization of various cytoskeletal components, including the membrane-associated periodic skeleton composed of actin rings interconnected by spectrin cross-bridges and stabilized

by adducin, neurofilaments, and microtubules [25, 132–136]. Accurate determination of axonal diameter is challenging with conventional light microscopy so to examine whether relaxation behavior depends on thickness, we divided axons in our experiments into just two groups based on their measured diameters: *thin axons* (diameter $< 1.5\ \mu$m) and *thick axons* (diameter $\geq 1.5\ \mu$m) (Figure 3.11). Thick axons tended to relax more slowly than thin axons overall, suggesting that axonal diameter may modestly influence the rate of strain recovery following stretch. This slower relaxation might be related to an altered composition or ratio of cytoskeletal elements in thicker axons [137].

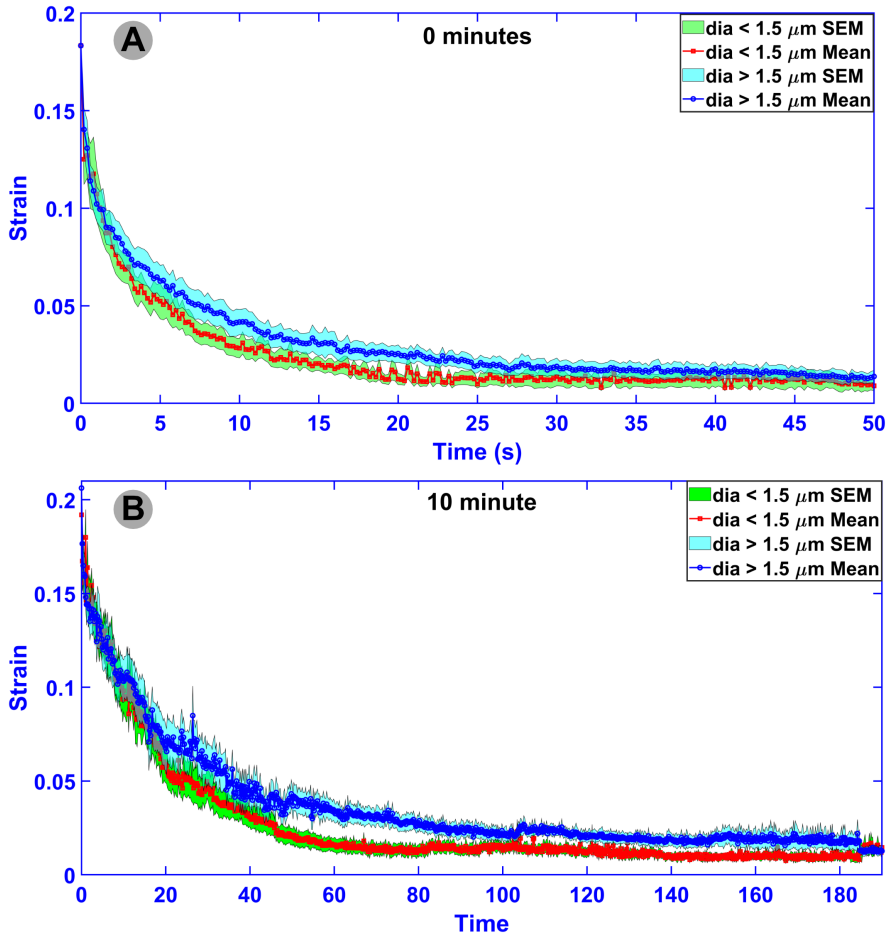


Figure 3.11: Dependence of strain relaxation on axonal diameter. Axons were categorised into two bins in order to investigate the effect of diameter on strain response. **(A)** Strain relaxation of thin ($< 1.5\mu$m) and thick ($> 1.5\mu$m) axons when subjected to immediate release. **(B)** Strain response of thin and thick axons when a wait time of 10 min is introduced before release. Note that thicker axons have notably slower strain relaxation in comparison to thinner axons.

Quantitatively, for thick axons (diameter $\geq 1.5\ \mu$m), the fast and slow relaxation timescales in the immediate release condition are $\tau_f \approx 0.42$ s and $\tau_s \approx 8.95$ s, compared to $\tau_f \approx 0.52$ s and $\tau_s \approx 6.85$ s for thin axons (diameter $< 1.5\ \mu$m), corresponding to a ~20% decrease in τ_f and a ~30% increase in τ_s. In the delayed (10 min) release condition, thick axons show $\tau_f \approx 0.93$ s and $\tau_s \approx 30.66$ s, compared to $\tau_f \approx 0.76$ s and $\tau_s \approx 18.99$ s for thin axons, corresponding to an increase of ~22% in τ_f and ~60% in τ_s. Overall, the more consistent trend is observed in the slow relaxation timescale, which tends to increase for thicker axons, while changes in the fast timescale are smaller and less systematic. More precise measurements of axonal diameter would be required to establish this trend more conclusively.

3.6 Discussion and possible explanation

Based on the experimental results presented in this chapter, we approximated the axon as a parallel arrangement of structural components with two distinct mechanical responses (Figure 3.12). One component is the membrane–periodic skeleton (MPS). This lattice behaves as a tension-buffering viscoelastic solid, where energy dissipation and delayed relaxation arise after stretching due to the unfolding and refolding dynamics of spectrin repeat domains, with stress reaching a nonzero steady-state value [12]. This stress stored in the MPS during stretch forms a mechanical "stress memory," allowing it to recover its original configuration through the reversible refolding of spectrin domains upon subsequent release.

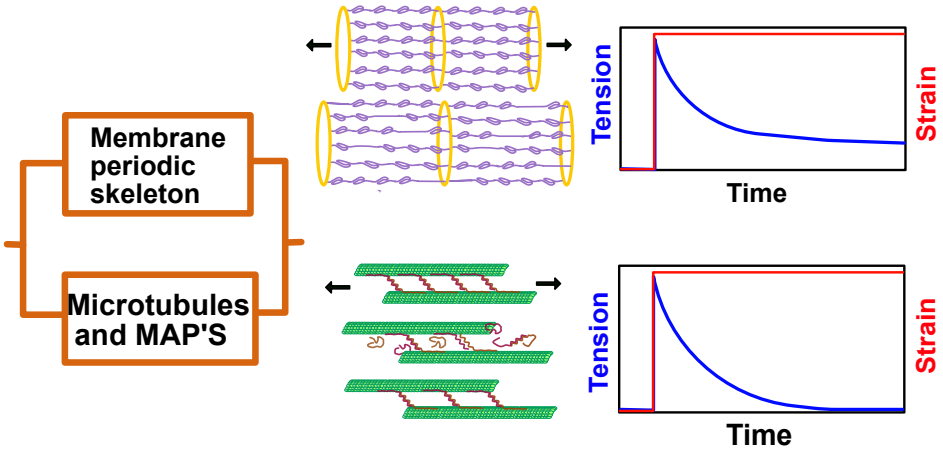


Figure 3.12: Schematic diagram showing the distinct mechanical behaviors of actin and microtubule based axonal scaffolds. Based on the experiments presented here, the axon can be approximated by a parallel arrangement of two structural elements with very different mechanical responses. The periodically arranged actin rings which are interconnected by α/β-spectrin tetramers act as a tension buffering viscoelastic solid. The tension buffering property and dissipation arises from the unfolding/refolding dynamics of the repeat domains of spectrins [12]. Owing to the periodic nature of this lattice, and assuming that annealing of the structure takes long times (> 10 min), this scaffold act as a solid at long times. The microtubule bundle, on the other hand act as a solid to fast stretch–when MAPs do not have time to unbind–and as a fluid at long times. The fluid behavior arises due to microtubule sliding mediated by transient unbinding of crosslinks [96]. Note that when subjected to a step-strain, stresses in the periodic lattice relaxes to a finite value as seen in earlier experiments [12], while stresses in the microtubule bundle can relax all the way to zero due to sliding.

Another component is the microtubule bundle cross linked by MAPs, which behaves as a solid under rapid stretching–when MAPs do not have sufficient time to unbind—and as a fluid over longer timescales. The fluid-like response arises from microtubule sliding enabled by the transient unbinding of MAPs. Since the axons in our experiments were stretched at a relatively slow rate (approximately $1\%\,\mathrm{s}^{-1}$), the likelihood of MAPs unbinding increases, permitting stress relaxation through microtubule rearrangement and sliding. Previous studies have also shown that when the microtubule–MAPs bundle is stretched at a rate of approximately $1\%\,\mathrm{s}^{-1}$, tau proteins detach at a small strain of about 4% [96]. This implies that in our case, where axons are stretched by about 20%, most of the crosslink connections are likely to break, although some new ones may reform

during stretching.

Upon immediate release after stretch (i.e., without a hold period), the MPS doesn't get sufficient time to relax and therefore carries the majority of the residual stress, effectively exhibiting a higher apparent elastic modulus and relaxing more rapidly after unloading. In contrast, the microtubule bundle, once MAPs have detached, loses mechanical stress memory and can slide freely, offering minimal resistance. The combined response of these two elements—one long-term solid-like and the other long-term fluid-like can accounts for the biphasic relaxation pattern observed experimentally.

When axons are released after a prolonged stretch, the MPS can soften due to its tension-buffering ability, leading to a decrease in its effective elastic modulus. During this period, microtubule cross-linkers can reform, and upon release, the MPS will relaxes slowly relative to immediate release while the microtubule bundle provides greater resistance, as microtubule sliding becomes more restricted, which can account for the slower strain relaxation observed in this case. This adaptive behavior suggests that axons actively remodel under sustained deformation, which may represent a protective mechanism against mechanical damage.

Pharmacological perturbations provide additional context for this interpretation. When microtubules are disrupted using Nocodazole, depolymerization reduces microtubule mass [138] and shortens filament length [129], and can result in the fewer cross link bridges per microtubule. Short microtubules have been shown to move more freely within the axon [139, 140]. Consequently, axons can exhibit faster strain relaxation compared to control, as seen in the case of axons released after prolonged stretch, consistent with increased microtubule mobility. Notably, this does not explain the lack of a pronounced effect in the immediate-release case, and the origin of this discrepancy remains unclear. In contrast, treatment with Taxol increases microtubule mass and decreases the rate of microtubule breakage by suppressing depolymerization, thereby limiting the capacity for microtubule sliding. Taxol does this by reducing the effective rate at which MAP crosslinkers

detach, since the loss of lattice binding sites caused by microtubule shortening is minimized. Thus, the crosslink bridges between adjacent microtubules remain intact for longer durations, increasing resistance to sliding and prolonging relaxation. The combined effect is a significantly larger resistance during recovery, resulting in longer relaxation times compared to both control and Nocodazole-treated axons.

Disruption of the actin–spectrin lattice by Latrunculin-A reduces the elasticity of the MPS [12], weakening its ability to exert restoring forces on the microtubule bundle. This diminished strength of the MPS can results in slower strain relaxation through a mechanism distinct from microtubule stabilization: rather than restricting microtubule sliding, it reduces the restoring force that drives recovery. Together, these results indicate that microtubules predominantly regulate the magnitude of resistance to strain recovery—accelerated by depolymerization and slowed by stabilization—whereas the MPS acts as a stress-memory unit via reversible folding. Overall, the findings highlight that axonal strain relaxation is not governed by a single cytoskeletal element, but instead emerges from the coordinated interaction between the MPS and microtubule bundles. This synergy enables axons to maintain mechanical resilience while adapting dynamically to sustained loads, which may be essential for normal physiological processes such as growth and movement, as well as protection during mechanical injury.

3.7 Conclusion and summary

In this chapter, we investigated how axons relax mechanical strain following stretch and release. Axons consistently exhibited biphasic viscoelastic relaxation, and recovery slowed markedly when release occurred after a 10-minute sustained stretch, indicating a time-dependent structural response. Pharmacological perturbations further showed that microtubule stabilization (Taxol) and actin disruption (Latrunculin A) both slow relaxation, whereas microtubule depolymerization (Nocodazole) has little effect under immediate release but accel-

erates recovery after delayed release.

Collectively, the findings establish that axonal strain recovery reflects the integrated behavior of multiple cytoskeletal elements and evolves over sustained loading. This work provides a mechanical basis for understanding axonal resilience and motivates future studies aimed at identifying the molecular mechanisms that underlie these time-dependent processes and how they influence physiological function and injury response.

Chapter 4

Theoretical modeling of axonal strain relaxation dynamics

4.1 Introduction and motivation

Understanding the mechanical behavior of axons requires not only experimental characterization but also theoretical modeling that captures the underlying physical mechanisms governing their response to deformation. In the previous chapter, we demonstrated through stretch–release experiments that axons exhibit a distinct biphasic viscoelastic relaxation, with fast and slow timescales, and that this response is modulated in very specific ways by specific cytoskeletal perturbations, the duration for which the stretch is applied, and to a lesser extent by axonal thickness. The existence of two characteristic time scales suggests that multiple viscoelastic processes act in parallel, likely associated with distinct cytoskeletal subsystems, as discussed in the previous chapter.

Several theoretical models have been used to describe axonal mechanical responses, beginning with classical viscoelastic formulations based on combinations of springs and dashpots [81, 85, 141, 142]. However, these models have not been systematically evaluated against the experimental strain–relaxation curves, in-

cluding the fast and slow relaxation times observed in our measurements, nor have they been examined in the context of cytoskeletal perturbations such as microtubule stabilization or actin disruption. This gap motivates the development of an improved mechanical description capable of explaining the experimentally observed dynamics.

In this chapter, we first extend previously used spectrin folding–refolding based models, originally developed to understand axonal tension buffering [12]. We then evaluate a parallel combination of Maxwell and Kelvin–Voigt elements, followed by a Zener–Maxwell parallel configuration. Each model is introduced as a progression from the previous one, highlighting the limitations of simpler descriptions and demonstrating how additional mechanical elements are needed to account for features such as changes in the strain relaxation rate and the two relaxation time scales observed experimentally, as well as how these timescales depend on the underlying material parameters. This modeling approach provides a mechanistic perspective on the coordinated contributions of the microtubule bundle and the actin–spectrin cortex to axonal mechanics, and offers a foundation for future investigation of nonlinear and active force-generating elements such as molecular motors in neurons. By systematically varying viscoelastic parameters, we aim to gain mechanistic insight into how different cytoskeletal structures may shape axonal viscoelastic behavior and influence adaptive responses under prolonged stretch.

4.2 Analytical models previously used to describe axonal viscoelasticity

To better understand the viscoelastic behavior of axons observed in this study, it is useful to briefly revisit the analytical models that have been previously developed to describe axonal mechanical responses. Previous studies have shown that when a step displacement is applied at the base of a cantilever probe, with its

tip in contact with the axon to impose deformation, the axon elongates and the resulting force relaxes to a steady-state level (Figure 4.1A). Early models, such as those proposed by Dennerll et al. [85], treated axons as passive viscoelastic materials and used a combination of springs and dashpot to explain force relaxation during mechanical stretching. This approach included a spring (k_1) in series with Kelvin-Voigt element which have a spring (k_2) in parallel with a dashpot (η_1) (Figure 4.1B). The former represents the rapid elastic response, whereas the latter captures a slower, solid-like viscoelastic relaxation that manifests over extended timescales. While these passive models capture the viscoelastic behavior of axons, they do not account for towed growth, which occurs when the applied force exceeds a certain threshold, [85, 88, 143]. O'Toole et al. [141, 144] suggested that axons can elongate either by tip growth or by stretching, depending on the force generated at the growth cone, the intrinsic viscosity of the axon, and the level of adhesions along its length. Building on the model proposed by Dennerll et al. [85], O'Toole and colleagues extended the framework to the entire axon (Figure 4.1D). In this model, an additional dashpot is introduced in series with the existing spring and Kelvin–Voigt elements, modeling the time-dependent, irreversible lengthening of the axon under sustained tension. Forces applied at the growth cone are partially dissipated by adhesions along the axon, capturing both local elongation and the effect of tension propagation throughout the axon (Figure 4.2). This approach provides a mechanistic explanation of how tension at the growth cone can drive axonal stretching while accounting for the dissipative effects of substrate adhesion.

Furthermore, axons can undergo active contraction, a phenomenon where their length decreases over time [81, 110, 111] due to the activity of molecular motors such as myosin [111]. To incorporate this behavior, an active contractile element is added in parallel with the Kelvin–Voigt section of the model (Figure 4.1C), representing internally generated forces that actively shorten the axon independently of external loads [81]. The modified model provides a consistent framework for describing the active tension generated in axons.

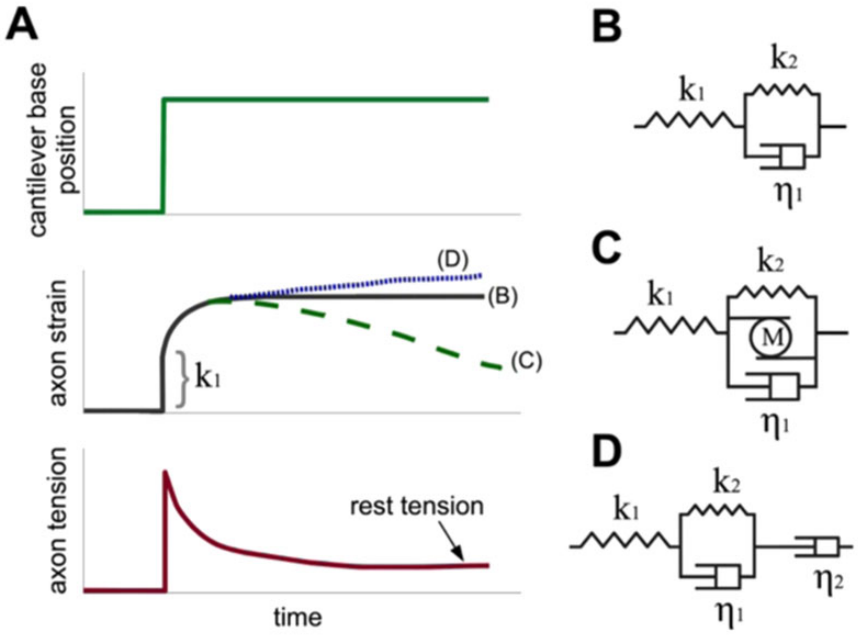


Figure 4.1: **(A)** Schematic depicting a step-like displacement of the micro-needle base, with its tip in contact with the axon, and the resulting axonal strain over time predicted by three different viscoelastic models (B–D). The strain responses of the three models are shown: the solid black curve for model B, the long green dashed line for model C, and the fine blue dotted line for model D. The tension response of model B is also included, indicating that axonal tension relaxes to a non-zero value after prolonged stretching. **(B)** Representation of the spring-dashpot model used in early studies to capture the viscoelastic behavior observed in micro-needle experiments. The spring k_1 responds instantaneously, while the Voigt element—comprising a spring k_2 in parallel with a dashpot η_1—accounts for the time-dependent response of both axonal strain and tension [85]. **(C)** Model describing the active contractile behavior of the axon. The non-linear element M, positioned in parallel with the Voigt element, represents the contribution of molecular motors, enabling the axon to generate contractile forces at low deformation rates [81]. **(D)** At extended timescales, stretched axons display growth-associated elongation that can resemble a flow-like response. To capture this behavior, a second dashpot η_2 was incorporated into the passive model, allowing it to represent the short-term elastic, intermediate viscoelastic, and long-term growth-driven deformation of the axon [85]. Adapted from Ghose and Pullarkat, Seminars in Cell & Developmental Biology (2022), ©Elsevier [145]. Used with permission.

In another study, De Rooij et al. modeled the axon as an active viscoelastic continuum by integrating passive mechanical components with force-generating elements [142], as shown in Figure 4.3. In their formulation Maxwell unit captures the time-dependent mechanical response of specific proteins like dynein, tau, or myosin. In addition, motor elements were incorporated to represent the internally

generated forces actively produced by cytoskeletal motors. The comprehensive model further integrates viscoelastic elements representing cross-links between actin and microtubules. Using this framework, the authors showed that treatment with taxol, which stabilizes microtubules, markedly increased the axon's effective viscosity and reduced its elongation rate.

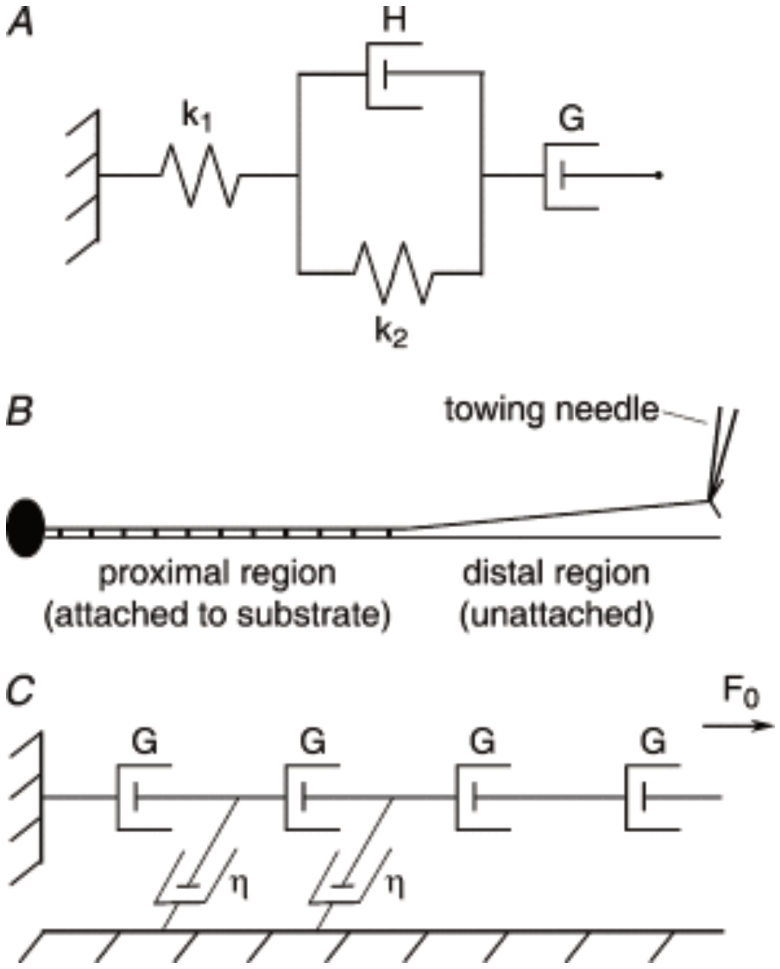


Figure 4.2: Schematic representation of a towed neurite modeled as a series of dashpots. (A) The axon is conceptualized as a series of Burgers elements, where each element includes two elastic components and a free dashpot (with constant G) representing towed growth. (B) Illustration of a neurite during towing: the distal portion is detached from the substrate, while multiple adhesions in the proximal region keep the neurite anchored. (C) Under a constant applied tension (F_0), the free dashpot dominates the response of a Burgers element. The neurite under constant tension is thus modeled as a series of dashpots, with substrate attachments represented by frictional dashpots (constant η). Tension remains uniform in the distal region but is dissipated by adhesions in the proximal region. (Adapted from O'Toole et al. [141])

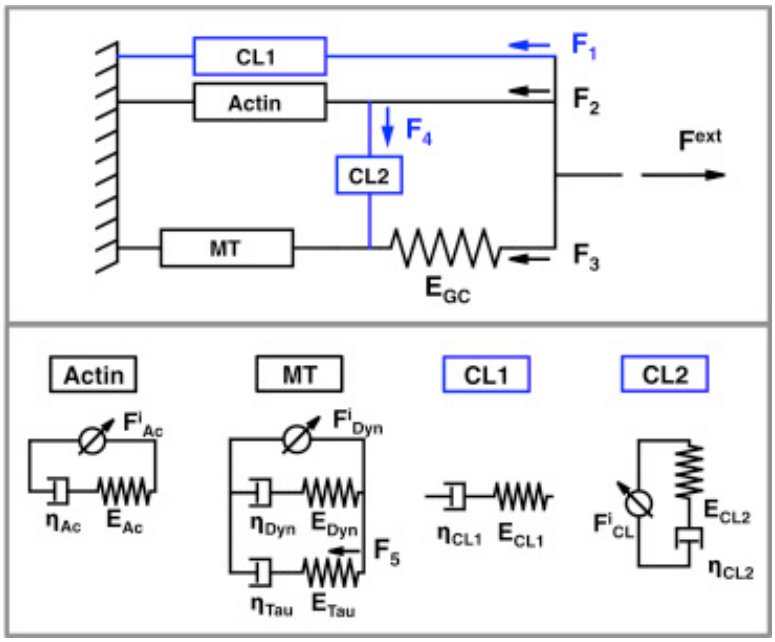


Figure 4.3: Schematic of the analytical axon model. The simplest model (bottom) treats actin and microtubule networks in parallel, each represented by one or two Maxwell viscoelastic elements with an internally generated force. Each Maxwell element captures the elastic and viscous behavior of proteins such as dynein, tau, or myosin. The full model (top) includes cross-links between actin and microtubules through additional Maxwell elements. Interaction with the growth cone is modeled by a spring of stiffness E_{GC}. Adapted from De Rooij et al., 2018 [142], ©Elsevier.

4.3 Computational models for viscoelastic behavior of axons

While the previous section highlighted how analytical models contribute to our understanding of axonal mechanics through simplified frameworks and theoretical insights, more complex biological scenarios often require additional modeling approaches. To address factors such as intricate geometries, heterogeneous material properties, and localized deformations, researchers have increasingly turned to computational methods-including finite element methods (FEM), molecular dynamics (MD), and coarse-grained simulations. These models enable detailed investigation of axonal behavior under a variety of loading and physiological conditions, complementing analytical approaches and offering a more comprehensive

view of axonal mechanics. At the molecular level, de Rooij et al.(2017) [146] developed a continuum model of the axon composed of parallel microtubule systems interconnected by motor proteins and passive cross-linkers. In their axonal cross-section model, they considered 19 potential microtubule sites, of which only half were occupied by microtubules. Each microtubule was connected to neighboring microtubules via 12 cross-linkers, representing passive or motor-mediated interactions. Their model used Maxwell elements to capture axonal viscoelasticity, showing that stiffness and viscosity scale with cross-link density and depend on cross-link binding and unbinding kinetics. Active cross-linking by molecular motors (e.g., dynein) generates internal stresses via cyclic detachment and reattachment, causing contraction or elongation depending on motor configuration, and producing emergent behaviors typical of active viscoelastic materials. In a subsequent study, the same authors investigated how dynamic cross-link behavior and microtubule polymerization affect axonal stiffness and mechanical failure under different loading conditions [147]. Their work builds on earlier computational efforts that demonstrated how the viscoelastic properties of tau, along with strain rate sensitivity and transient cross-link dynamics, critically influence microtubule integrity under mechanical stress [95,96]. These earlier models revealed that high strain rates (on the order of 22–44% s^{-1}) can outpace the ability of tau proteins to dissipate stress, leading to localized force concentration and ultimately microtubule breakage, especially when cross-links cannot detach rapidly enough. Building on these insights, they showed that under slow loading, axonal softening occurs due to progressive cross-link detachment, whereas rapid loading leads to abrupt failure as cross-links bear the majority of the mechanical load [147]. Additionally, they found that polymerization delays cross-link reformation because new tubulin subunits must first be added before new binding sites become available, whereas existing microtubule segments allow reattachment without this delay. In contrast, depolymerization causes immediate detachment, reducing the system's effective viscosity. Together, these diverse computational frameworks highlight how key axonal mechanical properties—including viscoelastic relax-

ation, tension generation, fatigue response, and bending mechanics—emerge from complex interactions between cytoskeletal architecture, cross-link dynamics, and tissue-level coupling. These models provide critical insights into both normal axonal function and mechanical vulnerability, offering predictive tools for studying growth, remodeling, and injury.

4.4 Modeling the mechanical responses of the actin–spectrin scaffold

Recent advances in experimental biophysics have revealed that axonal mechanical resilience is strongly influenced by the MPS which lies just beneath the axonal membrane. High-resolution force measurements using optical fiber–based system [13] (see Chapter 2 for details) have demonstrated that the MPS contributes significantly to the axonal elastic modulus measured at steady state (zero frequency) during stretching [12]. Tension–extension measurements performed under multiple step-strain protocols display a characteristic tension-buffering behavior, in which tension saturates after an initial rise (Figure 4.4). Concurrently, the effective Young's modulus decreases with increasing strain, reflecting a strain-softening response. This behavior contrasts sharply with the well-known strain stiffening of conventional biopolymer networks as well as in cells, where the elastic modulus typically increases with deformation due to entropic elasticity and filament alignment effects [148,149]. Such unexpected softening responses cannot be explained within the framework of classical viscoelastic models discussed earlier, which treat the axon as a combination of linear springs and dashpots. These simplified representations fail to capture the non-monotonic variation of tension and stress relaxation time observed experimentally. To account for these observations, a new theoretical framework was proposed in which the spectrin molecules—forming the periodic links between actin rings—undergo force-dependent and reversible unfolding of their tandem-repeat domains.

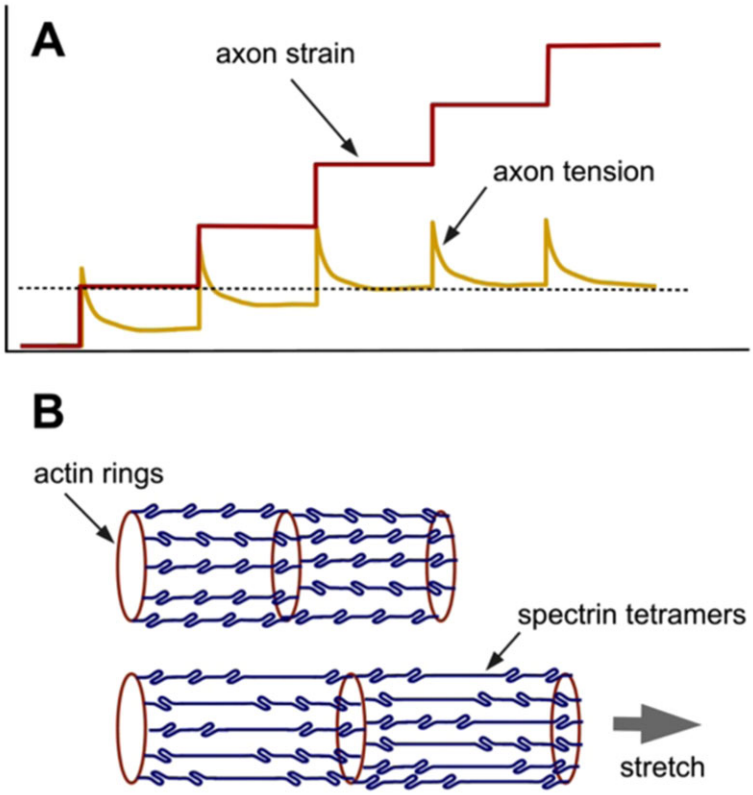


Figure 4.4: Viscoelastic tension response and proposed molecular origin of tension buffering in axons (A) Schematic representation of the axonal tension response to successive step increases in strain. Each strain increment produces an immediate rise in tension followed by viscoelastic relaxation toward a steady-state level within a few minutes. The steady-state tension initially increases with strain but eventually saturates, indicating an intrinsic tension-buffering mechanism. (B) Illustration of a possible microscopic mechanism for this buffering behavior, in which reversible unfolding and refolding of spectrin repeats within the axonal cytoskeleton modulate the effective contour length of the network, allowing it to accommodate strain while buffering tension. Adapted from Ghose and Pullarkat, Seminars in Cell & Developmental Biology (2022), ©Elsevier [145]. Used with permission.

Each unfolding event locally releases stored hidden length, allowing the structure to dissipate energy and buffer applied tension. This mechanism enables the scaffold to act as a molecular shock absorber, reducing the likelihood of structural failure during large deformations. The spectrin tetramer is modeled as a worm-like chain (WLC), where the tension–extension relationship captures the entropic elasticity of the molecule under applied strain [150, 151] and is given by

$$T_s = \frac{1}{\beta l_p}\left(\frac{1}{4(1-\frac{\ell'}{\ell})^2} + \frac{\ell'}{\ell} - \frac{1}{4}\right) \tag{4.1}$$

where ℓ is the contour length, ℓ' is the end-to-end length, and l_p is the persistence length of the spectrin. The parameter $\beta = (k_B T)^{-1}$, where k_B is the Boltzmann constant and T is the absolute temperature. T_s denotes the tension in the spectrin molecule.

Generally tension not only promotes the unfolding of spectrin repeats but also suppresses their re-folding, making it a central factor in the mechanical response of the molecule. At the molecular level, each spectrin repeat is viewed as transitioning between two adjacent minima on an effective energy landscape (Figure 4.5A). When mechanical tension is applied, this landscape becomes asymmetrically tilted toward the unfolded configuration, effectively lowering the energy barrier for unfolding while raising it for re-folding. In a first-order approximation [152], the corresponding unfolding and folding rates can therefore are given by

$$\nu_u = \nu_u(0) e^{\beta T_s \Delta x_{fu}} \tag{4.2}$$

$$\nu_f = \nu_f(0) e^{-\beta T_s \Delta x_{uf}} \tag{4.3}$$

Here, ν_u and ν_f denote the tension-dependent unfolding and refolding rates of a spectrin repeat, respectively. $\nu_u(0)$ and $\nu_f(0)$ represent the corresponding zero-force rate constants. The parameters Δx_{fu} and Δx_{uf} describe the distances along the reaction coordinate from the folded and unfolded states, respectively, to the transition state (x_t). That is, $\Delta x_{fu} = x_t - x_f$ for unfolding and $\Delta x_{uf} = x_t - x_u$ for refolding. These quantities determine how mechanical tension modulates the activation barriers for spectrin domain unfolding and refolding.

The tension-dependent unfolding and refolding rates determine how the contour length of a spectrin tetramer evolves over time. As domains unfold, the contour length increases, whereas refolding decreases it. This dynamic can be described

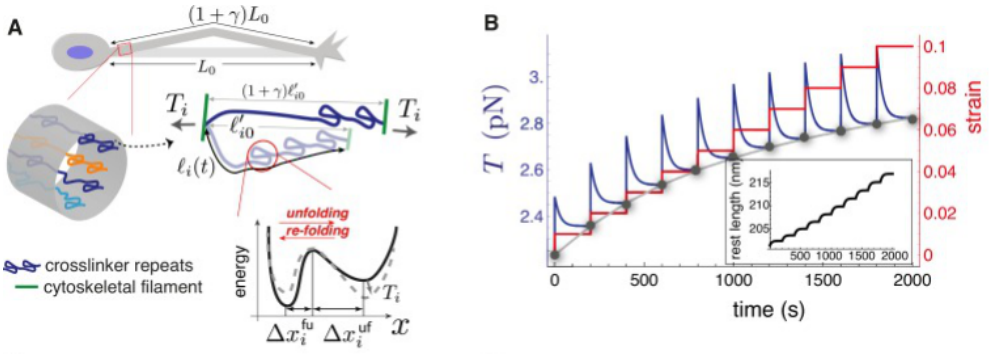


Figure 4.5: **(A)** Schematic representation of axon extension. An axon initially of length L_0 is stretched to $(1+\gamma)L_0$, imposing strain γ on crosslinking proteins bridging cytoskeletal filaments. These crosslinkers can vary their contour length $\ell_i(t)$ through repeat unfolding and refolding, modeled by a double-well energy landscape. Increasing tension T_i tilts the landscape toward the unfolded state, where the subscript i denotes the i-th crosslinking element. **(B)** Model response of a single crosslinking element under multi-step strain input. Each strain increment (red) produces a rapid rise in tension (purple), followed by relaxation to a steady value (gray dots) that approaches the equilibrium tension–extension relation (gray curve). This relaxation corresponds to progressive repeat unfolding, reflected in the increasing rest length $\ell(t)$ (inset).

by a first-order kinetic equation:

$$\frac{d\ell}{dt} = -\nu_f(\ell - \ell_f) + \nu_u(\ell_u - \ell), \tag{4.4}$$

where ℓ is the instantaneous contour length, and ℓ_f and ℓ_u are the fully folded and unfolded lengths, respectively. Here, $\ell - \ell_f$ represents the available length for folding, while $\ell_u - \ell$ represents the available length for unfolding at any given time. Model calculations in this model are done using the following parameters for spectrin: l_p = 20 nm [153], L_0 = 170 nm [43], x_{fu} = 2.5 nm, x_{uf} = 12 nm, ℓ_u = 1200nm, ℓ_f = 200 nm, $\nu_f(0)$ = $100s^{-}1$, $\nu_u(0)$ = $10^{-5}s^{-}1$ [154], and k_bT= 4 pN.nm. Model calculations for tension-buffering behavior as shown in Figure 4.5B are performed by applying a step strain, setting $L = L_0(1+\gamma)$, where γ is the applied strain step, as described in detail in Dubey et al. [12].

Beyond capturing tension buffering and relaxation dynamics, this framework also predicts a nonlinear elastic response characterized by an initial strain-softening regime followed by strain stiffening (Figure 4.6). The strain softening arises from

stress relaxation associated with spectrin domain unfolding, which effectively increases the contour length and reduces the incremental stiffness at low to intermediate strains. Such softening behavior has been observed experimentally in axons and was previously reported in axonal stretch–relaxation experiments [12]. At larger strains, as an increasing fraction of domains becomes unfolded, the mechanical response transitions to strain stiffening, dominated by the nonlinear elasticity of the extended polymer backbone modeled as a worm-like chain. A similar crossover from strain softening to strain stiffening has been reported in spider silk [11], suggesting that domain unfolding followed by entropic stiffening constitutes a general mechanical motif in protein-based load-bearing structures.

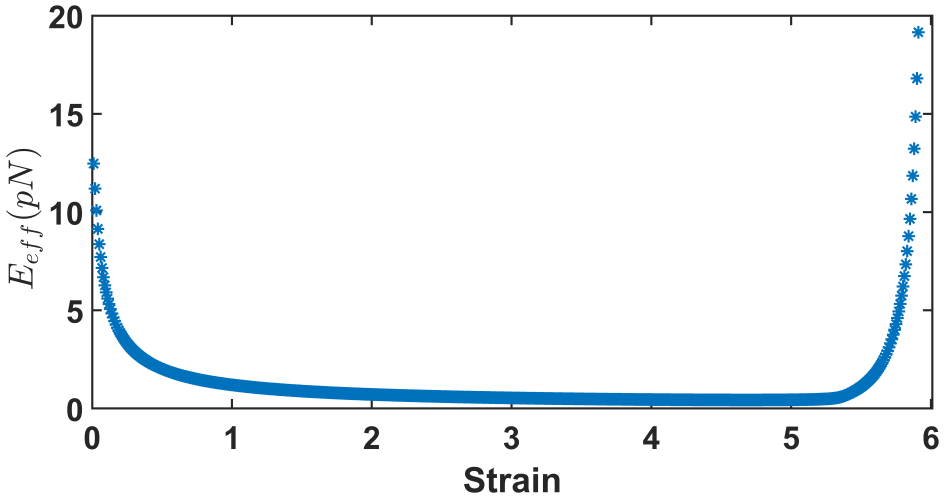


Figure 4.6: Elastic modulus as a function of applied strain. The effective elastic modulus initially decreases with increasing strain, reflecting strain-induced softening due to progressive domain unfolding. At larger strains, the modulus increases, indicating strain stiffening as the response becomes dominated by extended, unfolded spectrin domains.

Building on the framework described above, we next investigate the time-dependent strain relaxation behavior of spectrin. While the tension-buffering model captures the tension response of the molecule under an applied strain, the relaxation analysis focuses on how the contour length and end-to-end extension evolve over time when the applied tension is suddenly released. To model strain relaxation, the system is first subjected to a 20% strain and obtain the corresponding steady-

state contour length and tension. At steady state ($\frac{d\ell}{dt} = 0$), the effective contour length is given by

$$\ell_{ss} = \frac{\nu_f \ell_f + \nu_u \ell_u}{\nu_f + \nu_u}. \tag{4.5}$$

This steady-state contour length is then used to calculate the corresponding steady-state tension. These quantities serve as the initial conditions for the relaxation process. The steady-state tension, T, can be expressed as the sum of a baseline (rest) tension T_0 of an initial straight axon and an additional component ΔT arising from the applied stretch, such that $T = T_0 + \Delta T$. To understand strain relaxation, the additional applied tension ΔT is removed, and the subsequent evolution of strain is computed. In reality, axonal tension is expected to decrease more gradually because parallel structures such as the microtubule bundle share the load, but this simplified approach isolates the contribution of the actin–spectrin scaffold.

After quenching the applied tension from T to T_0, the rate equation governing the evolution of the contour length given by equation (4.4), after substituting the expressions for the tension-dependent unfolding and refolding rates given by equations (4.2) and (4.3), can be expressed as

$$\frac{d\ell}{dt} = -\nu_f(0)\, e^{-\beta T_0 \Delta x_{uf}} (\ell - \ell_f) + \nu_u(0)\, e^{\beta T_0 \Delta x_{fu}} (\ell_u - \ell) \tag{4.6}$$

Equation (4.6) is numerically solved in MATLAB (R2023b) to obtain the time evolution of the contour length, as shown in Figure 4.7. The results capture how the spectrin molecule gradually refolds and returns toward its folded contour length following the sudden release of excess tension.

Following the contour length relaxation, the corresponding strain relaxation of the spectrin molecule is obtained using the WLC tension–extension relationship (equation (4.1)). The time-dependent contour length, $\ell(t)$, obtained from equation (4.6), is used to compute the instantaneous strain response. The boundary condition $T = T_0 + \Delta T$ at $t = 0$ represents the pre-quench state, while $T = T_0$ for

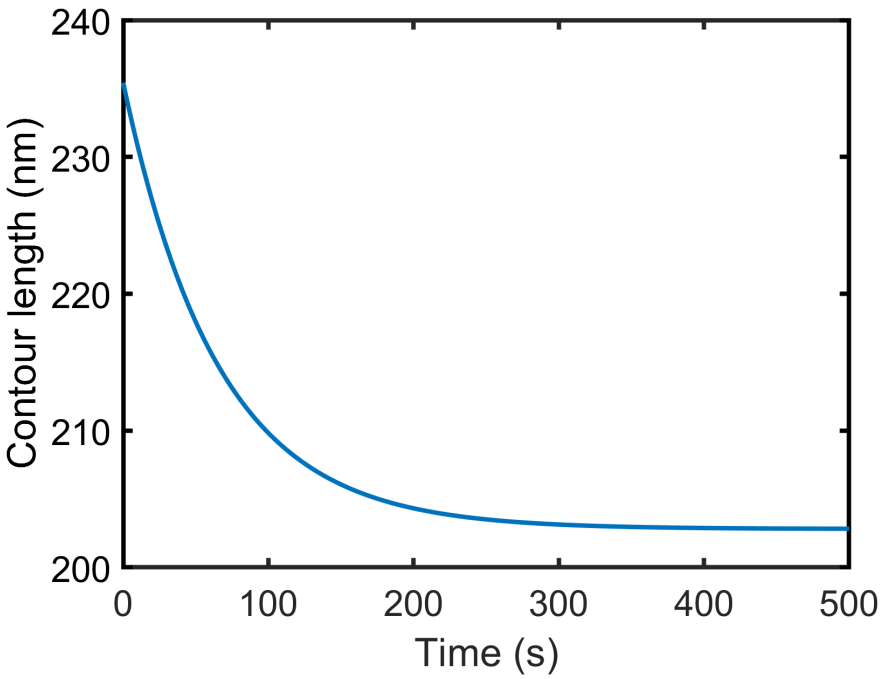


Figure 4.7: Contour length relaxation of spectrin following a tension quench. Time evolution of the spectrin contour length $\ell(t)$ after a sudden reduction of the applied tension from T to the quenched (rest) value T_0. The contour length decreases towards its new steady state value as spectrin repeats refold. Results were obtained by numerically solving equation (4.6) in MATLAB (R2023b).

$t > 0$ corresponds to the configuration after the sudden release of tension. The resulting strain–time profile, shown in Figure 4.8, illustrates the decay of strain as spectrin repeats refold and the system approaches its new steady configuration. As evident from the figure, the strain profile exhibits an initial rapid drop due to elastic recoil, followed by a slower relaxation phase driven by the refolding of spectrin domains toward their steady-state configuration. This type of behavior—an initial elastic recovery followed by slower protein-mediated strain relaxation—shares qualitative similarities with experimental observations, although the gradual relaxation phase in experiments often shows slightly different kinetics [155].

The strain relaxation, following the initial elastic recoil, exhibits a clear single-exponential decay. This behavior is evident from Figure 4.9, which shows the strain relaxation data fitted to a single-exponential function of the form $a\,e^{-t/\tau}+b$. Here, τ represents the characteristic timescale associated with the refolding of

spectrin repeats and the gradual recovery of the system toward its new steady-state configuration.

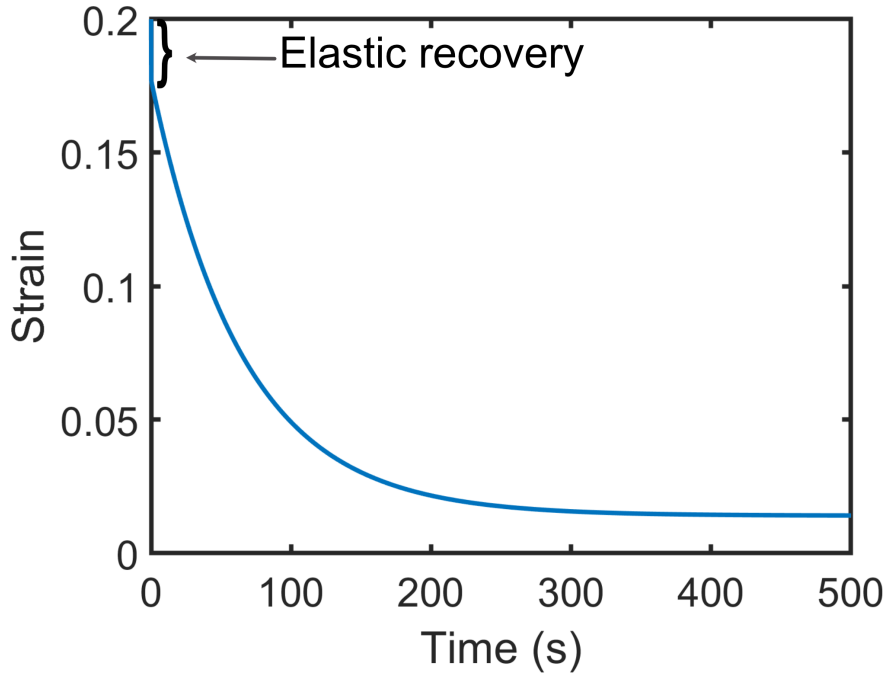


Figure 4.8: Strain relaxation in spectrin after tension is quenched to rest tension. After the applied tension corresponding to 20% strain, is quenched to the rest tension, the spectrin network exhibits an initial rapid drop in strain due to elastic recoil, followed by a gradual recovery driven by the refolding of spectrin domains toward their new steady state configuration.

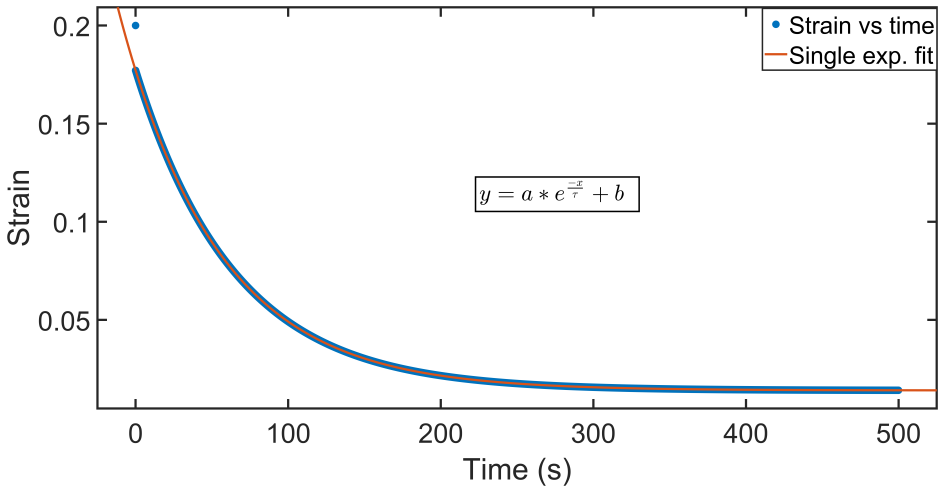


Figure 4.9: Single-exponential fit to spectrin strain relaxation data. A single-exponential function fits the relaxation data well, except for the first point, which lies outside the slow relaxation trend and reflects the rapid elastic recovery described in the previous figure. The fitted curve provides an estimate of the characteristic time scale of spectrin strain relaxation.

It is important to note that the experimentally measured strain relaxation of axons exhibits a double-exponential behavior, indicating the presence of at least two distinct timescales. In contrast, the strain relaxation predicted by the spectrin-based model captures only a single timescale, corresponding to the refolding of spectrin repeats, and therefore cannot fully account for the multi-timescale behavior observed experimentally.

4.5 Axon as Kelvin–Voigt and Maxwell models in parallel

In this section, we consider a viscoelastic model consisting of a Kelvin–Voigt element in parallel with a Maxwell element (Figure 4.10) to understand the strain relaxation behaviour observed experimentally in axons. This choice is guided by biological insights into the distinct roles of cytoskeletal components: the actin–spectrin lattice, with its folding–unfolding dynamics, provides a long-term solid-like response, whereas the microtubule bundle, regulated by MAPs binding

and unbinding, can contribute to a long-term fluid-like behavior. In the earlier spectrin-only model, the contribution of the microtubule bundle was neglected, which may explain the discrepancy between the model predictions and the experimental observations. In the present model, we aim to incorporate both types of behavior—solid-like and fluid-like—simultaneously, reflecting the distinct contributions of different cytoskeletal components within the axon. Although our previous work demonstrated strain-softening behavior, with the effective elastic modulus decreasing with increasing strain, here for simplicity, we adopt a linear viscoelastic model in which the elastic and viscous parameters are assumed independent of strain, to start with. In this framework, the Kelvin–Voigt element represents the spectrin-driven solid-like contribution that resists deformation over time, while the Maxwell element captures the fluid-like relaxation of the microtubule bundle. Together, this parallel combination provides a minimal yet biologically meaningful model that can reproduce the dual viscoelastic behaviors observed in axonal strain relaxation experiments. The dynamics of the system are governed by the following representative differential equation:

$$\sigma + \frac{\eta_m}{E_m}\dot{\sigma} = E_k\gamma + \left(\eta_k + \eta_m + \frac{\eta_m E_k}{E_m}\right)\dot{\gamma} + \frac{\eta_k \eta_m}{E_m}\ddot{\gamma} \tag{4.7}$$

Where γ is the strain and σ is the applied stress in the system. E_m and η_m are the elastic and viscous moduli of the Maxwell element, and E_k and η_k are the elastic and viscous moduli of the Kelvin–Voigt element. For a detailed derivation of the equation (4.7), see Appendix E.1.

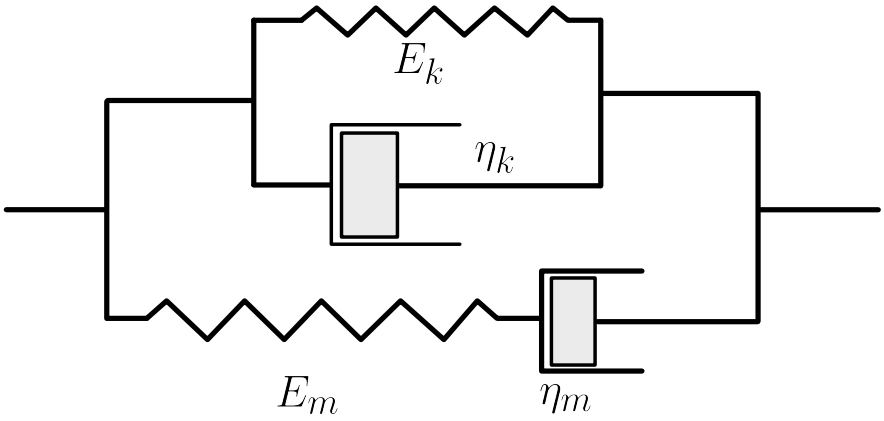


Figure 4.10: The Kelvin-Maxwell model in parallel configuration. The model consists of a Kelvin-Voigt element—a spring and dashpot in parallel— arranged in parallel with a Maxwell element, which contains a spring and dashpot in series.

4.5.1 Creep and recovery response of the Kelvin-Voigt and Maxwell models in parallel

To understand the dynamics of strain relaxation in the Kelvin–Voigt and Maxwell elements arranged in parallel, we consider a simple creep test and observe the resulting time-dependent strain response. In this test a constant stress is applied at time $t = t_{load}$ until the strain reaches saturation and removed at time $t = t_{rel.}$. Following removal of the applied stress also, the strain relaxation is computed. The applied stress is defined as

$$\sigma(t) = \sigma_0(H(t - t_{load}) - H(t - t_{rel.})) \tag{4.8}$$

where σ_0 is the magnitude of the applied stress and $H(t)$ denotes the Heaviside step function. From equation (4.7) and (4.8) we get

$$\left(H(t - t_{load}) - H(t - t_{rel.}) + \frac{\eta_m}{E_m}(\delta(t - t_{load}) - \delta(t - t_{rel.}))\right)\sigma = E_k\gamma + \left(\eta_k + \eta_m + \frac{\eta_m E_k}{E_m}\right)\dot{\gamma} + \frac{\eta_k\eta_m}{E_m}\ddot{\gamma} \tag{4.9}$$

To obtain representative parameter values for the Kelvin–Voigt and Maxwell elements, we estimate elastic and viscous properties based on spectrin and tau

proteins, which are known to contribute significantly to axonal mechanical response. Using an average axonal modulus $E_{\text{axon}} \approx 100$ kPa for 4 div axons, an estimated spectrin number of approximately $N_{\text{spectrin}} \approx 300$ molecules for an axon of $1\,\mu$m diameter [12], and a spectrin cross sectional radius of around 5 nm [156], the spectrin area fraction is $f_{\text{spectrin}} = A_{\text{spectrin}}/A_{\text{axon}} = 0.03$ which yields an effective elastic modulus $E_{\text{spectrin}} \approx E_{\text{axon}}/f_{\text{spectrin}} \approx 3$ MPa which is consistent in order of magnitude with values reported in simulation studies [157], although the exact numbers vary. It should be noted that the spectrin backbone, with a diameter of approximately 1.2 nm, is known to fold into a structure with a diameter of about 10 nm [156]. Accordingly, for simplicity, a spectrin radius of 5 nm is considered to obtain an estimate of the spectrin area fraction and the effective elastic modulus of spectrin. A more accurate calculation would require explicit consideration of the detailed folded geometry and the complex interactions within the spectrin lattice. Taking an average relaxation time of $\tau_{\text{spectrin}} \approx 20$ s [12] gives $\eta_{\text{spectrin}} \approx 60$ MPa $\cdot$ s. We assign these values to the Kelvin branch ($E_k \approx E_{\text{spectrin}}$, $\eta_k \approx \eta_{\text{spectrin}}$). For the Maxwell branch, we use reported values for tau proteins, taking $E_\tau \approx 5$ MPa [158–160] and a dwell time $\tau_\tau \approx 4$ s [161], giving a viscosity $\eta_\tau = E_\tau \tau_\tau \approx 20$ MPa $\cdot$ s, and therefore set $E_m \approx E_\tau$, $\eta_m \approx \eta_\tau$. Microtubules, although abundant, are much stiffer in the longitudinal direction (order of GPa) and are therefore assumed not to deform appreciably under the small strains considered here. These values are order-of-magnitude estimates and represent simplified effective parameters for single elements. Since real axons contain many spectrin and tau molecules arranged in a specific manner, as well as additional cytoskeletal components, accurate parameter values should consider the combined effects of these multiple, interacting elements. Since the objective of the model at this stage is to explore qualitative relaxation behaviour rather than to provide exact quantitative predictions, such approximations are sufficient for the present analysis.

Using these estimated parameter values, equation (4.9) was initially solved in MATLAB (R2023a) using Laplace and inverse Laplace transforms to obtain the

strain evolution under the creep test, and the result is shown in Figure 4.11. In response to the applied stress, the strain increases gradually and approaches a steady-state value. Once the stress is removed, the strain relaxes smoothly back toward zero, showing viscoelastic behaviour. The second part of the response mimics the axonal relaxation after release. This solution also served as a cross-check for the subsequent analytical solution, which is presented in the next subsection, ensuring consistency and minimizing the likelihood of errors.

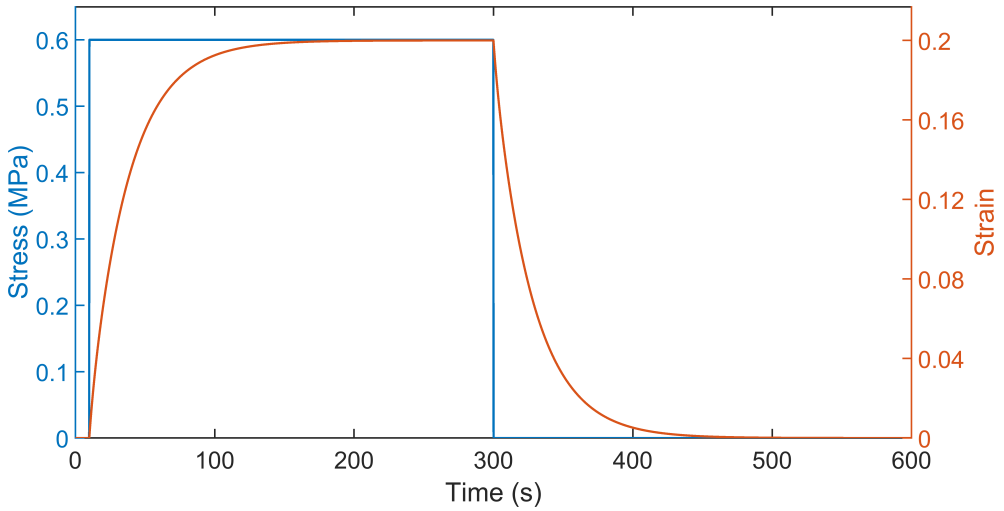


Figure 4.11: Creep and recovery response of the Kelvin–Voigt and Maxwell models in parallel (solution obtained using MATLAB 2023b). This combined model exhibits time-dependent strain evolution during creep, saturating after some time, and strain recovery occurring once the stress is removed, influenced by both Kelvin-Voigt and Maxwell elements.

4.5.2 Analytical solution for the parallel combination of Kelvin-Voigt and Maxwell models:

For simplicity, we first consider the loading phase, where a step stress of the form

$$\sigma = \sigma_o H(t); \tag{4.10}$$

is applied. Re-writing equation (4.7)

$$\sigma + A\dot{\sigma} = E_k\gamma + B\dot{\gamma} + C\ddot{\gamma} \tag{4.11}$$

where $A = \frac{\eta_m}{E_m}$, B=$\eta_k + \eta_m + \frac{\eta_m E_k}{E_m}$ and C=$\frac{\eta_k \eta_m}{E_m}$. From equation (4.10) and (4.11) we get

$$(H(t) + A\delta(t))\sigma_0 = E_k\gamma + B\dot{\gamma} + C\ddot{\gamma} \tag{4.12}$$

By solving equation (4.12) using Laplace and inverse Laplace transforms, the following expression for the strain is obtained (see Appendix E.2 for the full derivation)

$$\gamma(t) = \frac{\sigma_0}{E_k} + \frac{\sigma_0}{\sqrt{B^2 - 4E_kC}}\left(\left(\frac{2C}{-B + \sqrt{B^2 - 4E_kC}} + A\right)e^{\frac{-B+\sqrt{B^2-4E_kC}}{2C}t} - \left(\frac{2C}{-B - \sqrt{B^2 - 4E_kC}} + A\right)e^{\frac{-B-\sqrt{B^2-4E_kC}}{2C}t}\right) \tag{4.13}$$

Let τ_f and τ_s represent the relaxation times. Then, equation (4.13) can be written as:

$$\gamma(t) \;=\; f_1 - f_2 e^{-t/\tau_s} - f_3 e^{-t/\tau_f}, \qquad t > 0,$$

with

$$f_1 = \frac{\sigma_0}{E_k},$$

$$f_2 = -\frac{\sigma_0}{\sqrt{B^2 - 4E_kC}}\left(\frac{2C}{-B + \sqrt{B^2 - 4E_kC}} + A\right),$$

$$f_3 = \frac{\sigma_0}{\sqrt{B^2 - 4E_kC}}\left(\frac{2C}{-B - \sqrt{B^2 - 4E_kC}} + A\right),$$

where f_1, f_2 and f_3 are constants determined from the equilibrium conditions and τ_f and τ_s are given by

$$\tau_{s,f} = \left(\frac{2C}{B \mp \sqrt{B^2 - 4E_kC}}\right) \tag{4.14}$$

After substituting values of B and C we obtain

$$\tau_{s,f} = \left(\frac{2\frac{\eta_k \eta_m}{E_m}}{\eta_k + \eta_m + \frac{\eta_m E_k}{E_m} \mp \sqrt{(\eta_k + \eta_m + \frac{\eta_m E_k}{E_m})^2 - \frac{4E_k \eta_k \eta_m}{E_m}}} \right) \tag{4.15}$$

Factoring out E_m in both the numerator and denominator, we obtain:

$$\tau_{s,f} = \left(\frac{2\eta_k \eta_m}{E_m(\eta_k + \eta_m) + \eta_m E_k \mp \sqrt{(E_m(\eta_k + \eta_m) + \eta_m E_k)^2 - 4E_k E_m \eta_k \eta_m}} \right) \tag{4.16}$$

Similarly, for the stress-release phase at time $t = t_{\text{rel}}$, the strain evolution (See Appendix E.2 for derivation.) can be expressed as:

$$\gamma(t - t_{\text{rel}}) = f_2\, e^{-(t-t_{\text{rel}})/\tau_s} + f_3\, e^{-(t-t_{\text{rel}})/\tau_f}, \qquad t \geq t_{\text{rel}}, \tag{4.17}$$

By combining the loading and release phases, the complete time-dependent strain response of the system can be expressed as:

$$\gamma(t) = \begin{cases} f_1 - f_2 e^{-t/\tau_s} - f_3 e^{-t/\tau_f}, & t < t_{\text{rel}}, \\ f_2 e^{-(t-t_{\text{rel}})/\tau_s} + f_3 e^{-(t-t_{\text{rel}})/\tau_f}, & t \geq t_{\text{rel}}. \end{cases} \tag{4.18}$$

The analytical expression given in equation (4.18) was used to plot the time-dependent strain evolution during loading and relaxation as shown in the Figure 4.12. The first term describes strain accumulation under applied stress ($t < t_{\text{rel}}$), while the second captures exponential strain recovery after stress removal ($t \geq t_{\text{rel}}$). This analytical solution illustrates the characteristic creep and recovery behavior of the combined Kelvin–Voigt and Maxwell model, and the results are consistent with those obtained previously using Laplace and inverse Laplace transforms in MATLAB.

Importantly, the model predicts a double-exponential relaxation, characterized by fast and slow relaxation times τ_f and τ_s, which is in qualitative agreement with experimentally measured axonal strain–relaxation dynamics. This similar-

ity supports the hypothesis that axonal viscoelasticity arises from two distinct viscoelastic processes operating together over different timescales, with one acting solid-like and the other exhibiting fluid-like behavior over longer durations.

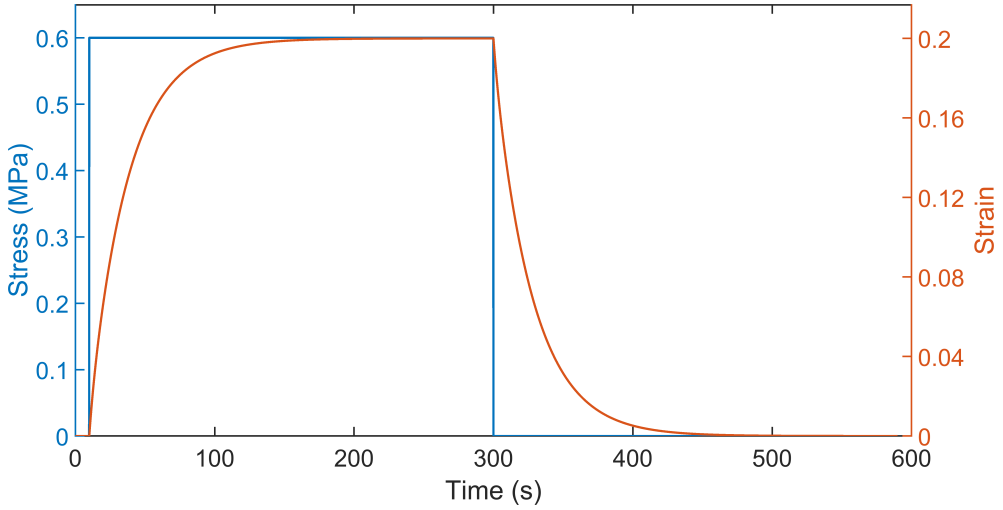


Figure 4.12: Creep and recovery response of the Kelvin–Voigt and Maxwell elements in parallel, plotted using the analytical solution given in equation (4.18). The analytical result reproduces the characteristic time-dependent strain evolution previously obtained using Laplace and inverse Laplace transforms in MATLAB, demonstrating consistency between the approaches.

4.5.3 Influence of model parameters on strain relaxation and characteristic time scales

In this subsection, we investigate how variations in the model parameters—the elastic and viscous moduli of the Kelvin–Voigt and Maxwell elements—affect the strain relaxation behavior of the axonal model. The time-dependent strain responses are plotted for different parameter values to facilitate a direct comparison of relaxation dynamics. In addition, the corresponding characteristic relaxation time scales (τ_f and τ_s) are evaluated to quantify how changes in elasticity and viscosity influence the rate and pattern of strain recovery. This analysis is motivated by the fact that cytoskeleton-perturbing drugs can modulate these mechanical parameters, thereby altering axonal relaxation behavior.

Treatment with Taxol, which stabilizes microtubules (MTs), was found to increase

the relaxation times in axons, as discussed earlier in this chapter. Taxol has been shown to increase axonal viscosity [142], likely due to changes in microtubule mass or number [128] within the axon, which can contribute to the increased viscosity of microtubule–MAPs bundles. Conversely, actin destabilization disrupts the actin–spectrin lattice, leading to decreased axonal elasticity [12], which can be attributed to reduced stiffness of the MPS. Variation of strain relaxation with increasing Maxwell viscosity (related to microtubule–MAPs bundle viscosity) and decreasing Kelvin elasticity (related to MPS elasticity) is shown in Figure 4.13. Corresponding changes in the characteristic relaxation times (τ_f and τ_s) are shown in Figures 4.14A and 4.14B, respectively. As shown in the figures, increasing the Maxwell viscosity slows down strain relaxation, with both characteristic times, τ_f and τ_s, increasing. Decreasing the Kelvin elasticity further slows strain relaxation and also results in increased values of τ_f and τ_s. Overall, the observed pattern of strain relaxation and changes in characteristic time scales is similar to the relaxation behavior reported in chapter 3.

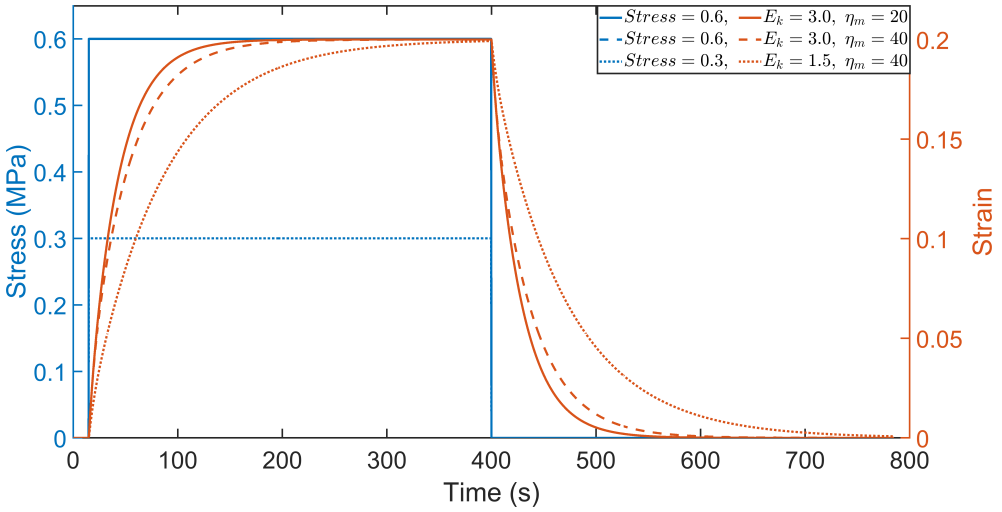


Figure 4.13: Comparison of strain evolution for varying model parameters. Increasing the Maxwell viscosity (dashed orange line) or decreasing the Kelvin–Voigt elasticity (dotted orange line) slows down strain evolution. The applied stress is normalized when reducing Kelvin–Voigt elasticity to ensure that the maximum strain remains the same across all runs.

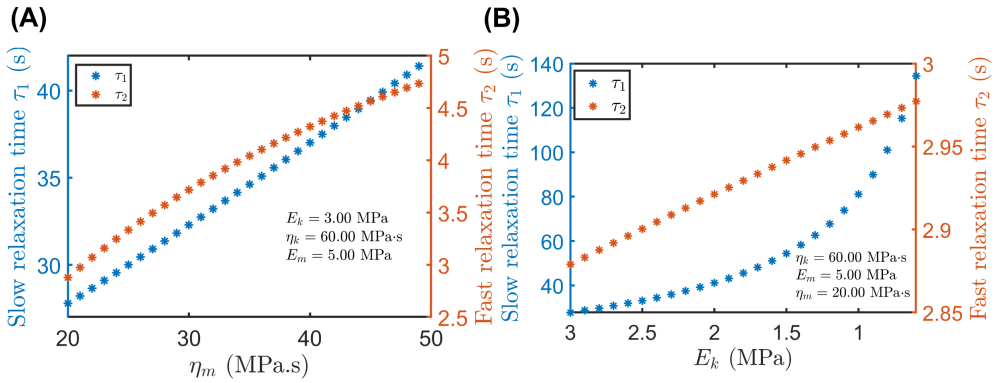


Figure 4.14: Dependence of the strain relaxation time scales on material parameters. Variation of the fast relaxation time τ_f and the slow relaxation time τ_s for the parallel combination of the Kelvin–Voigt and Maxwell models: (A) with increasing Maxwell viscosity and (B) with decreasing Kelvin–Voigt elasticity. Both time scales are calculated using the analytical expression given by equation (4.16). Figures (A) and (B) show that increasing Maxwell viscosity or decreasing Kelvin–Voigt elasticity leads to a systematic increase in both relaxation times, indicating slower overall strain relaxation.

In addition, experimental evidence indicates that Taxol enhances the steady-state (zero-frequency) elastic modulus of axons [12], which can similarly be attributed to an increase in microtubule content. This suggests that Taxol can increase both the elastic and viscous moduli of microtubule bundles, motivating an analysis of how variations in these parameters affect axonal strain relaxation. As discussed earlier, actin destabilization disrupts the MPS, thereby reducing its elasticity. Since spectrin contributes to the MPS elasticity and the unfolding of spectrin repeats gives rise to tension-buffering behavior similar to a viscous response, such disruption is also expected to lower the effective viscosity of the MPS. To mimic these conditions in the model, both the elastic and viscous moduli of the Maxwell element were increased to simulate Taxol treatment. Similarly, both the elastic and viscous moduli of the Kelvin element were decreased to simulate actin–spectrin lattice disruption. In both cases, the two moduli were scaled by the same ratio for simplicity, as the precise scaling of individual parameters following drug treatment remains unknown. The effects of these parameter changes on strain relaxation are illustrated in Figure 4.15, showing the impact of increasing the Maxwell moduli and decreasing the Kelvin moduli (both elasticity and viscosity).

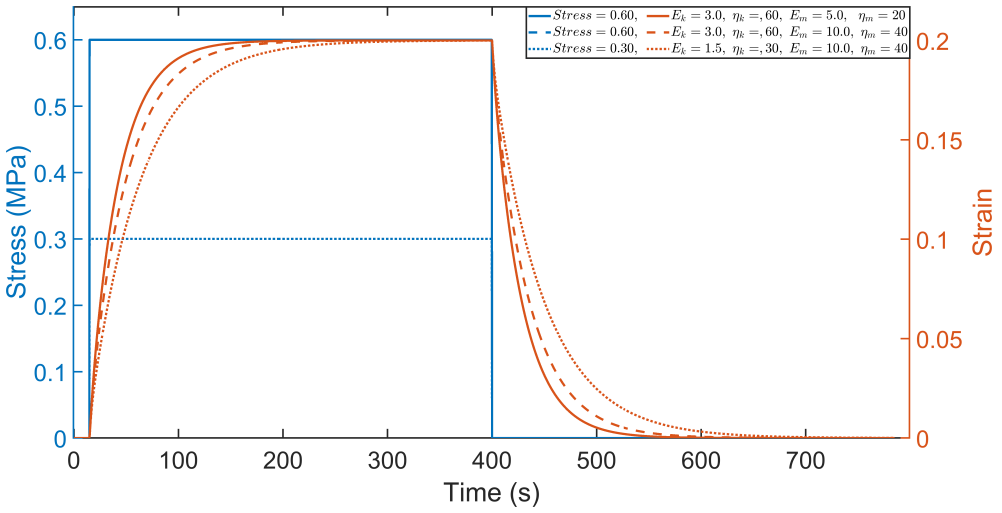


Figure 4.15: Effect of varying elasticity and viscosity simultaneously on strain relaxation. The plot illustrates the strain evolution for different values of model parameters. Increasing Maxwell viscosity and elasticity slows strain relaxation, resulting in longer recovery times (dashed line). Similarly, decreasing Kelvin elasticity and viscosity also slows the relaxation process (dotted line). In both cases, the overall strain returns to baseline more gradually, demonstrating that higher Maxwell parameters or lower Kelvin parameters lead to slower strain recovery.

The corresponding variations in the characteristic relaxation times (τ_f and τ_s) are presented in Figures 4.16A and 4.16B, respectively. Overall, the strain relaxation becomes slower (Figure 4.15) with these parameter changes, similar to the experimental trends. However, in both cases, τ_s increases while τ_f decreases, which differs from the experimental observations discussed in chapter 3.

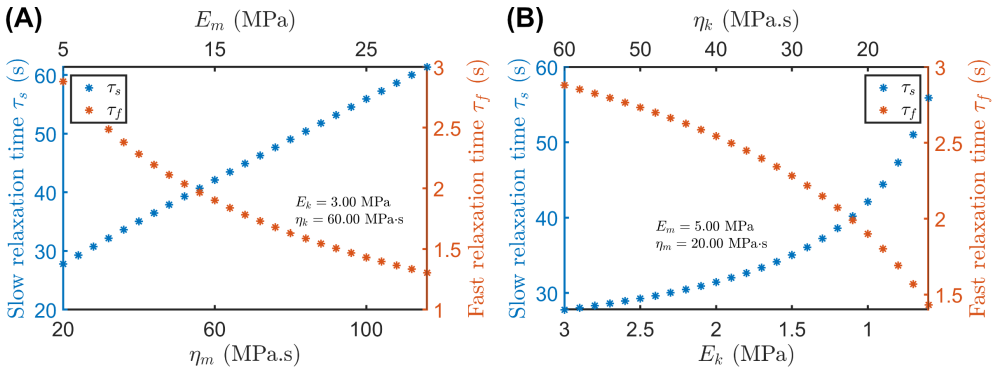


Figure 4.16: Dependence of the strain relaxation time scales on material parameters. Panels (A) and (B) illustrate the effect of proportionally scaling both the viscosity and elasticity within each viscoelastic element of the model. In panel (A), both the viscosity and elasticity of the Maxwell branch are increased by the same ratio, whereas in panel (B), both the viscosity and elasticity of the Kelvin–Voigt branch are decreased by the same ratio. In both cases, τ_f decreases while τ_s increases, demonstrating that the fast and slow relaxation modes respond differently to coordinated changes within each viscoelastic element. This simplified parameter scaling is used because the exact changes in viscosity and elasticity after cytoskeletal drug perturbation are not known.

4.6 Motivation for the Zener–Maxwell model

The previous results using the Kelvin–Voigt and Maxwell elements in parallel highlight key aspects of axonal strain relaxation, but also reveal some limitations. While the overall strain relaxation pattern slows down, similar to experimental observations, the characteristic relaxation times (τ_f and τ_s) do not fully match in the more plausible scenario where both moduli are varied simultaneously, indicating that the current model cannot capture all aspects of axon mechanics observed experimentally. An important physical feature not captured by the model is the ability of cytoskeletal proteins to undergo rapid extension through backbone stretching, allowing them to accommodate sudden strains. However, a pure Kelvin element cannot respond instantaneously, as the dashpot in parallel with the spring resists sudden deformation. To address these limitations, we consider a Zener (standard linear solid) element in parallel with a Maxwell element (Figure 4.17). The Zener element consists of an elastic spring E_{z1} in series with a Kelvin–Voigt branch. Notably, a previous study has successfully applied the

Zener model to MPS, demonstrating its relevance for capturing complex axonal mechanical responses [162]. Under a fast stretch, the first spring E_{z1} responds quickly, analogous to the immediate extension of the protein backbone. At the larger timescales the parallel combination of spring E_{z2}, representing the elasticity of protein domains that can refold, and dashpot η_z, representing dissipation due to unfolding, governs the time-dependent response. This configuration allows the model to reproduce both the immediate elastic response during fast stretches and the relaxation under slower loading. Figure 4.17 illustrates a cartoon of a protein under fast and slow stretch, along with the corresponding responses predicted by the Zener model.

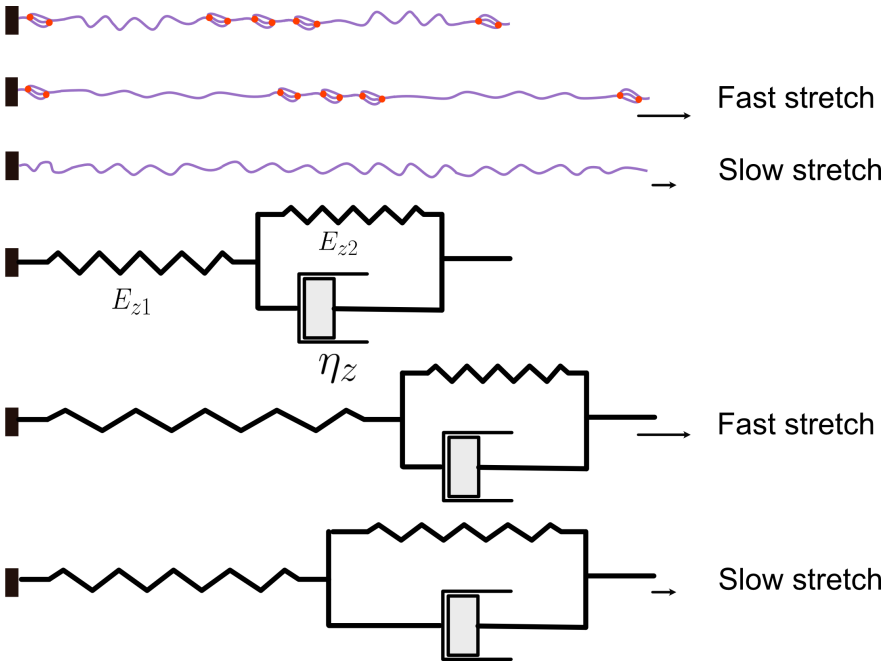


Figure 4.17: Similarity between molecular stretching behavior and Zener viscoelastic model. Schematic illustration showing how the rate-dependent mechanical response of a modular protein can be captured by a Zener (standard linear solid) model. Under fast stretch, folded domains do not have time to unfold, so the response is dominated by the elastic backbone—analogous to the first spring (E_{z1}) in the Zener model. Under slow stretch, domains gradually unfold and refold, allowing stress relaxation through the viscous element, producing a softer, time-dependent response consistent with viscoelastic behavior.

4.7 Zener and maxwell models in parallel combination

This model integrates the Zener and Maxwell models in a parallel configuration as shown in Figure (4.18). The dynamics of the system are governed by the following representative differential equation (See Appendix F.1 for detailed derivation):

$$\left(1+\frac{E_{z2}}{E_{z1}}\right)\sigma+\left(\frac{\eta_z}{E_{z1}}+\left(1+\frac{E_{z2}}{E_{z1}}\right)\frac{\eta_m}{E_m}\right)\dot{\sigma}+\frac{\eta_z\eta_m}{E_{z1}E_m}\ddot{\sigma}$$
$$=E_{z2}\gamma+\left(\eta_z+\left(1+\frac{E_{z2}}{E_{z1}}\right)\eta_m+\frac{E_{z2}\eta_m}{E_m}\right)\dot{\gamma}+\left(\frac{\eta_z\eta_m}{E_{z1}}+\frac{\eta_z\eta_m}{E_m}\right)\ddot{\gamma} \quad (4.19)$$

Where γ is the strain and σ is the stress in the system. Let $A = 1+\frac{E_{z2}}{E_{z1}}$, B=$\frac{\eta_z}{E_{z1}}$ + $(1+\frac{E_{z2}}{E_{z1}})\frac{\eta_m}{E_m}$, C=$\frac{\eta_z\eta_m}{E_{z1}E_m}$, D=$\eta_z+\left(1+\frac{E_{z2}}{E_{z1}}\right)\eta_m+\frac{E_{z2}\eta_m}{E_m}$ and $E = \frac{\eta_z\eta_m}{E_{z1}}+\frac{\eta_z\eta_m}{E_m}$ then equation (4.19) can be written as

$$A\sigma+B\dot{\sigma}+C\ddot{\sigma}=E_{z2}\gamma+D\dot{\gamma}+E\ddot{\gamma} \quad (4.20)$$

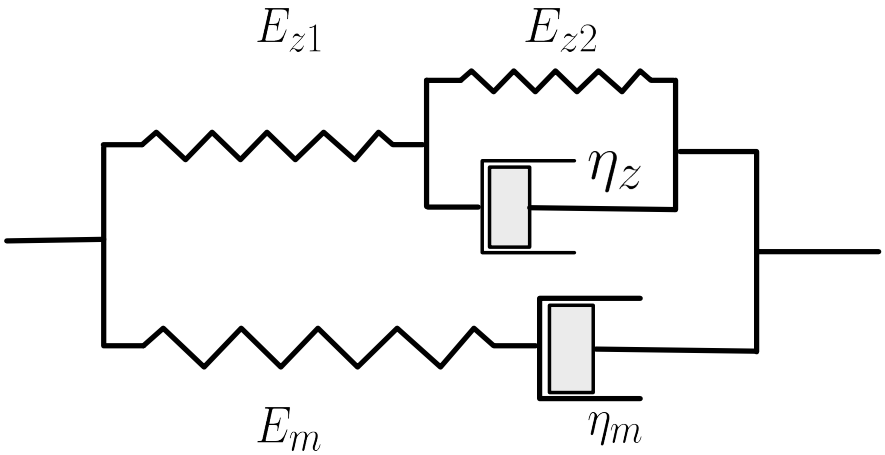


Figure 4.18: The Zener-Maxwell model in parallel configuration. This model combines the Zener model, consisting of two springs (spring constant E_{z1} and E_{z2}) and dashpot (viscosity η_z) in parallel, with the Maxwell model, which comprises a spring (spring constant E_m) and dashpot (viscosity η_m) in series.

4.7.1 Stretching and releasing (strain relaxation)

Let us consider a stress of the form

$$\sigma = \sigma_o(H(t - t_{load}) - H(t - t_{rel.})); \tag{4.21}$$

is applied to the system then from equation (4.20) and (4.21) we get

$$(A(H(t-t_{load})-H(t-t_{rel.}))+B(\delta(t-t_{load})-\delta(t-t_{rel.})))+C(\dot{\delta}(t-t_{load}))-\dot{\delta}(t-t_{rel.})))\sigma_0 = E_{z2}\gamma+D\dot{\gamma}+E\ddot{\gamma} \tag{4.22}$$

4.7.2 Analytical solution for the parallel combination of Zener and Maxwell models:

For simplicity a stress of the form

$$\sigma = \sigma_o H(t); \tag{4.23}$$

is applied. From equation (4.20) and (4.23) we get

$$(AH(t) + B\delta(t) + C\dot{\delta}(t))\sigma_0 = E_{z2}\gamma + D\dot{\gamma} + E\ddot{\gamma} \tag{4.24}$$

By solving equation (4.24) using Laplace transform we get (See Appendix F.2 for detailed derivation):

$$\gamma(t) \;=\; f_1 - f_2 e^{-t/\tau_s} - f_3 e^{-t/\tau_f}, \qquad t > 0, \tag{4.25}$$

with

$$f_1 = \frac{A\sigma_0}{E_{z2}},$$

$$f_2 = -\frac{\sigma_0}{\sqrt{D^2 - 4E_{z2}E}}\left(\frac{2AE}{-D - \sqrt{D^2 - 4E_{z2}E}} + B + \frac{C(-D - \sqrt{D^2 - 4E_{z2}E})}{2E}\right),$$

$$f_3 = \frac{\sigma_0}{\sqrt{D^2 - 4E_{z2}E}}\left(\frac{2AE}{-D + \sqrt{D^2 - 4E_{z2}E}} + B + \frac{C(-D + \sqrt{D^2 - 4E_{z2}E})}{2E}\right),$$

where τ_f and τ_s are the relaxation times and are given by

$$\tau_{s,f} = \left(\frac{2E}{D \mp \sqrt{D^2 - 4E_{z2}E}}\right) \tag{4.26}$$

Finally, the relaxation time constants can be written explicitly by substituting their definitions as;

$$\tau_{s,f} = \frac{2\left(\frac{\eta_z\eta_m}{E_{z1}} + \frac{\eta_z\eta_m}{E_m}\right)}{\left(\frac{E_{z2}\eta_m}{E_{z1}} + \frac{E_{z2}\eta_m}{E_m} + \eta_z + \eta_m\right) \mp \sqrt{\left(\frac{E_{z2}\eta_m}{E_{z1}} + \frac{E_{z2}\eta_m}{E_m} + \eta_z + \eta_m\right)^2 - 4E_{z2}\left(\frac{\eta_z\eta_m}{E_{z1}} + \frac{\eta_z\eta_m}{E_m}\right)}} \tag{4.27}$$

Similarly, during the stress-release phase at time $t = t_{\text{rel}}$, the strain evolution (full derivation in Appendix F.2) can be expressed as:

$$\gamma(t - t_{\text{rel}}) = f_2\, e^{-(t-t_{\text{rel}})/\tau_s} + f_3\, e^{-(t-t_{\text{rel}})/\tau_f}, \quad t \geq t_{\text{rel}}, \tag{4.28}$$

where f_2, f_3, τ_s, and τ_f are the same coefficients and time constants defined in the loading case. Combining the two cases, the full response can be written compactly as

$$\gamma(t) = \begin{cases} f_1 - f_2 e^{-t/\tau_s} - f_3 e^{-t/\tau_f}, & t < t_{\text{rel}}, \\ f_2 e^{-(t-t_{\text{rel}})/\tau_s} + f_3 e^{-(t-t_{\text{rel}})/\tau_f}, & t \geq t_{\text{rel}}. \end{cases} \tag{4.29}$$

Equation (4.29) describes a double-exponential response, consistent with the ex-

perimental data, and was used to plot the strain evolution during both loading and recovery (Figure 4.19). The parameters for the Maxwell element, E_m and η_m, were chosen identical to those in the Kelvin–Maxwell model. For the Zener element, the viscosity was taken to match the Kelvin viscosity, while the spring constants E_{z1} and E_{z2} were set equal and twice the value of the Kelvin spring. This ensures that the effective elasticity of the two-series Zener springs is equivalent to that of the single Kelvin spring. Although E_{z1} and E_{z2} were taken equal for simplicity, they could differ in principle. In Figure 4.19, the model first exhibits an initial elastic jump in strain, followed by a gradual increase until reaching a steady state during the loading phase. During the unloading phase, it shows an initial elastic recovery, followed by a gradual relaxation of strain back toward zero. In our experiments, this elastic response is not clearly visible, likely due to the relatively slow imaging frame rate (5 fps), which limits the ability to capture rapid initial deformation. However, previous studies have reported the elastic response of axons under loading conditions [81, 85].

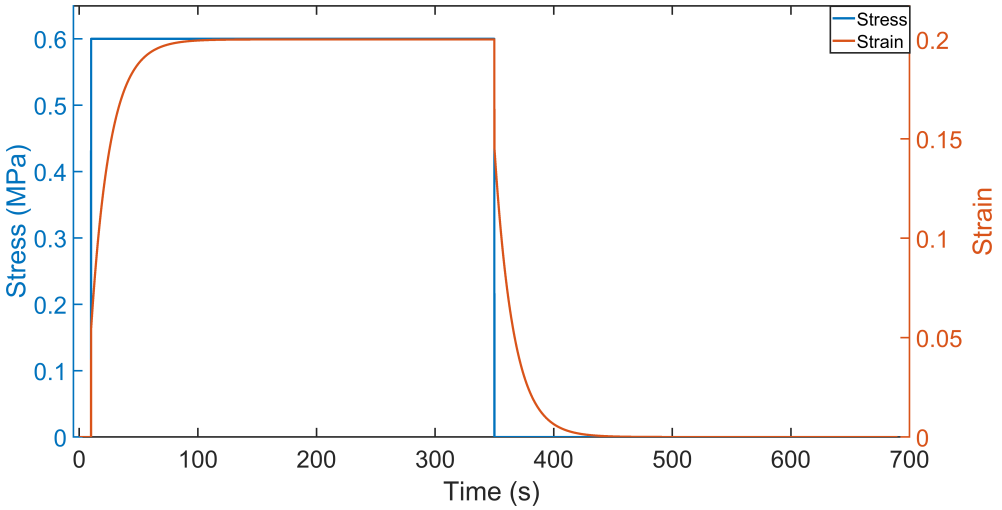


Figure 4.19: Creep and recovery response of the Zener and Maxwell models in parallel. The combined Zener–Maxwell parallel model exhibits an immediate elastic strain upon stress application, followed by time-dependent creep that gradually saturates. Upon stress removal, a portion of the strain recovers instantly due to the elastic elements, while the remaining strain gradually recovers over time through viscoelastic relaxation governed by both the Zener and Maxwell components.

4.7.3 Strain relaxation vs model parameters (varying elastic and viscus modulus)

To investigate the effects of microtubule stabilization and MPS disruption within the Zener–Maxwell framework, we adapted the model parameters following the approach described for the Kelvin–Maxwell combination (see above). Taxol treatment was simulated by increasing both the elastic (E_m) and viscous (η_m) moduli of the Maxwell element. Conversely, actin–spectrin lattice disruption was mimicked by reducing the corresponding moduli of the Zener element, representing the decreased elasticity (E_{z1} and E_2) and viscosity (η_z) due to MPS destabilization. In both cases, the elastic and viscous moduli were scaled by the same ratio for simplicity. Figure 4.20 illustrates the resulting effects on strain relaxation (we also tested increasing only the Maxwell viscosity and decreasing Zener elasticity, which gave qualitatively similar results), showing that increasing the Maxwell parameters slows strain evolution, while further decreasing the Zener parameters leads to an additional slowdown, consistent with experimental observations.

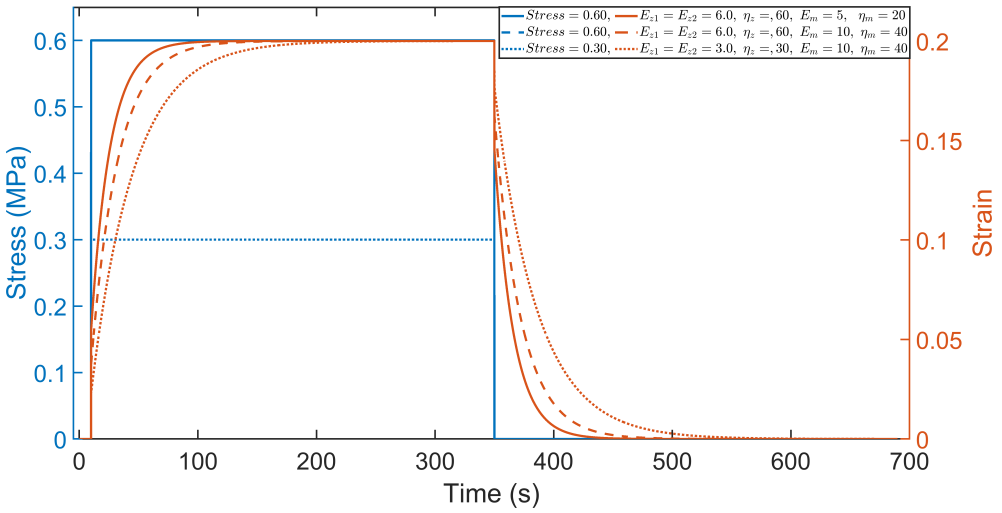


Figure 4.20: Effect of Maxwell and Zener parameter variation on creep and recovery behavior. This figure highlights the influence of viscoelastic parameters on the creep and recovery response of the Zener–Maxwell parallel model. First, Maxwell parameters are increased (dashed line) to demonstrate their effect on delayed strain recovery. Then, Zener parameters are decreased (dotted line) to illustrate their role in controlling creep saturation and the rate of viscoelastic relaxation. While varying Zener parameters, the applied stress is adjusted to ensure that the steady-state strain remains comparable across all cases. The control case is shown as a solid line.

The variation in relaxation time scales with changing model parameters is shown in Figure 4.21. As illustrated, increasing the microtubule viscosity (Figure 4.21 A) or decresing Zener elasticity (Figure 4.21B) leads to longer relaxation times. Similarly, simultaneously increasing both Maxwell moduli (Figure 4.21C) and decreasing both Zener moduli (Figure 4.21D) also results in an increase in the relaxation time scales. These trends highlight how modifications to the elastic and viscous elements of the model can quantitatively tune the rate of strain relaxation, providing further consistency with the experimental observations described earlier.

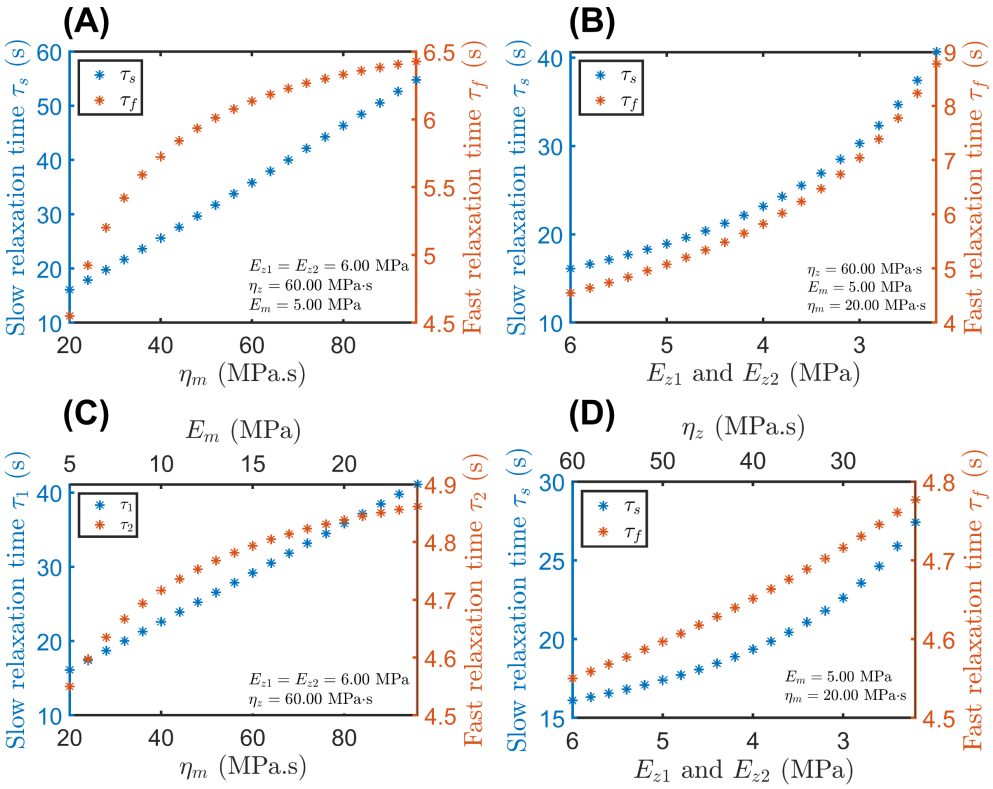


Figure 4.21: Dependence of the strain relaxation time scales on viscoelastic material parameters. Variation of the fast (τ_f) and slow (τ_s) relaxation time scales for the parallel Zener–Maxwell model. Panels (A) and (B) show the effect of changing a single material parameter: in (A) the Maxwell viscosity is increased, and in (B) the Zener elasticity is decreased. Panels (C) and (D) show the effect of simultaneously scaling both viscosity and elasticity within each branch: in (C) both parameters in the Maxwell element are increased, and in (D) both parameters in the Zener element are decreased. In all cases, both τ_f and τ_s increase, indicating a slower overall strain relaxation as model parameters are modified.

4.8 Conclusion and summary

In this chapter, we developed viscoelastic models to understand the strain relaxation behavior of axons and to understand how different cytoskeletal components contribute to the fast and slow relaxation time scales. We first examined a spectrin-based membrane periodic skeleton (MPS) model, motivated by the known unfolding and refolding dynamics of spectrin repeats. This model could not reproduce the biexponential relaxation observed experimentally and therefore was insufficient to explain the presence of two distinct relaxation time constants.

To address this limitation, we then considered classical viscoelastic elements and explored parallel combinations of Kelvin–Voigt and Maxwell components to reproduce the experimentally observed biphasic behavior. Although this model captured some qualitative trends when elastic and viscous parameters were varied independently, it could not reproduce the full range of changes observed across different perturbation conditions, demonstrating its limited ability to represent coupled cytoskeletal behavior.

We next implemented a parallel Zener–Maxwell framework, which incorporates two elastic elements and a viscous element in the Zener branch alongside a Maxwell element. This model successfully reproduced the experimentally observed trends in both relaxation time constants (τ_f and τ_s). The parameter dependence revealed that increasing the Maxwell viscosity and decreasing the Zener elasticity both lead to slower relaxation, consistent with the effects of cytoskeletal perturbations and prolonged stretching observed experimentally. These results suggest that the microtubule–MAPs bundle behaves as a viscoelastic liquid on long timescales, contributing to axonal recovery once external forces are removed, potentially through microtubule sliding dynamics.

Together, these modeling results suggest that the axonal cytoskeleton can be approximated as two viscoelastic subsystems acting in parallel: a microtubule–MAPs bundle that does not exhibit long-term mechanical memory, and an actin–spectrin lattice that retains long-term mechanical memory. The Zener–Maxwell model provides a mechanistic framework linking macroscopic strain responses to underlying cytoskeletal organization and offers a foundation for future efforts to incorporate nonlinear, adaptive, or active elements relevant to living neurons.

Chapter 5

Buckling response of axons to mechanical stimuli

5.1 Introduction

One important mechanical response of axons under perturbation is buckling, which manifests as a lateral instability along the axon. Unlike strain relaxation, which involves a monotonic recovery of axial strain, buckling appears as a wavy deformation that initially grows and then gradually diminishes and disappears over time. This behavior likely occurs when compressive forces—either externally applied or internally generated—exceed a critical threshold, leading to structural instability and, in some cases, localized cytoskeletal damage or remodeling [94,112,125]. In axons, buckling is particularly relevant because it can signal localized failure or reorganization of the underlying cytoskeleton, especially the microtubule bundles. Such behavior has been reported in stretch-injury models and is believed to play a critical role in the early mechanical response to traumatic loading [62]. Understanding buckling, together with viscoelastic relaxation, offers valuable insight into axonal resilience and the mechanisms that govern structural failure under mechanical stress.

In this chapter, our focus is on axonal buckling behavior following a stretch-and-release protocol and examine how the characteristic buckling wavelength evolves over time. To achieve this, we employed the micro-extensional rheometer setup for mechanical loading–unloading with simultaneous imaging. We also study the effect of microtubule stability on the buckling wavelength. We then develop mechanical models that capture the interaction between the microtubule core and the surrounding cortical layer, enabling interpretation of wavelength selection and its dependence on axonal material properties. These analyses establish a framework for understanding transient mechanical instability in axons and motivate exploration of the factors governing buckling dynamics.

5.2 Earlier studies on axonal buckling

Axonal buckling has been observed in a range of experimental and pathological contexts as shown in Figure (5.1), reflecting axonal deformation in response to stress or chemically driven perturbations. *In-vitro* experiments that mimic stretch injury have been particularly useful in demonstrating this phenomenon. For example, axons cultured on compliant Polydimethylsiloxane (PDMS) membranes were rapidly stretched using a controlled pressure pulse, after which the PDMS membrane returned to its original position upon release [62, 94, 125]. Although the membrane recovered immediately, the axons exhibited a transient buckling response, initially forming pronounced wavy deformations whose amplitude gradually diminished over time. The applied strain was delivered at a high stretch rate of 44% s^{-1}, emphasizing the rapid mechanical loading. Immunolabeling for βIII-tubulin highlighted the altered cytoskeletal organization, with axons displaying characteristic buckling patterns along their length (Figure 5.1A) [62]. These controlled in vitro findings have striking parallels in human pathology. For example, in the corpus callosum of an 18-year-old male examined 10 h after fatal traumatic brain injury caused by blunt force trauma, axons displayed characteristic buckling with pronounced undulations (Figure 5.1B) [62]. Immunohistochemistry

specific for amyloid precursor protein (APP), the gold-standard marker for axonal injury [163, 164], confirmed the presence of damaged axons. APP accumulation possibly arises from disrupted axonal transport, making it a sensitive indicator of injury. The resemblance between these in vivo and in vitro patterns strongly suggests that buckling represents a fundamental response of axons to mechanical loading.

Beyond stretch and release injury, axonal buckling can also emerge during chemically induced retraction (Figure 5.1C). Nitric oxide, which is well known to drive axonal retraction during vertebrate nervous system development [165, 166], was applied in the form of the donor compound NOC-7 (1 mM) to cultures of chick sensory neurons, where it caused significant retraction within the first 30 min [112]. During this process, axons developed pronounced undulations and bends, underscoring that buckling can arise not only from mechanical insults but also from molecular perturbations that hamper cytoskeletal integrity.

A different line of experimental work has highlighted axonal buckling in response to localized injury. When individual axons were subjected to targeted full or partial laser ablation (Figure 5.1D–E), they underwent retraction. In full ablation, the axon was transected into two independent segments, whereas in partial ablation, the cytoskeleton was locally disrupted but the membrane remained intact, forming a tether between the two ends. Retraction was accompanied by buckling deformations along the axonal length. These findings emphasize that even highly localized perturbations can trigger global mechanical responses within axons, revealing the interplay between localized damage and the broader cytoskeletal architecture.

Taken together, these earlier studies converge on the finding that axonal buckling is a robust and reproducible morphological response to diverse stimuli, whether mechanical, biochemical, or direct physical disruption. The occurance of buckling across such varied experimental paradigms emphasizes its importance as a hallmark of axonal vulnerability and a useful indicator for probing the biomechanical

and structural resilience of neurons. We next describe our experimental methods and observations.

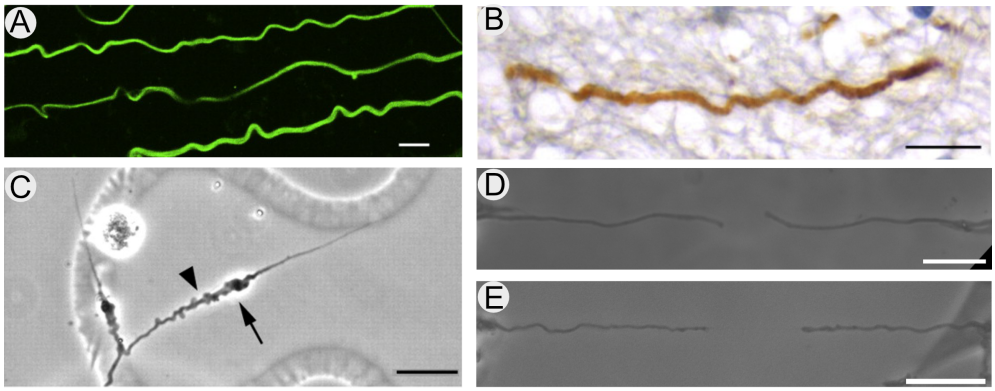


Figure 5.1: Axonal buckling phenomena reported in previous studies. Different examples of axonal buckling are shown in panels (A–E), each corresponding to a distinct case reported in the literature. **(A)** Multiple axons exhibiting undulating morphologies immediately (≤2 min) after dynamic stretch on a PDMS substrate, labeled for β-III-tubulin (scale bar ≈5 μm) [62]. **(B)** In the corpus callosum of an 18-year-old male 10 h after acute severe traumatic brain injury (blunt force trauma), axons show undulating morphologies reminiscent of in vitro stretch-induced buckling, labeled for APP (scale bar: 25 μm) [62]. **(C)** Cultures of chick sensory neurons treated with 1 mM NOC-7 (nitric oxide donor) exhibit pronounced axon retraction and undulations within the first 30 min [112]. **(D-E)** Axons respond to targeted full (**D**) and partial (**E**) laser ablation with buckling and retraction occurring during viscoelastic relaxation. **Panels (A–B):** Adapted from Tang-Schomer et al., 2012, *Experimental Neurology*, 233(1), 364–372. ©2012 Elsevier. Used with permission. **Panel (C):** Adapted from He et al., 2002, *J. Neurosci.*, 22(14), 5982–5991. ©2002 Society for Neuroscience. Used with permission. **Panels (D–E):** Representative images provided by Ashish Kumar Mishra, Raman Research Institute. Used with permission.

5.3 Method

The experimental procedures used in this study are the same as those described in detail in Chapter 3 and are only summarized here briefly. Axons were cultured and subjected to controlled stretch–release protocols using a cantilever-based setup, following the same conditions as in the strain-relaxation experiments. Axons were stretched up to approximately 20% strain and released either immediately or after a prolonged hold period (typically 10 minutes). Time-lapse imaging was performed throughout the stretch and release process to capture the

evolution of axonal morphology. Axonal tracking methodology, used to quantify deformation and buckling patterns, is described in Chapter 3, while details regarding the mechanical setup and its calibration are provided in Chapter 2.

5.4 Axonal buckling under mechanical stretch and release

A noticeable feature of the stretch–release experiments is that axons develop waviness when they are released from the cantilever after being stretched to approximately 20% strain, as shown in Figure 5.2A. To quantify this behavior, the axonal contour was analyzed by comparing the total contour length with the length of its smoothed mean conformation obtained via a moving-average procedure (Figure 5.2B). This smoothed contour represents an estimate of the underlying axonal shape in the absence of buckling—dominated only by the largest-scale curvature imposed by cantilever deflection—and therefore serves as a reference configuration against which the emergence of shorter-wavelength undulations can be measured. The difference between these two lengths, termed the "extent of buckling" provides a quantitative indicator of buckling following release. The temporal evolution of this extent of buckling for both immediate and delayed releases is presented in Figure 5.2C, with additional examples shown in Figure 5.3. Interestingly, the extent of buckling is significantly greater when axons are released after a 10-minute hold period compared to those released immediately after stretching.

Even though the overall axonal strain decreases monotonically following release, the extent of buckling first increases before decaying over time, particularly in the case of the 10-minute hold experiments. This suggests a transient amplification of structural undulations before the system gradually relaxes to a straighter configuration. Furthermore, the characteristic wavelength of the buckling pattern decreases monotonically with time, as shown in Figure 5.2A and also quantified

by the spatial autocorrelation of the transverse displacement along the axonal contour, which provides an estimate of the dominant wavelength of the buckling pattern (Figure 5.2D). This progressive shortening of the buckling wavelength highlights the dynamic nature of axonal structural rearrangements as internal stresses relax.

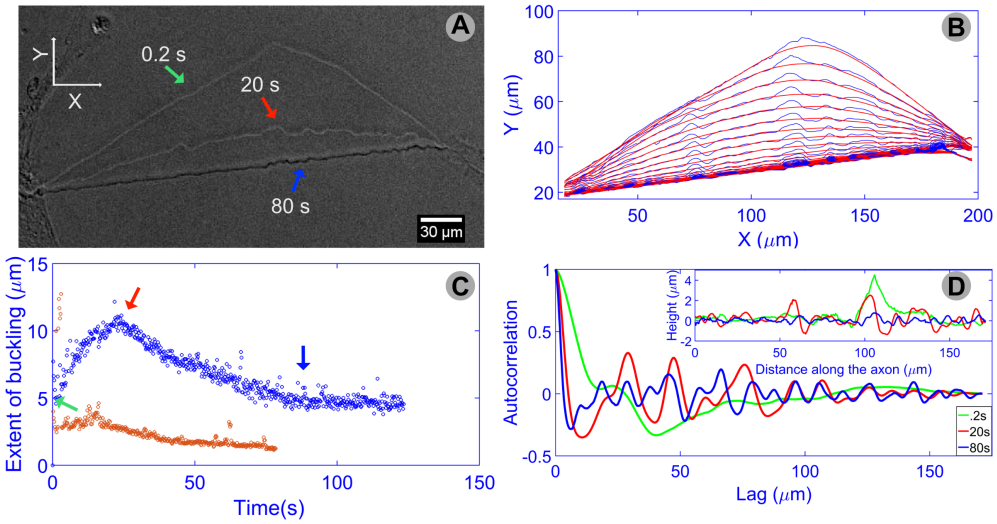


Figure 5.2: Analysis of axon buckling response. **(A)** A sequence of images showing axonal buckling after the axon is released from the cantilever following a 10-minute wait period. This images is obtained by subtracting images of different time points from the first frame and adding these subtracted images. **(B)** Axonal contour obtained through image analysis (blue curves), together with its smoothed mean position (red curves) computed using a moving-average procedure applied to the contour. For clarity, both the contour and its smoothed representation are shown only for a subset of time points. **(C)** Curves showing the extent of buckling for the same axon when it was subjected to immediate release (Orange) and when it was released after a 10 min wait time (blue). The extent of buckling is quantified by taking the difference between the lengths of the blue and red lines for each time point shown in **B**. Note that buckling is much more prominent in the wait-and-release cases, where it first increases after release, reaches a maximum, and then decreases with time. The colored arrows shows the time points corresponding to the images shown in **A**. **(D)** Time evolution of the position-position autocorrelation of the examples shown in **A** shows that the buckling wavelength decreases with time after the axon is released with color coding matching the arrows indicating the corresponding time points in the composite image in **A**. The inset shows the variation of "height" of the axon contour with respect to its "mean position" as defined in **B** which is used to calculate the autocorrelation functions.

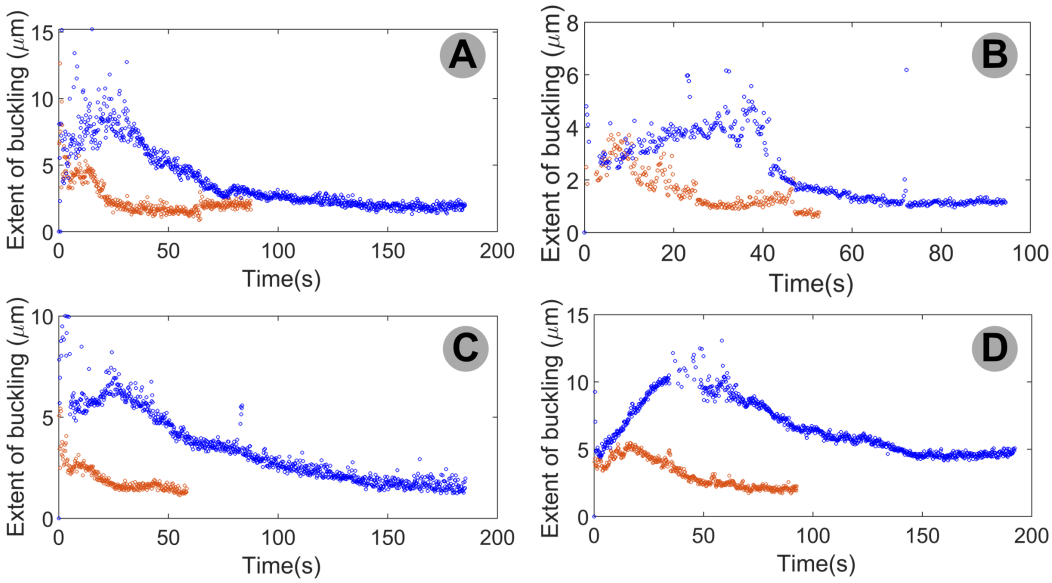


Figure 5.3: Curves illustrating the extent of buckling for the same axon subjected to immediate release (orange) and release after a 10-minute hold period (blue), shown for four different axons (A–D). In all cases, buckling is noticeably more pronounced in the wait-and-release condition, where the extent of buckling initially increases immediately after release and subsequently decreases over time.

5.5 Effect of microtubule stabilization on buckling wavelength

To investigate how microtubule stability and number density influence axonal buckling, we employed Taxol, a microtubule-stabilizing agent. When cells are treated with Taxol (10 μM), axons exhibit buckling patterns with noticeably longer wavelengths compared to controls. Representative examples of control and Taxol-treated axons are shown in Figure 5.4, illustrating this difference in post-release morphology. The temporal evolution of the "extend of buckling" for Taxol-treated axons is shown in Figure 5.5, illustrating the buckling dynamics following release under microtubule-stabilized conditions. The position–position autocorrelation functions for control and Taxol-treated axons (Figures 5.6A and 5.6B, respectively) further confirm this observation and demonstrate that Taxol treatment consistently increases the characteristic wavelength of axonal buckling. Taken together, both the raw images and quantitative analyses demonstrate that

microtubule stabilization by Taxol leads to the formation of longer-wavelength buckling modes and slower relaxation dynamics, hinting at increased bending stiffness.

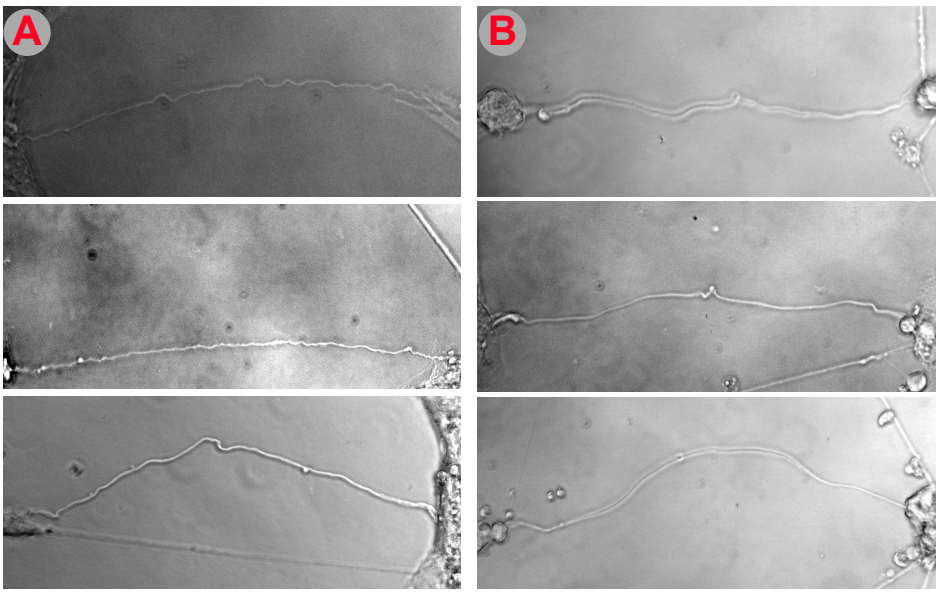


Figure 5.4: Effect of microtubule stabilization on axonal buckling wavelength. Post-release axons after a 10-minute hold: **(A)** controls, **(B)** Taxol-treated. Taxol-treated axons display longer buckling wavelengths than controls.

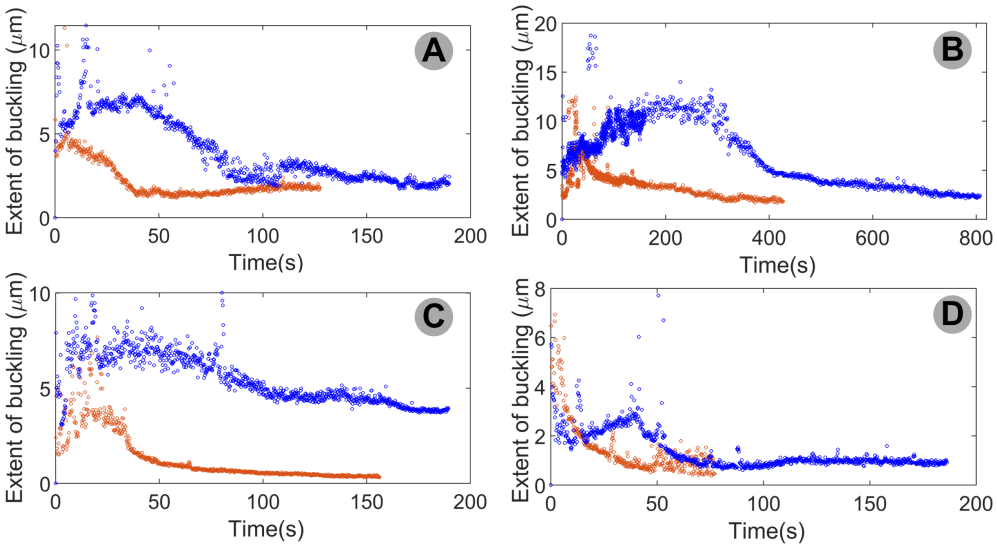


Figure 5.5: Plots showing the evolution of buckling for four Taxol-treated axons (A–D), each subjected to immediate release (orange) and release after a 10-minute hold period.

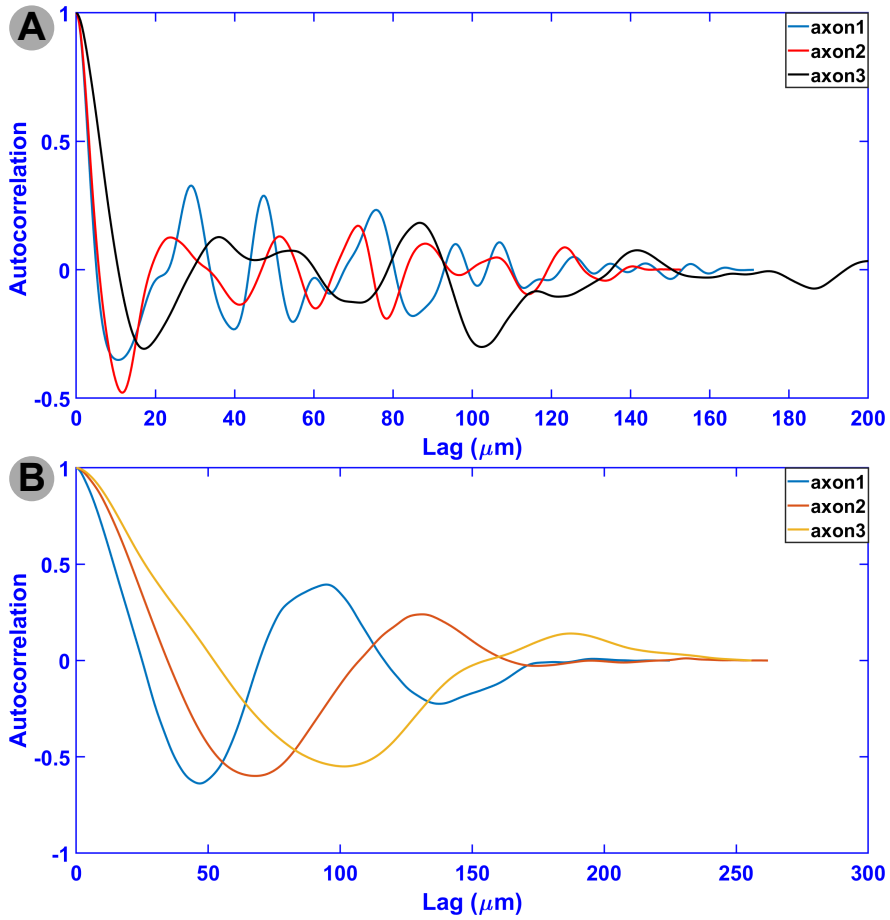


Figure 5.6: Effect of Microtubule Stabilization on Axonal Buckling Wavelength. **(A)** Position–position autocorrelation functions of axonal contours after release for three control axons and **(B)** Autocorrelation functions for Taxol-treated axons. This analysis focuses on experiments where axons were released following a 10-minute wait. Compared to control, Taxol treatment results in a consistently longer buckling wavelength. The autocorrelation functions are calculated at the time point where buckling reaches its maximum, defined by the difference between the axonal contour length and its smoothed mean length.

5.6 Previous modeling approaches to axonal buckling

Previous modeling efforts have sought to understand the mechanical stability of axons under loading, with particular attention to their susceptibility to buckling. Several approaches have been proposed, motivated by the recognition that buckling is a key failure mode in axons, especially in the context of traumatic brain

injury. Soheilypour et al. [159] focused on bundled microtubules as the primary load-bearing elements, analyzing their susceptibility to Euler-type buckling while accounting for the mechanical support of the surrounding cytoplasmic environment. Their simulations showed that the surrounding viscous medium suppresses classical long-wavelength Euler modes and instead promotes short-wavelength, tip-localized buckling with exponentially decaying amplitude. Crosslinking between filaments (e.g., via tau) further increases the effective compressive load they can withstand and alters how forces are distributed within the bundle, leading to unequal buckling onset among individual filaments.

In this context, Lang et al. (2017) [167] developed a continuum model of axonal buckling following stretch injury, in which the axon is idealized as a planar Euler beam resting on an elastic foundation representing the viscoelastic support of the surrounding brain tissue (Figure 5.7). A key assumption in their model is that immediately after a rapid stretch-and-release, the surrounding foundation returns to its original length much faster than the axon itself. Because the axon recovers more slowly, it temporarily remains longer than the supporting foundation, leading to a compressive state within the axon. As a result, transient buckling and undulations can emerge, offering a mechanistic explanation for post-stretch instabilities observed experimentally.

Beyond simplified elastic rod theories, recent coarse-grained molecular dynamics models have incorporated the composite architecture of the axonal cytoskeleton—comprising bundled microtubules, spectrin tetramers, and periodic actin rings [168]. These models demonstrate that actin rings significantly increase the critical buckling force of the microtubule bundle and that the characteristic buckling wavelength is strongly dependent on loading rate and surrounding viscosity. In these simulations, buckling adopts short-wavelength modes rather than classical long-wavelength Euler modes, and this behavior is attributed to spectrin reinforcement, which enhances lateral support and allows the bundle to bear larger compressive forces before buckling.

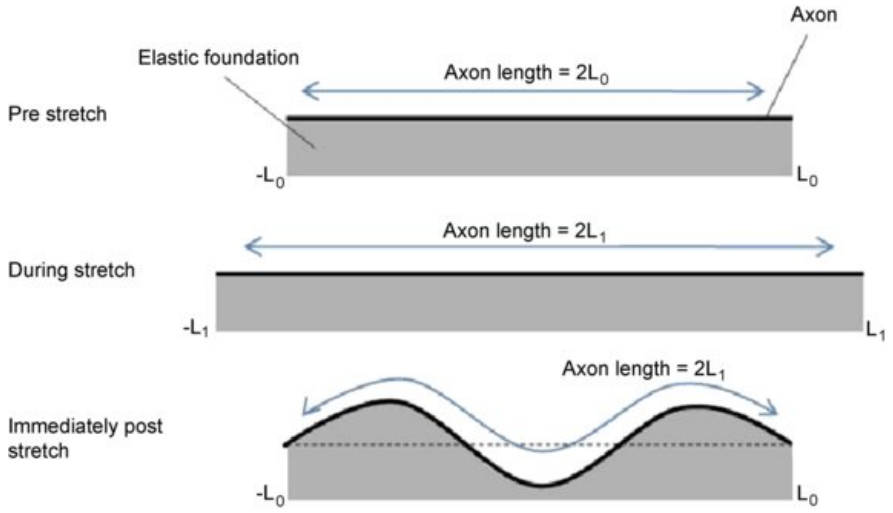


Figure 5.7: Schematic of the model: the axonal core is idealized as an Euler beam supported by an elastic foundation, where the foundation represents the surrounding brain tissue. Reproduced with permission from Lang et al., *Journal of Elasticity*, 2017, © Springer Nature [167].

In addition to axon-scale modeling, studies on individual microtubules embedded in elastic media have provided insight into how mechanical coupling to the surrounding cytoskeleton modifies buckling behavior. Whereas a freely suspended microtubule behaves as a classical Euler beam exhibiting long-wavelength buckling at relatively low critical loads, microtubules constrained within an elastic network (e.g., an actin-rich cytoskeletal matrix) display significantly shorter buckling wavelengths and enhanced load-bearing capacity. Brangwynne *et al.* [169] showed that these differences arise from lateral reinforcement by the surrounding network, which resists transverse displacements and alters the energetics of deformation. In their formulation, the total energy of a compressed microtubule is expressed as a sum of bending energy, energy released by axial compression, and energy stored in the deformed matrix,

$$E = \int \left[\frac{B}{2} \left(\frac{d^2u}{dx^2} \right)^2 - \frac{T_0}{2} \left(\frac{du}{dx} \right)^2 + \frac{K}{2} u^2 \right] dx,$$

where B is the bending rigidity of the microtubule, T_0 is the compressive load, $u(x)$ is the transverse displacement, and K represents the effective stiffness of the

embedding network. Minimization of this energy predicts a preferred buckling wavelength that decreases with increasing matrix stiffness, providing a mechanistic explanation for the short-wavelength undulations observed in embedded filaments. These findings are relevant for axons, as the axonal microtubule core is similarly constrained by surrounding cytoskeletal and extracellular components, motivating models in which the microtubules bundle is treated as an Euler beam supported by a surrounding foundation that provides lateral reinforcement. In our experiments, axonal undulations emerged at relatively short wavelengths. This behavior contrasts with classical Euler buckling of a free slender rod, which favors deformation at the longest possible wavelength [124]. The discrepancy indicates that the surrounding material plays an active mechanical role in selecting the buckling wavelength.

5.7 Model of axonal buckling

Motivated by recent experimental and theoretical evidence that axonal microtubules are mechanically reinforced by their surrounding environment, we construct an analytical framework for axonal buckling in which the microtubule bundle is approximated as a slender filament laterally reinforced by the actin–spectrin cortical lattice. This reduced description focuses on the dominant load-bearing elements and allows us to examine how elastic and viscoelastic cortical coupling influences the onset of buckling, the selection of a characteristic wavelength, and the evolution of undulation patterns during relaxation.

To motivate these models, we first summarize the main features of axonal buckling observed in our experiments:

- An axon is stretched by cantilever deflection. Upon release, axon buckles with an initial wavelength which is much shorter then axonal length.
- Over time, this wavelength decreases.
- Taxol treatment, which stabilizes microtubules (MTs), leads to increased

buckling wavelength.

We propose the following model:

- We model the MT core as a viscoelastic fluid: it behaves as an elastic rod at short times, but crosslink turnover enables microtubules within the bundle to slide past one another, allowing bending stresses to relax and giving the core fluid-like behavior at long times.
- The mechanism of buckling is taken as follows: axon stretching results in tension in the axonal cortex, whereas the MT core remains effectively stress-free just before release. Upon release, the cortex relaxes and exerts compression on the MT core. This compression triggers buckling. Short wavelength buckling (as opposed to classic long wavelength Euler buckling) occurs because bending of the MT core is opposed by elastic resistance of the surrounding cytoskeleton.
- We simplify the above mechanism as follows: we consider a viscoelastic fluid rod subject to uniform, axial compression, and bathed in an infinite elastic medium. This simplification will be found to recapitulate the observation of short wavelength buckling.

5.8 Model details

5.8.1 Model geometry

The MT core is modeled as an inextensible viscoelastic rod bending in a plane. The coordinate along its length is denoted by s, and the rod is assumed to bend in the plane (Figure 5.8). The local unit tangent and normal vectors are $\hat{t}(s)$ and $\hat{n}(s)$. The curvature $C(s)$ of the rod is defined as:

$$C(s) = \hat{n} \cdot \partial_s \hat{t} = -\hat{t} \cdot \partial_s \hat{n}. \tag{5.1}$$

The second equality follows from the condition $\hat{t}.\hat{n} = 0$

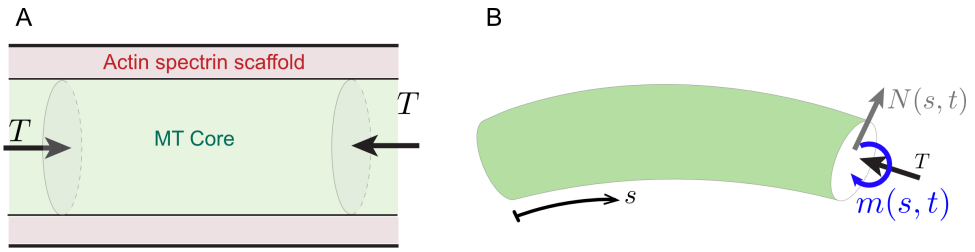


Figure 5.8: Schematic representation of the axonal shaft and coordinate system used for the theoretical description of buckling. (A) Cross-sectional view of the axon showing the outer actin-spectrin cortex (pink) that provides membrane-cytoskeleton support, and the inner microtubule (MT) core (green) formed by bundled MTs associated with MAPs. Axial compressive forces T act at both ends of the MT bundle. (B) Side view illustrating the continuum representation of the axonal shaft. The arc length coordinate s parameterizes the centerline, with tangent vector $\hat{t}$, normal vector $\hat{n}$, and bending moment $m(s,t)$ describing the local mechanics during deformation and buckling, with the normal force component denoted by $N(s,t)$.

5.8.2 Force balance along the rod

We denote by $f(s)$ the internal force acting along a rod cross-section whose normal is $\hat{t}$. This force will have tangential and normal components:

$$\vec{f}(s) = T(s)\hat{t} + N(s)\hat{n}, \tag{5.2}$$

The force balance on an element of rod between s and $s + ds$ is given by

$$\partial_s \vec{f} + \vec{F}_{\text{ext}} = 0. \tag{5.3}$$

Here, F_{ext} is the external force per unit length acting along the MT core. Note that we have neglected inertia in the above force balance. Using the definition of curvature given by equation 5.1, the above equation can be projected along tangent and normal directions:

$$\partial_s T - CN = -F_{\text{ext},t}, \tag{5.4}$$

$$\partial_s N + CT = -F_{\text{ext},n}. \tag{5.5}$$

In general the tangent and normal components $F_{\text{ext},t}$ and $F_{\text{ext},n}$ are non-zero and spatially distributed. We make the simplifying assumption that the compressive force exerted on the MT core by the relaxing cortex can be approximated as a concentrated (Dirac delta) at the ends of the core. In this case the right-hand side in equation 5.4 is zero except at the ends. Furthermore, for small deformations of an initially stress-free, straight rod, the term CN is negligible. From equation 5.4 we find that, to leading order,

$$T = T_0, \tag{5.6}$$

where $T_0 < 0$ is the uniform compressive force on the rod.

Next, we consider equation 5.5. We denote $u(s)$ the transverse defection of the microtubule bundle due to buckling relative to its undeformed (straight) configuration (Figure 5.9). Then, the normal component of the external force is assumed to be given by Hooke's law as

$$F_{\text{ext},n} = -Ku, \tag{5.7}$$

where K is an elastic constant of the medium surrounding the MT core (Figure 5.9).

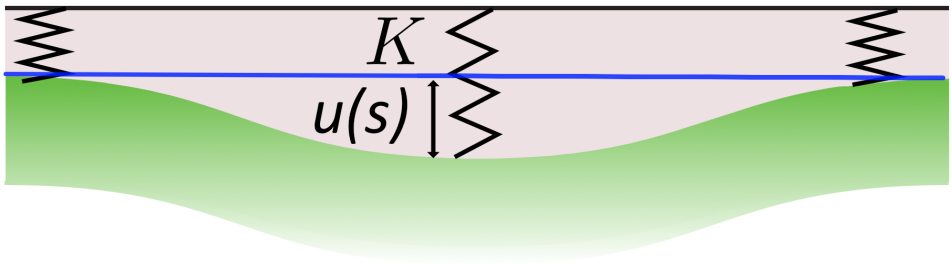


Figure 5.9: Elastic coupling between the microtubule core and the surrounding axonal cortex during buckling. A large initial strain mismatch suggests that the microtubule (MT) core undergoes buckling. The deflection between the MT bundle and the outer axonal scaffold—separated by intermediate protein filaments (e.g., actin–spectrin links or cross-linking MAPs)—generates a restoring force. In the model, this restoring effect is represented as a distributed spring density K, which couples the MT bundle to the outer axonal structure.

Noting that in the small defection approximation $C \approx \partial_s^2 u$, equation 5.5 can be written as

$$\partial_s N + T_0 \partial_s^2 u = Ku. \tag{5.8}$$

5.8.3 Torque balance and moment-curvature Relation

The normal force $N(s)$ appearing in equation 5.8 is related to the net bending moment acting on a rod element between s and $s + ds$. We denote the vector moment by $\mathbf{m} = m(s)\,\hat{t} \times \hat{n}$. The net torque balance acting on the rod element between s and $s + ds$ about an origin passing through s is given by

$$\partial_s m + N = 0, \tag{5.9}$$

5.8.4 Moment-Curvature relation

To complete the description we require a relation between the internal moment $m(s)$ and the deformed shape of the rod. We model this as a Maxwell-type viscoelastic constitutive relation for a viscoelastic rod:

$$(1 + \tau\partial_t)m = B\tau\partial_t C, \tag{5.10}$$

In this relation τ is the relaxation time and B is the bending elastic modulus of the rod. Note that at short times equation 5.10 yields $m \simeq BC$ i.e., the usual elastic relation for rod bending; whereas at long times it yields $m \simeq \eta_m \partial_t C$, where $\eta_m \equiv B\tau$ is the viscosity of the Maxwell viscoelastic rod. Physically, this reflects elastic bending of a crosslinked microtubule bundle at short times, followed at longer times by relaxation of bending stresses through crosslink turnover and microtubule sliding. These limiting behaviors are consistent with a Maxwell-type constitutive response.

5.8.5 Linear stability analysis

We next perform a linear stability analysis relative to the straight configuration of the rod ($N = m = u = C = 0$), under uniform compressive prestress T_0. To identify the characteristic buckling wavelength we perturb u and m around their zero values in the straight core configuration:

$$\{m, u\} \sim e^{iqs+\omega t}. \tag{5.11}$$

Combining equation 5.8, 5.9, 5.10, and 5.11 we obtain the dispersion relation (Derivation provided in Appendix G.1) for the wavevector dependent growth rate $\omega(q)$:

$$\omega\tau = -\frac{T_0 q^2 + K}{Bq^4 + T_0 q^2 + K}. \tag{5.12}$$

In the above recall that $T_0 < 0$, as required for buckling.

5.8.6 Marginal stability and cutoff wavelength

The marginal (cutoff) condition is obtained by setting the growth rate to zero ($\omega = 0$). From equation 5.12 we obtain the critical value

$$T_0 q_c^2 + K = 0 \quad \Longrightarrow \quad q_c^2 = -\frac{K}{T_0}.$$

Hence the critical wavenumber and wavelength are

$$q_c = \sqrt{-\frac{K}{T_0}} = \sqrt{\frac{K}{|T_0|}}, \qquad \lambda_c = \frac{2\pi}{q_c} = 2\pi\sqrt{-\frac{T_0}{K}}.$$

Therefore modes with

$$\boxed{q > q_c = \sqrt{\frac{K}{|T_0|}}}$$

have $\omega > 0$ and are expected to grow (unstable); buckling modes with longer wavelengths (i.e. $q < q_c$) are suppressed. Having established the cutoff condition

above, we next investigate whether there exists a most dominant (i.e. maximally growing) mode among the unstable wavenumbers. This requires analyzing the extrema of the dispersion relation itself. Let $x = q^2$ then equation 5.12 becomes

$$\omega(x) = -\frac{T_0 x + K}{Bx^2 + T_0 x + K}.$$

Let $N(x) = -(T_0 x + K)$ and $D(x) = Bx^2 + T_0 x + K$. Then

$$\frac{d\omega}{dx} = \frac{N'D - ND'}{D^2}, \qquad N' = -T_0, \quad D' = 2Bx + T_0.$$

Simplifying,

$$\frac{d\omega}{dx} = \frac{B\,x\,(T_0 x + 2K)}{(Bx^2 + T_0 x + K)^2}.$$

For identifying a maximum or minimum of the growth rate, we set $\frac{d\omega}{dq} = 2q\frac{d\omega}{dx} = 0$. Since buckling requires real nonzero wavenumbers, we assume $x = q^2 > 0$. which gives

$$T_0 x + 2K = 0 \quad \Longrightarrow \quad x_* = -\frac{2K}{T_0} \quad \Longleftrightarrow \quad q_* = \sqrt{-\frac{2K}{T_0}},$$

which is real only if $T_0 < 0$ (compressive prestress) and

$$\boxed{\left.\frac{d^2\omega}{dq^2}\right|_{q_*} < 0}$$

(See Appendix G.1 for details) so the stationary point $q_* = \sqrt{-2K/T_0}$ is a local maximum of $\omega(q)$, corresponding to the most-dominant (most unstable) mode.

Dimensionless formulation

Since the exact values of the parameters are not known, and moreover they can vary from axon to axon, we nondimensionalize them with respect to characteristic reference values T_0^*, B^*, K^*, and η_m^*. While this procedure sets the reference scale of each parameter to 1, in reality the physical parameters may differ from one another and need not be equal. Since the primary aim of this work is to

understand the qualitative behavior and scaling properties of the buckling response rather than to reproduce specific numerical values, this nondimensional formulation provides a minimal yet general description. Moreover, the resulting equations remain sufficiently flexible to allow parameter variation and contrast to be investigated. After nondimensionalization, we vary the nondimensional parameters to examine how changes in material properties influence the predicted buckling behavior. In particular, we define

$$\tilde{K} = \frac{K}{K^*}, \qquad \tilde{B} = \frac{B}{B^*}, \qquad \tilde{T}_0 = \frac{T_0}{T_0^*}, \qquad \tilde{\eta}_m = \frac{\eta_m}{\eta_m^*}, \qquad \tilde{q} = \frac{q}{q_{\text{ref}}}.$$

Here q_{ref} denotes a reference wavenumber used for nondimensionalization. With these definitions, the dispersion relation can be written in the dimensionless form

$$\omega\tilde{\tau} = -\frac{\tilde{T}_0\tilde{q}^2 + \tilde{K}}{\tilde{B}\tilde{q}^4 + \tilde{T}_0\tilde{q}^2 + \tilde{K}}. \tag{5.13}$$

From this expression we plot the growth rate $\omega(\tilde{q})$ as a function of q for decreasing values of $\tilde{T}_0$ (Figure 5.10A). Only modes with $\tilde{q} > \tilde{q}_c$ ($\omega(\tilde{q}) > 0$) grow dynamically, corresponding to shorter wavelengths ($\lambda = 2\pi/\tilde{q}$), whereas modes with $\tilde{q} < \tilde{q}_c$ ($\omega(\tilde{q}) < 0$) remain stable and correspond to longer wavelengths, and therefore do not contribute to buckling. As the magnitude of the prestress decreases (i.e., as $\tilde{T}_0$ becomes less negative), the threshold wavevector for instability increases, leading to shorter buckling wavelengths. This trend matches experimental observations, where relaxation of cortical tension after release drives the dynamic shortening of the buckling wavelength over time.

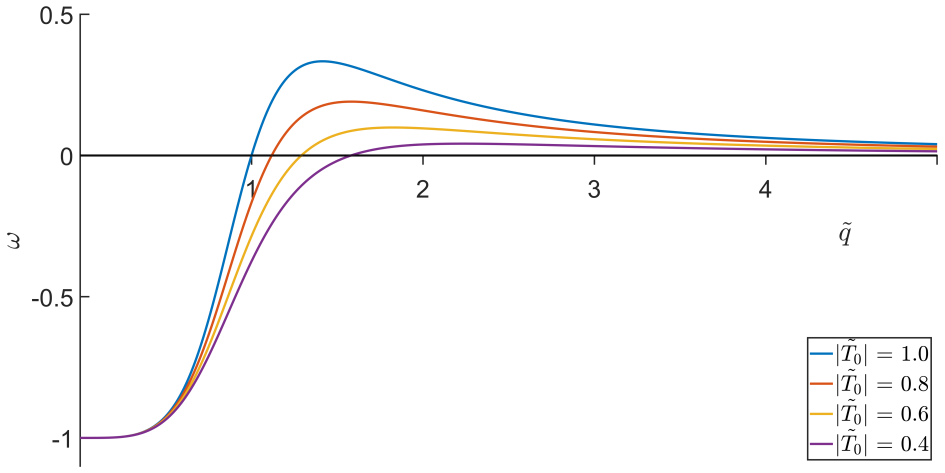


Figure 5.10: Growth rate ω versus wavevector $\tilde{q}$ with decreasing compressive stress. Only modes with $\tilde{q} > \tilde{q}_c$ become unstable and grow dynamically, while long-wavelength modes ($\tilde{q} < \tilde{q}_c$) remain stable. As the magnitude of the compressive stress decreases (i.e. $\tilde{T}_0$ becomes less negative), both the cutoff wavevector $\tilde{q}_c$ and the most unstable wavevector $\tilde{q}_*$ shift to higher values, corresponding to shorter-wavelength buckling modes.

5.8.7 Effect of bending rigidity and viscosity in the Maxwell model with elastic foundation

Taxol treatment, which stabilizes microtubules (MTs), leads to an increased buckling wavelength in our experiments. Taxol stabilizes microtubules (MTs), and is reported to increase MT mass and structural stability [128]. An increase in MT content and stabilization is expected to enhance the effective bending modulus B of the axonal MT bundle, thereby raising the energetic cost of curvature. Consistent with this expectation, Taxol-treated axons in laser-ablation experiments behave nearly as rigid rods and do not exhibit the post-ablation short-wavelength buckling (Figure 5.11) [170] observed in untreated axons as shown earlier in this chapter (Figure 5.1E). This suppression of buckling following Taxol treatment provides direct experimental evidence that $\tilde{B}$ might be increase after Taxol treatment.

In addition to bending rigidity, stabilizing agents such as Taxol have been reported to increase the effective viscosity of microtubule networks [142]. An in-

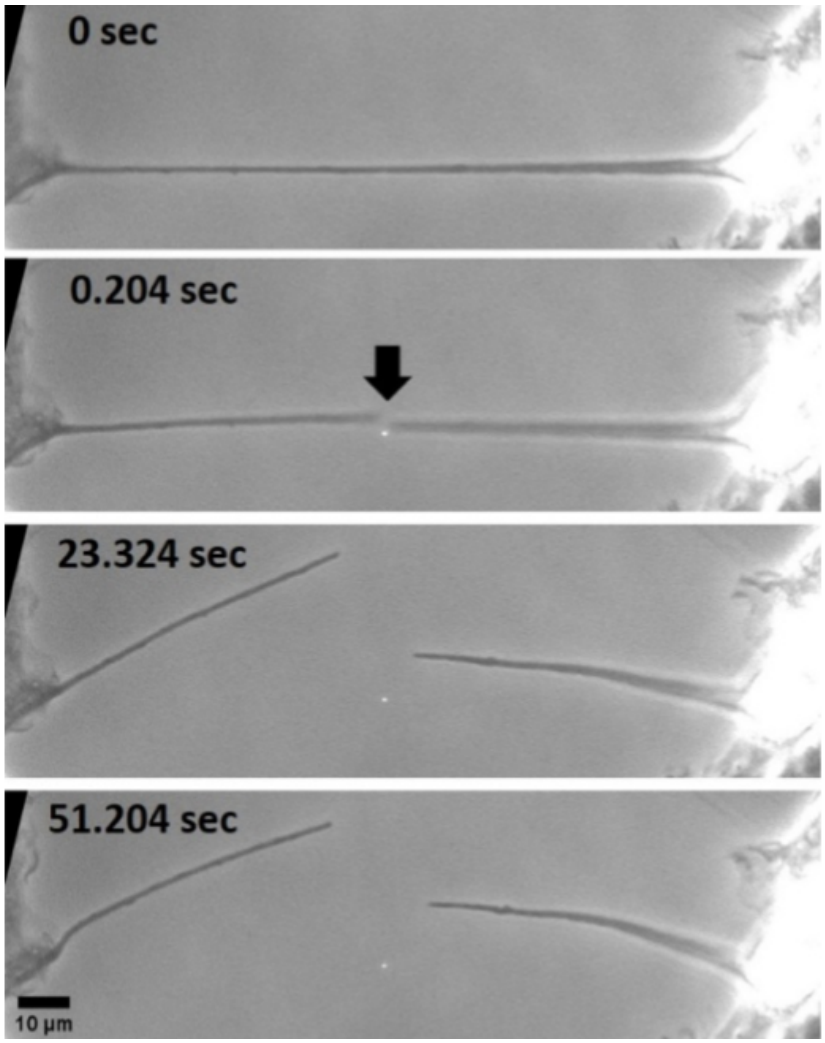


Figure 5.11: Laser ablation response of Taxol-treated axons. Representative time sequence showing the mechanical response of axons subjected to laser ablation after Taxol treatment. Taxol-treated axons behave as nearly rigid rods and do not exhibit post-release buckling, indicating a substantial increase in bending stiffness and/or effective viscosity of the microtubule bundle. Images adapted from Mishra (2025) [170]. Used with permission.

creased microtubule viscosity $\tilde{\eta_m}$ provides additional damping, resisting rapid shape changes and can modifying the growth rates of unstable modes during axonal relaxation. Our strain-relaxation experiments and the modelling results presented in earlier chapters also support the interpretation that Taxol treatment increases axonal viscosity.

To examine these effects, we explore how variations in the nondimensional bending modulus $\tilde{B}$ and viscosity $\tilde{\eta}_m$ influence the growth rate $\omega(\tilde{q})$ and the dominant

unstable wavelength predicted by the dispersion relation (Figure 5.12). The plot shows that both the cut-off wavelength and the dominant wavelength are unaffected by changes in $\tilde{B}$ and $\tilde{\eta}_m$. This absence of a dependence of the most unstable mode on $\tilde{B}$ and $\tilde{\eta}_m$ is surprising, and so we re-examined the basis of our model. We thus realized an important ingredient was missing, namely the viscoelasticity of the actin–spectrin cortex. In order to account for the Taxol experiments, we therefore modify the model by incorporating these cortical viscoelastic effects in the next section.

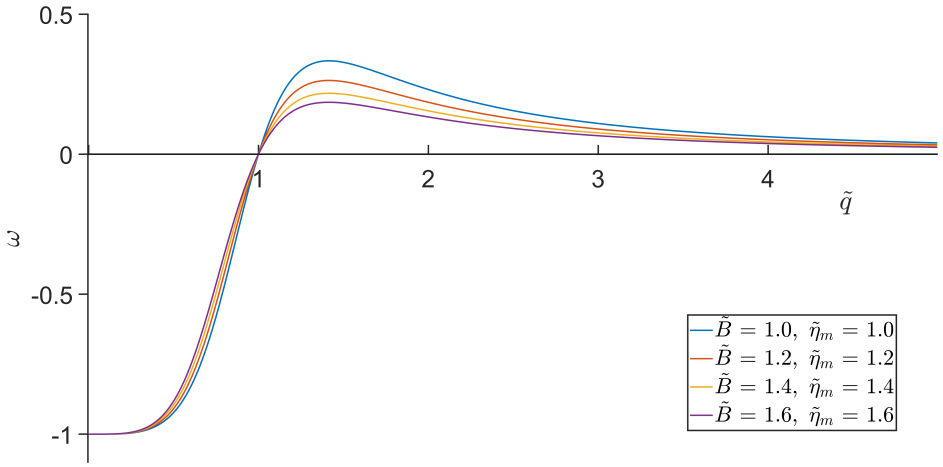


Figure 5.12: Growth rate ω as a function of wavevector $\tilde{q}$ for increasing values of the nondimensional bending modulus $\tilde{B}$ and viscosity $\tilde{\eta}_m$. Increasing $\tilde{B}$ and $\tilde{\eta}_m$ progressively suppresses the growth rate of unstable modes, reducing the maximum amplification rate while leaving both the cutoff wavevector $\tilde{q}_c$ and the dominant unstable mode $\tilde{q}$ unchanged. Thus, although enhanced bending rigidity and increased viscosity slow the buckling dynamics, they do not modify the characteristic buckling wavelength.

5.9 Effect of the axonal cortex as a viscoelastic solid

Although the previous section explains how axonal buckling evolves from long to short wavelengths as the internal tension relaxes over time, it does not account for the observed dependence of buckling wavelength on axonal bending rigidity and internal viscosity. This limitation motivates the next modeling approach, which explicitly incorporates the viscoelastic properties of the axonal outer cor-

tex surrounding the microtubule core, allowing us to investigate how interactions between the core and its surrounding cortex influence transient buckling dynamics.

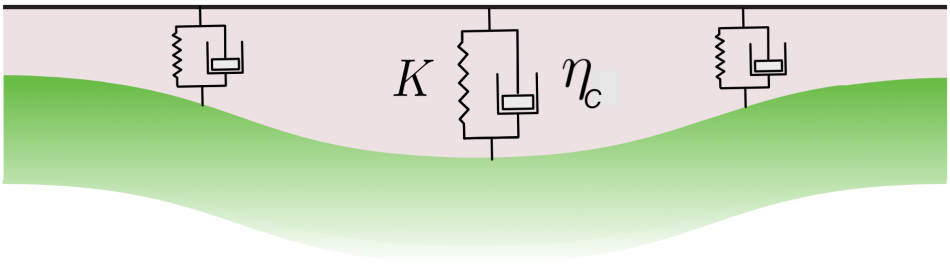


Figure 5.13: Kelvin–Voigt viscoelastic coupling during axonal buckling. The coupling between the microtubule (MT) core and surrounding axonal scaffold is modeled by a Kelvin–Voigt element, where a distributed spring density K and dashpot viscosity η act in parallel. This formulation captures both elastic resistance and viscous relaxation of the axon–MT system under buckling.

Since the outer layer of the axon behaves like a viscoelastic solid, we model the normal force exerted by the cortex on the microtubule core using a Kelvin–Voigt viscoelastic foundation. In this framework, the restoring force is

$$F_{\text{ext},n} = -(Ku + \eta_c \partial_t u), \tag{5.14}$$

where η_c is the viscosity of kelvin-voigt element. If we follow the same procedure and carry out a linear stability analysis (See Appendix G.2 for details), we obtain the following dispersion relation (in dimensionless form):

$$\omega^2 + \frac{\tilde{B}\tilde{\tau}\tilde{q}^4 + \tilde{T}_0\tilde{\tau}\tilde{q}^2 + \tilde{K}\tilde{\tau} + \tilde{\eta}_c}{\tilde{\eta}_c\tilde{\tau}}\,\omega + \frac{\tilde{T}_0\tilde{q}^2 + \tilde{K}}{\tilde{\eta}_c\tilde{\tau}} = 0. \tag{5.15}$$

Let ω_1 and ω_2 be the roots of the equation, given by

$$\omega_{1,2} = -\frac{1}{2}\left(\frac{\tilde{B}\tilde{\tau}\tilde{q}^4 + \tilde{T}_0\tilde{\tau}q^2 + \tilde{K}\tilde{\tau} + \tilde{\eta}_c}{\tilde{\eta}_c\tilde{\tau}}\right) \pm \frac{1}{2}\sqrt{\left(\frac{\tilde{B}\tilde{\tau}\tilde{q}^4 + \hat{T}_0\tilde{\tau}\tilde{q}^2 + \tilde{K}\tilde{\tau} + \tilde{\eta}_c}{\tilde{\eta}_c\tilde{\tau}}\right)^2 - 4\frac{\tilde{T}_0\tilde{q}^2 + \tilde{K}}{\tilde{\eta}_c\tilde{\tau}}}. \tag{5.16}$$

If the roots are real and distinct (with at least one root expected to be positive for buckling to occur), the time variation of the transverse displacement $u(t)$ can

be written as

$$u(t) \sim u_1 e^{\omega_1 t} + u_2 e^{\omega_2 t} \tag{5.17}$$

where u_1 and u_2 are constants determined from the initial conditions. The variation of ω_1 and ω_2 with $\tilde{q}$ for decreasing $\tilde{T}_0$ is shown in Figure 5.14. Figure 5.14 shows that ω_1 is positive over a certain range of wavevector $\tilde{q}$, leading to buckling in this regime. As $\tilde{T}_0$ decreases (i.e., $\tilde{T}_0$ becomes less negative), both the cutoff and most unstable wave vector increase (or corresponding wavelength decreases), consistent with the experimentally observed temporal decrease in wavelength during relaxation.

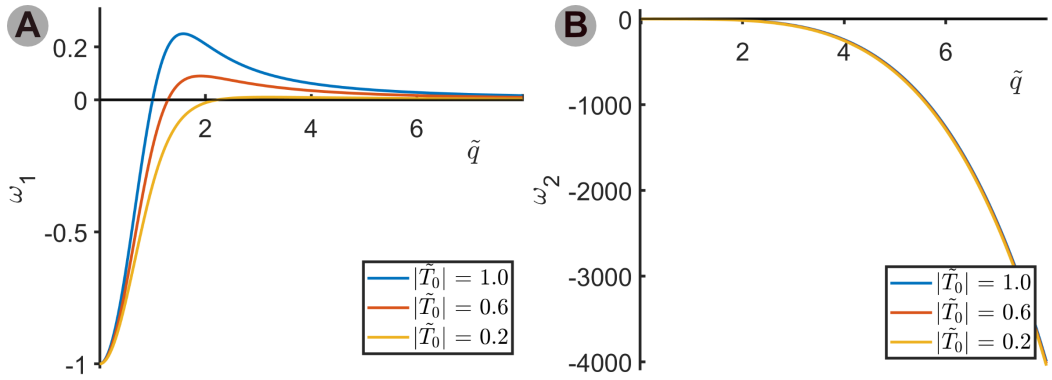


Figure 5.14: Roots of growth rate ω as a function of wavenumber $\tilde{q}$ obtained from dispersion relation: (A) first root and (B) second root.

5.9.1 Influence of bending rigidity and viscosity in the Maxwell model with Kelvin–Voigt foundation

The growth rate $\omega(q)$ for increasing values of the nondimensional bending modulus $\tilde{B}$ and viscosity $\tilde{\eta}_m$ is shown in Figure 5.15. The plot demonstrates that the most dominant unstable wavevector $\tilde{q}_*$ shifts toward lower values as $\tilde{B}$ and $\tilde{\eta}_m$ increase. This trend is consistent with the experimentally observed increase in buckling wavelength following Taxol treatment. In addition, the overall magnitude of the growth rate decreases for larger $\tilde{B}$ and $\tilde{\eta}_m$, indicating slower buckling dynamics, which also aligns with the experimentally measured slower relaxation in Taxol-stabilized axons. Together, these results suggest that increases in bending

rigidity and cytoskeletal viscosity act to suppress short-wavelength instabilities and delay the relaxation process.

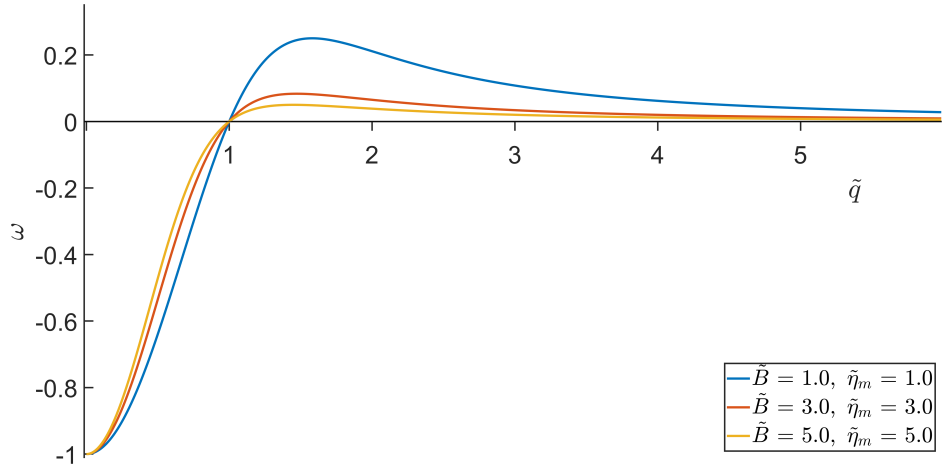


Figure 5.15: Dominant growth rate ($\max(\omega_1, \omega_2)$) as a function of wavenumber $\tilde{q}$ for increasing values of the nondimensional bending modulus $\tilde{B}$ and viscosity $\tilde{\eta}_m$. Increasing $\tilde{B}$ and $\tilde{\eta}_m$ shifts the most unstable mode toward lower wavevectors and reduces the overall growth rate.

5.10 Conclusion

Experiments on axonal relaxation following dynamic stretch demonstrate that short-wavelength buckling undulations appear after release, undergo a transient amplification, and then decay as internal tension relaxes. The buckling wavelength decreases as axonal relaxation proceeds. In addition, Taxol treatment, which stabilizes microtubules, results in longer-wavelength buckling.

To interpret these behaviors, we first developed an analytical model treating the microtubule core as an Euler beam on an elastic foundation. This framework successfully captures the temporal evolution from long- to short-wavelength buckling as tension relaxes, consistent with experiments. However, because the dominant unstable wavelength in this formulation is independent of bending rigidity, additional mechanisms are required to account for the increased wavelength observed following Taxol treatment.

We therefore extended the analysis by incorporating a Kelvin–Voigt viscoelastic

foundation to represent the axonal cortical layer surrounding the microtubule core. In addition to capturing the experimentally observed progression toward shorter wavelengths as tension decrease, the viscoelastic extension predicts that higher bending rigidity and viscosity favor longer-wavelength instabilities. These predictions are consistent with experimental observations and suggest that axonal buckling is governed by the coupled viscoelastic interaction between the microtubule core and its surrounding cortex, rather than internal tension alone.

Chapter 6

Investigating cytoskeletal structural changes in the axons after mechanical stimuli

6.1 Introduction

In the previous chapters, we described stretch and release experiments on axons and presented a model to understand these based on how cytoskeletal components—such as the MPS, microtubules, and MAPs—may respond to mechanical perturbations. Building on this framework, the present chapter focuses specifically on the MPS, whose organized architecture is thought to confer elasticity and buffer tension [12]. While its periodic organization in axons is well established [43, 44], the extent to which the MPS structure adapts, deforms, or recovers after mechanical stretch remains unclear. Here, we examine how the MPS reorganizes following mechanical stretch by comparing its structure in unstretched and stretched axons using a home-built stretching device combining with super-resolution imaging, in collaboration with Dr. Aurnab Ghose and Dr. Shivani Bodas (IISER, Pune).

6.2 Device design and stretching protocol

We developed a home-built stretching device (Figure 6.1A) compatible with STED super-resolution imaging [171, 172]. While its design can be adapted to investigate other cytoskeletal components, in the present work this device was used to study the effect of mechanical stretch on MPS organization. The device enables controlled equibiaxial strain to be applied to neurons cultured on circular PDMS substrates. In this configuration, the PDMS membrane is mounted on the top of the device and fixed in place by clamping it between a central cylindrical post and the surrounding outer ring. The assembled device is shown in Figure 6.1A, and the corresponding schematic geometry is shown in Figure 6.1C. The device supports two modes of applying stretch: vacuum-based loading and indenter-based loading. The indenter component of the device is shown in Figure 6.1B, and schematic representations of both loading modes are shown in Figure 6.1D and E. In the vacuum-based configuration, negative pressure applied within the chamber pulls the PDMS membrane downward, thereby imposing mechanical strain on neurons adhered to its surface. This mode also enables in-situ stretching during live microscopic imaging. In the indenter-based configuration, stretch is generated by pressing a cylindrical indenter downward, which pushes the PDMS membrane into the annular region between the central post and the outer cylinder, producing controlled deformation of the substrate.(Figure 6.1E). In this mode, the resulting strain is determined by the imposed indentation depth. The indenter can be mechanically secured to the lower base using clamping screws to maintain a constant strain, making the setup compatible with long-term and super-resolution imaging (e.g., STED). In the present work, this indenter-based configuration was used for axonal stretching and subsequent MPS analysis using STED nanoscopy.

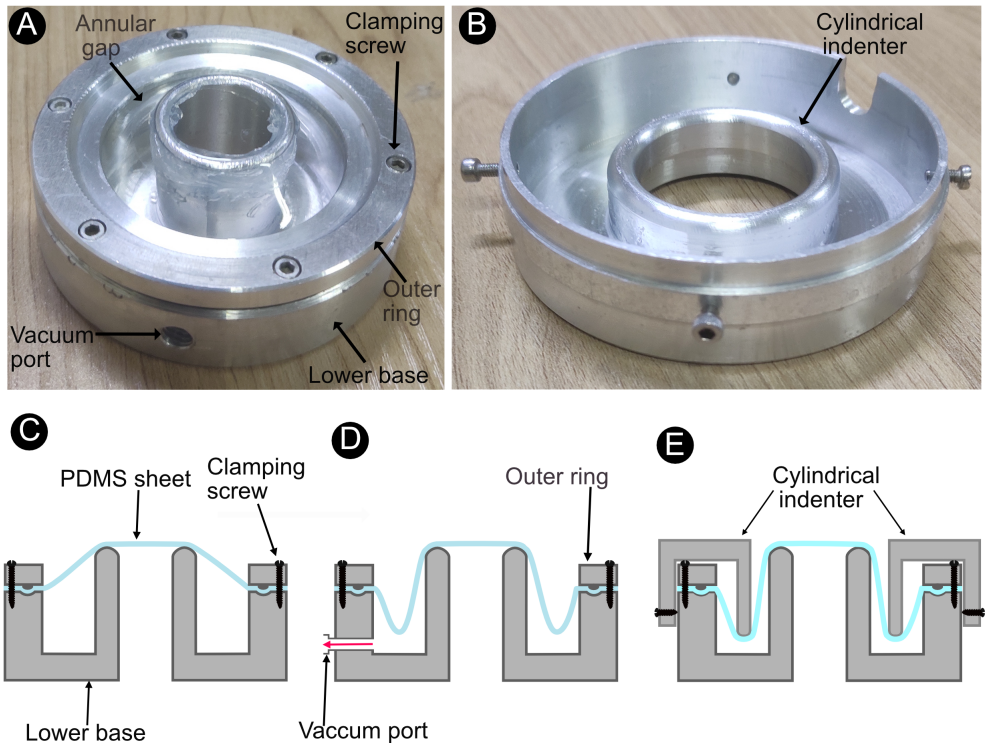


Figure 6.1: Mechanical stretching device and loading configurations. (A) Photograph of the lower base component showing the central cylindrical post and surrounding outer ring used to clamp the PDMS membrane. Neurons are cultured on the PDMS surface mounted across the top opening. The annular gap between the post and outer ring defines the region into which the membrane is pushed; a vacuum port enables optional vacuum-based loading. **(B)** Photograph of the cylindrical indenter used to displace the membrane downward during indentation-based stretching. **(C–E)** Schematic representation of the membrane clamping and loading steps. **(C)** PDMS membrane clamped between the central post and outer ring (a thin layer of vacuum grease on the central post is applied to improves sealing and reduces friction). **(D)** Vacuum loading, in which suction applied via the vacuum port pulls the membrane downward to generate tensile strain. **(E)** Indentation loading, in which the indenter displaces the membrane into the annular region to produce tensile strain.

6.3 Strain measurement in PDMS sheet

To estimate the mechanical strain applied to the PDMS substrate during stretching, strain measurements were performed using soda-lime glass beads (500 µm diameter) dipped in glycerol to promote adhesion and placed at random locations on the PDMS surface as positional reference points. The region of interest above the central cylindrical post was first imaged using a 10× objective prior to

stretching. Multiple images were acquired and stitched to produce a single image covering the full area of interest.

The PDMS substrate was then stretched using the indenter-based configuration, and the same region was imaged again under identical acquisition conditions. Distances between identical pairs of beads were measured before and after stretching, and the relative change in separation was used to calculate the substrate strain. As shown in Figure 6.2, the PDMS membrane experienced an average equibiaxial strain of approximately 35% when stretch was applied by setting the cylindrical indenter such that it was 6 mm away from the lower surface of the device. The same indenter position were used for all axonal stretching and subsequent imaging experiments. The strain measurements showed modest scatter, likely due to thickness variations in the PDMS sheets, which were cast manually by pouring the PDMS–curing agent mixture into petri dishes. Using spin coating to prepare PDMS sheets could yield more uniform thickness and help determine whether thickness non-uniformity contributes to the observed scatter [173].

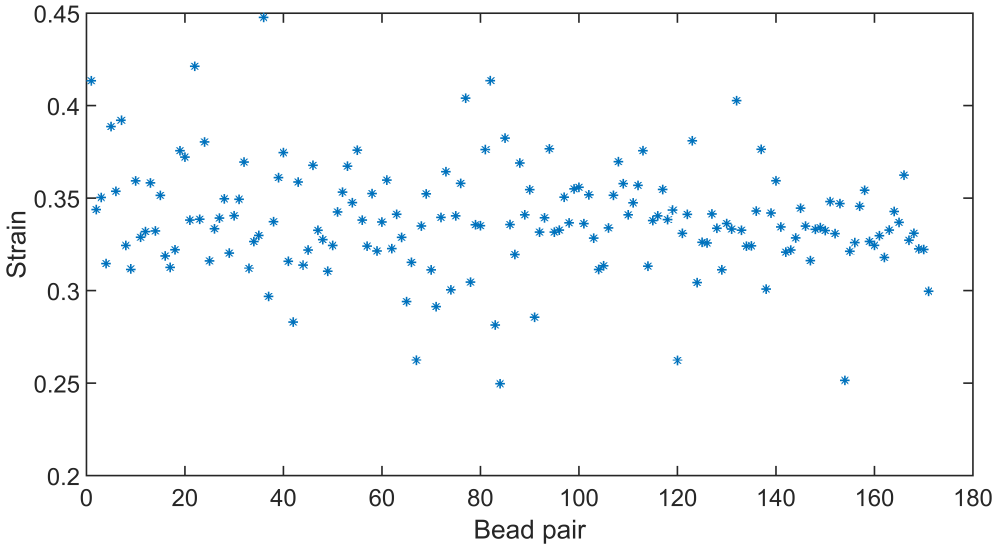


Figure 6.2: Graph depicting strain measurements of the PDMS substrate obtained using multiple bead pairs as positional reference markers in indenter-based stretching. Strain was calculated from the relative change in inter-bead distances measured before and after stretching, providing an estimate of the substrate strain applied during experiments.

6.4 Immunostaining and super-resolution imaging protocol

Neurons cultured on PDMS substrates (see Appendix D for PDMS functionalization protocols and Appendix A for neuronal cell culture procedures) were fixed using 1 ml of 4% (v/v) paraformaldehyde (PFA) prepared in 1× PHEM/PBS for 10 minutes at room temperature. Following fixation, excess fixative was removed by three washes with 1 ml of PHEM/PBS, each lasting 5 minutes. Unless otherwise stated, all subsequent washing steps were performed 3–4 times with 1 ml of PHEM/PBS, with each wash lasting approximately 5 minutes.

To permeabilize the cells, samples were incubated with 1 ml of 0.1% Triton X-100 (v/v) in PHEM/PBS for 5 minutes at room temperature, followed by thorough washing with PHEM/PBS to remove residual detergent. Blocking was performed by incubating samples in 1 ml of 3% (w/v) bovine serum albumin (BSA) in PHEM/PBS for 1 hour at room temperature to minimize nonspecific antibody binding.

For primary labeling, cells were incubated with 500 μl of anti-βII spectrin mouse monoclonal antibody (BD Biosciences, 612563), diluted 1:700 in blocking buffer, for 3 hours at 37 °C. After washing to remove unbound antibody, samples were incubated with 500 μl of Alexa Fluor 488–conjugated anti-mouse secondary antibody (Invitrogen, A-11001), diluted 1:500 in 3% BSA, for 1 hour at room temperature, followed by additional washes in PHEM/PBS.

After the final wash, buffer was removed and a drop of ProLong^{TM} Glass Antifade Mountant (Thermo Fisher, P36982) was applied directly to the sample. A 1.5 mm thick square coverslip (Corning, 2870-18) was carefully placed on top, and samples were allowed to cure at room temperature for 24 hours prior to imaging.

Super-resolution imaging was performed at IISER Pune, imaging facility on a Leica TCS SP8 STED 3× system (Leica Microsystems). Because optical imaging

through the PDMS substrate is not feasible due to working-distance constraints and optical aberrations introduced by the PDMS thickness, the stretching device was inverted and mounted onto a custom stage adaptor, allowing imaging from the coverslip side. Samples were imaged using an HC PL APO CS2 100×/1.4 NA STED oil immersion objective in both confocal and STED modes. Image acquisition was performed with 16× line averaging and time-gated detection enabled on a Leica Hybrid Detector (HyD), using a gating window of 0.3–8 ns to reduce background fluorescence. A 6× digital zoom was applied, resulting in a final pixel size of approximately 20 nm. Fluorescence depletion was achieved using a 592 nm STED laser, and all imaging parameters were kept constant across experiments. Raw image stacks were subsequently deconvolved using Huygens Professional software to enhance signal-to-noise ratio prior to quantitative analysis. A representative STED image of β-II spectrin in unstretched axons cultured on PDMS substrates is shown in Figure 6.3.

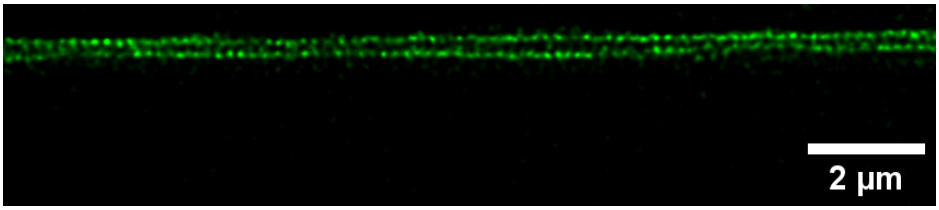


Figure 6.3: Representative STED image of βII-spectrin in control axons cultured on PDMS substrates.

6.5 Assessment of MPS spacing reproducibility

To quantify MPS spacing, a line was drawn along one edge of the axon in the STED images, and the corresponding fluorescence intensity profile was extracted (Figure 6.4). Only the axonal region that remained in focus within the field of view was used for analysis, generally corresponding to the imaged axonal segment and not exceeding 20 μm in length. Here, MPS spacing refers to the axial distance between successive repeats of the MPS pattern along the axon. The fluorescence intensity profiles were analyzed in MATLAB to identify spectrin-

ring peak positions using a custom MATLAB (2023b) script. The separation between consecutive peaks was then calculated to obtain peak-to-peak distance.

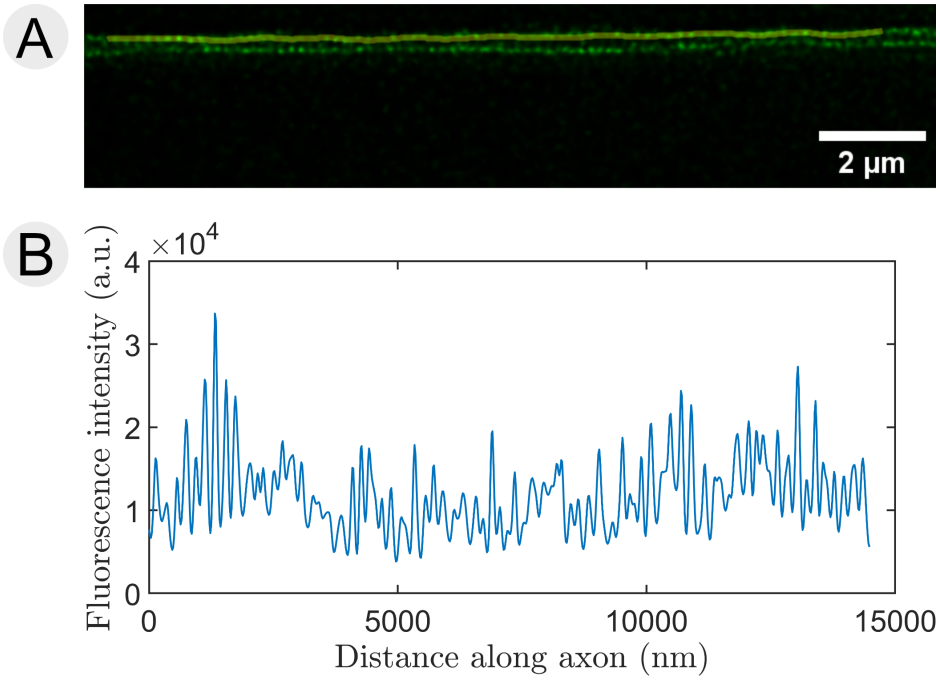


Figure 6.4: **(A)** Super-resolution (STED) image of βII-spectrin in an unstretched 4 DIV axon. A line was drawn along one edge of the axon over the region that remained in focus within the field of view for quantitative analysis. **(B)** Corresponding fluorescence intensity profile extracted from the line in (A), used for spectrin peak detection and spacing analysis.

To assess reproducibility across independent neuronal cultures, MPS spacing was compared between two control datasets obtained from unstretched axons. Peak-to-peak spacing distributions from both control sets exhibited comparable mean values (Figure 6.5), suggesting that MPS spacing values were similar across independent neuronal cultures and imaging sessions. The similarity between control datasets indicates reproducibility of the measured MPS spacing across independent experiments. While peak-to-peak analysis captures local spacing variations along individual axons, it is sensitive to local irregularities. Autocorrelation analysis was therefore employed to quantify changes in MPS periodicity between unstretched and stretched conditions.

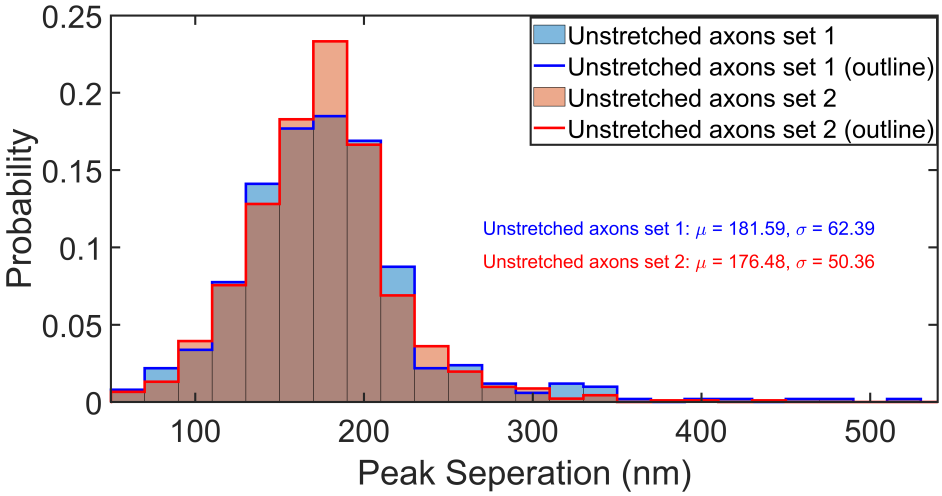


Figure 6.5: Comparison of MPS spacing distributions in two independent control datasets. Histograms show MPS spacing measured from unstretched axons cultured and imaged in independent experiments (dataset 1: $n = 7$ axons, outlined in blue; dataset 2: $n = 11$ axons, outlined in red). The substantial overlap between the two distributions, together with their comparable mean spacing, indicates reproducibility of MPS spacing measurements across independent culture preparations and imaging sessions, suggesting minimal day-to-day variability under control conditions.

6.6 Quantitative analysis of MPS periodicity in control and stretched axons

To qualitatively assess the effect of mechanical stretch on the MPS organization, STED images were also acquired from stretched axons. In these experiments, axons were stretched to approximately 35% strain over the course of about one minute. The periodic βII spectrin pattern remained visible along stretched axons as shown in Figure 6.6.

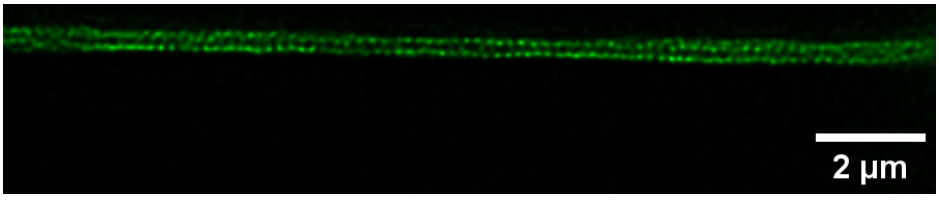


Figure 6.6: Representative STED image of βII-spectrin in stretched axons cultured on PDMS substrates.

For autocorrelation analysis, fluorescence intensity profiles were extracted from multiple 1 µm-long segments along one edge of each axon. For both unstretched and stretched conditions, these intensity profiles were used to compute the one-dimensional autocorrelation function for each segment, providing a measure of repeating periodic patterns within the MPS (Figure 6.7A). The observation of clear autocorrelation peaks suggests the presence of an underlying periodic organization in stretched axons, consistent with the qualitative features observed in the STED images.

From each autocorrelation curve, the position of the first correlation peak was identified and taken as the characteristic periodic spacing for that segment. Periodicity values obtained from multiple segments were then compiled to generate the overall distribution of MPS spacing for both unstretched and stretched axons (Figure 6.7B). Autocorrelation analysis revealed a shift in the MPS periodicity distribution between unstretched and stretched axons, indicating an increase in the characteristic spacing following mechanical stretch. However, the shift in periodicity was modest: the mean increase was roughly 10%, substantially smaller than the 35% substrate strain applied to the PDMS.

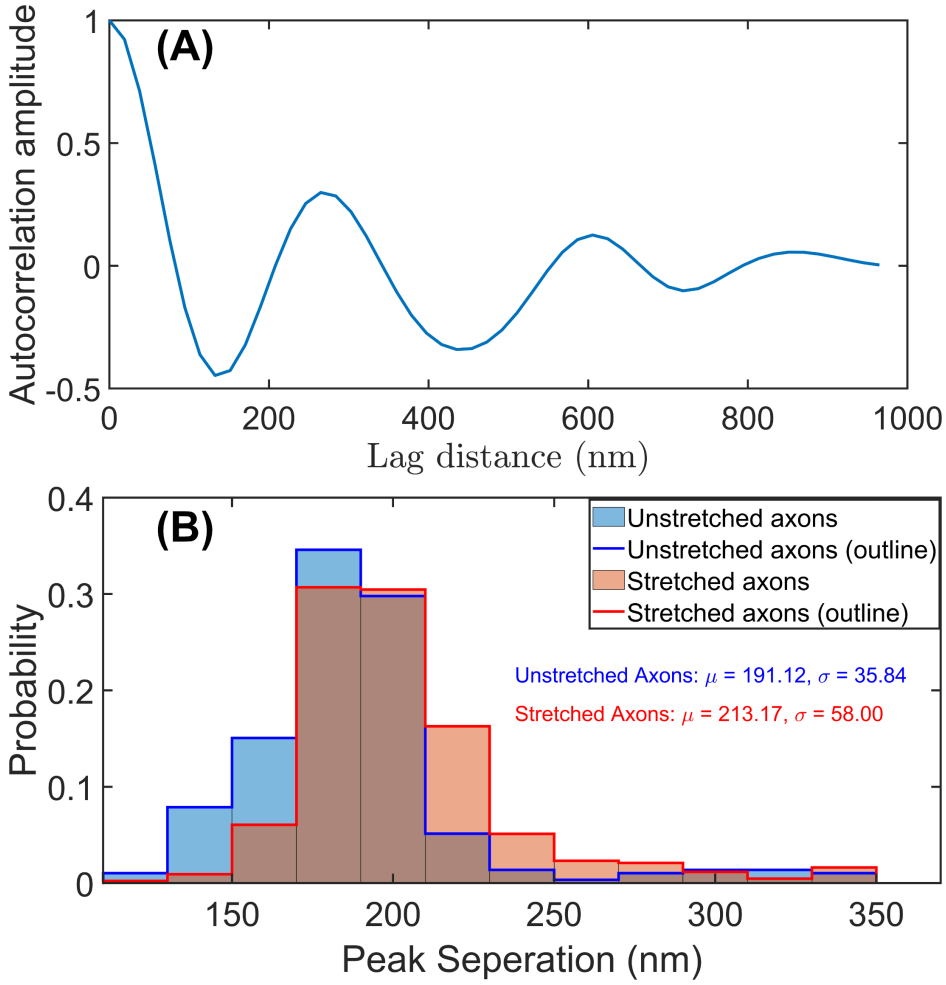


Figure 6.7: Comparison of MPS periodicity using autocorrelation analysis. **(A)** Representative autocorrelation curves illustrate the periodic nature of the MPS. Although multiple peaks reflect repeated periodic organization, the position of the first peak was used as a measure of the characteristic MPS periodicity. **(B)** The summary plot compares the periodicity values for control (outlined in blue. $n = 301$ segments from 23 axons) and stretched (outlined in red. $n = 430$ segments from 29 axons) conditions. Although increase in periodic spacing was observed following mechanical stretch, the magnitude of change (~10%) was notably smaller than the applied substrate strain (~35%).

6.7 Discrepancy between applied strain and MPS periodicity change

Despite evidence that axons experienced mechanical stretch, the periodicity of the MPS increased only modestly (~ 10%) compared to the applied strain on

the PDMS substrate (~ 35%). Notably, this increase was substantially smaller even than the lowest substrate strains measured in our experiments (~ 25%), indicating that the limited change in periodicity cannot be explained by variability in applied strain. This discrepancy suggests that the structural response of the MPS does not directly scale with substrate deformation, motivating further investigation into the underlying mechanisms. It should also be noted that the exact strain experienced by individual axons may differ from the macroscopic substrate strain due to local variations in adhesion, introducing uncertainty in the effective mechanical load at the cellular level. This mismatch motivated us to verify whether axons indeed experienced tensile deformation during PDMS stretching, rather than detaching or slipping on the substrate.

6.8 Confirming axonal stretch following PDMS stretching

Direct live imaging of axonal deformation during stretching is limited at high magnification due to constraints imposed by the stretching device geometry. To assess whether axons were mechanically deformed under substrate stretch and remained attached to the PDMS during stretching and fixation, neurons cultured on PDMS membranes were stretched and fixed while the substrate was held in the deformed state. Following fixation, the indenter was removed, releasing the applied deformation and allowing the PDMS substrate to relax.

Upon release, axons exhibited pronounced and persistent buckling (Figure 6.8). This behavior indicates that axons underwent elongation during substrate stretching and that this deformation was retained during fixation. The resulting permanent buckling upon release reflects a loss of viscoelastic behavior after chemical fixation, which increases the rigidity of the axonal cytoskeleton and prevents recovery to the pre-stretch configuration. While these observations suggest effective mechanical coupling between axons and the substrate, partial decoupling cannot

be excluded.

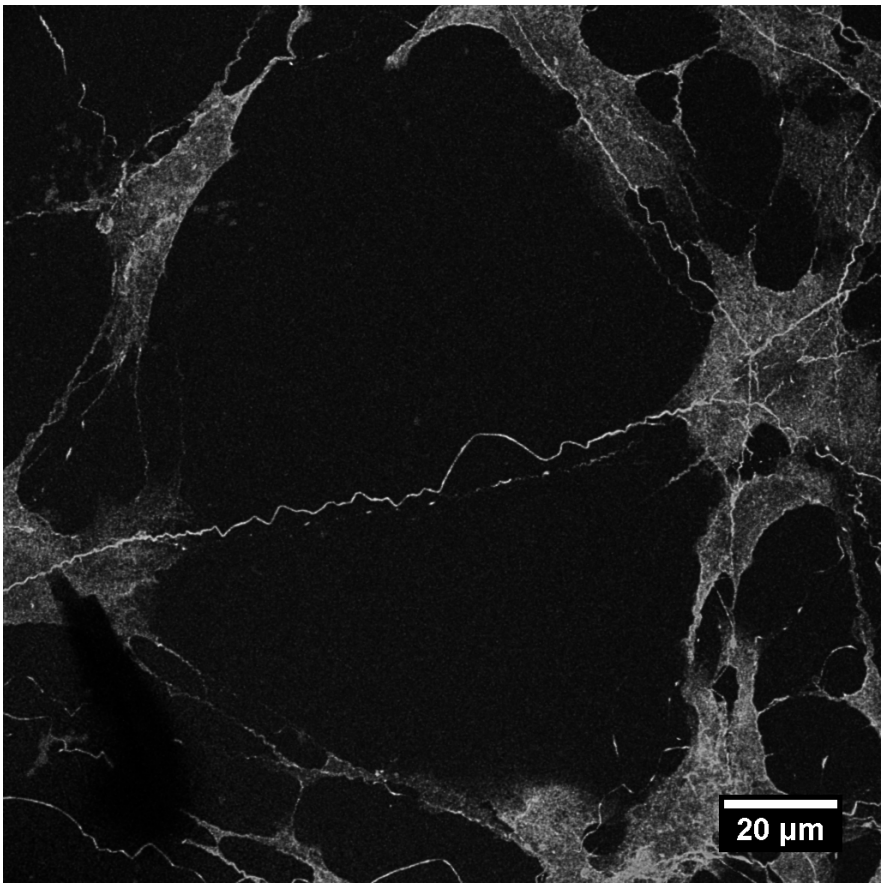


Figure 6.8: Axonal buckling following stretch–fix–release. Confocal image of neurons cultured on PDMS membranes stretched and fixed in the stretched state. Release of the substrate stretch induces pronounced axonal buckling, indicating retention of stretch-induced deformation after fixation.

6.9 Possible influence of axonal curvature on the observed periodicity shift

One possible factor contributing to the smaller-than-expected increase in MPS periodicity can be the initial curvature of axons prior to stretching. In many cultures, axons exhibited a curved geometry, as observed in low-magnification (10×) phase-contrast images acquired after removing the PDMS membrane from the stretching device and imaging it (Figure 6.9). Although changes in axonal curvature during stretching were not directly quantified, it is conceivable that a

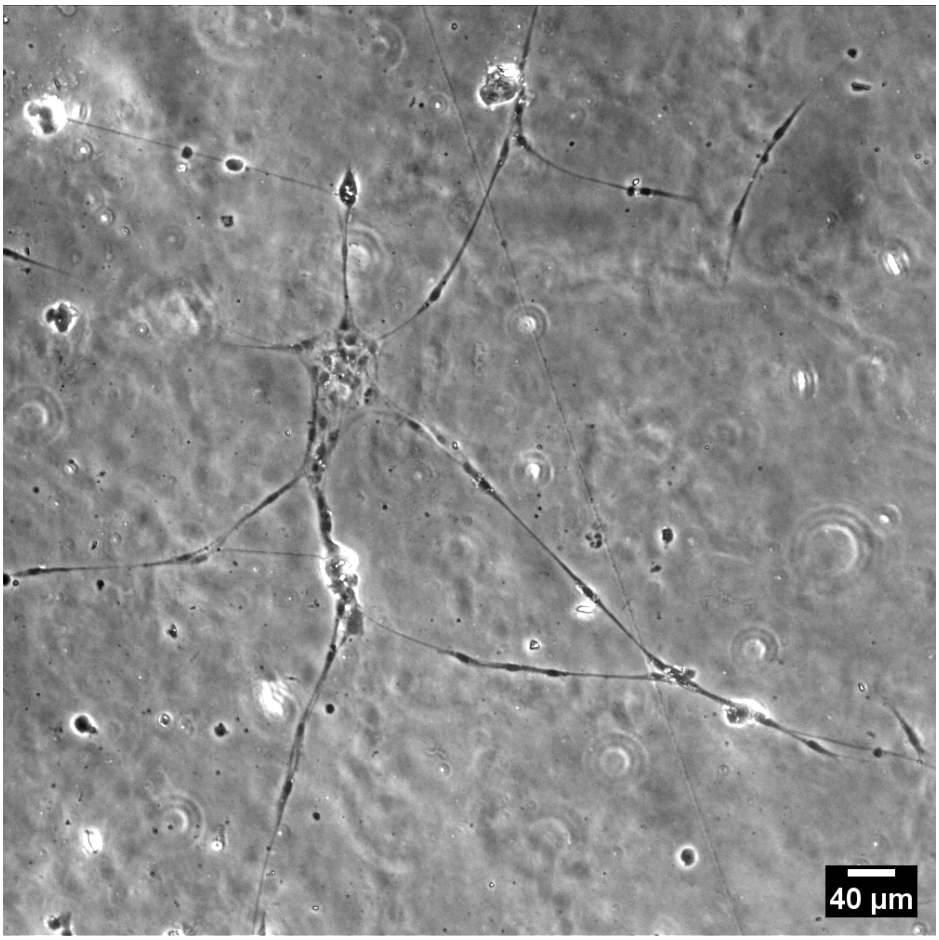


Figure 6.9: Phase-contrast image showing curved axons on the PDMS substrate. Although curvature changes during stretch were not directly measured, such geometries could potentially straighten under applied tension, thereby reducing the effective strain transmitted to the axonal cytoskeleton.

portion of the applied strain may be accommodated by geometric straightening of axons rather than by elongation along their length. A schematic illustrating such curvature-driven strain accommodation is shown in Figure 6.10. If adhesions along the axon partially detach or slide during deformation, curved axons may reorient and straighten before experiencing significant tensile strain. This effect could reduce the effective strain transmitted to the underlying cytoskeletal lattice and may therefore contribute to the modest shift in MPS periodicity observed under stretched conditions. Future studies assessing axonal geometry dynamically during stretch will be important to determine the extent to which curvature-dependent strain accommodation contributes to the observed MPS periodicity

changes, while acknowledging that additional mechanisms may also be involved.

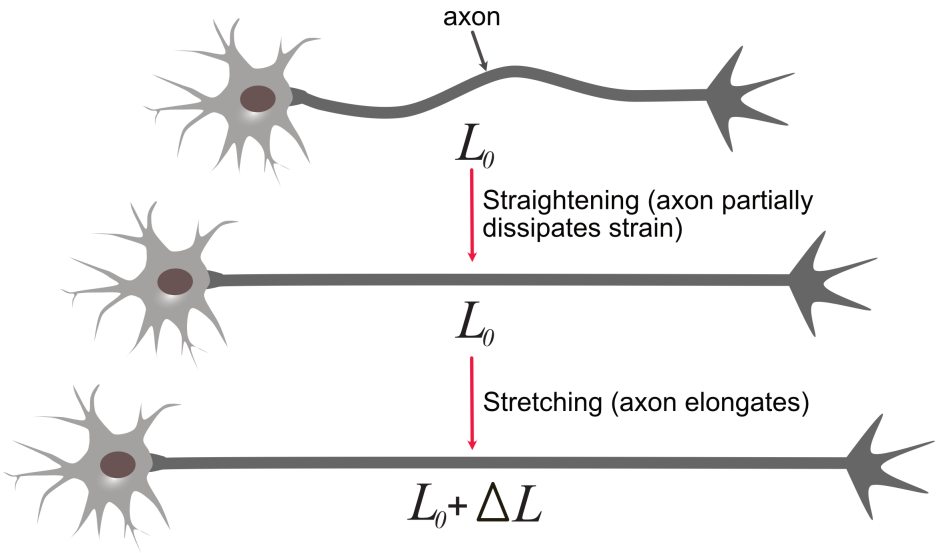


Figure 6.10: Schematic of axonal response to PDMS stretch (top to bottom). Initially curved axons with contour length L_0 straighten as the substrate is stretched, allowing part of the applied strain to be absorbed geometrically. Upon further stretching, axons elongate as strain is transferred to them.

6.10 Conclusion

In this chapter, we examined how the axonal membrane-associated periodic skeleton responds to externally applied mechanical stretch. Super-resolution imaging revealed a reproducible but modest increase in actin–spectrin periodicity following stretching, substantially smaller than the macroscopic strain applied to the PDMS substrate. These findings indicate that MPS deformation does not scale directly with substrate strain, suggesting that additional factors—such as axonal geometry and strain accommodation mechanisms—modulate how mechanical loads are transmitted to the cytoskeletal lattice.

Chapter 7

Summary and future directions

7.1 Overview of the Chapter

The preceding chapters described the development of custom experimental tools, a systematic investigation of axonal mechanics, theoretical modeling, and high-resolution imaging. This final chapter highlights the key findings, methodological innovations, and theoretical contributions of the thesis. It also discusses the broader implications of these results for understanding axonal mechanics and cytoskeletal dynamics, and outlines potential directions for future research in this area.

7.2 Key findings and contributions

The application of the MER in this thesis enabled several novel insights into axonal mechanics. Our experimental results showed that axons exhibit viscoelastic strain relaxation, with the relaxation rate dependent on the duration of applied stretch as well as actin and microtubule stability. Holding axons under stretch for extended periods before release led to slower relaxation and more pronounced buckling, indicating time-dependent cytoskeletal rearrangements. Pharmacological perturbations further highlighted the distinct roles of cytoskeletal components:

microtubule stabilization slowed strain relaxation and increased buckling wavelengths, whereas microtubule and actin destabilization also altered relaxation rates, demonstrating that axonal mechanical behavior exhibits specific dependencies on the microtubule bundle and the actin–spectrin scaffold, which appear to dominate under the mechanical conditions examined here.

To complement these experimental insights, mechanical modeling was developed to capture the key features of axonal responses. Initial viscoelastic models combined Kelvin-Voigt and Maxwell elements in parallel, followed by Zener and Maxwell elements, also arranged in parallel, providing a simplified understanding of strain relaxation. The latter model accounted for the cytoskeleton-dependent changes in relaxation times, capturing the effects of microtubule and actin perturbations observed experimentally.

Furthermore, modeling the microtubule bundle as a Maxwell-like viscoelastic core elastically coupled to the surrounding cortex explains the emergence of short-wavelength buckling and the progression of wavelengths as tension decreases (analogous to increasing time), but it fails to account for the increased buckling wavelengths observed after microtubule stabilization. This limitation is resolved by incorporating viscoelastic coupling between the microtubule core and the outer cortex.

Finally, structural studies using a home-built stretcher combined with STED nanoscopy revealed stretch-induced remodeling of the membrane-associated cytoskeleton. Although changes in periodicity were smaller than the applied PDMS stretch, they were nonetheless measurable, demonstrating that molecular-scale rearrangements accompany and likely contribute to the mechanical responses observed at the axonal level.

Overall, this thesis provides a multiscale understanding of axonal mechanics, combining experimental measurements with modeling and structural investigations. The findings highlight the interplay between cytoskeletal organization, axonal geometry, and mechanical forces, offering insights relevant to neuronal mechanobi-

ology. These findings provide a basis for the future directions discussed in the following section and may inform additional lines of inquiry.

7.3 Future direction

7.3.1 Rate-dependent axonal mechanics using linear loading-unloading protocols

A ramp protocol represents a promising future direction for probing strain rate– and amplitude-dependent axonal mechanics. Such protocols can be extended to systematic loading–unloading cycles, from which energy dissipation can be quantified through force–strain hysteresis. An example of this approach is shown in Figure 7.1, where an axon subjected to cyclic strain exhibits hysteresis in the tension–strain response. In this experiment, the axon was initially pre-stretched by 2% to prevent slackening, followed by cyclic loading with a strain amplitude of 6% at a frequency of 0.01 Hz. Repeated cycling is seemed to lead to convergence toward a stable force–strain response, enabling robust characterization of hysteresis and dissipative behavior. Systematic variation of the loading rate and amplitude would further provide insight of the axonal mechanical responses.

7.3.2 Axonal mechanics at physiological temperature

All experiments in this work were performed at room temperature, where the activity of molecular motors and other polymerization-depolymerization processes are reduced. Extending these measurements to physiological temperature (~37°C) represents an important future direction, as active processes are expected to contribute to axonal mechanical responses. Comparing axonal mechanics at room and physiological temperatures may therefore reveal additional active contributions to force generation, relaxation, and dissipation that are not captured under current experimental conditions.

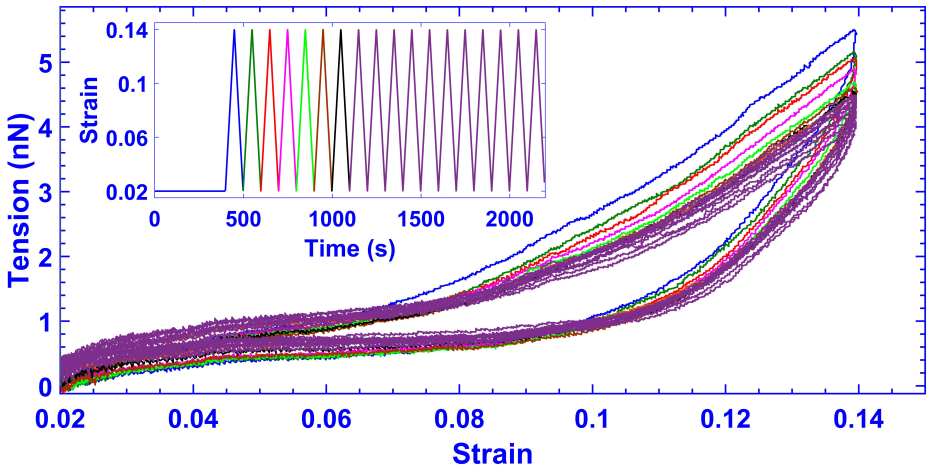


Figure 7.1: Response of an axon to cyclic strain. The inset shows the imposed cyclic strain applied to an axon. The axon was initially stretched to a pre-strain of 2% to avoid slackening of the axon during cycles. The strain amplitude was 6% and cycle frequency was 0.01 Hz. The main plot shows the hysteresis loops for tension vs. strain obtained using this cyclic strain protocol.

7.3.3 Extensions of viscoelastic models

The viscoelastic models developed in this work treat the axon as a parallel combination of solid- and fluid-like elements with linear, strain-independent material parameters. While this framework captures key features of axonal strain relaxation, experimental observations indicate that axons exhibit viscoelastic strain-softening behavior [12]. Such nonlinearity has been attributed to spectrin folding–unfolding dynamics within the membrane-associated periodic skeleton (MPS). In addition, unbinding and rebinding of microtubule cross-linkers, which are influenced by the applied force, may further contribute to the nonlinear mechanical response. Incorporating these mechanisms into future models would enable a more realistic description of axonal mechanics.

7.3.4 Structural dynamics of the axonal cytoskeleton during stretching

An important future direction is to investigate the structural dynamics of the axonal cytoskeleton during mechanical stretching in greater detail. In particu-

lar, further studies of MPS are needed to address several open questions raised in Chapter 6 regarding its reorganization. In parallel, exploring the role of microtubule sliding and rearrangement during stretching may provide additional insight into how axons accommodate large deformations while maintaining structural integrity. Combining mechanical measurements with high-resolution imaging will be essential for elucidating the coupled dynamics of these cytoskeletal components.

Beyond these structural considerations, several open questions remain regarding the molecular contributors to axonal mechanical behavior during stretching. Future studies could examine the relative roles of microtubule cross-linkers, including passive cross-linkers such as tau proteins and active cross-linkers such as molecular motors. In addition, investigating axonal mechanics in spectrin-deficient cell lines, such as spectrin knockout models derived from SH-SY5Y cells, may help clarify the specific contribution of the spectrin-based cytoskeleton to mechanical stability and strain accommodation.

A DRG neuronal culture

- Fertilised Giriraja-2 chicken eggs were procured from the Karnataka Veterinary, Animal and Fisheries Sciences University, Bangalore, India.
- Eggs were incubated for 8–9 days to allow embryonic development.
- Dorsal Root Ganglia (DRG) were isolated and dissociated following a standard protocol.
- Dissociated cells were plated on thoroughly cleaned glass coverslips. A hole was drilled in the bottom of the Petri plates, and the coverslip was affixed on the underside to cover the opening, then thoroughly cleaned before use.
- Cells were cultured in L-15 medium (21083–027, Thermo Fisher Scientific) thickened with 0.006 g/ml methyl cellulose (34516, ColorconID) and supplemented with the following:
  - 10% Fetal Bovine Serum (10100–147, Thermo Fisher Scientific),
  - 2% D-glucose (G6152, Sigma-Aldrich),
  - 20 ng/ml Nerve Growth Factor NGF-7S (13290–010, Thermo Fisher Scientific),
  - 0.5 mg/ml Penicillin-Streptomycin-Glutamine (100×) (10378–016, Thermo Fisher Scientific).
- Cells were grown at 37°C for 4 DIV before the experiments.
- Prior to force measurement experiments, neurons were transferred to supplemented L-15 medium without methyl cellulose and incubated for 30 minutes.

B Contour length analysis in stretch and release experiments

To quantify axonal strain relaxation and buckling response, we tracked the contour length of individual axons from the acquired image sequences. The analysis was performed after the experiments, using images obtained during the stretch and release protocols. In most cases, phase-contrast imaging was used, where slight defocusing rendered axons brighter than the background; in some experiments, differential interference contrast (DIC) images were also acquired. For this purpose, the contour length was measured with a custom-written MATLAB program (The MathWorks, Natick, MA). In the image just before release, three points were selected: the left end of the axon, the cantilever tip (at the midpoint where the axon was pulled), and the right end of the axon. The maximum applied strain was determined from this image. Immediately after release, the axon, along with its ends, was tracked between the left and right points. Before tracking, images were rotated such that the line joining the axonal endpoints was approximately aligned with the x-axis. For each column, the vertical intensity profile was evaluated only within a local window $(y - w : y + w)$ around the current estimated axonal position, rather than over the full image height. This restricted search window ensured that the centroid determination remained robust and computationally efficient, and prevented interference from other cellular structures or background features present in the field of view. To enhance the accuracy of centroid determination, the image intensity was first converted to double precision and then raised to a power N $(10 \leq N \leq 250)$. This nonlinear transformation effectively suppresses background noise while amplifying the contribution of the brightest pixels along the axon. As a result, the computed intensity-weighted centroid is more robust against noise and better aligned with the true axonal profile. After that corresponding y-position was determined using

an intensity-weighted centroid:

$$\bar{y} = \frac{\sum_i I_i^N y_i}{\sum_i I_i^N},$$

Here, $\bar{y}$ denotes the intensity-weighted centroid of the values y_i, where y_i are the pixel positions and I_i^N represents the weight assigned to each pixel, with I_i being the image intensity and N a chosen exponent that enhances contrast. The numerator $\sum_i I_i^N y_i$ computes the total contribution of all pixel positions scaled by their weighted intensities, while the denominator $\sum_i I_i^N$ normalizes the result by the sum of the weights, ensuring that the centroid is properly scaled. In the next step, the centroid calculated for the current column is used as a reference y-coordinate to define a local window for the next column, from which the intensity profile is extracted again and a new centroid is computed. This procedure is repeated sequentially between the two endpoints of the axon, allowing the full contour of the axon to be reconstructed. This process was automated and repeated across all frames. The resulting y-values were first saved as matrices in a text file and then passed through a running average filter to reduce noise and improve the accuracy of contour detection. After obtaining the filtered y-values, the contour length was calculated by summing the lengths of line segments between consecutive points using the discrete Euclidean distance formula:

$$L = \sum_{i=1}^{n-1} \sqrt{(x_{i+1} - x_i)^2 + (y_{i+1} - y_i)^2},$$

where (x_i, y_i) and (x_{i+1}, y_{i+1}) are the coordinates of consecutive points along the axonal segment.

C PDMS sheet preparation protocol

- The required volumes of base elastomer and curing agent were calculated using a 10:1 (w/w) ratio, in amounts sufficient to form a ~1 mm thick sheet

in an 8–8.5 cm diameter petri dish.

- The measured base and curing agent were transferred into a 50 ml Falcon tube.
- The components were mixed thoroughly by hand or using a vortex mixer for approximately 10 minutes to ensure uniformity.
- The mixed PDMS was poured into the prepared petri dish.
- The dish was placed in a desiccator and vacuum was applied for 30 minutes to remove entrapped air bubbles.
- To ensure uniform thickness, the petri dish was placed on a levelled stand inside an oven; a spirit level was used to verify that the setup was even.
- The PDMS was cured at 80°C for 2 hours. The curing time was not exceeded to avoid over-curing.
- Proper curing was confirmed by gently touching the edge of the sheet; the cured PDMS felt solid and non-tacky.
- After curing, the PDMS sheet was allowed to rest overnight at room temperature to ensure complete cross-linking and mechanical stability.

D Chemical oxidation of PDMS sheet

- Performed all steps in a chemical fume hood to ensure safety during handling of hazardous reagents.
- **Device cleaning**:
  - The device was cleaned thoroughly with 70% ethanol.
  - The device was then exposed to UV light for at least two cycles for sterilization.
- **PDMS attachment**:

  - The PDMS sheet was secured onto the device.
  - Vacuum grease was applied along the PDMS edges to ensure a tight seal.
  - A white cylinder was placed over the culture chamber on the PDMS and sealed with vacuum grease.

- **Surface oxidation**:
  - A solution with a 5:1:1 volume ratio of H_2O : H_2O_2 : 30 N HCl was prepared.
  - This solution was applied to the PDMS surface until bubbling was observed.
  - The surface was then rinsed twice with deionized water.

- **Silane functionalization**:
  - The surface was treated with 10% APTES in acetone for 10 minutes at room temperature.
  - The surface was rinsed twice with water.

- **Crosslinking treatment**:
  - A 0.01% glutaraldehyde solution in water was applied for 4–5 minutes.
  - The surface was rinsed five times with water.

- **Blocking step**:
  - The surface was incubated with 0.1 M glycine for 10 minutes.

- **Surface coating**:
  - Poly-D-lysine (1 mg/mL) was added and incubated for 2 hours at 37°C.
  - The surface was washed three times with PBS.
  - Laminin (5–10 μg/mL) was added and incubated for 2 hours at 37°C.

E Kelvin–Voigt and Maxwell models in parallel

E.1 Derivation of the differential equation for the parallel combination of Kelvin–Voigt and Maxwell model

The Kelvin-Voigt model consists of a spring and dashpot connected in parallel. The total stress is the sum of the elastic and viscous stresses, while the strain is the same across both elements. The constitutive relation is given by:

$$\sigma_k = E_k \gamma + \eta_k \dot{\gamma} \tag{1}$$

where σ_k is the stress, γ is the strain, E_k is the elastic modulus, and η_k is the viscosity of the Kelvin-Voigt model. The Maxwell model features a spring and dashpot connected in series. In this configuration, the total strain is the sum of the strains in the spring and dashpot, and the stress is the same in both. The resulting differential equation is:

$$\frac{\dot{\sigma_m}}{E_m} + \frac{\sigma}{\eta_m} = \dot{\gamma} \tag{2}$$

Here again, E_m is the elastic modulus, and η_m is the viscosity of the Maxwell model. Writing σ_m from equation (2) in the operator form

$$\sigma_m = \frac{\frac{d\gamma}{dt}}{\frac{1}{E_m}\frac{d}{dt} + \frac{1}{\eta_m}} \tag{3}$$

In a parallel combination of the Kelvin-Voigt and Maxwell models, the total stress is the sum of the stresses in both components:

$$\sigma = \sigma_k + \sigma_m \tag{4}$$

Substituting equations (1) and (3) into equation (4) yields the following differential equation:

$$\sigma + \frac{\eta_m}{E_m}\dot{\sigma} = E_k\gamma + \left(\eta_k + \eta_m + \frac{\eta_m E_k}{E_m}\right)\dot{\gamma} + \frac{\eta_k\eta_m}{E_m}\ddot{\gamma} \tag{5}$$

This is the constitutive differential equation for the combined Kelvin–Voigt and Maxwell viscoelastic model used in this study.

E.2 Analytical solution for the step-stress and release protocol in a parallel combination of the Kelvin–Voigt and Maxwell models

Starting from equation (4.12) in chapter 3,

$$(H(t) + A\delta(t))\sigma_0 = E_k\gamma + B\dot{\gamma} + C\ddot{\gamma} \tag{6}$$

Before stress is applied, the model is considered to be in a stress-free and strain-free state, with initial conditions set to zero (i.e., $\gamma(t) = 0$ and $\sigma(t) = 0$ for $t = 0$). Applying the unilateral Laplace transform to equation (6), we obtain

$$\mathcal{L}\{(H(t) + A\delta(t))\sigma_0 = E_k\gamma + B\dot{\gamma} + C\ddot{\gamma}\}.$$

Using the standard Laplace transform identities $\mathcal{L}\{H(t)\} = \frac{1}{s}$, $\mathcal{L}\{\delta(t)\} = 1$, $\mathcal{L}\{\dot{\delta}(t)\} = s$, and, with zero initial conditions, $\mathcal{L}\{\dot{\gamma}(t)\} = s\Gamma(s)$, $\mathcal{L}\{\ddot{\gamma}(t)\} = s^2\Gamma(s)$, we take the Laplace transform of equation (4.12):

$$\mathcal{L}\{(H(t) + A\delta(t))\sigma_0\} = \mathcal{L}\{E_k\gamma + B\dot{\gamma} + C\ddot{\gamma}\},$$

which gives

$$\left(\frac{1}{s} + A\right)\sigma_0 = \left(E_k + Bs + Cs^2\right)\Gamma(s),$$

where $\Gamma(s) = \mathcal{L}\{\gamma(t)\}$. Rearranging the terms, we obtain

$$\Gamma(s) = \frac{\sigma_0}{C} \frac{1 + As}{s\left(s^2 + \frac{B}{C} + \frac{E_k}{C}\right)}.$$

The quadratic expression $s^2 + \frac{B}{C} + \frac{E_k}{C}$ can be factored as $(s - a_1)(s - a_2)$

$$s^2 + \frac{B}{C} + \frac{E_k}{C} = (s - a_1)(s - a_2),$$

where

$$a_{1,2} = -\frac{B}{2C} \pm \frac{1}{2}\sqrt{\left(\frac{B}{C}\right)^2 - \frac{4E_k}{C}},$$

which leads to

$$\Gamma(s) = \frac{\sigma_0}{C} \frac{1 + As}{s\,(s - a_1)(s - a_2)}.$$

Assume the decomposition

$$\frac{1 + As}{s\,(s - a_1)(s - a_2)} = \frac{D}{s} + \frac{E}{s - a_1} + \frac{F}{s - a_2}.$$

The residues (coefficients) are obtained by evaluating the original rational function at the poles

$$D = \left.\frac{1 + As}{(s - a_1)(s - a_2)}\right|_{s=0} = \frac{1}{(-a_1)(-a_2)} = \frac{1}{a_1 a_2},$$

$$E = \left.\frac{1 + As}{s(s - a_2)}\right|_{s=a_1} = \frac{1 + Aa_1}{a_1(a_1 - a_2)},$$

$$F = \left.\frac{1 + As}{s(s - a_1)}\right|_{s=a_2} = \frac{1 + Aa_2}{a_2(a_2 - a_1)}.$$

Hence

$$\Gamma(s) = \frac{\sigma_0}{C}\left(\frac{1}{a_1 a_2 s} + \frac{1 + Aa_1}{a_1(a_1 - a_2)}\frac{1}{s - a_1} + \frac{1 + Aa_2}{a_2(a_2 - a_1)}\frac{1}{s - a_2}\right).$$

Taking the inverse unilateral Laplace transform term by term, and using

$$\mathcal{L}^{-1}\left\{\frac{1}{s}\right\} = 1, \qquad \mathcal{L}^{-1}\left\{\frac{1}{s - a_i}\right\} = e^{a_i t}, \quad t > 0,$$

We obtain the expression for the strain in the time domain as follows:

$$\gamma(t) = \mathcal{L}^{-1}\{\Gamma(s)\} = \frac{\sigma_0}{C}\left(\frac{1}{a_1 a_2} + \frac{1 + Aa_1}{a_1(a_1 - a_2)}e^{a_1 t} + \frac{1 + Aa_2}{a_2(a_2 - a_1)}e^{a_2 t}\right).$$

Substituting the coefficients in terms of A, B, and C, the strain in the time domain can be expressed as

$$\gamma(t) \;=\; f_1 - f_2 e^{-t/\tau_s} - f_3 e^{-t/\tau_f}, \qquad t > 0,$$

with

$$f_1 = \frac{\sigma_0}{E_k},$$

$$f_2 = -\frac{\sigma_0}{\sqrt{B^2 - 4E_k c}}\left(\frac{2C}{-B + \sqrt{B^2 - 4E_k C}} + A\right),$$

$$f_3 = \frac{\sigma_0}{\sqrt{B^2 - 4E_k c}}\left(\frac{2C}{-B - \sqrt{B^2 - 4E_k C}} + A\right),$$

where f_1, f_2 and f_3 are constants determined from the equilibrium conditions and the time constants are defined by

$$\tau_{f,s} = \left(\frac{2C}{B \pm \sqrt{B^2 - 4E_k C}}\right) \tag{7}$$

where τ_f and τ_s denote the fast and slow relaxation times, respectively. For stress release at time $t = t_{\text{rel}}$ (after the system has reached equilibrium), the derivation proceeds analogously to the loading case. The main differences are:

- The applied stress is set to zero for $t \geq t_{\text{rel}}$, i.e. $\sigma(t) = 0$.

- The initial strain at $t = t_{\text{rel}}$ corresponds to the equilibrium value attained under the sustained load, namely $\gamma(t_{\text{rel}}) = \dfrac{\sigma_0}{E_k}$.

Following similar steps as in the loading case (without repeating the full derivation here), the strain during release can be written as

$$\gamma(t - t_{\text{rel}}) = f_2\, e^{a_1(t-t_{\text{rel}})} + f_3\, e^{a_2(t-t_{\text{rel}})}, \qquad t \geq t_{\text{rel}}, \tag{8}$$

where f_2 and f_3 are constants defined above. Combining the two cases, the complete strain response of the system is given by:

$$\gamma(t) = \begin{cases} f_1 - f_2 e^{-t/\tau_s} - f_3 e^{-t/\tau_f}, & t < t_{\text{rel}}, \\ f_2 e^{-(t-t_{\text{rel}})/\tau_s} + f_3 e^{-(t-t_{\text{rel}})/\tau_f}, & t \geq t_{\text{rel}}. \end{cases}$$

F A parallel combination of Zener and Maxwell models

F.1 Derivation of the differential equation for the parallel combination of Zener and Maxwell model

The Zener model, also known as the Standard Linear Solid model, consists of a Kelvin–Voigt model in series with a spring. The constitutive differential equation for the Zener model is:

$$\left(1 + \frac{E_{z2}}{E_{z1}}\right)\sigma_z + \frac{\eta_z}{E_{z1}}\dot{\sigma}_z = E_{z2}\gamma + \eta_z\dot{\gamma} \tag{9}$$

where σ_z is the stress, γ is the strain, E_{z1} is the elastic modulus of first spring (spring connected in series with the kelvin-voigt model), E_{z2} is the elastic modulus of second spring (the spring within the Kelvin–Voigt model), and η_z is the viscosity

of the Zener model. Writing σ_z from equation (9) in the operator form

$$\sigma_z = \frac{E_{z2}\gamma + \eta_z\dot{\gamma}}{\left(1 + \frac{E_{z2}}{E_{z1}}\right) + \frac{\eta_z}{E_{z1}}\frac{d}{dt}} \tag{10}$$

In a parallel combination of the Zener and Maxwell models, the total stress is the sum of the stresses in both components:

$$\sigma = \sigma_z + \sigma_m \tag{11}$$

By combining equations (3) and (10) with equation (11), and rearranging the terms, we obtain the following differential equation:

$$\left(1 + \frac{E_{z2}}{E_{z1}}\right)\sigma + \left(\frac{\eta_{z1}}{E_{z1}} + \left(1 + \frac{E_{z2}}{E_{z1}}\right)\frac{\eta_m}{E_m}\right)\dot{\sigma} + \frac{\eta_z\eta_m}{E_{z1}E_m}\ddot{\sigma}$$
$$= E_{z2}\gamma + \left(\eta_z + \left(1 + \frac{E_{z2}}{E_{z1}}\right)\eta_m + \frac{E_{z2}\eta_m}{E_m}\right)\dot{\gamma} + \left(\frac{\eta_z\eta_m}{E_{z1}} + \frac{\eta_z\eta_m}{E_m}\right)\ddot{\gamma} \tag{12}$$

This is the governing differential equation for the viscoelastic model used in this study, which combines the Zener and Maxwell elements in parallel configuration. Let $A = 1 + \frac{E_{z2}}{E_{z1}}$, B=$\frac{\eta_{z1}}{E_{z1}} + (1 + \frac{E_{z2}}{E_{z1}})\frac{\eta_m}{E_m}$, C=$\frac{\eta_z\eta_m}{E_{z1}E_m}$, D=$\eta_z + \left(1 + \frac{E_{z2}}{E_{z1}}\right)\eta_m + \frac{E_{z2}\eta_m}{E_m}$ and $E = \frac{\eta_z\eta_m}{E_{z1}} + \frac{\eta_z\eta_m}{E_m}$ then equation (15) can be written as

$$A\sigma + B\dot{\sigma} + C\ddot{\sigma} = E_{z2}\gamma + D\dot{\gamma} + E\ddot{\gamma} \tag{13}$$

F.2 Analytical solution for step-stress and release in a parallel combination of Zener and Maxwell models

Starting from equation(4.12) in Chapter 3,

$$(AH(t) + B\delta(t) + C\dot{\delta}(t))\sigma_0 = E_{z2}\gamma + D\dot{\gamma} + E\ddot{\gamma} \tag{14}$$

Prior to stress application, the axon is assumed to be unstressed and unstrained, so that all initial conditions are taken as zero (with $\gamma(t) = 0$ and $\sigma = 0$ for $t < 0$). By taking the unilateral Laplace transform of equation (14):

$$\mathcal{L}\{(AH(t) + B\delta(t) + C\dot{\delta}(t))\sigma_0\} = \mathcal{L}\{E_{z2}\gamma + D\dot{\gamma} + E\ddot{\gamma}\}.$$

Using $\mathcal{L}\{H(t)\} = 1/s$, $\mathcal{L}\{\delta(t)\} = 1$, $\mathcal{L}\{\dot{\delta}(t)\} = s$ and (with zero initial conditions) $\mathcal{L}\{\dot{\gamma}\} = s\Gamma(s)$, $\mathcal{L}\{\ddot{\gamma}\} = s^2\Gamma(s)$, we obtain

$$\sigma_0\left(\frac{A}{s} + B + Cs\right) = \Gamma(s)\,(E_{z2} + Ds + Es^2).$$

Thus,

$$\Gamma(s) = \frac{\sigma_0\left(\frac{A}{s} + B + Cs\right)}{Es^2 + Ds + E_{z_2}} = \frac{\sigma_0}{E}\,\frac{\frac{A}{s} + B + Cs}{s^2 + \frac{D}{E}s + \frac{E_{z2}}{E}}.$$

where $\Gamma(s) = \mathcal{L}\{\gamma(t)\}$. After rearranging, we obtain

$$\Gamma(s) = \frac{\sigma_0}{E}\,\frac{A + Bs + Cs^2}{s(s^2 + \frac{D}{E}\,s + \frac{E_{z2}}{E})}.$$

Let a_1, a_2 be the (generally complex) roots of the quadratic

$$s^2 + \frac{D}{E}\,s + \frac{E_{z2}}{E} = 0,$$

so that

$$s^2 + \frac{D}{E}\,s + \frac{E_{z2}}{E} = 0, = (s - a_1)(s - a_2),$$

The roots are given explicitly by

$$a_{1,2} = -\frac{D}{2E} \;\pm\; \frac{1}{2}\sqrt{\left(\frac{D}{E}\right)^2 - \frac{4E_{z2}}{E}}.$$

Write the partial fraction as

$$\Gamma(s) = \frac{\sigma_0}{E}\left[\frac{K}{s} + \frac{M}{s-a_1} + \frac{N}{s-a_2}\right],$$

which, after matching coefficients, gives

$$K = \frac{A}{a_1 a_2}, \qquad M = \frac{A + B\,a_1 + C\,a_1^2}{a_1(a_1 - a_2)}, \qquad N = \frac{A + B\,a_2 + C\,a_2^2}{a_2(a_2 - a_1)}.$$

Hence

$$\boxed{\Gamma(s) = \frac{\sigma_0}{E}\left[\frac{A}{a_1 a_2}\frac{1}{s} + \frac{A + Ba_1 + Ca_1^2}{a_1(a_1 - a_2)}\,\frac{1}{s-a_1} + \frac{A + Ba_2 + Ca_2^2}{a_2(a_2 - a_1)}\,\frac{1}{s-a_2}\right].}$$

Taking the inverse unilateral Laplace transform termwise, and using $\mathcal{L}^{-1}\{1/s\} = 1$ and $\mathcal{L}^{-1}\{1/(s-a_i)\} = e^{a_i t}$ for $t > 0$, we obtain the time-domain strain

$$\boxed{\gamma(t) = \frac{\sigma_0}{E}\left[\frac{A}{a_1 a_2} + \frac{A + Ba_1 + Ca_1^2}{a_1(a_1 - a_2)}\,e^{a_1 t} + \frac{A + Ba_2 + Ca_2^2}{a_2(a_2 - a_1)}\,e^{a_2 t}\right], \qquad t > 0.}$$

Substituting the expressions for A, B, C, D and E into the coefficients, the strain can be written as

$$\gamma(t) \;=\; f_1 - f_2 e^{-t/\tau_s} - f_3 e^{-t/\tau_f}, \qquad t > 0,$$

with

$$f_1 = \frac{A\sigma_0}{E_{z2}},$$

$$f_2 = -\frac{\sigma_0}{\sqrt{D^2 - 4E_{z2}E}}\left(\frac{2AE}{-D + \sqrt{D^2 - 4E_{z2}E}} + B + \frac{C(-D + \sqrt{D^2 - 4E_{z2}E})}{2E}\right),$$

$$f_3 = \frac{\sigma_0}{\sqrt{D^2 - 4E_{z2}E}}\left(\frac{2AE}{-D - \sqrt{D^2 - 4E_{z2}E}} + B + \frac{C(-D - \sqrt{D^2 - 4E_{z2}E})}{2E}\right),$$

Here the coefficients A, B, C, D, E are defined earlier in the text. The time constants are defined by

$$\tau_{f,s} = \left(\frac{2E}{D \pm \sqrt{D^2 - 4E_{z2}E}} \right) \tag{15}$$

where τ_f and τ_s denote the fast and slow relaxation times, respectively. Finally, the relaxation time constants can be written explicitly by substituting their definitions as;

$$\tau_{f,s} = \frac{2\left(\frac{\eta_z\eta_m}{E_{z1}} + \frac{\eta_z\eta_m}{E_m}\right)}{\left(\frac{E_{z2}\eta_m}{E_{z1}} + \frac{E_{z2}\eta_m}{E_m} + \eta_z + \eta_m\right) \pm \sqrt{\left(\frac{E_{z2}\eta_m}{E_{z1}} + \frac{E_{z2}\eta_m}{E_m} + \eta_z + \eta_m\right)^2 - 4E_{z2}\left(\frac{\eta_z\eta_m}{E_{z1}} + \frac{\eta_z\eta_m}{E_m}\right)}} \tag{16}$$

For stress release at time $t = t_{\text{rel}}$ (after the system has reached equilibrium), the derivation proceeds analogously to the loading case. The main differences are:

- The applied stress is set to zero for $t \geq t_{\text{rel}}$, i.e. $\sigma(t) = 0$.
- The initial strain at $t = t_{\text{rel}}$ corresponds to the equilibrium value attained under the sustained load, namely $\gamma(t_{\text{rel}}) = f_1$.

Following similar steps as in the loading case (without repeating the full derivation here), the strain during release is obtained as

$$\gamma(t - t_{\text{rel}}) = f_2\, e^{-(t-t_{\text{rel}})/\tau_s} + f_3\, e^{-(t-t_{\text{rel}})/\tau_f}, \quad t \geq t_{\text{rel}}, \tag{17}$$

where f_2, f_3, τ_s, and τ_f are the same coefficients and time constants defined in the loading case. Combining the two cases, the full response can be written compactly as

$$\gamma(t) = \begin{cases} f_1 - f_2 e^{-t/\tau_s} - f_3 e^{-t/\tau_f}, & t < t_{\text{rel}}, \\ f_2 e^{-(t-t_{\text{rel}})/\tau_s} + f_3 e^{-(t-t_{\text{rel}})/\tau_f}, & t \geq t_{\text{rel}}. \end{cases}$$

G Derivation of the Buckling Models

G.1 Buckling model with an elastic foundation

We perform a linear stability analysis about the straight configuration of the rod under a uniform compressive prestress T_0, for which

$$N = m = u = C = 0,$$

and consider modal solutions of the form:

$$\{m, u\} \sim e^{iqs+\omega t}. \tag{1}$$

For a viscoelastic rod, the constitutive relation is

$$(1 + \tau\partial_t)m = B\tau\partial_t C. \tag{2}$$

Using the modal ansatz $\{m, u\} \sim e^{iqs+\omega t}$, the derivatives act as

$$\partial_t \to \omega, \qquad \partial_s \to iq \quad (i.e.\ \partial_t e^{iqs+\omega t} = \omega e^{iqs+\omega t},\ \partial_s e^{iqs+\omega t} = iqe^{iqs+\omega t}) \tag{3}$$

and $C \approx \partial_s^2 u$, equation 2 becomes:

$$(1 + \omega\tau)m = -B\tau\omega q^2 u. \tag{4}$$

The torque balance is

$$\partial_s m + N = 0, \quad N = -\partial_s m \implies \partial_s N = -\partial_s^2 m = q^2 m. \tag{5}$$

The force balance is

$$\partial_s N + T_0\partial_s^2 u = Ku \implies q^2 m - T_0 q^2 u = Ku. \tag{6}$$

Substituting m from the previous equation gives:

$$q^2\left(-\frac{B\tau\omega q^2}{1+\omega\tau}u\right) - T_0 q^2 u = Ku,$$

$$B\tau\omega q^4 u + T_0 q^2(1+\omega\tau)u = -K(1+\omega\tau)u. \tag{7}$$

After rearranging and comparing coefficients of u on both sides, we obtain the dispersion relation for the growth rate ω

$$\omega\tau = -\frac{K + T_0 q^2}{Bq^4 + T_0 q^2 + K}. \tag{8}$$

This expression describes the growth rate of perturbations for a given wavenumber q.

Second derivative

Write

$$\frac{d\omega}{dx} = \frac{U(x)}{V(x)}, \qquad U(x) = B\,x\,(T_0 x + 2K), \quad V(x) = (Bx^2 + T_0 x + K)^2.$$

Then

$$\frac{d^2\omega}{dx^2} = \frac{U'V - UV'}{V^2}, \qquad U'(x) = 2B\,(T_0 x + K), \quad V'(x) = 2(Bx^2 + T_0 x + K)(2Bx + T_0).$$

At x_* we have $T_0 x_* + 2K = 0$, hence $U(x_*) = 0$ and

$$\left.\frac{d^2\omega}{dx^2}\right|_{x_*} = \frac{U'(x_*)}{V(x_*)}.$$

Compute

$$U'(x_*) = 2B\,(T_0 x_* + K) = 2B(-2K + K) = -2BK.$$

Also let,

$$D(x_*) = Bx_*^2 + T_0 x_* + K = \frac{4BK^2}{T_0^2} - K = \frac{K(4BK - T_0^2)}{T_0^2},$$

so

$$V(x_*) = D(x_*)^2 = \frac{K^2(4BK - T_0^2)^2}{T_0^4}.$$

Therefore

$$\left.\frac{d^2\omega}{dx^2}\right|_{x_*} = \frac{-2BK}{\frac{K^2(4BK-T_0^2)^2}{T_0^4}} = -\frac{2B\,T_0^4}{K(4BK - T_0^2)^2}.$$

Since $B > 0$, $K > 0$, this is strictly negative.

Convert to q

With $x = q^2$,

$$\frac{d}{dq} = 2q\,\frac{d}{dx} \quad \Rightarrow \quad \frac{d^2\omega}{dq^2} = 2\frac{d\omega}{dx} + 4q^2\frac{d^2\omega}{dx^2}.$$

At q_*, $\frac{d\omega}{dx} = 0$, so

$$\left.\frac{d^2\omega}{dq^2}\right|_{q_*} = 4q_*^2\left.\frac{d^2\omega}{dx^2}\right|_{x_*}.$$

Because $q_*^2 > 0$ and $\frac{d^2\omega}{dx^2}|_{x_*} < 0$, we conclude

$$\boxed{\left.\frac{d^2\omega}{dq^2}\right|_{q_*} < 0}$$

so the stationary point $q_* = \sqrt{-2K/T_0}$ is a local maximum of $\omega(q)$, corresponding to the most-dominant (most unstable) mode.

G.2 Viscoelastic foundation (Kelvin–Voigt model)

Assuming the external normal force follows a Kelvin–Voigt viscoelastic model, we have

$$F_{\text{ext},n} = -(Ku + \eta_c\,\partial_t u). \tag{9}$$

If we follow exactly the same procedure as in the case described above, then in Eq. 7 we simply replace K by $K + \eta_c\omega$.

$$B\tau\omega q^4 u + T_0 q^2(1 + \omega\tau)u = -(K + \eta_c\omega)(1 + \omega\tau)u. \tag{10}$$

After rearranging and comparing coefficients of u on both sides, we obtain:

$$\eta_c\tau\omega^2 + (B\tau q^4 + T_0\tau q^2 + K\tau + \eta_c)\omega + (T_0 q^2 + K) = 0$$

$$\omega^2 + \frac{B\tau q^4 + T_0\tau q^2 + K\tau + \eta_c}{\eta_c\tau}\,\omega + \frac{T_0 q^2 + K}{\eta_c\tau} = 0 \tag{11}$$

Let ω_1 and ω_2 are the roots of the equation, given by

$$\omega_{1,2} = -\frac{1}{2}\left(\frac{B\tau q^4 + T_0\tau q^2 + K\tau + \eta_c}{\eta_c\tau}\right) \pm \frac{1}{2}\sqrt{\left(\frac{B\tau q^4 + T_0\tau q^2 + K\tau + \eta_c}{\eta_c\tau}\right)^2 - 4\frac{T_0 q^2 + K}{\eta_c\tau}} \tag{12}$$

If the roots are real and distinct (with at least one root expected to be positive for buckling to occur), the time variation of the transverse displacement $u(t)$ can be written as

$$u(t) \sim u_1 e^{\omega_1 t} + u_2 e^{\omega_2 t} \tag{13}$$

where u_1 and u_2 are constants determined from the initial conditions. Since ω_2 is always negative for all $q > 0$, while ω_1 can become positive for certain values of q, it is ω_1 that represents the dominant growth rate responsible for buckling. So now I will focus on ω_1. Let $x = q^2$ and

$$a = \left(\frac{B\tau x^4 + T_0\tau x + K\tau + \eta_c}{\eta_c\tau}\right), \qquad b = \frac{T_0 x + K}{\eta_c\tau}. \tag{14}$$

Then ω_1 can be written as

$$\omega_1 = \frac{-a + \sqrt{a^2 - 4b}}{2}. \tag{15}$$

Cutoff wavelength

The cutoff (marginal stability) occurs where a growth-rate root crosses zero, i.e. when $\omega = 0$. Starting from the normalized quadratic form

$$\omega^2 + a(x)\,\omega + b(x) = 0, \qquad x = q^2,$$

set $\omega = 0$. This gives the algebraic condition

$$b(x) = 0.$$

At marginality one of the two algebraic roots $\omega_{1,2}$ must be zero. Since ω_2 is always nonpositive for all $q > 0$ (and in fact does not cross the axis), the root that crosses the axis at marginality is ω_1. Therefore at the cutoff we have

$$\boxed{\omega_1 = 0} \qquad \Longrightarrow \qquad b(x) = 0.$$

Using the explicit form

$$b(x) = \frac{T_0 x + K}{\eta_c \tau},$$

the marginal-stability (cutoff) condition reduces to the simple linear equation

$$T_0 x + K = 0 \quad \Longrightarrow \quad x_c = -\frac{K}{T_0}.$$

Recalling $x = q^2$, the critical wavenumber and corresponding wavelength are

$$q_c = \sqrt{x_c} = \sqrt{-\frac{K}{T_0}}, \qquad \lambda_c = \frac{2\pi}{q_c} = 2\pi\sqrt{-\frac{T_0}{K}}.$$

For a compressive load $T_0 < 0$ we have $x_c > 0$ and q_c is real.

Dominant value of ω_1.

We work with $x = q^2$ and

$$\omega_1(x) = \frac{-a(x) + \sqrt{a(x)^2 - 4b(x)}}{2},$$

where $a(x)$ and $b(x)$ are as defined previously. Differentiating ω_1 with respect to x gives (using $D = a^2 - 4b$)

$$\frac{d\omega_1}{dx} = \frac{-a'(x)}{2} + \frac{a(x)a'(x) - 2b'(x)}{2\sqrt{D(x)}}.$$

Since $x = q^2$, the chain rule yields

$$\frac{d\omega_1}{dq} = \frac{d\omega_1}{dx}\frac{dx}{dq} = 2q\frac{d\omega_1}{dx}. \tag{16}$$

Therefore, any nonzero point in x where $\frac{d\omega_1}{dx} = 0$ with $x > 0$ corresponds to a nonzero point in q where $\frac{d\omega_1}{dq} = 0$ with $q \neq 0$. Thus to find the most unstable wavenumber(s) it suffices to solve $d\omega_1/dx = 0$ for $x > 0$ (and check the second derivative or sign change to distinguish maxima from minima), then take $q = \sqrt{x}$. To calculate the dominant value of ω_1 and corresponding x, we require

$$\frac{d\omega_1}{dx} = 0,$$

which gives

$$\frac{-a'(x)}{2} + \frac{a(x)a'(x) - 2b'(x)}{2\sqrt{D(x)}} = 0.$$

After rearranging, we obtain

$$a'(x)\sqrt{D(x)} = a(x)a'(x) - 2b'(x).$$

Squaring both sides and simplifying using $D(x) = a(x)^2 - 4b(x)$ yields

$$a'(x)^2 b(x) - a(x)a'(x)b'(x) + b'(x)^2 = 0.$$

Next, we calculate the derivatives of $a(x)$ and $b(x)$

$$a(x) = \frac{B\tau x^2 + T_0\tau x + K\tau + \eta_c}{\eta_c\tau}, \qquad b(x) = \frac{T_0 x + K}{\eta_c\tau},$$

$$a'(x) = \frac{2B\tau x + T_0\tau}{\eta_c\tau} = \frac{2Bx + T_0}{\eta_c}, \qquad b'(x) = \frac{T_0}{\eta_c\tau}.$$

Substitute them into the above condition. By collecting terms in x^2, x, and the constant terms and clearing the common denominator $\eta_c^3\tau^2$ yields the numerator

polynomial

$$B x\tau\,(2BT_0\tau\,x^2 + (4BK\tau + T_0^2\tau)\,x + 2T_0(K\tau - \eta_c)) \;\; = \;\; 0.$$

Because $x = q^2$, the trivial root $x = 0$ corresponds to $q = 0$ and is usually excluded when searching for finite-wavelength modes. Dividing the cubic by x (assuming $x \neq 0$) and by the common factors B and τ (since B and $\tau > 0$) gives the quadratic equation that determines the nonzero dominant values of x:

$$2BT_0\tau\,x^2 + (4BK\tau + T_0^2\tau)\,x + 2T_0(K\tau - \eta_c) \;\; = \;\; 0.$$

Let $x_{1,2}$ are the two roots of the equation and are given by

$$\boxed{x_{1,2} \;\; = \;\; \frac{-(4BK\tau + T_0^2\tau) \;\pm\; \sqrt{\tau^2(4BK + T_0^2)^2 - 16BT_0^2\tau\,(K\tau - \eta_c)}}{4BT_0\tau}}\,.$$

The roots may also be written in the alternative form

$$\boxed{x_{1,2} \;\; = \;\; \frac{-(4BK\tau + T_0^2\tau) \;\pm\; \sqrt{\tau^2(4BK - T_0^2)^2 + 16BT_0^2\tau\eta_c}}{4BT_0\tau}}\,.$$

Determining maxima/minima of ω_1. To determine whether the nonzero stationary roots $x_{1,2}$ correspond to a maximum (dominant unstable mode) or a minimum, we examine the second derivative of ω_1 with respect to the wavenumber q. Using the chain-rule relation

$$\boxed{\frac{d^2\omega_1}{dq^2} = 4q^2\,\frac{d^2\omega_1}{dx^2}}$$

the sign of $\frac{d^2\omega_1}{dq^2}$ is determined by the sign of $\frac{d^2\omega_1}{dx^2}$ at the stationary value of x, because $4q^2 > 0$ for $q \neq 0$. Therefore, if

$$\frac{d^2\omega_1}{dx^2}\Big|_{x=x_i} < 0,$$

then $\omega_1(q)$ has a local maximum at $q = \sqrt{x_i}$, corresponding to the dominant growth rate responsible for buckling. Conversely, if the value is positive, the stationary point represents a local minimum.

Rather than presenting the full analytic form of $\frac{d^2\omega_1}{dx^2}$, which is lengthy and not particularly illuminating, we determine the sign of this second derivative numerically using MATLAB. The resulting dispersion curves $\omega_1(q)$ clearly identify the dominant wavenumber, since the peak of each curve corresponds directly to the most unstable wavelength. Thus, even without the explicit analytic expression, the dominant mode can be reliably located through numerical evaluation and visualization of the growth-rate curves.

Bibliography

[1] Eric R Kandel, James H Schwartz, Thomas M Jessell, Steven Siegelbaum, A James Hudspeth, Sarah Mack, et al. *Principles of neural science*, volume 4. McGraw-hill New York, 2000.

[2] Robert H Garman. Histology of the central nervous system. *Toxicologic pathology*, 39(1):22–35, 2011.

[3] Victoria E Johnson, William Stewart, and Douglas H Smith. Axonal pathology in traumatic brain injury. *Experimental neurology*, 246:35–43, 2013.

[4] Rijk De Rooij and Ellen Kuhl. Physical biology of axonal damage. *Frontiers in cellular neuroscience*, 12:144, 2018.

[5] Kimberly S Topp and Benjamin S Boyd. Structure and biomechanics of peripheral nerves: nerve responses to physical stresses and implications for physical therapist practice. *Physical therapy*, 86(1):92–109, 2006.

[6] James B Phillips, Xander Smit, N De Zoysa, Andrew Afoke, and Robert A Brown. Peripheral nerves in the rat exhibit localized heterogeneity of tensile properties during limb movement. *The Journal of physiology*, 557(3):879–887, 2004.

[7] Barry D Jordan. The clinical spectrum of sport-related traumatic brain injury. *Nature Reviews Neurology*, 9(4):222–230, 2013.

[8] Paul Weiss. Nerve patterns: the mechanisms of nerve growth. *Growth*, 5:163–203, 1941.

[9] Douglas H Smith. Stretch growth of integrated axon tracts: extremes and exploitations. *Progress in neurobiology*, 89(3):231–239, 2009.

[10] Chirag Kalelkar, Pramod A Pullarkat, et al. Optical fiber-based force transducer for microscale samples. *Review of Scientific Instruments*, 84(10), 2013.

[11] Sushil Dubey, Chinmay Hemant Joshi, Sukh Veer, Divya Uma, Hema Somanathan, Sayantan Majumdar, and Pramod A Pullarkat. Strain softening and stiffening responses of spider silk fibers probed using a micro-extension rheometer. *Soft Matter*, 16(2):487–493, 2020.

[12] Sushil Dubey, Nishita Bhembre, Shivani Bodas, Sukh Veer, Aurnab Ghose, Andrew Callan-Jones, and Pramod Pullarkat. The axonal actin-spectrin lattice acts as a tension buffering shock absorber. *Elife*, 9:e51772, 2020.

[13] Sushil Dubey, Sukh Veer, RV Seshagiri Rao, Chirag Kalelkar, and Pramod A Pullarkat. Investigation of soft and living matter using a micro-extensional rheometer. *Journal of Physics: Condensed Matter*, 33(8):084003, 2020.

[14] Melanie D. Sweeney, Kassandra Kisler, Axel Montagne, Arthur W. Toga, and Berislav V. Zlokovic. The role of brain vasculature in neurodegenerative disorders. *Nature Neuroscience*, 21(10):1318–1331, October 2018.

[15] Lei Yang, Mengping Wei, Biyu Xing, and Chen Zhang. Extracellular matrix and synapse formation. *Bioscience Reports*, 43(1):BSR20212411, January 2023.

[16] Hemanth Mohan, Matthijs B. Verhoog, Keerthi K. Doreswamy, Guy Eyal, Romy Aardse, Brendan N. Lodder, Natalia A. Goriounova, Boateng Asamoah, A.B. Clementine B. Brakspear, Colin Groot, Sophie van der Sluis, Guilherme Testa-Silva, Joshua Obermayer, Zimbo S.R.M. Boudewijns, Rajeevan T. Narayanan, Johannes C. Baayen, Idan Segev, Huibert D. Mansvelder, and Christiaan P.J. de Kock. Dendritic and Axonal Archi-

tecture of Individual Pyramidal Neurons across Layers of Adult Human Neocortex. *Cerebral Cortex (New York, NY)*, 25(12):4839–4853, December 2015.

[17] Douglas H. Smith. Stretch growth of integrated axon tracts: Extremes and exploitations. *Progress in Neurobiology*, 89(3):231–239, November 2009.

[18] Dominique Debanne, Emilie Campanac, Andrzej Bialowas, Edmond Carlier, and Gisèle Alcaraz. Axon physiology. *Physiological Reviews*, 91(2):555–602, April 2011.

[19] Daniel A. Fletcher and R. Dyche Mullins. Cell mechanics and the cytoskeleton. *Nature*, 463(7280):485–492, January 2010.

[20] The Principles of Nerve Cell Communication. *Alcohol Health and Research World*, 21(2):107–108, 1997.

[21] Alberto E. Pereda. Electrical synapses and their functional interactions with chemical synapses. *Nature Reviews Neuroscience*, 15(4):250–263, April 2014.

[22] Cellular neurometabolism: a tentative to connect cell biology and metabolism in neurology - García-Cazorla - 2018 - Journal of Inherited Metabolic Disease - Wiley Online Library.

[23] Thomas C. Burdett and Marc R. Freeman. Astrocytes eyeball axonal mitochondria. *Science (New York, N.Y.)*, 345(6195):385–386, July 2014.

[24] Stephen G. Waxman, Jeffery D. Kocsis, and Peter K. Stys. *The Axon: Structure, Function, and Pathophysiology.* Oxford University Press, 1995. Google-Books-ID: tMXYkA_G7MkC.

[25] János A. Perge, Jeremy E. Niven, Enrico Mugnaini, Vijay Balasubramanian, and Peter Sterling. Why Do Axons Differ in Caliber? *The Journal of Neuroscience*, 32(2):626–638, January 2012.

[26] Conrad Kiyoshi and Andrea Tedeschi. Axon growth and synaptic function:

a balancing act for axonal regeneration and neuronal circuit formation in CNS trauma and disease. *Developmental neurobiology*, 80(7-8):277–301, July 2020.

[27] Robert R. Bernhardt, Ajay B. Chitnis, Laurie Lindamer, and John Y. Kuwada. Identification of spinal neurons in the embryonic and larval zebrafish. *Journal of Comparative Neurology*, 302(3):603–616, December 1990.

[28] Jay B. Angevine Jr. Nervous system, organization of. 2002.

[29] Cyrus R. Safinya, Uri Raviv, Daniel J. Needleman, Alexandra Zidovska, Myung Chul Choi, Miguel A. Ojeda-Lopez, Kai K. Ewert, Youli Li, Herbert P. Miller, Joel Quispe, Bridget Carragher, Clinton S. Potter, Mahn Won Kim, Stuart C. Feinstein, and Leslie Wilson. Nanoscale Assembly in Biological Systems: From Neuronal Cytoskeletal Proteins to Curvature Stabilizing Lipids. *Advanced materials (Deerfield Beach, Fla.)*, 23(20):10.1002/adma.201004647, May 2011.

[30] Drnnis Bray and Mary Bartlett Bunge. Serial analysis of microtubules in cultured rat sensory axons. *Journal of Neurocytology*, 10(4):589–605, August 1981.

[31] Pc Letourneau. Analysis of microtubule number and length in cytoskeletons of cultured chick sensory neurons. *The Journal of Neuroscience*, 2(6):806–814, June 1982.

[32] W Yu and Pw Baas. Changes in microtubule number and length during axon differentiation. *The Journal of Neuroscience*, 14(5):2818–2829, May 1994.

[33] Peter W. Baas, Anand N. Rao, Andrew J. Matamoros, and Lanfranco Leo. Stability properties of neuronal microtubules. *Cytoskeleton*, 73(9):442–460, 2016. _eprint: https://onlinelibrary.wiley.com/doi/pdf/10.1002/cm.21286.

[34] Lukas C. Kapitein and Casper C. Hoogenraad. Building the Neuronal

Microtubule Cytoskeleton. *Neuron*, 87(3):492–506, August 2015.

[35] Cecilia Conde and Alfredo Cáceres. Microtubule assembly, organization and dynamics in axons and dendrites. *Nature Reviews Neuroscience*, 10(5):319–332, May 2009.

[36] Lawrence S. B. Goldstein and Zhaohuai Yang. Microtubule-Based Transport Systems in Neurons: The Roles of Kinesins and Dyneins. *Annual Review of Neuroscience*, 23(1):39–71, March 2000.

[37] N Hirokawa, Y Shiomura, and S Okabe. Tau proteins: the molecular structure and mode of binding on microtubules. *The Journal of cell biology*, 107(4):1449–1459, October 1988.

[38] J. Chen, Y. Kanai, N. J. Cowan, and N. Hirokawa. Projection domains of MAP2 and tau determine spacings between microtubules in dendrites and axons. *Nature*, 360(6405):674–677, December 1992.

[39] Andreas Prokop. Cytoskeletal organization of axons in vertebrates and invertebrates. *The Journal of Cell Biology*, 219(7):e201912081, July 2020.

[40] K.E. Kasza, C.P. Broedersz, G.H. Koenderink, Y.C. Lin, W. Messner, E.A. Millman, F. Nakamura, T.P. Stossel, F.C. MacKintosh, and D.A. Weitz. Actin Filament Length Tunes Elasticity of Flexibly Cross-Linked Actin Networks. *Biophysical Journal*, 99(4):1091–1100, August 2010.

[41] Gordon Ruthel and Gary Banker. Actin-dependent anterograde movement of growth-cone-like structures along growing hippocampal axons: A novel form of axonal transport? *Cell Motility*, 40(2):160–173, 1998.

[42] Archan Ganguly, Yong Tang, Lina Wang, Kelsey Ladt, Jonathan Loi, Bénédicte Dargent, Christophe Leterrier, and Subhojit Roy. A dynamic formin-dependent deep F-actin network in axons. *Journal of Cell Biology*, 210(3):401–417, August 2015.

[43] Ke Xu, Guisheng Zhong, and Xiaowei Zhuang. Actin, Spectrin, and Asso-

ciated Proteins Form a Periodic Cytoskeletal Structure in Axons. *Science*, 339(6118):452–456, January 2013.

[44] Jiang He, Ruobo Zhou, Zhuhao Wu, Monica A. Carrasco, Peri T. Kurshan, Jonathan E. Farley, David J. Simon, Guiping Wang, Boran Han, Junjie Hao, Evan Heller, Marc R. Freeman, Kang Shen, Tom Maniatis, Marc Tessier-Lavigne, and Xiaowei Zhuang. Prevalent presence of periodic actin–spectrin-based membrane skeleton in a broad range of neuronal cell types and animal species. *Proceedings of the National Academy of Sciences*, 113(21):6029–6034, May 2016.

[45] Boran Han, Ruobo Zhou, Chenglong Xia, and Xiaowei Zhuang. Structural organization of the actin-spectrin–based membrane skeleton in dendrites and soma of neurons. *Proceedings of the National Academy of Sciences*, 114(32), August 2017.

[46] Erika A. Ding and Sanjay Kumar. Neurofilament Biophysics: From Structure to Biomechanics. *Molecular Biology of the Cell*, 35(5):re1, May 2024.

[47] Elisabetta Zucchi, Valentina Bonetto, Gianni Sorarù, Ilaria Martinelli, Piero Parchi, Rocco Liguori, and Jessica Mandrioli. Neurofilaments in motor neuron disorders: towards promising diagnostic and prognostic biomarkers. *Molecular Neurodegeneration*, 15(1):58, October 2020.

[48] Hong Chen, Kun Qian, Zhongwei Du, Jingyuan Cao, Andrew Petersen, Huisheng Liu, Lisle W. Blackbourn, CindyTzu-Ling Huang, Anthony Errigo, Yingnan Yin, Jianfeng Lu, Melvin Ayala, and Su-Chun Zhang. Modeling ALS with iPSCs Reveals that Mutant SOD1 Misregulates Neurofilament Balance in Motor Neurons. *Cell Stem Cell*, 14(6):796–809, June 2014.

[49] P Kaplan, S M Chin, H Fliegner, and K H Liem. dnternexin, a Novel Neuronal Intermediate Filament Protein, Precedes the Low Molecular Weight Neurofilament Protein (NF-L) in the Developing Rat Brain.

[50] Atsuko Uchida, Tomoko Tashiro, Yoshiaki Komiya, Hiroshi Yorifuji, Takeo Kishimoto, and Shin-ichi Hisanaga. Morphological and biochemical changes of neurofilaments in aged rat sciatic nerve axons. *Journal of Neurochemistry*, 88(3):735–745, 2004. _eprint: https://onlinelibrary.wiley.com/doi/pdf/10.1046/j.1471-4159.2003.02201.x.

[51] Alessandro Didonna and Puneet Opal. The role of neurofilament aggregation in neurodegeneration: lessons from rare inherited neurological disorders. *Molecular Neurodegeneration*, 14(1):19, December 2019.

[52] Gregory A. Elder, Victor L. Friedrich, Alla Margita, and Robert A. Lazzarini. Age-Related Atrophy of Motor Axons in Mice Deficient in the Mid-Sized Neurofilament Subunit. *The Journal of Cell Biology*, 146(1):181–192, July 1999.

[53] Aidong Yuan, Mala V. Rao, Veeranna, and Ralph A. Nixon. Neurofilaments and Neurofilament Proteins in Health and Disease. *Cold Spring Harbor Perspectives in Biology*, 9(4):a018309, April 2017.

[54] Jessy V. Van Asperen, Farah Kotaich, Damien Caillol, and Pascale Bomont. Neurofilaments: Novel findings and future challenges. *Current Opinion in Cell Biology*, 87:102326, April 2024.

[55] N. Hirokawa. Cross-linker system between neurofilaments, microtubules, and membranous organelles in frog axons revealed by the quick-freeze, deep-etching method. *The Journal of Cell Biology*, 94(1):129–142, July 1982.

[56] N Hirokawa, M A Glicksman, and M B Willard. Organization of mammalian neurofilament polypeptides within the neuronal cytoskeleton. *The Journal of cell biology*, 98(4):1523–1536, April 1984.

[57] Nobutaka Hirokawa, Shinsuke Niwa, and Yosuke Tanaka. Molecular Motors in Neurons: Transport Mechanisms and Roles in Brain Function, Development, and Disease. *Neuron*, 68(4):610–638, November 2010.

[58] Ana Rita Costa and Monica M. Sousa. Non-Muscle Myosin II in Axonal Cell Biology: From the Growth Cone to the Axon Initial Segment. *Cells*, 9(9):1961, September 2020. Number: 9.

[59] Ronald K.H. Liem. Cytoskeletal Integrators: The Spectrin Superfamily. *Cold Spring Harbor Perspectives in Biology*, 8(10):a018259, October 2016.

[60] Damaris N. Lorenzo. Cargo hold and delivery: Ankyrins, spectrins, and their functional patterning of neurons. *Cytoskeleton*, 77(3-4):129–148, 2020. _eprint: https://onlinelibrary.wiley.com/doi/pdf/10.1002/cm.21602.

[61] Hiroto Shinomiya. Plastin Family of Actin-Bundling Proteins: Its Functions in Leukocytes, Neurons, Intestines, and Cancer. *International Journal of Cell Biology*, 2012(1):213492, 2012. _eprint: https://onlinelibrary.wiley.com/doi/pdf/10.1155/2012/213492.

[62] Min D. Tang-Schomer, Victoria E. Johnson, Peter W. Baas, William Stewart, and Douglas H. Smith. Partial interruption of axonal transport due to microtubule breakage accounts for the formation of periodic varicosities after traumatic axonal injury. *Experimental Neurology*, 233(1):364–372, January 2012.

[63] Douglas H. Smith and David F. Meaney. Axonal Damage in Traumatic Brain Injury. *The Neuroscientist*, 6(6):483–495, December 2000.

[64] Victoria E. Johnson, William Stewart, and Douglas H. Smith. Axonal pathology in traumatic brain injury. *Experimental Neurology*, 246:35–43, August 2013.

[65] Sung Ho Jang, Oh Lyong Kim, Seong Ho Kim, and Jong Bum Kim. The Relation Between Loss of Consciousness, Severity of Traumatic Brain Injury, and Injury of Ascending Reticular Activating System in Patients With Traumatic Brain Injury. *American Journal of Physical Medicine & Rehabilitation*, 98(12):1067–1071, December 2019.

[66] John A. Wolf and Paul F. Koch. Disruption of Network Synchrony and

Cognitive Dysfunction After Traumatic Brain Injury. *Frontiers in Systems Neuroscience*, 10:43, May 2016.

[67] Adam D. Falchook, Eric C. Porges, Stephen E. Nadeau, Susan A. Leon, John B. Williamson, and Kenneth M. Heilman. Cognitive–motor dysfunction after severe traumatic brain injury: A cerebral interhemispheric disconnection syndrome. *Journal of Clinical and Experimental Neuropsychology*, 37(10):1062–1073, November 2015. _eprint: https://doi.org/10.1080/13803395.2015.1077930.

[68] Douglas H. Smith, Masahiro Nonaka, Reid Miller, Matthew Leoni, Xiao-Han Chen, David Alsop, and David F. Meaney. Immediate coma following inertial brain injury dependent on axonal damage in the brainstem. *Journal of Neurosurgery*, 93(2):315–322, August 2000.

[69] Kendall Rae Walker and Giuseppina Tesco. Molecular mechanisms of cognitive dysfunction following traumatic brain injury. *Frontiers in Aging Neuroscience*, 5, July 2013.

[70] Wei Ouyang, Qichao Yan, Yu Zhang, and Zhiheng Fan. Moderate injury in motor-sensory cortex causes behavioral deficits accompanied by electrophysiological changes in mice adulthood. *PLoS ONE*, 12(2):e0171976, February 2017.

[71] Saurav Bhowmick, Veera D'Mello, Nizmi Ponery, and P. M. Abdul Muneer. Neurodegeneration and Sensorimotor Deficits in the Mouse Model of Traumatic Brain Injury. *Brain Sciences*, 8(1):11, January 2018. Number: 1.

[72] Vitalii I. Tsymbaliuk, Milan V. Vorodi, Taras I. Petriv, Iaroslav V. Tsymbaliuk, and Oleksii S. Nekhlopochyn. Peripheral nerve traction injury. Literature review. *Ukrainian Neurosurgical Journal*, 29(3):19–25, September 2023.

[73] J.A. Machado, M.F. Ghizoni, J. Bertelli, Gabriel C. Teske, Guilherme C. Teske, D.F. Martins, L. Mazzardo-Martins, E. Cargnin-Ferreira, A.R.S.

Santos, and A.P. Piovezan. Stretch-induced nerve injury: a proposed technique for the study of nerve regeneration and evaluation of the influence of gabapentin on this model. *Brazilian Journal of Medical and Biological Research*, 46(11):929–935, November 2013.

[74] Bruna Lopes, Patrícia Sousa, Rui Alvites, Mariana Branquinho, Ana Catarina Sousa, Carla Mendonça, Luís Miguel Atayde, Ana Lúcia Luís, Artur S. P. Varejão, and Ana Colette Maurício. Peripheral Nerve Injury Treatments and Advances: One Health Perspective. *International Journal of Molecular Sciences*, 23(2):918, January 2022.

[75] Ghulam Hussain, Jing Wang, Azhar Rasul, Haseeb Anwar, Muhammad Qasim, Shamaila Zafar, Nimra Aziz, Aroona Razzaq, Rashad Hussain, Jose-Luis Gonzalez de Aguilar, and Tao Sun. Current Status of Therapeutic Approaches against Peripheral Nerve Injuries: A Detailed Story from Injury to Recovery. *International Journal of Biological Sciences*, 16(1):116–134, January 2020.

[76] Margo A. Lillie, A. Wayne Vogl, Kelsey N. Gil, John M. Gosline, and Robert E. Shadwick. Two Levels of Waviness Are Necessary to Package the Highly Extensible Nerves in Rorqual Whales. *Current Biology*, 27(5):673–679, March 2017.

[77] R. Adalbert and M. P. Coleman. Review: Axon pathology in age-related neurodegenerative disorders. *Neuropathology and Applied Neurobiology*, 39(2):90–108, 2013. _eprint: https://onlinelibrary.wiley.com/doi/pdf/10.1111/j.1365-2990.2012.01308.x.

[78] James Fawcett. The Struggle to Make CNS Axons Regenerate: Why Has It Been so Difficult? *Neurochemical Research*, 45, January 2020.

[79] Palaniappan Ganesh Nagappan, Hong Chen, and De-Yun Wang. Neuroregeneration and plasticity: a review of the physiological mechanisms

for achieving functional recovery postinjury. *Military Medical Research*, 7(1):30, June 2020.

[80] Patrick Cooke, Haley Janowitz, and Sarah E. Dougherty. Neuronal Redevelopment and the Regeneration of Neuromodulatory Axons in the Adult Mammalian Central Nervous System. *Frontiers in Cellular Neuroscience*, 16, April 2022.

[81] Roberto Bernal, Pramod A. Pullarkat, and Francisco Melo. Mechanical Properties of Axons. *Physical Review Letters*, 99(1), July 2007.

[82] Joshua Chetta, Cecilia Kye, and Sameer B. Shah. Cytoskeletal dynamics in response to tensile loading of mammalian axons. *Cytoskeleton*, 67(10):650–665, 2010. _eprint: https://onlinelibrary.wiley.com/doi/pdf/10.1002/cm.20478.

[83] Md Saddam Hossain Joy, Duncan L. Nall, Bashar Emon, Ki Yun Lee, Alexandra Barishman, Movviz Ahmed, Saeedur Rahman, Paul R. Selvin, and M. Taher A. Saif. Synapses without tension fail to fire in an in vitro network of hippocampal neurons. *Proceedings of the National Academy of Sciences*, 120(52):e2311995120, December 2023.

[84] Grace A. Woods, Nicholas J. Rommelfanger, and Guosong Hong. Bioinspired Materials for In Vivo Bioelectronic Neural Interfaces. *Matter*, 3(4):1087–1113, October 2020.

[85] T J Dennerll, P Lamoureux, R E Buxbaum, and S R Heidemann. The cytomechanics of axonal elongation and retraction. *The Journal of cell biology*, 109(6):3073–3083, December 1989.

[86] T J Dennerll, H C Joshi, V L Steel, R E Buxbaum, and S R Heidemann. Tension and compression in the cytoskeleton of PC-12 neurites. II: Quantitative measurements. *The Journal of cell biology*, 107(2):665–674, August 1988.

[87] D. Bray. Axonal growth in response to experimentally applied mechanical

tension. *Developmental Biology*, 102(2):379–389, April 1984.

[88] J Zheng, P Lamoureux, V Santiago, T Dennerll, Re Buxbaum, and Sr Heidemann. Tensile regulation of axonal elongation and initiation. *The Journal of Neuroscience*, 11(4):1117–1125, April 1991.

[89] Jagannathan Rajagopalan, Alireza Tofangchi, and M. Taher A. Saif. Drosophila Neurons Actively Regulate Axonal Tension In Vivo. *Biophysical Journal*, 99(10):3208–3215, November 2010.

[90] Roberto Bernal, Francisco Melo, and Pramod A. Pullarkat. Drag Force as a Tool to Test the Active Mechanical Response of PC12 Neurites. *Biophysical Journal*, 98(4):515–523, February 2010.

[91] Hui Ouyang, Eric Nauman, and Riyi Shi. Contribution of cytoskeletal elements to the axonal mechanical properties. *Journal of Biological Engineering*, 7(1):21, December 2013.

[92] Ze Gong, Chao Fang, Ran You, Xueying Shao, Xi Wei, Raymond Chuen-Chung Chang, and Yuan Lin. Distinct relaxation timescales of neurites revealed by rate-dependent indentation, relaxation and micro-rheology tests. *Soft Matter*, 15(2):166–174, January 2019.

[93] Thomas Grevesse, Borna E. Dabiri, Kevin Kit Parker, and Sylvain Gabriele. Opposite rheological properties of neuronal microcompartments predict axonal vulnerability in brain injury. *Scientific Reports*, 5(1):9475, March 2015.

[94] Min D. Tang-Schomer, Ankur R. Patel, Peter W. Baas, and Douglas H. Smith. Mechanical breaking of microtubules in axons during dynamic stretch injury underlies delayed elasticity, microtubule disassembly, and axon degeneration. *The FASEB Journal*, 24(5):1401–1410, May 2010.

[95] Hossein Ahmadzadeh, Douglas H. Smith, and Vivek B. Shenoy. Viscoelasticity of Tau Proteins Leads to Strain Rate-Dependent Breaking of Microtubules during Axonal Stretch Injury: Predictions from a Mathemat-

ical Model. *Biophysical Journal*, 106(5):1123–1133, March 2014. Ahmazadeh_el_el_microtubule_damage_during_stretching.

[96] Hossein Ahmadzadeh, Douglas H. Smith, and Vivek B. Shenoy. Mechanical Effects of Dynamic Binding between Tau Proteins on Microtubules during Axonal Injury. *Biophysical Journal*, 109(11):2328–2337, December 2015.

[97] Marc Hammarlund, Erik M. Jorgensen, and Michael J. Bastiani. Axons break in animals lacking -spectrin. *The Journal of Cell Biology*, 176(3):269–275, January 2007.

[98] Michael Krieg, Alexander R. Dunn, and Miriam B. Goodman. Mechanical control of the sense of touch by -spectrin. *Nature Cell Biology*, 16(3):224–233, March 2014.

[99] Ana Rita Costa, Sara C Sousa, Rita Pinto-Costa, José C Mateus, Cátia DF Lopes, Ana Catarina Costa, David Rosa, Diana Machado, Luis Pajuelo, Xuewei Wang, Feng-quan Zhou, António J Pereira, Paula Sampaio, Boris Y Rubinstein, Inês Mendes Pinto, Marko Lampe, Paulo Aguiar, and Monica M Sousa. The membrane periodic skeleton is an actomyosin network that regulates axonal diameter and conduction. *eLife*, 9:e55471, March 2020.

[100] Tong Wang, Wei Li, Sally Martin, Andreas Papadopulos, Merja Joensuu, Chunxia Liu, Anmin Jiang, Golnoosh Shamsollahi, Rumelo Amor, Vanessa Lanoue, Pranesh Padmanabhan, and Frédéric A. Meunier. Radial contractility of actomyosin rings facilitates axonal trafficking and structural stability. *Journal of Cell Biology*, 219(5):e201902001, May 2020.

[101] L. Kreplak, H. Bär, J.F. Leterrier, H. Herrmann, and U. Aebi. Exploring the Mechanical Behavior of Single Intermediate Filaments. *Journal of Molecular Biology*, 354(3):569–577, December 2005.

[102] Oliver I. Wagner, Sebastian Rammensee, Neha Korde, Qi Wen, Jean-

Francois Leterrier, and Paul A. Janmey. Softness, strength and self-repair in intermediate filament networks. *Experimental cell research*, 313(10):2228–2235, June 2007.

[103] Oliver I. Wagner, Jennifer Ascaño, Mariko Tokito, Jean-Francois Leterrier, Paul A. Janmey, and Erika L. F. Holzbaur. The Interaction of Neurofilaments with the Microtubule Motor Cytoplasmic Dynein. *Molecular Biology of the Cell*, 15(11):5092–5100, November 2004.

[104] Cheolwha Jung, Teresa M. Chylinski, Aurea Pimenta, Daniela Ortiz, and Thomas B. Shea. Neurofilament Transport Is Dependent on Actin and Myosin. *The Journal of Neuroscience*, 24(43):9486–9496, October 2004.

[105] Martin Nötzel, Gonzalo Rosso, Stephanie Möllmert, Anne Seifert, Raimund Schlüßler, Kyoohyun Kim, Andreas Hermann, and Jochen Guck. Axonal Transport, Phase-Separated Compartments, and Neuron Mechanics - A New Approach to Investigate Neurodegenerative Diseases. *Frontiers in Cellular Neuroscience*, 12, October 2018.

[106] Lilli Winter and Gerhard Wiche. The many faces of plectin and plectinopathies: pathology and mechanisms. *Acta Neuropathologica*, 125(1):77–93, January 2013.

[107] Yongcheol Cho, Dongeun Park, and Valeria Cavalli. Filamin A Is Required in Injured Axons for HDAC5 Activity and Axon Regeneration. *The Journal of Biological Chemistry*, 290(37):22759–22770, September 2015.

[108] Kalynn M Bird and Paul M Jenkins. Regulation of neuronal ankyrin localization and function by post-translational modifications. *Biochemical Society Transactions*, 2025.

[109] Nicole H. Romano, Christopher M. Madl, and Sarah C. Heilshorn. Matrix RGD ligand density and L1CAM-mediated Schwann cell interactions synergistically enhance neurite outgrowth. *Acta biomaterialia*, 11:48–57, January 2015.

[110] Alireza Tofangchi, Anthony Fan, and M. Taher A. Saif. Mechanism of Axonal Contractility in Embryonic Drosophila Motor Neurons In Vivo. *Biophysical Journal*, 111(7):1519–1527, October 2016.

[111] Sampada P. Mutalik, Joby Joseph, Pramod A. Pullarkat, and Aurnab Ghose. Cytoskeletal Mechanisms of Axonal Contractility. *Biophysical Journal*, 115(4):713–724, August 2018. Citation key.

[112] Yan He, Wenqian Yu, and Peter W. Baas. Microtubule Reconfiguration during Axonal Retraction Induced by Nitric Oxide. *The Journal of Neuroscience*, 22(14):5982–5991, July 2002.

[113] Anil Bagri, Hwai-Jong Cheng, Avraham Yaron, Samuel J. Pleasure, and Marc Tessier-Lavigne. Stereotyped Pruning of Long Hippocampal Axon Branches Triggered by Retraction Inducers of the Semaphorin Family. *Cell*, 113(3):285–299, May 2003.

[114] Kristian Franze, Jens Gerdelmann, Michael Weick, Timo Betz, Steve Pawlizak, Melike Lakadamyali, Johannes Bayer, Katja Rillich, Michael Gögler, Yun-Bi Lu, Andreas Reichenbach, Paul Janmey, and Josef Käs. Neurite Branch Retraction Is Caused by a Threshold-Dependent Mechanical Impact. *Biophysical Journal*, 97(7):1883–1890, October 2009.

[115] Liqun Luo and Dennis D.M. O'Leary. AXON RETRACTION AND DEGENERATION IN DEVELOPMENT AND DISEASE. *Annual Review of Neuroscience*, 28(1):127–156, July 2005.

[116] Xueying Shao, Ran You, Tsz Hin Hui, Chao Fang, Ze Gong, Zishen Yan, Raymond Chuen Chung Chang, Vivek B. Shenoy, and Yuan Lin. Tension- and Adhesion-Regulated Retraction of Injured Axons. *Biophysical Journal*, 117(2):193–202, July 2019.

[117] Gianluca Gallo. Myosin II activity is required for severing-induced axon retraction in vitro. *Experimental Neurology*, 189(1):112–121, September 2004.

[118] Hong-jun Song and Mu-ming Poo. Signal transduction underlying growth cone guidance by diffusible factors. *Current opinion in neurobiology*, 9(3):355–363, 1999.

[119] P Baas. Force generation by cytoskeletal motor proteins as a regulator of axonal elongation and retraction. *Trends in Cell Biology*, 11(6):244–249, June 2001.

[120] Wen Lu and Vladimir I. Gelfand. Moonlighting motors: kinesin, dynein and cell polarity. *Trends in cell biology*, 27(7):505–514, July 2017.

[121] Dietmar B. Oelz, Urko del Castillo, Vladimir I. Gelfand, and Alex Mogilner. Microtubule Dynamics, Kinesin-1 Sliding, and Dynein Action Drive Growth of Cell Processes. *Biophysical Journal*, 115(8):1614–1624, October 2018.

[122] Sagnik Paul, Chirag Kalelkar, and Pramod A. Pullarkat. Oscillatory extensional rheology of microscale fluid filaments. *Rheologica Acta*, 56(2):113–122, February 2017.

[123] Himanshu Marwah, Hetarth Bhatt, Neeraj Fartyal, Rohit Nautiyal, Sukh Veer, and Sreenath Balakrishnan. Estimating anisotropy of single cells using a compliant biaxial stretcher.

[124] LD Landau and EM Lifshitz. Theory of elasticity elsevier. *Ltd., Amsterdam, Netherlands*, 1986.

[125] Douglas H. Smith, John A. Wolf, Theresa A. Lusardi, Virginia M.-Y. Lee, and David F. Meaney. High Tolerance and Delayed Elastic Response of Cultured Axons to Dynamic Stretch Injury. *The Journal of Neuroscience*, 19(11):4263–4269, June 1999.

[126] David F. Meaney, Inifome Ewoterai, John A. Wolf, Theresa G. Lusardi, and Douglas H. Smith. Mechanical Recovery of Cultured Axons After Dynamic Stretch: Correlation to Cytoskeletal Changes.

[127] Saumya Yadav and Ambarish Kunwar. Temperature-Dependent Activity of Motor Proteins: Energetics and Their Implications for Collective Behavior. *Frontiers in Cell and Developmental Biology*, 9:610899, February 2021.

[128] P F Turner and R L Margolis. Taxol-induced bundling of brain-derived microtubules. *The Journal of cell biology*, 99(3):940–946, September 1984.

[129] Peter W. Baas and Fridoon J. Ahmad. Beyond taxol: microtubule-based treatment of disease and injury of the nervous system. *Brain*, 136(10):2937–2951, October 2013.

[130] Yue Qu, Ines Hahn, Stephen E.D. Webb, Simon P. Pearce, and Andreas Prokop. Periodic actin structures in neuronal axons are required to maintain microtubules. *Molecular Biology of the Cell*, 28(2):296–308, January 2017.

[131] Anagha Datar, Jaishabanu Ameeramja, Alka Bhat, Roli Srivastava, Ashish Mishra, Roberto Bernal, Jacques Prost, Andrew Callan-Jones, and Pramod A. Pullarkat. The Roles of Microtubules and Membrane Tension in Axonal Beading, Retraction, and Atrophy. *Biophysical Journal*, 117(5):880–891, September 2019.

[132] Sérgio Carvalho Leite, Paula Sampaio, Vera Filipe Sousa, Joana Nogueira-Rodrigues, Rita Pinto-Costa, Luanne Laurel Peters, Pedro Brites, and Mónica Mendes Sousa. The Actin-Binding Protein -Adducin Is Required for Maintaining Axon Diameter. *Cell Reports*, 15(3):490–498, April 2016.

[133] Ana Rita Costa, Rita Pinto-Costa, Sara Castro Sousa, and Mónica Mendes Sousa. The Regulation of Axon Diameter: From Axonal Circumferential Contractility to Activity-Dependent Axon Swelling. *Frontiers in Molecular Neuroscience*, 11:319, September 2018.

[134] Jasna Križ, Qinzang Zhu, Jean-Pierre Julien, and Ante L. Padjen. Electrophysiological properties of axons in mice lacking neurofilament subunit genes: disparity between conduction velocity and axon diameter in absence of NF-H. *Brain Research*, 885(1):32–44, December 2000.

[135] Reinhard L. Friede and T. Samorajski. Axon caliber related to neurofilaments and microtubules in sciatic nerve fibers of rats and mice. *The Anatomical Record*, 167(4):379–387, August 1970.

[136] L. Alfei, L. Medolago Albani, A. R. Mosetti, C. Scarfo, and A. Stefanelli. Cytoskeletal components and calibers in developing fish Mauthner axon (*Salmo gairdneri Rich*). *Journal of Comparative Neurology*, 314(1):164–170, December 1991.

[137] Adam J. Fournier, James D. Hogan, Labchan Rajbhandari, Shiva Shrestha, Arun Venkatesan, and K. T. Ramesh. Changes in Neurofilament and Microtubule Distribution following Focal Axon Compression. *PLoS ONE*, 10(6):e0131617, June 2015.

[138] W Yu and Pw Baas. The growth of the axon is not dependent upon net microtubule assembly at its distal tip. *The Journal of Neuroscience*, 15(10):6827–6833, October 1995.

[139] Shrobona Guha, Ankita Patil, Hemalatha Muralidharan, and Peter W. Baas. Mini-review: Microtubule sliding in neurons. *Neuroscience Letters*, 753:135867, May 2021.

[140] Peter W. Baas, C. Vidya Nadar, and Kenneth A. Myers. Axonal Transport of Microtubules: the Long and Short of It. *Traffic*, 7(5):490–498, 2006. _eprint: https://onlinelibrary.wiley.com/doi/pdf/10.1111/j.1600-0854.2006.00392.x.

[141] Matthew O'Toole, Phillip Lamoureux, and Kyle E. Miller. A Physical Model of Axonal Elongation: Force, Viscosity, and Adhesions Govern the Mode of Outgrowth. *Biophysical Journal*, 94(7):2610–2620, April 2008.

[142] Rijk de Rooij, Ellen Kuhl, and Kyle E. Miller. Modeling the Axon as an Active Partner with the Growth Cone in Axonal Elongation. *Biophysical Journal*, 115(9):1783–1795, November 2018.

[143] D. Bray. Axonal growth in response to experimentally applied mechanical

tension. *Developmental Biology*, 102(2):379–389, April 1984.

[144] Matthew O'Toole, Phillip Lamoureux, and Kyle E. Miller. Measurement of Subcellular Force Generation in Neurons. *Biophysical Journal*, 108(5):1027–1037, March 2015.

[145] Aurnab Ghose and Pramod Pullarkat. The role of mechanics in axonal stability and development. *Seminars in Cell & Developmental Biology*, 140:22–34, May 2023.

[146] R. De Rooij, K. E. Miller, and E. Kuhl. Modeling molecular mechanisms in the axon. *Computational Mechanics*, 59(3):523–537, March 2017.

[147] Rijk de Rooij and Ellen Kuhl. Microtubule Polymerization and Cross-Link Dynamics Explain Axonal Stiffness and Damage. *Biophysical Journal*, 114(1):201–212, January 2018.

[148] Cornelis Storm, Jennifer J. Pastore, F. C. MacKintosh, T. C. Lubensky, and Paul A. Janmey. Nonlinear elasticity in biological gels. *Nature*, 435(7039):191–194, May 2005.

[149] Pablo Fernández, Pramod A. Pullarkat, and Albrecht Ott. A Master Relation Defines the Nonlinear Viscoelasticity of Single Fibroblasts. *Biophysical Journal*, 90(10):3796–3805, May 2006.

[150] John F Marko and Eric D Siggia. Stretching dna. *Macromolecules*, 28(26):8759–8770, 1995.

[151] Matthias Rief, Jaime Pascual, Matti Saraste, and Hermann E Gaub. Single molecule force spectroscopy of spectrin repeats: low unfolding forces in helix bundles. *Journal of Molecular Biology*, 286(2):553–561, February 1999.

[152] Qiang Zhu and Robert J. Asaro. Spectrin Folding versus Unfolding Reactions and RBC Membrane Stiffness. *Biophysical Journal*, 94(7):2529–2545, April 2008.

[153] B T Stokke, A Mikkelsen, and A Elgsaeter. Spectrin, human erythrocyte

shapes, and mechanochemical properties. *Biophysical Journal*, 49(1):319–327, January 1986.

[154] Kathryn A Scott, Sarah Batey, Karen A Hooton, and Jane Clarke. The Folding of Spectrin Domains I: Wild-type Domains Have the Same Stability but very Different Kinetic Properties.

[155] Julio M. Fernandez and Hongbin Li. Force-Clamp Spectroscopy Monitors the Folding Trajectory of a Single Protein. *Science*, 303(5664):1674–1678, March 2004.

[156] Md Nahian Bin Hossain and Ashfaq Adnan. Mechanical characterization of spectrin at the molecular level. *Scientific Reports*, 14:16631, July 2024.

[157] Md Ishak Khan, Sheikh Fahad Ferdous, and Ashfaq Adnan. Mechanical behavior of actin and spectrin subjected to high strain rate: A molecular dynamics simulation study. *Computational and Structural Biotechnology Journal*, 19:1738–1749, March 2021.

[158] Stephen J. Peter and Mohammad R.K. Mofrad. Computational Modeling of Axonal Microtubule Bundles under Tension. *Biophysical Journal*, 102(4):749–757, February 2012.

[159] Mohammad Soheilypour, Mohaddeseh Peyro, Stephen J. Peter, and Mohammad R.K. Mofrad. Buckling Behavior of Individual and Bundled Microtubules. *Biophysical Journal*, 108(7):1718–1726, April 2015.

[160] Fuad Hasan, Kah Al Mahmud, Md. Ishak Khan, and Ashfaq Adnan. Viscoelastic damage evaluation of the axon. *Frontiers in Bioengineering and Biotechnology*, 10:904818, October 2022.

[161] Sven Konzack, Edda Thies, Alexander Marx, Eva-Maria Mandelkow, and Eckhard Mandelkow. Swimming against the Tide: Mobility of the Microtubule- Associated Protein Tau in Neurons.

[162] Zhaojie Chai, Shiju Gu, and George Lykotrafitis. Dynamics of the axon

plasma membrane skeleton. *Soft Matter*, 19(14):2514–2528, 2023.

[163] Catherine Gorrie, Samantha Oakes, Johan Duflou, Peter Blumbergs, and Phil M.E. Waite. Axonal Injury in Children after Motor Vehicle Crashes: Extent, Distribution, and Size of Axonal Swellings Using -APP Immunohistochemistry. *Journal of Neurotrauma*, 19(10):1171–1182, October 2002.

[164] R. Ross Reichard, Charles L. White, Christa L. Hladik, and David Dolinak. Beta-Amyloid Precursor Protein Staining of Nonaccidental Central Nervous System Injury in Pediatric Autopsies. *Journal of Neurotrauma*, 20(4):347–355, April 2003.

[165] Karina S. Cramer, Catherine A. Leamey, and Mriganka Sur. Chapter 8 Nitric oxide as a signaling molecule in visual system development. In *Progress in Brain Research*, volume 118, pages 101–114. Elsevier, 1998.

[166] Alan F. Ernst, Gianluca Gallo, Paul C. Letourneau, and Steven C. McLoon. Stabilization of Growing Retinal Axons by the Combined Signaling of Nitric Oxide and Brain-Derived Neurotrophic Factor. *The Journal of Neuroscience*, 20(4):1458–1469, February 2000.

[167] Georgina E. Lang, Sarah L. Waters, Dominic Vella, and Alain Goriely. Axonal Buckling Following Stretch Injury. *Journal of Elasticity*, 129(1-2):239–256, December 2017.

[168] Yanzhong Wang, Xi Wei, Bo Gong, and Yuan Lin. Coarse-Grained Modeling and Mechanical Behaviors of Actin–Spectrin–Microtubule Complex in Axonal Cytoskeleton. *International Journal of Applied Mechanics*, 14, May 2022.

[169] Clifford P. Brangwynne, Frederick C. MacKintosh, Sanjay Kumar, Nicholas A. Geisse, Jennifer Talbot, L. Mahadevan, Kevin K. Parker, Donald E. Ingber, and David A. Weitz. Microtubules can bear enhanced compressive loads in living cells because of lateral reinforcement. *The Journal of Cell Biology*, 173(5):733–741, June 2006.

[170] Ashish Kumar Mishra. *Mechanical responses of laser ablated axons of neuronal cells*. PhD thesis, Raman Research Institute, Bangalore, India, 2025. Doctoral thesis.

[171] Stefan W. Hell and Jan Wichmann. Breaking the diffraction resolution limit by stimulated emission: stimulated-emission-depletion fluorescence microscopy. *Optics Letters*, 19(11):780, June 1994.

[172] Thomas A. Klar, Stefan Jakobs, Marcus Dyba, Alexander Egner, and Stefan W. Hell. Fluorescence microscopy with diffraction resolution barrier broken by stimulated emission. *Proceedings of the National Academy of Sciences*, 97(15):8206–8210, July 2000.

[173] G. Firpo, E. Angeli, L. Repetto, and U. Valbusa. Permeability thickness dependence of polydimethylsiloxane (PDMS) membranes. *Journal of Membrane Science*, 481:1–8, May 2015.